The role of the autosomal recessive primary microcephaly protein ASPM: A protein involved in mitosis

Marcus John Edward Holt

Submitted in accordance with the requirements for the degree of
Doctor of Philosophy

The University of Leeds
Faculty of Biological Sciences

March 2021

Acknowledgements

I would first like to thank my supervisors, Michelle Peckham and Jacquelyn Bond for their continued help and support throughout my PhD. Without their help, support and guidance, I would not have been able to complete this work. I would also like to thank to the White Rose Doctoral Training Partnership for the many training days and the opportunity to meet and collaborate with other PhD students from around Yorkshire. I would also like to thank the BBSRC for the funding to make this project possible.

I would also like to express my thanks to Sally Boxall and Ruth Hughes for their help with FACS and microscopy related issues, to David Cases-Mao and Glenn Carrington for their help with all things EM. Thanks also go to Alice Lake and Tetsushi Sakuma for assisting with the CRISPR work.

I would also like to acknowledge the past and present members of the Peckham lab group, in no particular order: Marta K, Marcin, Peter, Ruth, Glenn, Brendan, Louise, Charlie, Fran, Alistair, Marta G and David. Particular thanks go to: Marta Kurzawa for training me in all things Sf9, without which none of this thesis would be possible; Louise for listening to all of my venting; Brendan for showing me that breaks are important; and Glenn for providing the very stimulating ‘would you rather’ conundrums.

Finally, I would like to thank my parents for not holding me back. More importantly I would like to thank Emma for constantly believing in me, being there for me and supporting me along the way.

Abstract

Human autosomal recessive primary microcephaly (MCPH) is a hereditary disorder associated with a small brain and associated intellectual disability. Mutations in the gene Assembly factor for spindle microtubules (ASPM) are the most common causes of MCPH. ASPM, a large (~400 kDa) protein, is important in mitosis. It anchors the mitotic spindle at the spindle poles and is essential for normal cytokinesis. However, the complete structure-function of ASPM is not well understood.

The N-terminal domain of ASPM contains 2 tandem calponin homology (CH) domains and binds microtubules. However, the location of the specific binding site is unclear. Two tandem CH domains typically bind actin, whereas single CH domains bind microtubules suggesting the CH domains of ASPM bind actin. The region following the CH domains contains 81 isoleucine-glutamine (IQ) motifs, known to bind light chains such as calmodulin. These motifs form a single alpha-helix to which the light chains bind, suggesting an overall elongated structure for ASPM. Current methods of visualising endogenous ASPM are limited. Therefore, the requirement for the development of tools will aid in understanding how ASPM is involved in mitosis.

Using a combination of mass spectrometry and flow cell assays, it was determined that the tandem CH domains of ASPM bind to microtubules, and not actin, suggesting that the CH domains may be the key binding site of ASPM for microtubules within the N-terminus. Negative stain electron microscopy of a central 21 IQ motif containing domain revealed a long semi-flexible molecule, fully decorated with light chains. These data thus start to reveal the structure and function of ASPM. Initial attempts to visualise ASPM with the use of CRISPR/Cas system proved difficult. However, an Affimer was raised against the tandem CH domains, providing a promising tool to visualise ASPM *in vivo*.

Table of Contents

List of Figures

List of Tables

Abbreviations

2D	Two dimensional
3D	Three dimensional
a.u.	Arbitrary units
ABD	Actin binding domain
AIM	Auto Induction Media
ANKLE2	Ankyrin repeat and LEM domain-containing protein 2
APC	Adenomatous polyposis coli
APC/C	Anaphase-promoting complex
APS	Ammonium persulphate
aRG	Apical radial glial
ARM	Armadillo-like sequence
ASH	ASPM, SPD-2, Hydin
ASNP	ASPM N-proximal
asp	Drosophila abnormal spindle
ASPM	Assembly factor for spindle microtubules
ATCC	American Type Culture Collection
bp	Base pairs
bRG	Basal radial glial
BSA	Bovine serum albumin
CALM2	Calmodulin
Cas	CRISPR-associated protein
Cdk2	Cyclin dependent kinase 2
CDK5RAP2	CDK5 regulatory subunit-associated protein 2
CDK6	Cyclin-dependent kinase 6
cDNA	Coding DNA
CENPE	Centromere-associated protein E
CENPJ	Centromere protein J
CEP135	Centrosomal protein of 135 kDa
CEP152	Centrosomal protein of 152 kDa
CH	Calponin homology
CIP	Calf Intestinal Phosphatase

CITK	Citron Rho-interacting kinase
CNBr	Cyanogen bromide-activated agarose
COPB2	Coatomer subunit beta-2
CP	Cortical plate
CRISPR	Clustered, regularly interspaced, short palindromic repeats
CTR	C-terminal region
DAPI	4’,6-diamidino-2-phenylindole
DMEM	Dulbecco's Modified Eagle Medium
DMSO	Dimethyl sulphoxide
DNA	Deoxyribonucleic acid
dNTPs	Deoxyribonucleotide triphosphate
DPBS	Dulbecco’s phosphate buffered saline
DSHB	Developmental Studies Hybridoma Bank
DSMZ	Deutsche Sammlung von Mikroorganismen und Zellkulturen
DTT	1,4-Dithiothreitol
Dvl-3	Disheleved-3
EB1	End-binding 1
EDTA	Ethylenediaminetetraacetic acid
eGFP	Enhanced Green Fluorescent Protein
EGTA	Ethylene glycol-bis(β-aminoethyl ether)-N,N,N′,N′-tetraacetic acid
ELC	Essential light chain
ELISA	Enzyme-linked immunosorbent assay
ERK1	Extracellular regulated kinase 1
ESCRT	Endosomal sorting complexes required for transport
EtBr	Ethidium bromide
FBS	Foetal bovine serum
FEG	Field Emission Gun
FIJI	FIJI is just imageJ
GBSA	General Borne Surface Area
gDNA	Genomic DNA
GFP	Green Fluorescent Protein
gRNA	Guide RNA
GST	Glutathione S-transferase
GTP	Guanosine triphosphate

H2B	Histone H2B
HA	Homology arm
HDR	Homology driven repair
HEAT	Huntingtin, elongation factor 3 (EF3), protein phosphatase 2A (PP2A), TOR1
HEPES	(4-(2-hydroxyethyl)-1-piperazineethanesulphonic acid)
HP1	Heterochromatin protein 1 homologue
HRP	Horseradish peroxidase
HRV	Human rhinovirus
IC50	Half maximal inhibitory concentration
IF	Immunofluorescence,
IMDM	Iscove's Modified Dulbecco's Medium
IP	Intermediate progenitor
IPTG	Isopropyl β-D-1-thiogalactopyranoside
IQ	Isoleucine-Glutamine
IZ	Intermediate zone
K	Kelvin
kbp	Kilo base pairs
KIF14	Kinesin family member 14
KNL1	Kinetochore scaffold 1
LB	Luria-Bertani
LHS	Left hand side
LIN-5	Abnormal cell LINeage 5
MAP11	Microtubule-associated protein 11
MBP	Maltose Binding Protein
MCPH	Autosomal Recessive Primary Microcephaly
MD	Molecular dynamics
MFSD2A	Sodium-dependent lysophosphatidylcholine symporter 1
MMEJ	Microhomology-mediated end-joining
MOI	Multiplicity of infection
MOPS	3-(N-morpholino)propanesulphonic acid
MSP	Major sperm protein
MT	Microtubules
MTOC	Microtubule organising centre
MW	Molecular weight

MWCO	Molecular weight cut-off
MYL6B	Myosin light chain 6B
MZ	Marginal zone
NCAPD2	Condensin complex subunit 1
NCAPD3	Condensin-2 complex subunit D3
NCAPH	Condensin-2 complex subunit H2
NE	Neuroepithelial
NEB	New England Biolabs
Ni-NTA	Nickel-Nitrilotriacetic acid
NLS	Nuclear localisation signal
nsEM	Negative stain electron microscopy
nt	Nucleotide
NuMA1	Nuclear mitotic apparatus protein 1
NUP37	Nucleoporin 37 kDa
OD	Optical density
PALM	Photoactivatable light microscopy
PAM	Protospacer adjacent motifs
PBS	Phosphate buffered saline
PBS-T	PBS-Tween20
PCM	Pericentriolar matrix
PCR	Polymerase chain reaction
PDB	Protein data bank (base)
PEI	Polyethylenimine
PFA	Paraformaldehyde
PFU	Plaque forming units
PHC1	Polyhomeotic-like protein 1
PI	Post infection
PIPES	Piperazine-N,N′-bis(2-ethanesulphonic acid
PKA	cAMP-dependent protein kinase catalytic subunit a
PMSF	Phenylmethylsulphonyl fluoride
PTMs	Post translational modifications
RHS	Right hand side
RNA	Ribonucleic acid
RNP	Ribonuclear particle

RPM	Rounds per minute
SASS6	Spindle assembly abnormal protein 6 homologue
SCH	Sha1 C-terminal homology
SD	Standard deviation
SDS	Sodium dodecyl sulphate
SDS-PAGE	Sodium dodecyl sulphate polyacrylamide gel electrophoresis
Sf9	*Spodoptera frugiperda*
SF9-ET	Sf9-Easy Titre
sgRNA	Single guide RNA
SOC	Super Optimal broth with Catabolite repression
ssDNA	Single stranded DNA
STIL	SCL-interrupting locus
SVZ	Subventricular zone
TCEP	Tris(2-carboxyethyl)phosphine hydrochloride
TCID50	Median Tissue Culture Infectious Dose
TEMED	N,N,N’,N’-tetramethylethane-1,2-diamine
TEV	Tobacco Etch Virus
Tris	Tris(hydroxymethyl)aminomethane
VZ	Ventricular zone
WB	Western blot
WDFY3	WD repeat and FYVE domain-containing protein 3
WDR62	WD repeat-containing protein 62
ZNF335	Zinc finger protein 335

1. Introduction

1.1 ASPM

The *ASPM* (Assembly factor for spindle microtubules) gene spans 62,567 base pairs (bp) of genomic sequence and has an open reading frame of 10,434 bp and 28 exons (Figure 1.1A) (Bond et al., 2002; Higgins et al., 2010). ASPM is a large protein with multiple domains consisting of 3,477 amino acids with a molecular mass of ~410 kDa (Bond et al., 2002). It is comprised of a microtubule (MT) interacting N-terminal domain, which contains, an ASH domain (ASPM, SPD-2, Hydin), two highly conserved ASNP (ASPM N-proximal) repeats and two tandem calponin-homology (CH) domains (Figure 1.1B). This is followed by 81 Isoleucine-Glutamine (IQ) motifs, which are predicted to bind E-F hand motif light chains such as calmodulin and myosin light chains. The IQ repeats are followed by a C-terminal region (CTR), which contains an armadillo-like sequence (ARM), thought to interact with the cleavage furrow protein, citron kinase (Figure 1.1B) (Bond et al., 2002; Higgins et al., 2010; Kouprina et al., 2005; Paramasivam et al., 2007).

The specific cellular roles of ASPM are not well understood. However, ASPM is a homologue of *Drosophila* abnormal spindle gene (*asp*), which is known to play a role in microtubule organisation during mitosis and cytokinesis (Ito & Goshima, 2015; Wakefield et al., 2001). Experiments in *Drosophila* revealed that asp has actin and calmodulin binding capabilities and associates with MTs at the mitotic spindle (Saunders et al., 1997). A reduction in expression levels of *asp* resulted in metaphase checkpoint arrest and failure of the spindle microtubules to focus at the spindle poles. This suggests ASPM is also likely important in the organisation of the mitotic spindle and orientation of the cleavage furrow (Bond et al., 2002; do Carmo Avides & Glover, 1999; do Carmo Avides et al., 2001; Fish et al., 2006; Higgins et al., 2010; Schoborg et al., 2015).

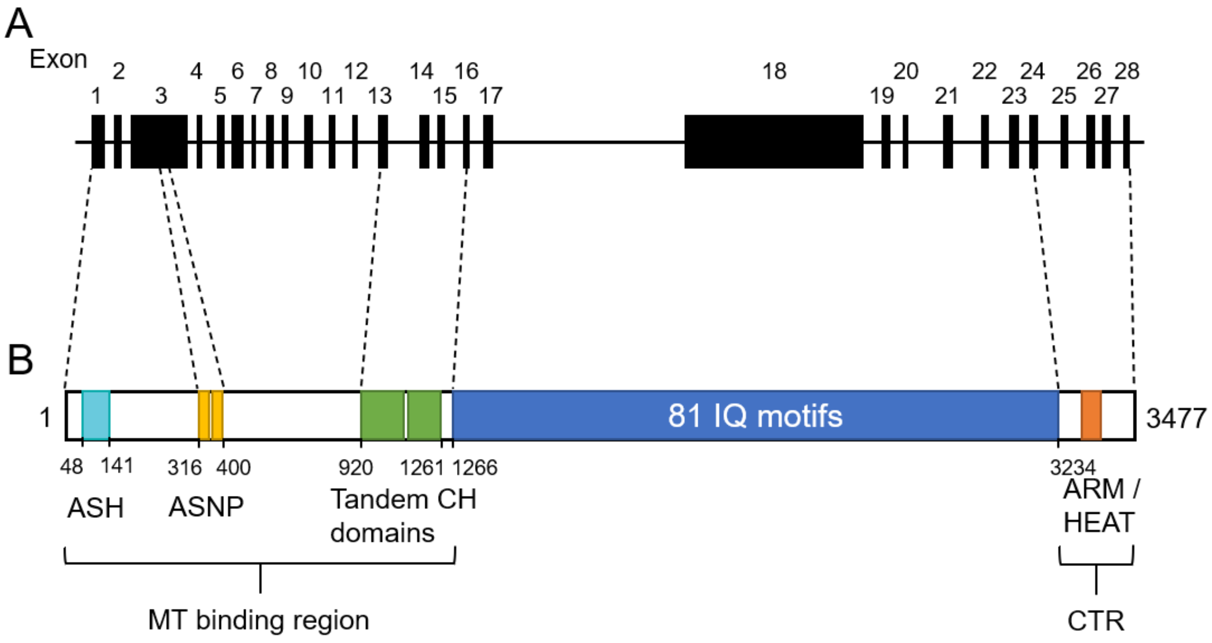

Figure 1.1 – Genomic structure of ASPM and the resulting protein.

(A) The genomic structure of *ASPM* which contains 10,434 bp contained within 28 exons. The dotted lines denote the exon location of each domain of the ASPM protein. (B) The 3,477 amino acid protein ASPM, the regions corresponding to the ASH domain are shown in cyan (48-141); N-proximal repeats are shown in yellow (316-342 and 366-400); tandem calponin-homology (CH) domains are shown as green (920-1,261); 81 IQ motifs are depicted in blue (1,266-3,234); the C-terminal region (CTR) (3,235-3,477) which contains the armadillo-like domain (ARM: 3,294-3,327) is shown in orange.

1.1.1 Cellular localisation of ASPM

ASPM is thought to be involved in several stages of mitosis (Bond et al., 2002; Higgins et al., 2010; Zhong et al., 2005). In interphase, it is located predominantly in the nucleus (Figure 1.2) (Bond et al., 2002), where it is thought to control the activity of the Cyclin dependent kinase 2/cyclin E complex (Capecchi & Pozner, 2015). During prometaphase, ASPM then migrates to the spindle poles (Figure 1.2), more specifically the pericentriolar matrix surrounding the spindle poles, where it remains through to telophase (Bond et al., 2002; Higgins et al., 2010; Zhong et al., 2005). The N-terminal region of ASPM (residues 1-920) has been linked to the organisation of the minus end of microtubules at the spindle poles and ASPM is thought to focus the spindle microtubules during these stages (Ito & Goshima, 2015). This spindle focusing is thought to contribute to the role of ASPM in the symmetric versus asymmetric division of stem cells (Fish et al., 2006; Higgins et al., 2010).

During cytokinesis, ASPM is located in the midbody during abscission (Figure 1.2) (Bond et al., 2002; Higgins et al., 2010; Zhong et al., 2005). It has been proposed that the C-terminal region of ASPM (residues 3,327-3,477) interacts with the cleavage furrow protein: citron kinase. A recent study, using a proximity ligation assay, showed these two proteins to be less than 40 nm apart (Gai et al., 2017). However, ASPM was shown to localised to the midbody only, whereas citron kinase is localised to the cleavage furrow and the midbody, therefore overlap was seen at the midbody only. Interestingly, immunostaining additionally showed that ASPM and citron kinase co-localised throughout the cytoplasm and at the spindle pole indicating that citron kinase interacts with both microtubule-associated ASPM and the cytoplasmic ASPM pool. Co-immunoprecipitation of the ASPM-C-terminal region revealed that it interacted with different regions of citron kinase proposing that the C-terminal region of ASPM may potentially play a role in regulating abscission (Gai et al., 2017). In addition, this interaction was shown to be required for the correct orientation of the mitotic spindle and microtubule stability as ASPM depletion resulted in poor localisation of citron kinase to the spindle pole. The co-localisation of both proteins has been shown to be required for complete abscission at the end of cytokinesis (Gai et al., 2017; Paramasivam et al., 2007), therefore suggesting their importance in the completion of mitosis.

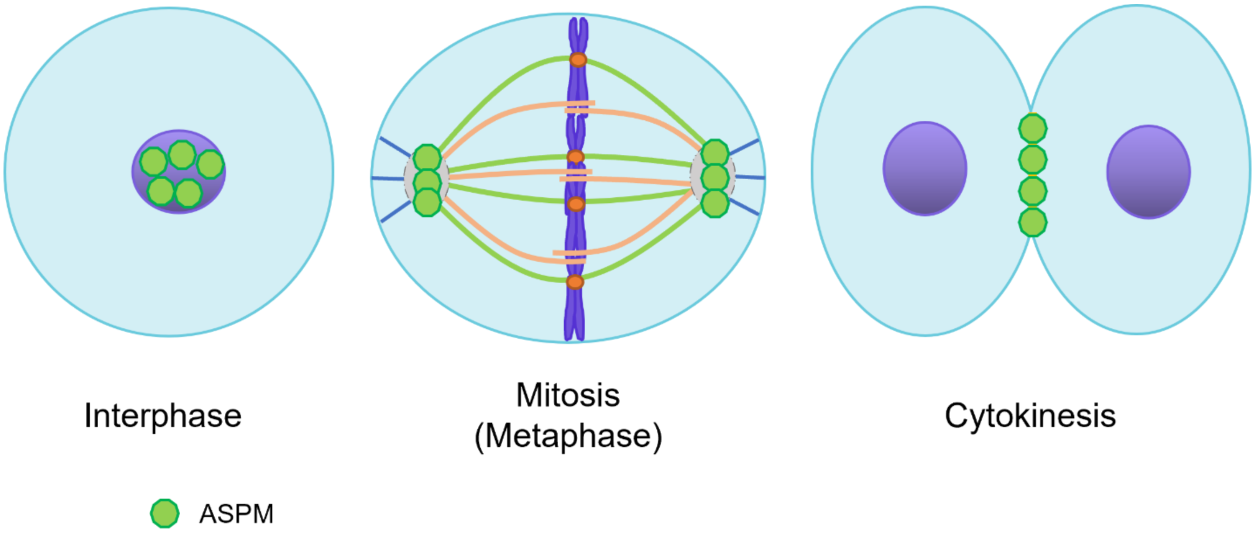

Figure 1.2 – The cellular localisation of ASPM.

ASPM (green) localises to the nucleus (purple) during interphase. Upon entering mitosis, ASPM migrates to the spindle pole (grey) where it is thought to interacts with microtubules (blue, green and orange lines). It remains at the spindle pole until cytokinesis where it localises to the midbody.

1.1.2 The domains of ASPM

1.1.2.1 N-terminal region

The N-terminal region comprises residues 1-1,266 of Human ASPM. The entire N-terminal region has also been shown to interact with MT as shown by Far-Westerns conducted with denatured protein (Saunders et al., 1997) and, more recently, through RNAi knockdown and rescue (Ito & Goshima, 2015). However, the exact location of MT binding is not yet precisely identified. An ASH (ASPM, SPD-2, Hydin) domain lies within the N-terminal 200 residues (residues 48-141). It has been suggested that the sequence of this domain is similar to that of the major sperm protein (MSP) (Jiang et al., 2017; Ponting, 2006), however, BLAST alignment of these two sequences showed no significant similarities. ASH domains may bind MT as MT binding for *D. melanogaster* asp has been localised to this region (Saunders et al., 1997). In agreement with this, SPD-2 which also contains an ASH domain and interacts with centrioles, interacts with microtubules potentially through this domain (Kemp et al., 2004).

Downstream from the ASH domain are two highly conserved repeats originally identified as ASNP (ASPM N-proximal) repeats, 32 and 35 residues in length, located between residues 316-347 and 366-400 (Figure 1.1B). These repeats both start with the consensus sequence LSPDSF[VI]NN and end with LSX[DN]XF[ML]KDN (where X is any amino acid). The central region is more variable (Figure 1.3A) (Kouprina et al., 2005). Initially, the function of these repeats was unknown, however, the conservation of these repeats between multiple species indicated they may be important for ASPM function. Recently, they were shown to bind katanin, a microtubule-severing protein involved in spindle organisation (Ahmad et al., 1999; Jiang et al., 2017). Katanin was shown to bind to three of the four of the tandem repeats (Figure 1.3B). It is not yet clear if these repeats are structurally and functionally distinct.

A

```
ASPM 316-347 | LSPDSFVNNSHGANNELELV---TCLSSDMFMKDN     32

ASPM 366-400 | LSPDSFIKDNYGLNQDLESESVNPILSPNQFLKDN     35

               ******:::.:* *::**       ** : *:***
```

B

```
ASPM 316-324 |      LSPDSFVNN-9  #

ASPM 338-347 |      LSSDMFMKDN10

ASPM 366-375 |      LSPDSFIKDN10 #

ASPM 391-400 |      LSPNQFLKDN10 #

                    ** : *:::
```

Figure 1.3 – Alignment of ASNP repeats.

(A) Alignment of the two original ASPM N-proximal repeats (Kouprina et al., 2005). (B) Alignment of the ASPM N-proximal repeats as depicted by (Jiang et al., 2017), ‘**#**’ indicates katanin binding abilities based on pull-down experiments. Alignments were performed using CLUSTAL Omega, ‘*****’ indicates fully conserved residues, ‘**:**’ indicates strongly similar propertied between residues (>0.5 in the Gonnet PAM 250 matrix), ‘**.**’ indicates weakly similar properties between residues (<0.5 in the Gonnet PAM 250 matrix) (Sievers et al., 2011).

The N-terminal region of ASPM also contains two calponin homology (CH) domains. CH domains were first identified at the N-terminus of calponin, an actin binding protein found in smooth muscle and multiple types of non-muscle cells (Kolakowski et al., 1995; Liu & Jin, 2016; Takahashi et al., 1986). They are approximately 100 amino acids in length (Korenbaum & Rivero, 2002). CH domains have a conserved hydrophobic core and are usually comprised of six α-helices, four of which make up the core (I, III, IV and VI) and two shorter α-helices involved in stabilising the three-dimensional structure (II and V). Of the core α-helices, three (III, IV, VI) form a triple helix bundle and helix I binds across the surface of helices III and VI (Figure 1.4) (Bramham et al., 2002; Ishida et al., 2008). Despite a common overall fold, the sequence of CH domains is divergent, and these domains display a wide variety of binding interactions, such as cytoskeletal proteins and signal transduction (Yin et al., 2020).

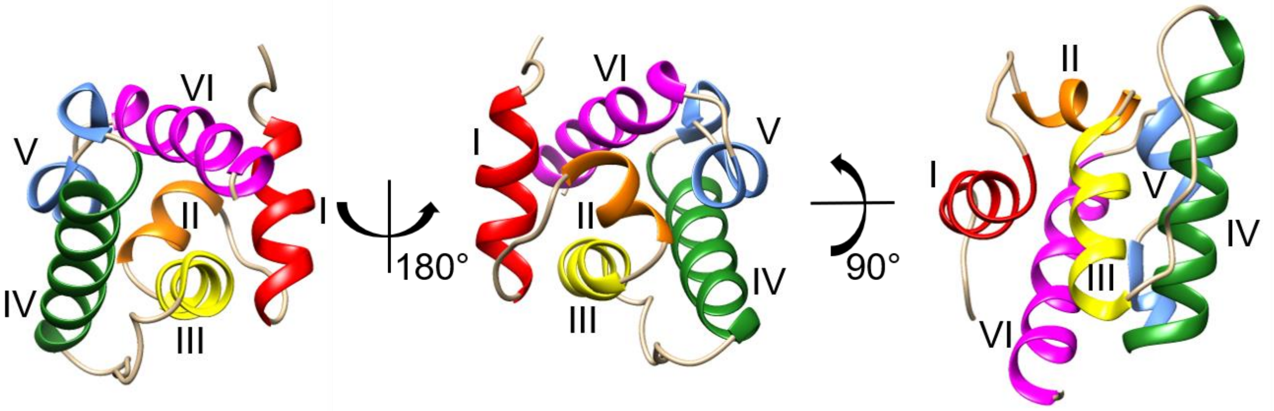

Figure 1.4 – The structure of the CH domain.

(PBD: 1H67) The tertiary structure of the calponin CH domain generated by NMR. The CH domains are compact and globular and contain a total of six α-helices, four main helices (I, III, IV and VI) connected by long loops with two shorter helices (II and V). Structure was generated with Chimera V1.14.

The mechanism by which CH selectively binds to specific targets remains unclear but is thought to be associated with factors such as CH number (whether single or as a tandem pair) or conformational differences within the 3D structure (Bañuelos et al., 1998). CH domains have been classified into several classes based on function, protein family and structure (if known) (Korenbaum & Rivero, 2002). A phylogenetic analysis of CH domain super-family (Figure 1.5) shows the three main subgroups of CH domains. Most of the proteins in these groups contain tandem pairs of CH domains (Type 1 CH + Type 2 CH) that are involved in binding to actin filaments (Gimona et al., 2002). Actin is a globular protein that polymerises into filaments. It can be present in one of two forms; G-actin, which is a free monomer; or F-actin, which is a linear polymer (Gimona et al., 2002). However, some contain a single CH domain (e.g. CAMSAPS, EBs) which typically bind to MT. Microtubules are polymers of a dimer of alpha- and beta- tubulin which form a protofilament. When thirteen protofilaments associate laterally they form a hollow microtubule. Proteins that contain Type 3 CH domains (e.g. IQGAPs and Calponins) are predicted to function differently to Type 1 and 2 CH domains. Although the majority of these Type 3 CH domains bind actin, some (e.g. those found in VAVs) are thought to act as a regulatory domain where it sterically blocks a protein binding interface (Abe et al., 2000). Interestingly, few proteins, which contain a single CH domain, bind neither actin nor microtubules, but to another protein. For example, the Type 3 CH domain in calponin has been shown to interact with extracellular regulated kinase 1 (ERK1) (Leinweber et al., 1999), indicating a potential role for CH domains in signalling pathways.

Not very much is known about how the CH domains interact with their binding partners. It is suggested, however, that the Type 1 CH + Type 2 CH domains interact with actin through helix I where they adopt an open conformation. As such, mutations in helix I of α-actinin CH2 domain and β-III-spectrin caused a conformational change in the Type 1 CH + Type 2 CH which resulted in a more open conformation and an increase in the binding capabilities of these CH domain to actin (Avery et al., 2017; Shams et al., 2016). Whereas in microtubule binding CH domains, they interact with microtubules through helix IV. Mutations in helix IV of EB1 was shown to abolish this interaction with microtubules (Hayashi & Ikura, 2003).

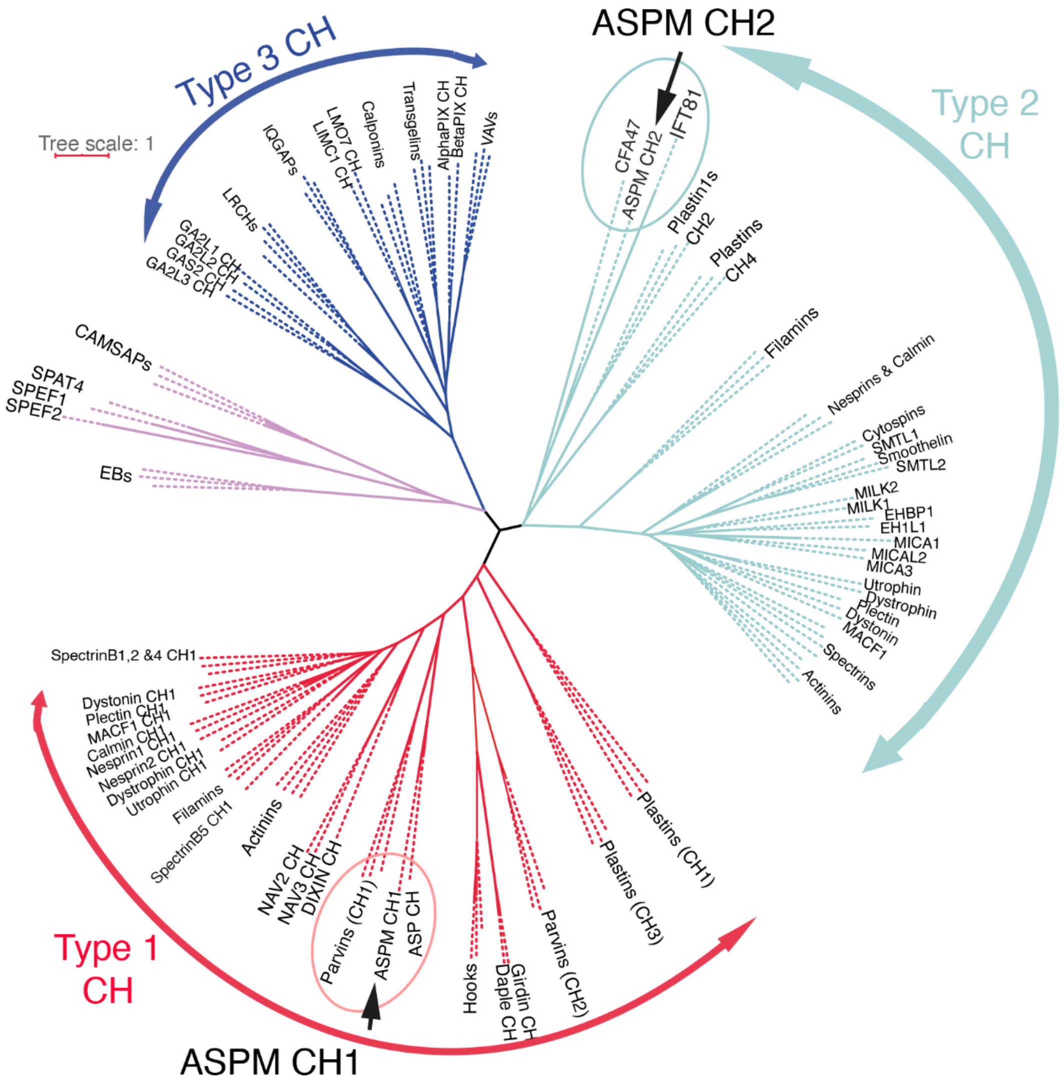

Figure 1.5 – Location of the ASPM CH domains within the CH phylogenetic tree.

Phylogenetic position of CH domains of ASPM, and phylogenetic analysis of CH domains (using Phylogeny.fr).

The presence of tandem (Type 1 + Type 2) CH domains in ASPM has suggested that, like other tandem CH domains, they might bind actin. *Drosophila* asp contains a single CH domain, which is most similar in sequence to CH1 of ASPM. A splice variant of asp in which residues 574-972 (containing the single asp CH domain) were deleted, impaired the normal location of asp and decreased microtubule stability during cell division (Ito & Goshima, 2015). This region of asp was shown to be required for microtubule bundling and crosslinking, and to anchor asp to the spindle pole. F-actin is present at the spindle poles and it has been suggested that ASPM may be able to regulate mitotic spindles by interacting with actin through these CH domains (Woolner et al., 2008). It is possible that ASPM could bind to F-actin as well as cross-link and anchor the microtubules to the spindle poles as part of its role in regulating the plane of cell division during mitosis. It is not yet known if the human ASPM CH domains bind to either F-actin or microtubules and this needs to be elucidated to fully understand the overall protein function.

1.1.2.2 IQ motifs

The central region of ASPM is made up of a staggering 81 IQ (Isoleucine, Glutamine) motifs in Human ASPM. IQ motifs are approximately 20-27 residues in length, have the consensus sequence of [ILVF]QXXX[RK]GXXX[RK] (where X is any amino acid), and they are predicted to adopt an amphipathic α-helical structure (O'Neil & Degrado, 1990). IQ domains were first discovered in unconventional myosin and are repeated in tandem in the heavy chain of all myosins where they typically bind myosin-associated light chains or calmodulin (Houdusse & Cohen, 1995).

The number of ASPM IQ motifs varies between species; *C. elegans* aspm-1 has two, the *Drosophila* homologue *asp* contains 24, mouse Aspm contains 62 and human ASPM contains 81, the largest number of IQ repeats reported in a protein (Kouprina et al., 2005). The large number of IQ motifs, mostly encoded by the largest exon in ASPM (exon 18; 4,755 bp), is thought to result from a single large duplication of 900 bp creating an exon that encodes 67 IQ repeats (Bond et al., 2002; Kouprina et al., 2005).

A bioinformatic analysis of the IQ motifs of ASPM has identified a pattern in their length where 55% of the total IQ domains follow the pattern: 23 amino acids, 23 amino acids, 27 amino acids. The other 45% do not follow this triplet pattern and have a variable length, with the smallest IQ motif being 14 amino acid and the largest, 38 (Kouprina et al., 2005). The significance of this pattern has yet to be investigated.

Calmodulin, a Ca^{2+} sensing protein, binds to a wide variety of target proteins modifying their function in turn. Ca^{2+} binding occurs in the two homologous helix-loop-helix domains known as EF-hands. Calmodulin assumes one of two forms; 'open', where the Ca^{2+} is bound; and 'closed' (or apo) where Ca^{2+} is absent. The 'open' conformation is termed the 'gripping' form and it binds to hydrophobic regions of a target protein. The 'closed' conformation is termed the ‘non-gripping’ form and it is this form that binds to the IQ motifs of the myosin heavy chain (Houdusse et al., 1996). Due to the hydrophobic nature of the IQ domain, calmodulin is thought to bind tightly to the IQ motif in the absence of Ca^{2+} (Houdusse & Cohen, 1995).

The evidence of an association between ASPM and calmodulin localisation is strong (Schoborg et al., 2015; van der Voet et al., 2009). During mitosis, the distribution of calmodulin and ASPM has been shown to be almost identical indicating the possibility of an interaction (Schoborg et al., 2015). This binding has been confirmed by co-immunoprecipitation and calmodulin is thought to bind via the IQ motifs of ASPM (Xu et al., 2012). However, due to the sequence variation of the IQ motifs within ASPM, it is currently unknown as to whether ASPM binds calmodulin at each of its 81 motifs (Bahler & Rhoads, 2002; Kouprina et al., 2005). The IQ motifs of ASPM have been shown to interact with calmodulin and the essential myosin light chain 6B (MYL6B) by yeast two-hybrid experiments (J Bond – personal communication). MYL6B (previously known as MLC1SA) is a light chain that is known to bind IQ motifs of non-muscle myosin-2, however, unlike calmodulin, MYL6B does not bind in a Ca^{2+} dependent manner (Heissler & Sellers, 2014). Clearly, more work is required to understand the structure and function of this 81 IQ motif and its specific binding capabilities.

1.1.2.3 C-terminal region

The C-terminal domain of ASPM (residues 3,235-3,477) is thought to contain at least one armadillo (ARM) repeat domain of ~42 residues (Higgins et al., 2010). Using i-Tasser to find the structure shows a region of 243 residues adopts a helical fold similar to that of other ARM domains, with up to five ARM repeats (Figure 1.6). Tandem ARM repeats adopt a right-handed superhelix of helices to provide a surface for protein-protein interactions (Coates, 2003; Reichen et al., 2014). ARM repeats adopt a cylindrical structure with a positively charged groove that interacts with the acidic surface of binding partners. For example, for β-catenin (which contains 12 ARM domains) the ARM domain allows it to bind to cadherins (Huber et al., 1997). Other proteins that contain multiple armadillo repeats include adenomatous polyposis coli (APC), which together with β-catenin are involved in signal transduction through the Wnt signalling pathway (Mayor & Theveneau, 2014). The Wnt pathway is involved in promoting neural progenitor proliferation by up-regulating proliferative genes, such as cyclin D1 (Shtutman et al., 1999). A study by Buchman et al., (2011), which links ASPM to the Wnt signalling pathway has shown that a knockdown of ASPM in neuronal progenitor cells resulted in a decrease of Wnt-mediated transcription. This indicates that ASPM has the potential to be a positive regulator of Wnt signalling activity, whether this is due to the ARM domain is yet to be determined.

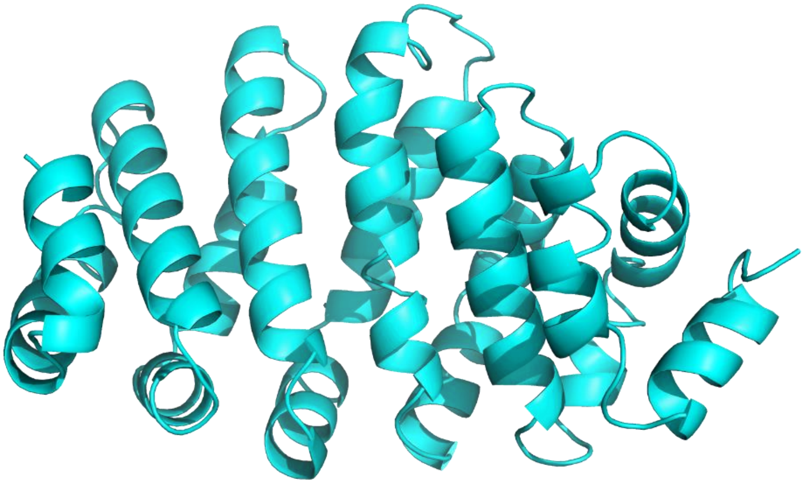

Figure 1.6 – i-Tasser model of the C-terminal region including the ARM domain.

A prediction model of the C-terminal fragment of ASPM (residues 3235-3477). Displayed N-terminal to C-terminal. Showing the five potential ARM repeats (from i-Tasser).

Recent studies have suggested that the ARM domain is instead a HEAT repeat (standing for: Huntingtin, elongation factor 3 (EF3), protein phosphatase 2A (PP2A), TOR1) (Jiang et al., 2017; Tungadi et al., 2017). HEAT repeats are structurally similar to ARM repeats in that they both, when in tandem, form extended super helical structures (Kajava et al., 2004). It is difficult to distinguish between ARM / HEAT domains from sequence alone as the main difference is 3-

dimensional structure; where HEAT consist of two helices and ARM consist of three (Kippert & Gerloff, 2009).

Models generated from the i-Tasser modelling server show better fits to ARM domains than to HEAT repeats. However, protein fold prediction programmes can overpredict the presence of ARM over HEAT domains (Kippert & Gerloff, 2004). Solving the structure of the C-terminal region of ASPM would reveal if it is an ARM or a HEAT domain. A further paper suggested that this region of ASPM forms an SCH (Sha1 C-terminal homology) domain (Rhoads & Kenguele, 2005). However, Sha1 was later found to be the mouse homologue Aspm.

Despite this discrepancy in the literature, studies into the interactions within this region have provided some insight into the potential function. Previous work has shown that this region is important for the interaction of ASPM with citron kinase (Paramasivam et al., 2007). Citron kinase is also involved in microtubule organisation and has been linked to primary microcephaly (MCPH17, (Basit et al., 2016)). It colocalises with ASPM during metaphase, anaphase and cytokinesis suggesting any interaction is important in these parts of the cell cycle (Gai et al., 2017). This was supported by experiments with a GFP tagged C-terminal construct (residues 2,880-3,133 of rat Aspm which corresponds to residues 3,225-3,477 of human ASPM), which localised to the midbody ring during cytokinesis and co-immunoprecipitated with citron kinase. A recent study showed that this interaction was critical for spindle symmetry by influencing astral microtubule organisation (Gai et al., 2017). However, the function of the C-terminal region is not yet fully understood.

1.2 ASPM in disease

1.2.1 Autosomal recessive primary microcephaly (MCPH)

1.2.1.1 MCPH as a disease

Microcephaly is defined as a measured head circumference that is greater than 3 standard deviations (SD) below the average head circumference for normal age- and sex-matched individuals (Faheem et al., 2015). It can occur pre- or postnatally. A primary microcephaly is a static developmental anomaly, whereas secondary microcephaly can indicate a neurodegenerative condition (Woods, 2004). Microcephaly can be accompanied by additional abnormalities such as primordial dwarfism, mild seizures and reduced fertility (Morris-Rosendahl & Kaindl, 2015). Neurological defects related to microcephaly, include hyperactivity, speech delay and varying degrees of intellectual disability (Kaindl et al., 2010).

A pure form of microcephaly, that has no other significant complications, is known as Autosomal Recessive Primary Microcephaly (or MCPH standing for Microcephaly primary hereditary). MCPH is defined by a small brain with a reduced head circumference of less than 3 SD below the mean. It particularly affects the cerebral cortex and is associated with mild to moderate intellectual disability, but generally there are few other significant neurological changes. Despite the reduced head circumference and brain size, MRI scans show that the cerebral cortex is architecturally normal, comprising 6 layers of outer grey matter, which contains myelinated axons and neurons (Bond et al., 2002; Faheem et al., 2015), suggesting that MCPH arises due to a decrease in cell number (Higgins et al., 2010).

1.2.1.2 The genes associated with MCPH

MCPH is a heterogenous disorder, currently with mutations in at least 25 genes known to cause MCPH. MCPH typically arises from mutations in genes involved in mitosis or cell division that are critical in determining the fate of stem cells, in particular neuronal progenitor cells (Jayaraman et al., 2016). *ASPM* is one of the first genes identified to be associated with MCPH (Bond et al., 2002) and mutations in *ASPM* is one of the most common cause of MCPH accounting for ~46% of reported cases (Jayaraman et al., 2016; Roberts et al., 2002). Together with *WDR62* (WD repeat-containing protein 62) at the *MCPH2* loci, mutations in these two genes account for over 50% of reported cases of MCPH, worldwide. Both regulate the plane of cell division (Jayaraman et al., 2016; Roberts et al., 2002).

Of the 25 genes currently considered to cause MCPH (MCPH1-MCPH25) (Table 1.1), not all purely cause MCPH as some (MCPH6, MCPH9 and MCPH13) are also involved in primordial dwarfism (Passemard et al., 2013). Most of the disease-causing mutations in these genes result in a frameshift mutation, nonsense mutation or nonsense mediated decay. These are predicted to lead to truncated proteins that are non-functional (Barbelanne & Tsang, 2014). 23 of the 25 genes linked to MCPH are in some way involved in mitosis (Figure 1.7) or cell differentiation (Table 1.1) and are expressed during early brain development (Cox et al., 2006; Hagemann, 2008).

Table 1.1 - Overview of known MCPH causing genes and their molecular function.

Gene name	Protein name	Cellular localisation	Molecular function and effect of mutation	Reference
MCPH1	Microcephalin	Nucleus	Regulates chromosome condensation and DNA-repair. Mutations in *microcephalin* trigger premature chromosome condensation perturbing the cell cycle during neurogenesis resulting in a thin outer cortex layer.	(Cox et al., 2006; Trimborn et al., 2004)
MCPH2	WD repeat domain 62 (WDR62)	Nucleus / Centrosome	Preserves spindle pole integrity. Mutations in *WDR62* lead to spindle misorientation and trigger premature asymmetric division leading to a reduced neuroepithelial cell pool.	(Barbelanne & Tsang, 2014; Yu et al., 2010)
MCPH3	CDK5 regulatory subunit-associated protein 2 (CDK5RAP2)	Centrosome	Involved in centrosome cohesion and engagement with spindle poles. Recruits the ɣ-tubulin ring complex to the centrosome to regulate centrosomal maturation. Mutations in *CDK5RAP2* decrease stem-cell proliferation.	(Issa et al., 2013)
MCPH4	Kinetochore scaffold 1 (CASC5 (KNL1))	Kinetochore	Required for correct microtubule attachment to the kinetochore and controls the spindle assembly checkpoint. Mutations cause chromosome misalignment.	(Genin et al., 2012; Szczepanski et al., 2016)
MCPH5	Assembly factor for spindle microtubules (ASPM)	Nucleus / Pericentrosomal Matrix / Midbody	Mitotic spindle orientation, microtubule organisation and cytokinesis. Mutations in *ASPM* influence the divisional symmetry, mitotic progression and cytokinesis failure leading to a reduced neural progenitor cell pool.	(Fish et al., 2006; Higgins et al., 2010)
MCPH6	Centromere protein J (CENPJ)	Centrosome	Involved in stabilising the centriole and participates in centriole duplication. Inhibits microtubule nucleation from the centrosome. Mutations disturb centrosome integrity, resulting in multiple spindle poles and cause mitotic arrest and apoptosis.	(Bond et al., 2005; Cho et al., 2006; Faheem et al., 2015)
MCPH7	SCL-interrupting locus (STIL)	Pericentrosomal / Centrosome	Essential for correct mitotic spindle organisation and apoptosis regulation. Mutations in *STIL* lead to mitotic failure and enhanced cell death.	(Kumar et al., 2009)
MCPH8	Centrosomal protein of 135 kDa (CEP135)	Centrosome	Plays a role in the organisation and structure of the centrosome. Mutations in *CEP135* compromise the structural integrity of centrioles resulting in disorganised mitotic spindles.	(Hussain et al., 2012; Ohta et al., 2002)
MCPH9	Centrosomal protein of 152 kDa (CEP152)	Centrosome	Organises microtubules and plays an essential role in cell shape, motility, polarity and cell division. Mutations lead to severe mitotic defects and the formation of monopolar spindles.	(Guernsey et al., 2010)
MCPH10	Zinc finger protein 335 (ZNF335)	Nucleus	Regulates neuronal gene expression and is involved in chromatin remodelling, cell fate and differentiation. Mutations generally lead to depletion of ZNF335 causing reduced dendritic maturation.	(Yang et al., 2012)
MCPH11	Polyhomeotic-like protein 1 (PHC1)	Nucleus	Involved in chromatin remodelling. Mutations in *PHC1* induces aberrant DNA damage and polyploidy.	(Awad et al., 2013)
MCPH12	Cyclin-dependent kinase 6 (CDK6)	Nucleus / Cytosol	Controls cell cycle and cell differentiation. Mutations in *CDK6* affects cell polarity and can induce aneuploidy.	(Hussain et al., 2013)

Table 1.1 - Continued

Gene name	Protein name	Cellular localisation	Molecular function and effect of mutation	Reference
MCPH13	Centromere-associated protein E (CENPE)	Kinetochore	Required for spindle microtubule capture and attachment. Mutations cause chromosome misalignment and segregation failure leading to premature asymmetric division.	(Mirzaa et al., 2014)
MCPH14	Spindle assembly abnormal protein 6 homologue (SASS6)	Centrosome	Necessary for centrosome formation and duplication. Mutations impair procentriole formation leading to defective cell division.	(Khan et al., 2014)
MCPH15	Sodium-dependent lysophosphatidylcholine symporter 1 (MFSD2A)	Cell membrane	Required for uptake of long-chain fatty acids in the brain. Mutations lead to a disrupted blood-brain barrier and cell death.	(Guemez-Gamboa et al., 2015)
MCPH16	Ankyrin repeat and LEM domain-containing protein 2 (ANKLE2 (LEM4))	Nuclear envelope	Plays a role in the reassembly of the nuclear envelope. Mutations lead to irregular nuclear envelope leading to decreased cell proliferation.	(Asencio et al., 2012)
MCPH17	Citron Rho-interacting kinase (CITK)	Cleavage furrow / Midbody	Plays a role in the regulation of cytokinesis. Mutations lead to defective cytokinesis resulting in genome instability.	(Basit et al., 2016; Gai et al., 2017)
MCPH18	WD repeat and FYVE domain-containing protein 3 (WDFY3 (ALFY))	Nucleus / Cytosol	Involved in autophagic degradation of cytoplasmic p62 bodies. Mutations cause abnormal activation of WNT signalling preventing cell differentiation.	(Kadir et al., 2016)
MCPH19	Coatomer subunit beta-2 (COPB2)	Cytosol	COPB2 is required for membrane budding from Golgi to ER transport. Mutations disrupt neural development due to increased apoptosis caused by failure of cargo transport.	(Distasio et al., 2017)
MCPH20	Kinesin family member 14 (KIF14)	Cytoskeleton	Microtubule motor protein that is involved in cell division and cytokinesis. Mutations cause abnormal cytokinesis and impair cell migration.	(Moawia et al., 2017)
MCPH21	Condensin complex subunit 1 (NCAPD2)	Nucleus	A subunit of the condensin complex which is required for transition of interphase chromatin into mitotic-like condensed chromosomes. Mutations cause abnormal recovery from mitotic condensation and impaired chromosome segregation.	(Martin et al., 2016)
MCPH22	Condensin-2 complex subunit D3 (NCAPD3)	Nucleus	A regulatory subunit of the condensin complex required for transition of interphase chromatin into mitotic-like condensed chromosomes. Mutations cause abnormal recovery from mitotic condensation and impaired chromosome segregation.	(Martin et al., 2016)
MCPH23	Condensin-2 complex subunit H2 (NCAPH)	Nucleus	A regulatory subunit of the condensin complex required for transition of interphase chromatin into mitotic-like condensed chromosomes. Mutations cause abnormal recovery from mitotic condensation and impaired chromosome segregation.	(Martin et al., 2016)
MCPH24	Nucleoporin 37 kDa (NUP37)	Nucleus	Component of Nup subcomplex of the nuclear pore complex and required for correct kinetochore microtubule attachment. Mutations alter chromatin organisation and reduced cellular proliferation.	(Braun et al., 2018)
MCPH25	Microtubule-associated protein 11 (MAP11)	Cytoskeleton	Plays a role in spindle dynamics and cytokinesis. Mutations in *MAP11* cause a decrease in proliferative capacity.	(Perez et al., 2019)

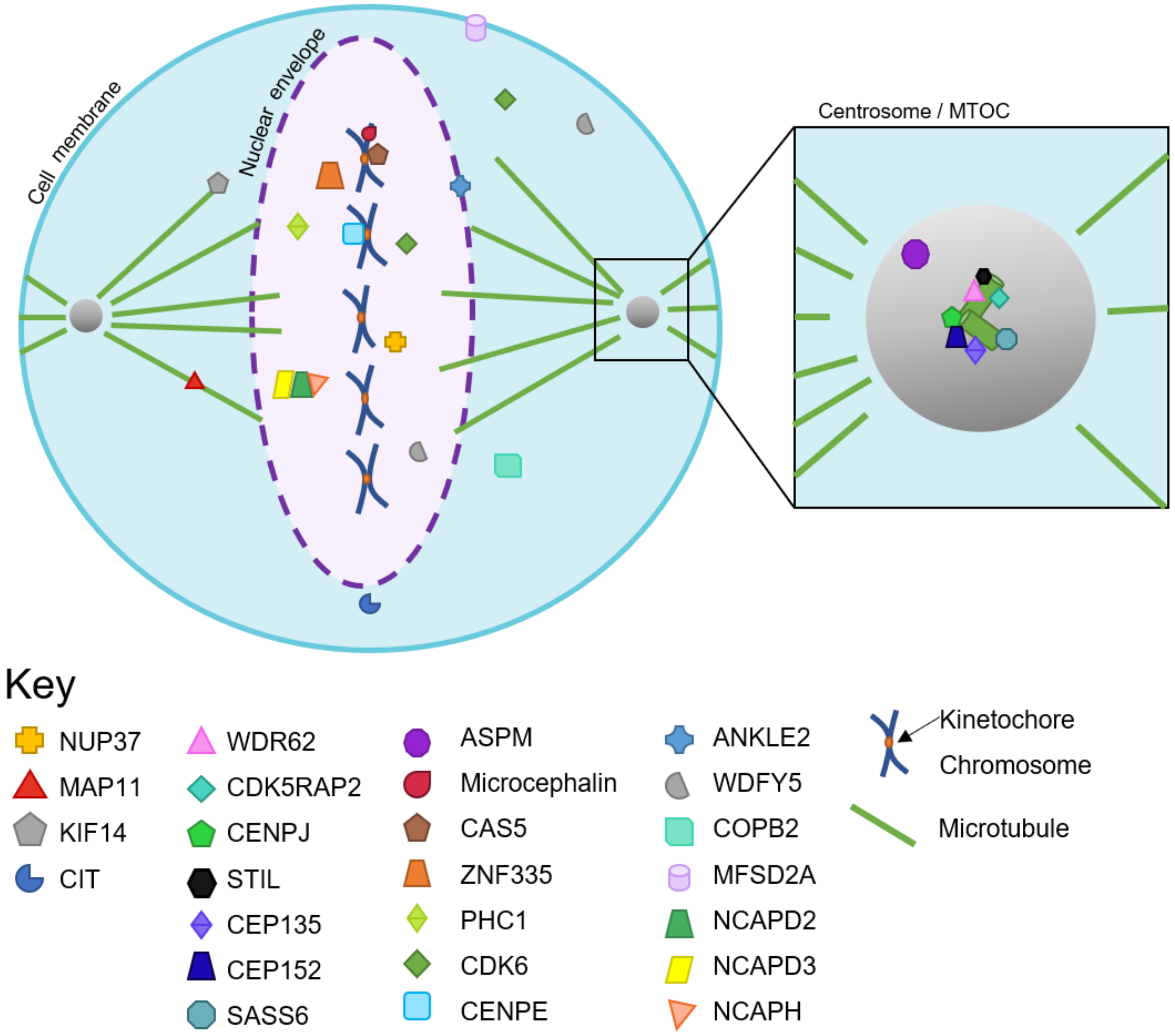

Figure 1.7 – Cellular locations of the MCPH genes.

The cellular localisations of the 25 known MCPH genes (listed in Table 1.1) in a cell undergoing mitosis, including those involved in the centrosomes (green barrels) and pericentriolar matrix (grey), MTOC; microtubule organising centre. Although not all MCPH genes are involved in mitosis (MCPH 15 (COPB2) and MCPH 19 (MFSD2A)), these have been included for informational reasons.

1.2.1.3 Mutations in ASPM cause MCPH

One of the most predominant types of mutations in ASPM is the introduction of a premature stop codon which is likely to result in reduced levels or absence of ASPM due to nonsense mediated decay (Bond et al., 2003). There are currently 225 known mutations in ASPM: 95 nonsense / missense, 84 of which result in a stop codon, 19 splice site mutations, 90 small deletions, 16 small insertions, 2 indels, 2 gross deletions and 1 complex rearrangement (Full mutation list in Appendix). All mutations are thought to cause a reduction in the neuroepithelial (NE) cell pool, and / or premature differentiation of NE cells and apical radial glial cells (aRG) cells by altering the plane of division (Bond et al., 2003; Chavali et al., 2014; Fish et al., 2006; Higgins et al., 2010). These cells are important in generating neurones forming the cerebral cortex. Depletion of the NE pool could thus account for the reduction in cortical size observed in ASPM.

There have been many mutations found in ASPM that cause MCPH (Figure 1.8). The majority of these are found within exons 3, 18 and 24 (Nicholas et al., 2009). All these mutations result in a similar phenotype even though they induce nonsense, frameshift, splice-site or translocation mutations (Bond et al., 2002; Bond et al., 2003; Kouprina et al., 2005; Kumar et al., 2004; Shen, 2005). However, most of the known disease-causing mutations typically cause premature stop codons predicted to result in protein truncation with the common loss of the ASPM C-terminal region (Bond et al., 2003; Nicholas et al., 2009). Interestingly, a single splice site mutation results in the loss of just 3 amino acids from the C-terminal region and is sufficient to cause MCPH, indicating the importance of the C-terminus in ASPM function in the development of the brain (Bond et al., 2003). Another known mutation results in a large deletion (21,844 bases) causing the loss of exons 2-13, but leaves the open reading frame intact (Nicholas et al., 2009). In addition to this, some mutations however result in a decreased amount of full-length ASPM at the spindle poles indicating a failure to correctly localise.

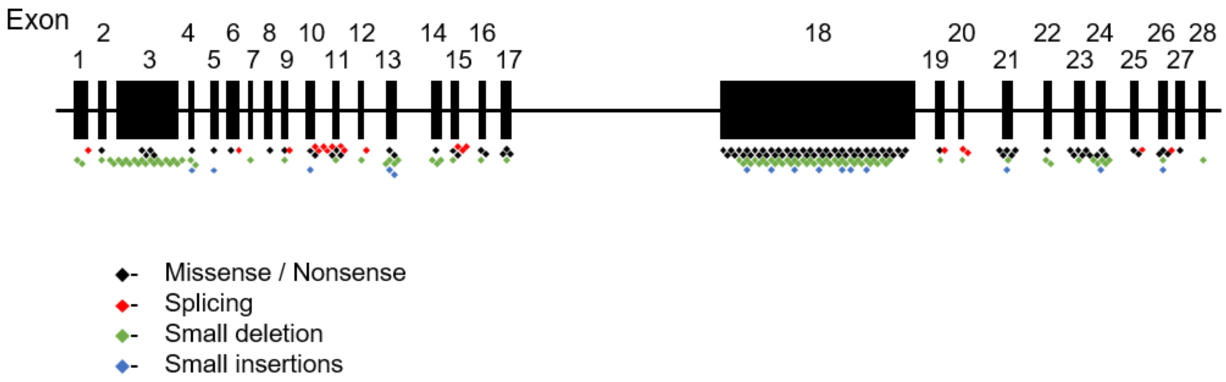

Figure 1.8 – ASPM gene and locations of MCPH causing mutation.

Exons 1-28 of the ASPM gene. Coloured diamonds indicate the location of a known MCPH mutation. Black diamond indicates missense / nonsense, red diamond indicates splicing, green diamond indicates a small deletion and blue diamond indicates a small insertion. A complete list of the mutations can be found in the Appendix.

1.2.2 Cancer

Aside from MCPH, ASPM is overexpressed in some cancers including bladder cancer (Xu et al., 2018), brain tumours (Bikeye et al., 2010), and prostate cancer (Pai et al., 2019) where it is associated with a poor prognosis. This is thought to be due to the increased levels of ASPM therefore increasing cell proliferation leading to tumour development. This is attributed to the role ASPM plays in the Wnt signalling pathway as a positive regulator, where it is thought to maintain the cancer stem cell subpopulation, potentiating cancer recurrence (Buchman et al., 2011; Pai et al., 2019). ASPM has been shown to activate the Wnt-β-catenin signalling pathway by associating with disheleved-3 (Dvl-3). ASPM maintains Dvl-3 protein stability by inhibiting proteasome-dependent degradation thus increasing signalling (Pai et al., 2019). These studies suggest that ASPM is an oncogene and provides a potential therapeutic target for research (Bruning-Richardson et al., 2011; Kato et al., 2011).

1.3 ASPM in development

1.3.1 Mitosis

Mitosis is the process of cell division in which genetic material is duplicated and two new duplicate daughter cells are formed. Periods of mitosis are separated by much longer periods of interphase, during which cells grow and duplicate their DNA in preparation for mitosis. ASPM is located in the nucleus during interphase. Mitosis is comprised of several discrete stages (Figure 1.9).

Mitosis starts with prophase. During prophase, the chromatin condenses, and transcription shuts down (Martínez-Balbás et al., 1995) and the nuclear envelope disperses (Chou et al., 1990; Mcintosh, 2016). In the cytoplasm, protein synthesis slows, microtubules (MTs) and actin stress fibres lose stability and depolymerise resulting in cell rounding (Maller, 1986). However, cortical actin on the inner surface of the cell membrane remains in preparation for cytokinesis (Figure 1.9A) (Mitsushima et al., 2010). During this time, new MTs form around the centrosome (Figure 1.9B) that will become the mitotic spindle poles (Ma & Poon, 2011). The centrosome is a cytoplasmic organelle comprised of two highly conserved nine-fold symmetric cylinders consisting mostly of microtubules, known as centrioles (Barbelanne & Tsang, 2014). There is a distinction between the two centrioles however: the mother centriole contains two sets of nine appendages at its distal end; the daughter centriole, which was assembled during the previous cell cycle, is roughly 80% the length of the mother centriole (Bornens, 2012). The two centrioles are connected via flexible interconnecting fibres and surrounded by the pericentriolar matrix (PCM) (Figure 1.9B). Both centrioles are involved in the nucleation of microtubules, however; only the mother centriole can anchor the minus end of microtubules during interphase (Barbelanne & Tsang, 2014). Anchoring the minus end of microtubules is necessary for mitotic spindle assembly and segregation of chromosomes. This process is tightly regulated during the cell cycle (Alieva & Uzbekov, 2008).

Prometaphase follows prophase. During this phase ASPM migrates to the pericentriolar matrix and focuses the spindle MTs as they begin to form (Higgins et al., 2010; Silkworth et al., 2012). There are three types of spindle MTs: astral microtubules, that are connected to the cell cortex through cortical dynein; kinetochore MT that attach to the chromatids; and central spindle MTs that emanate from apposing poles and span the length of the cell (Figure 1.9A). The kinetochore MT attach at structures known as kinetochores, a disk-shaped structure located at the centre of duplicated chromatids. Each chromatid has one kinetochore, which consists of a complex of over

100 proteins including KNL1 (Kinetochore scaffold 1; MCPH4) (Cheeseman, 2014; Szczepanski et al., 2016). Kinetochores also contain motor proteins that grasp spindle MTs and influence chromosome position. The kinetochore contains a MT minus-end directed motor, typically a dynein, and MT plus-end directed kinesins, such as the kinesin-7 (CENPE, MCPH13 (Wood et al., 2008)). Kinetochores also possess additional kinase activities, which recruit other kinetochore components in response to correct MT attachment and tension (Verhey & Hammond, 2009). This is known as the spindle assembly checkpoint. This checkpoint inhibits progression into anaphase until all chromosomes are properly attached to the spindle (Kirschner, 1986; Roberts et al., 1994).

During metaphase, which starts once spindle MTs have correctly attached to the kinetochores, the chromosomes migrate to the spindle equator, known as the metaphase plate (Figure 1.9A). During this time, spindle MTs are highly dynamic, quickly turning over large amounts of guanosine triphosphate (GTP) required for MT polymerisation (Mitchison, 1989). Spindle MTs display a flux towards the spindle poles (poleward), which requires kinesin-13 at the spindle poles to facilitate MT depolymerisation at their minus-ends while MTs polymerise at the kinetochores (Waterman-Storer & Salmon, 1997).

Anaphase begins once spindle MTs have attached to all the kinetochores, and the chromosomes are lined up on the metaphase plate. It is initiated by activation of the anaphase-promoting complex (APC/C), a polyubiquitin ligase (Acquaviva, 2006). APC/C poly-ubiquitinates key proteins (such as securin, a protein involved in the metaphase / anaphase transition, as well as cyclins A and B) leading to their degradation by the proteosome (Acquaviva, 2006; Alfieri et al., 2017). Degradation of these proteins lead to the activation of separase, a protease that degrades the adhesions between sister kinetochores (Hoyt, 2001) allowing the two chromosomes to separate (Uhlmann, 2001).

Kinesin and dynein motor proteins at the kinetochores induce MT depolymerisation which generates a force that pulls the chromosomes towards the poles (Sharp et al., 2000; Tanaka et al., 2007; Verhey & Hammond, 2009). Depolymerisation of MTs also occurs at the spindle pole where dynein interacts with NuMA1 which, in turn, interacts with the minus-end of spindle MTs (Elting et al., 2014). The loss of tubulin subunits of the spindle MTs at both the kinetochore (Mitchison et al., 1986), and at the poles (Maddox et al., 2002), cause spindle MT shortening and enable chromosomes to move polewards. Overlapping, extending, sliding spindle MTs at the spindle midplane ensures that the two sets of chromosomes are far enough apart so that cytokinesis will put one set into each daughter cell (Brust-Mascher & Scholey, 2011). The successful segregation of chromatids is enhanced by the symmetry of metaphase which is thought to be controlled by ASPM (Fish et al., 2006).

Once the separated chromatids have been moved to the region of the spindle poles, telophase starts, and two fully functioning nuclei begin to form. Chromosome arms contract drawing chromatin masses together next to the spindle pole, inner nuclear envelope proteins associate with the chromosomes and the nuclear envelope begins to rebuild (Güttinger et al., 2009). Once the nuclear membrane fuses, nuclear pore complexes reassemble and begin to establish the separation of the nucleoplasm and cytoplasm. Chromatin then begins to decompress; transcription restarts, the mitosis exit pathway is initiated, and the cells commence cytokinesis to produce two daughter cells (Mcintosh, 2016).

The final step is cytokinesis. This is the process of remodelling the cell cortex, constricting the cleavage furrow around the midbody, and severing the plasma membrane (Liu & Robinson, 2018). Initially, actin is recruited to the cleavage furrow and is assembled into bundles where it forms a ring that is closed by a pulling force generated by myosin-2. This is known as the contractile ring (Cheffings et al., 2016). At this point, bundles of MT derived from the mitotic spindle are present within the ring, and these are compacted into a structure called the midbody within the intercellular bridge (Mullins & Mcintosh, 1982). In the midbody, the central MT bundle contains many overlapping plus ends in a dense matrix. This central bulge contains over 450 assembled proteins, including ASPM potentially interacting with citron kinase and katanin (Gai et al., 2017), to serve as a platform to mediate abscission, the process of severing the intercellular bridge (Skop, 2004).

As cytokinesis proceeds, actin filaments need to be cleared at the abscission site to allow the plasma membrane to be constricted by the endosomal sorting complexes required for transport (ESCRT)-III machinery (Frémont et al., 2017). During abscission, MT severing machinery, such as the proteins Spastin and katanin (which is known to interact with ASPM), are also recruited to clear the abscission site of MTs (Jiang et al., 2017; Lumb et al., 2012). Once abscission is complete, the two daughter cells enter interphase to start the cycle again (Mcneely & Dwyer, 2020; Peterman et al., 2019).

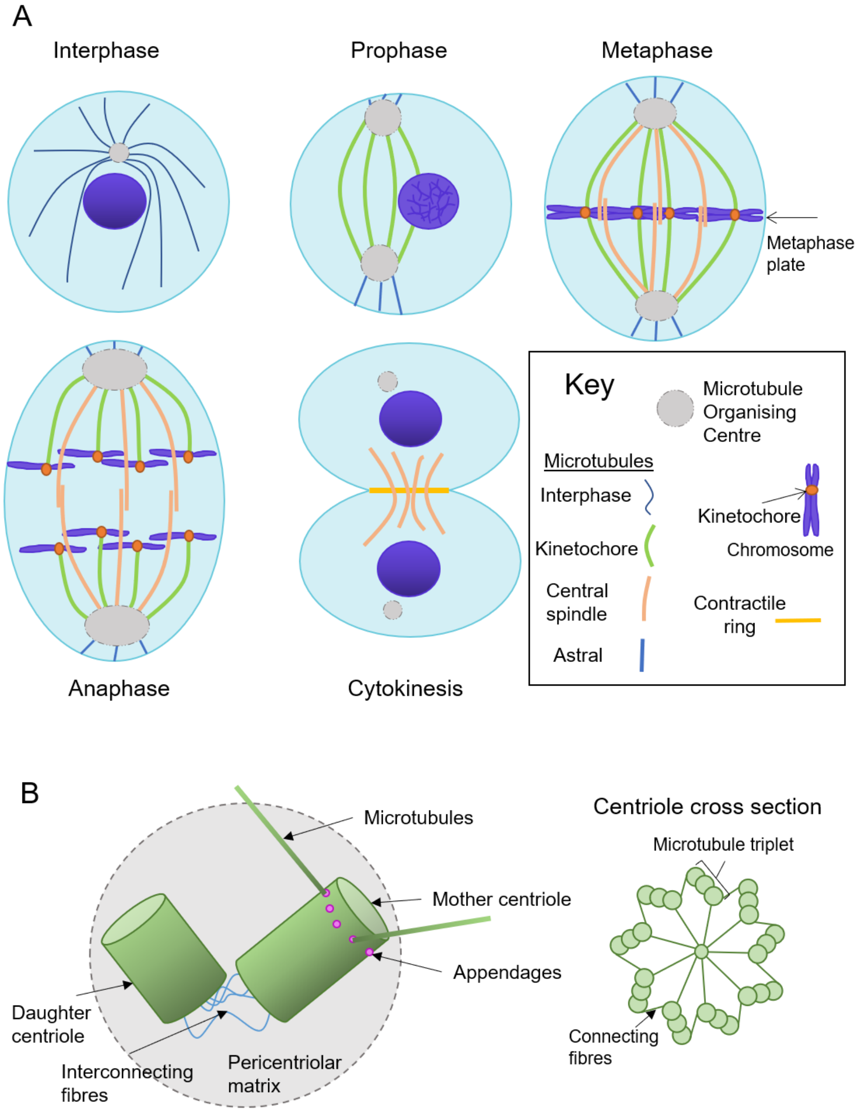

Figure 1.9 – Mitosis and the centrosome.

(A) Shows the stages of mitosis, and the organisation of the spindle and chromosomes within each stage. In interphase, the cell replicates its DNA and other cellular constituents; In Prophase, chromosomes condense, and the nuclear membrane breaks down; In Prometaphase, the spindle forms. The spindle is made up of microtubules (MTs). The kinetochore MT attach to the chromosomes and organise them along the metaphase plate; The astral microtubules project out towards the cell membrane and can be tethered to the actin cytoskeleton, the central spindle MTs are involved in the overall spindle shape and function. In Anaphase, the duplicated chromosomes are segregated and pulled towards the spindle poles. This is followed by cytokinesis which separates the cell generating the two daughter cells. (B) The centrosome (LHS) is a key component of the microtubule organising centre. It duplicates in each cell cycle and is important in generating the spindle poles in mitosis. Centrosomes are small organelles composed of two perpendicular centrioles (green cylinders), a mother and a daughter connected by interlinking fibres (blue). The two centrioles are surrounded by a pericentriolar matrix (PCM) (dotted grey), which contains the proteins involved in anchoring and nucleating microtubules. The mother centriole contains microtubule binding appendages (pink). A cross sectional view of a centriole (RHS) shows the nine-fold MT triplets connected by connecting fibres to a central hub.

1.3.2 Asymmetric and symmetric cell division, and stem cell fate

Cell polarity plays an important role in development and stem cell fate (Venkei & Yamashita, 2018). Cell polarity can be influenced by many factors including external stiffness, growth factors and gene expression (Campanale et al., 2017). The ability of a stem cell to proliferate and self-renew dictates the amount of stem cells available for differentiation. Symmetrical division of stem cells produce two daughter stem cells with identical fates thus increasing the stem cell reservoir. Whereas, asymmetrical division produces two daughter cells with distinct fates (Wagers et al., 2002), in which typically one cell becomes a new stem cell and the second goes on to differentiate.

The control between asymmetric and symmetric cell division is important for the fate of neuronal stem cells in early neurodevelopment. At gestation week 5-6 in humans, the central nervous system comprises the neural plate and neural tube that will later go on to form the brain and spinal cord (Götz & Huttner, 2005). The neural tube is composed entirely of neuroepithelial (NE) cells which form a single-layered pseudostratified epithelium. NE cells are classified as the primary progenitor cells from which all neurons and glial cells descend (Zecevic, 2004). During the cell cycle, NE cells undergo interkinetic nuclear migration whereby the cells nuclei migrate apically (towards the ventricular surface) to undergo mitosis before returning to the basal (or pial) surface to enter into S-phase (Figure 1.10A) (Penisson et al., 2019).

Initially, NE cells perform symmetrical (proliferative) division which produces two identical daughter NE cells thus increasing the NE reservoir (Figure 1.10A) (Taverna et al., 2014). However, during gestation weeks 10-25, NE cells begin to divide asymmetrically (neurogenic division) producing one NE cell which replenishes but does not increase the NE reservoir and one progenitor cell, which migrates and differentiates into a neuron (Figure 1.10B) (Taverna et al., 2014). Asymmetrical division and progenitor cell migration increases tissue thickness due to increased cell number and the cortical wall becomes divided into several planes, from apical to basal: the ventricular zone (VZ), the subventricular zone (SVZ), the intermediate zone (IZ), the cortical plate (CP) and the marginal zone (MZ) (Figure 1.11) (Penisson et al., 2019).

Asymmetrical division by the NE produces neuroprogenitor cells such as apical radial glial cells (aRG) which are highly polarised and are found in the VZ. Like NE cells, these neuroprogenitor cells also perform interkinetic nuclear migration during the cell cycle as they possess two processes (as depicted in Figure 1.10), an apical process and a longer basal process (Borrell & Götz, 2014; Götz & Huttner, 2005).

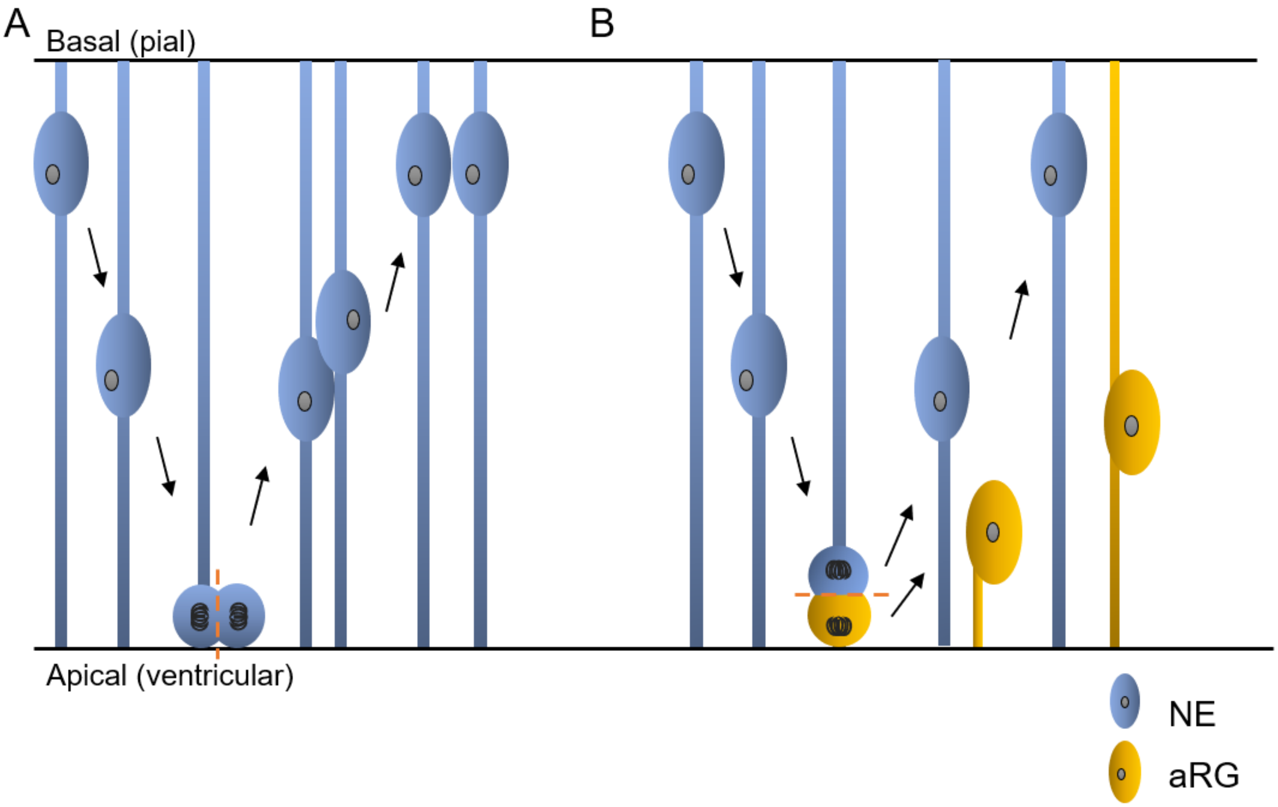

Figure 1.10 – Division of neuroepithelial cells during early neurodevelopment.

(A) During early brain development, neuroepithelial (NE) cells divide rapidly through symmetric division caused by a vertical (perpendicular) cleavage (orange dashed line) relative to the apical surface. This increases the NE cell pool. (B) After the onset of neurogenesis, NE cells divide asymmetrically to give rise to one apical radial glial cell (aRG) and one NE cell by an oblique (parallel) cleavage relative to the apical surface.

During early corticogenesis, when the cerebral cortex (the outer layer of the brain) is beginning to form, the majority of aRG divide horizontally (cleavage plane perpendicular to the ventricular surface) in order to self-renew, and eventually will divide vertically (parallel to the apical surface) (Borrell & Götz, 2014). Vertical (asymmetric) division produces a daughter cell that receives the basal process and becomes (more commonly) a basal radial glial cell (bRG) or a basal progenitor (BP), and the other cell becomes either an immature neuron, an intermediate progenitor (IP) or an aRG that remains attached to the ventricular surface (apical) and will regrow its basal process (Hansen et al., 2010). IP cells are located in the SVZ and in humans these can divide several times, amplifying the pool of IP cells before dividing asymmetrically to produce two immature neurons. The ability for these cells to control the plane of division is important as many divisions are required to increase the pool of cells before neurons are produced to achieve a brain of the correct size (Hansen et al., 2010). The immature neurones migrate basally (known as migrating neurones) where they differentiate into differentiated neurones in the CP or Cajal-Retzius cells, a transient cell population critical for brain development, in the marginal zone (Figure 1.11) (Gil-Sanz et al., 2013).

This highlights the importance to correctly control the plane of division in this highly complex developmental system. As ASPM is thought to play a role in the control of the plane of division, correctly functioning ASPM is pertinent in the early stages of development. Mutations in ASPM can affect how ASPM functions therefore losing the ability to finely control the division plane leading to a premature differentiation and the MCPH phenotype.

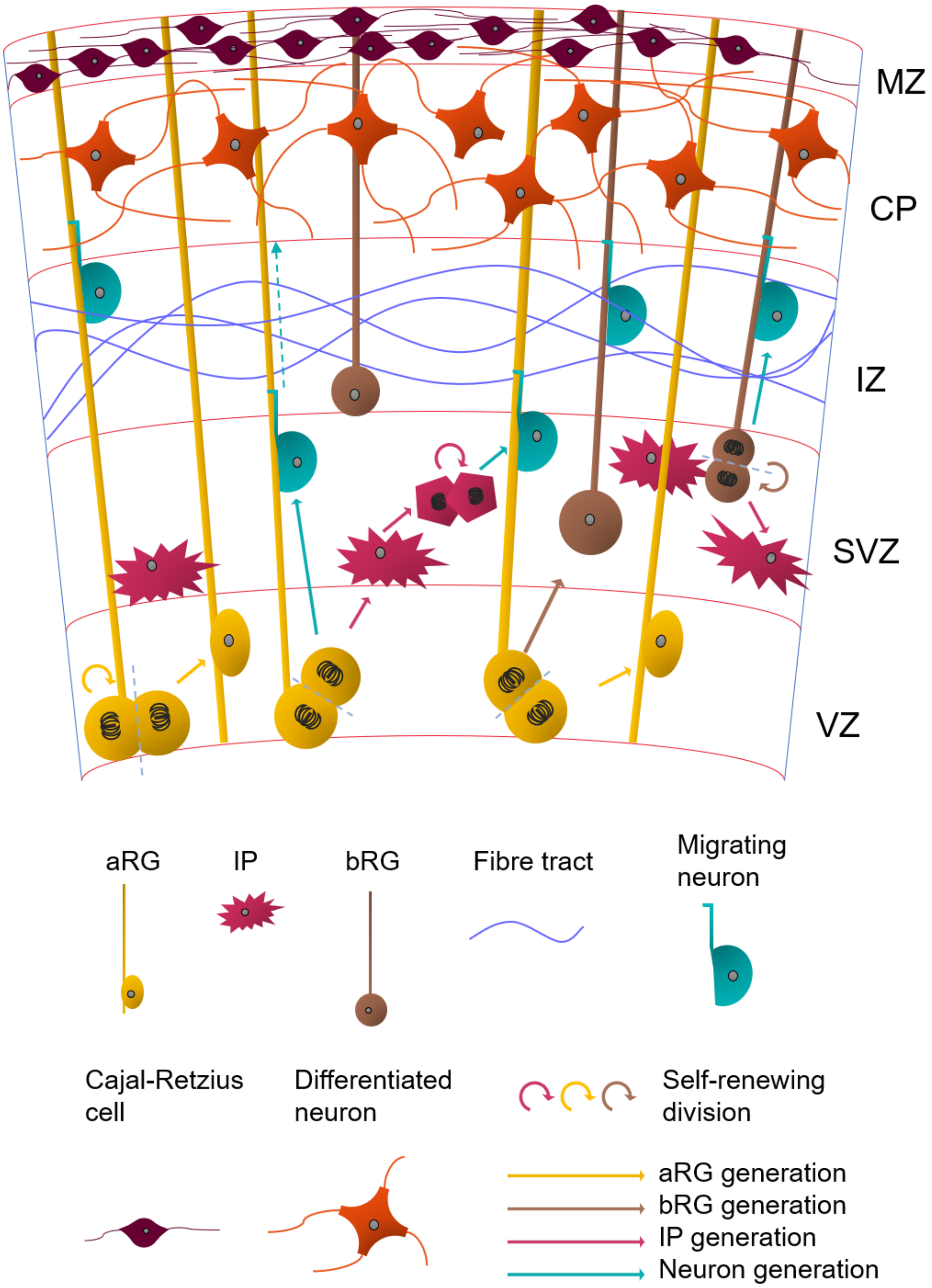

Figure 1.11 – Development of the cerebral cortex.

Schematic view of the embryonic cerebral cortex during corticogenesis. The cerebral cortex is split into 5 zones: VZ, ventricular zone; SVZ, subventricular zone; IZ, intermediate zone; CP, cortical plate; MZ, marginal zone. Apical radial glial (aRG) divide symmetrically to self-renew or asymmetrically to produce either an Intermediate progenitor (IP), migrating neuron, basal radial glial (bRG) or another aRG. IP cells divide symmetrically to self-renew or asymmetrically to produce migrating neurones. bRG divide symmetrically to self-renew or asymmetrically to produce IP or migrating neurons. Migrating neurones then travel to the CP and MZ to become differentiated neurons (CP) or Cajal-Retzius cells (MZ).

1.4 ASPM interacting partners

ASPM has been shown to interact with many proteins, however, not much is currently known about these interactions. Recent studies have shown ASPM to be potentially involved in a highly complex network of protein interactions, with the majority of these localising to the centrosomes and spindle poles (Table 1.2) (Gai et al., 2017; Jiang et al., 2017; van der Voet et al., 2009). However, how these interactions occur or what the role of these interactions are widely unknown.

Aside from the interacting proteins outlined above (Section 1.1.2) not all protein binding sites in ASPM are known. The majority of predicted ASPM interactors (Table 1.2) were indicated by mass spectrometry pull-down experiments, using ASPM tagged at the N-terminus. Many of these interactions have not yet been confirmed experimentally (Jiang et al., 2017). The remaining interactions have been confirmed with either co-localisation experiments, knockdown experiments, or a combination of both (Tungadi et al., 2017; van der Voet et al., 2009; Xu et al., 2012; Yuan et al., 2020).

A linkage between ASPM complexed with LIN-5 (Abnormal cell LINeage 5; known as NuMA in humans), a component of the spindle apparatus required for chromosome segregation in *C. elegans*, was shown to regulate symmetric cell division by interacting with the Cyclin dependent kinase 2 (Cdk2)/cyclin E complex (Capecchi & Pozner, 2015; van der Voet et al., 2009). In cells with truncated ASPM, a significant decrease in Cdk2/cyclin E activity was observed, preventing the cell from committing to cell division. However, where on ASPM LIN-5 interacts is still unclear.

More interestingly, ASPM has been shown to interact with the MCPH protein WDR62 (MCPH2) (Jayaraman et al., 2016). Knockout experiments suggest that both ASPM and WDR62 converge on CENPJ to allow duplication of the centrosome (Jayaraman et al., 2016). Loss of WDR62 and ASPM is thought to be responsible for an early expansion of basal progenitors (thus prematurely reducing the aRG cell pool) during mid-neurogenesis. With WDR62 and ASPM being the two highest MCPH causing genes, this interaction could explain this observation (Jayaraman et al., 2016).

Table 1.2 – Potential ASPM protein interactors.

Interactor name	Cellular localisation	Molecular function	ASPM binding site	Reference
WDR62 (*MCPH2*)	Centrosome / spindle pole	Mitotic spindle organisation and centriole duplication.	Not tested	(Jayaraman et al., 2016; Jiang et al., 2017)
NAP-1	Nucleus / cytosol	Histone binding.	Not tested	(Jiang et al., 2017)
NAP-4	Nucleus / cytosol	Nucleosome assembly.	Not tested	(Jiang et al., 2017)
RCN2	ER	Ion binding (calcium).	Not tested	(Jiang et al., 2017)
CMD-1 (CALM2)	Cytoskeleton	EF-hand containing protein that bind calcium. Known interactant of IQ motifs. Calcium sensing protein.	IQ motifs (residues 1267-3234) *****	(Jiang et al., 2017; van der Voet et al., 2009; Woods et al., 2005)
H2B	Nucleus	Core component of nucleosome, which wrap and compact DNA.	Not tested	(Jiang et al., 2017)
Gamma-1 tubulin	Centrosome / spindle pole	Microtubule minus-end nucleation.	Not tested	(Jiang et al., 2017)
GCP2, GCP3, GCP4, GCP5, GCP6	Centrosome	Microtubule nucleation at centrosome. Part of gamma tubulin complex.	Not tested	(Jiang et al., 2017)
VCP	ER / Golgi	Fragments Golgi stacks during mitosis.	Not tested	(Jiang et al., 2017)
PPP2R1A	Nucleus	Involved in chromosome segregation.	Not tested	(Jiang et al., 2017)
CHIP	Nucleus / cytosol	Degrades misfolded chaperone substrates. E3 ubiquitin ligase.	Not tested	(Jiang et al., 2017)
TRAFD1	Mitochondrion	Zinc finger domain containing protein. Regulates immune response.	Not tested	(Jiang et al., 2017)
KIF2A	Cytoskeleton	Plus-end microtubule-dependent motor protein.	Not tested	(Jiang et al., 2017)
Importin-7	Nucleus / cytosol	Nuclear protein import.	Not tested	(Jiang et al., 2017)
Importin-9	Nucleus	Nuclear transport receptor.	Not tested	(Jiang et al., 2017)
Katanin p60	Cytoskeleton	Microtubule severing protein.	ASPN (residues 316-400) *****	(Jiang et al., 2017)
Katanin p80	Cytoskeleton	Microtubule severing protein.	ASPN (residues 316-400) *****	(Jiang et al., 2017)
KIFC1	Cytoskeleton	Minus-end microtubule-dependent motor protein. Required for bipolar spindle formation.	Not tested	(Jiang et al., 2017)
Aurora A	Centrosome	Mitotic S/T kinase contributes towards cell cycle progression.	Not tested	(Jiang et al., 2017)
CEP170-like protein	-	Pseudogene – not transcribed.	Not tested	(Jiang et al., 2017)
Dynactin subunit 3	Centrosome / spindle pole	Binds dynein and may be involved spindle assembly and cytokinesis.	Not tested	(Jiang et al., 2017)

Table 1.2 – Continued.

Interactor name	Cellular localisation	Molecular function	ASPM binding site	Reference
MOZART2B	Centrosome / spindle pole	Organises mitotic spindle and recruits NuMA to mitotic centrosomes.	Not tested	(Jiang et al., 2017)
CEP63	Centrosome	Involved in mother-centriole-dependent centriole duplication	Not tested	(Jayaraman et al., 2016)
CDK5RAP2 (*MCPH3*)	Centrosome	Crucial for microtubule nucleation by regulating microtubule function and spindle checkpoint activation.	Somewhere between residues 1-3232	(Tungadi et al., 2017)
LIN5 (NuMA)	Centrosome / spindle pole	Involved in formation and maintenance of spindle poles and alignment during mitotic division.	Not tested	(van der Voet et al., 2009; Xu et al., 2012)
DHC-1	Cytoskeleton	Retrograde motility of vesicles and organelles along microtubules.	Not tested	(van der Voet et al., 2009)
Ac-tubulin	Cytoskeleton	A component of microtubules.	N-terminal region (residues 1-1261) *****	(Xu et al., 2012)
CITK (*MCPH17*)	Centrosome	Controls mitotic spindle orientation.	C-terminal (residues 3234-3477) *****	(Gai et al., 2017)
CENPJ/CPAP (*MCPH6*)	Centrosome	Involved in centriole duplication.	Not tested	(Duerinckx & Abramowicz, 2018; Jayaraman et al., 2016)
CDK4	Nucleus / cytosol	Regulates G1/S transition of the cell cycle	Not tested	(Yuan et al., 2020)

***** Indicates if the interaction has been experimentally proven.

1.5 Thesis aims

From the overview of ASPM provided above, it is clear that there is currently a lack in understanding of the structure of ASPM, how this contributes to its function, how ASPM interacts with its binding partners and how mutations can lead to MCPH. A better understanding of the structure and function of ASPM could also be key in developing drug targeted therapies to target ASPM, which is elevated in tumours with poor prognosis.

Currently there are many questions regarding the structure and function of ASPM. Here a chosen subset of questions were focused on. First, it is unclear whether the CH domains of human ASPM bind F-actin or microtubules. This is important to understand as this interaction will play a role in the location of ASPM in mitosis.

Second, it is unclear why human ASPM has such a large number of IQ motifs, what light chains they bind and what the overall structure of this domain is. Is it a semi-rigid rod or a flexible extended structure? This is important to understand as it likely contributes to the role of ASPM in the spindle and might predict if it has an extended structure *in vivo* or not.

Finally, to help with the understanding of how ASPM is organised into the spindle, improved cellular tools are needed. Therefore, CRISPR/Cas9 was used in an attempt to introduce a fluorescent label into the endogenous ASPM, and Affimers were raised against the CH domains of ASPM as tools to visualise ASPM in the cells.

The aims of this thesis are:

1. To determine if the CH domains of ASPM bind F-actin or microtubules *in vitro*.
2. To identify what light chains the IQ motifs of ASPM bind, to determine the overall structure of the IQ motifs and to explore the relevance, if any, of the length if the IQ repeats.
3. To develop a live cell model to determine the cellular location of endogenous ASPM and Affimers against the CH domains of ASPM to visualise where they are located in cells.

2. Methods

2.1 Materials, chemicals and enzymes

All chemicals, enzymes and reagents were supplied by Sigma, and restriction enzymes supplied by New England Biolabs (NEB), unless otherwise stated. For commonly used buffers see Table 2.1.

Table 2.1 – List of buffers used in this study.

Buffer name	Supplier	Buffer Composition
P1	QIAGEN	50 mM Tris-HCl, 10 mM EDTA, 100 µg mL^{-1} RNaseA, pH 8.0
P2	QIAGEN	200 mM NaOH, 1% SDS
N3	QIAGEN	4.2 M Gu-HCl, 0.9 M potassium acetate, pH 4.8
PE	QIAGEN	10 mM Tris-HCl, 80% ethanol, pH 7.5
QBT	QIAGEN	750 mM NaCl, 50 mM MOPS, 15% isopropanol, 0.15% Triton X-100, pH 7.0
QC	QIAGEN	1.0 M NaCl, 50 mM MOPS, 15% isopropanol, pH 7.0
QF	QIAGEN	1.25 M NaCl, 50 mM Tris-Cl, 15% isopropanol, pH 8.5
TE	-	10 mM Tris-HCl, 1 mM EDTA, pH 7.5
CutSmart	NEB	50 mM Potassium Acetate, 20 mM Tris-acetate, 10 mM Mg-acetate, 100 µg mL^{-1} BSA, pH 7.9

Table 2.2 – Strains of *E. coli* used in this study.

Strain Name	Genotype	Designed Use
NEB5a (NEB)	*fhuA2 Δ(argF-lacZ)U169 phoA glnV44 Φ80 Δ(lacZ)M15 gyrA96 recA1 relA1 endA1 thi-1 hsdR17*	Plasmid amplification / cloning
NEB10b (NEB)	Δ*(ara-leu) 7697 araD139 fhuA* Δ*lacX74 galK16 galE15 e14- ϕ80*d*lacZ*Δ*M15 recA1 relA1 endA1 nupG rpsL* (Str^{R}) *rph spoT1* Δ*(mrr-hsdRMS-mcrBC)*	Large (10 kb+) plasmid amplification
DH10 Bac (ThermoFisher)	F^{-}*mcr*A Δ(*mrr*-hsdRMS-*mcr*BC) Φ80*lac*ZΔM15 Δ*lac*X74 *rec*A1 *end*A1 *ara*D139 Δ(*ara*, *leu*)7697 *gal*U *gal*K λ^{-} *rps*L *nup*G/pMON14272/pMON7124	Bacmid transposition
One Shot Top10 (ThermoFisher)	F- *mcrA* Δ(*mrr-hsd*RMS-*mcr*BC) Φ80*lac*ZΔM15 Δ *lac*X74 *rec*A1 *ara*D139 Δ(*araleu*)7697 *gal*U *gal*K *rps*L (StrR) *end*A1 *nup*G	Plasmid amplification / cloning
Rosetta II (DE3) (Merck)	F^{-} *ompT hsdS*$_{B}$(r$_{B}^{-}$ m$_{B}^{-}$) *gal dcm* (DE3) pRARE2 (Cam^{R})	Expression Of rare codons
XL10-Gold (Agilent)	TetrD(mcrA)183 D(mcrCB-hsdSMR-mrr)173 endA1 supE44 thi-1 recA1 gyrA96 relA1 lac Hte [F´ proAB lacIqZDM15 Tn10 (Tetr) Amy Camr]	Large plasmid amplification / cloning
BL21 (DE3) pLysS (ThermoFisher)	F– *omp*T *hsdS*$_{B}$ (r$_{B}$–, m$_{B}$–) *gal dcm* (DE3) pLysS Cam^{R}	Expression

Table 2.3 – List of cell cultures used in this study.

Cell Type	Source	Media used	Conditions
HEK293	DSMZ	DMEM, 10% Foetal Bovine Serum (FBS, Gibco)	Adherent, 37°C, Stationary, 5.0% CO_2
HeLa	ATCC	DMEM, 10% Foetal Bovine Serum (FBS, Gibco)	Adherent, 37°C, Stationary, 5.0% CO_2
Sf9	ATCC	Insect Xpress	Suspension, 27°C, rotating 120 RPM
Sf9-ET	(Hopkins & Esposito, 2009)	Insect Xpress with 150 ng mL^{-1} G418	Suspension, 27°C, rotating 120 RPM
GFP-G1 Hybridoma	DSHB	IMDM	Suspension, 37°C, Stationary, 5.0% CO_2

DSMZ: Deutsche Sammlung von Mikroorganismen und Zellkulturen; ATCC: American Type Culture Collection; DSHB: Developmental Studies Hybridoma Bank; IMDM: Iscove's Modified Dulbecco's Medium; DMEM: Dulbecco's Modified Eagle Medium.

Table 2.4 – List of general primers used in this study.

Cloning primers for PCR can be found in their relevant chapter.

Primer name	Sequence (5' - 3')	Use	Annealing temp (°C)
M13 For	CCCAGTCACGACGTTGTAAAACG	Bacmid verification	55
M13 Rev	AGCGGATAACAATTTCACACAGG		
HRT Seq 1	TTGGCGGCCGGATGCAATCA	Sequencing	-
HRT Seq 2	ATGGCGAACCGCCGAGTGGG	Sequencing	-
pFastBac For	GGATTATTCATACCGTCCC	Sequencing	-
pFastBac Rev	CAAATGTGGTATGGCTGAT	Sequencing	-
pFastBac IQ seq For	CCATCAGCATAAGGAGTAT	Sequencing	-
LKO.1 5'	GACTATCATATGCTTACCGT	Sequencing	-
pFast-eGFP Seq	CAACGAGAAGCGCGATCA	Sequencing	-

Table 2.5 – List of plasmids used in this study.

Plasmid Name	Bacterial Resistance Gene	Expression Product	Tag	Source
pcDNA3-ASPM	Ampicillin (100 µg/mL)	ASPM	6x His	Gift from Dr. J. Bond, University of Leeds
pFastBac1	Ampicillin (100 µg/mL)	-	-	Gibco #10360014
pFastBac1-eGFP	Ampicillin (100 µg/mL)	eGFP	N-term FLAG	Generated by MH
pFastBac1-CH	Ampicillin (100 µg/mL)	CH domains (ASPM aa 920-1,261)	C-term FLAG	Generated by MH
pFastBac1-eGFP-CH	Ampicillin (100 µg/mL)	eGFP-CH domains (ASPM aa 920-1,261)	N-term FLAG-eGFP	Generated by MH
pFastBac1-eGFP-pp-CH	Ampicillin (100 µg/mL)	eGFP-pp-CH domains (ASPM aa 920-1,261)	N-term FLAG-eGFP	Generated by MH
pSecTag2A-eGFP-pp-CH	Ampicillin (100 µg/mL)	eGFP-pp-CH domains (ASPM aa 920-1,261)	N-term FLAG-eGFP	Generated by MH
pCMV-eGFP-pp-CH	Ampicillin (100 µg/mL)	eGFP-pp-CH domains (ASPM aa 920-1,261)	N-term FLAG-eGFP	Generated by MH
pFastBac1-eGFP-pp-CH2IQ	Ampicillin (100 µg/mL)	eGFP-pp-CH2IQ (ASPM aa 920-1,321)	N-term FLAG-eGFP	Generated by MH
pSecTag2A-eGFP-pp-CH2IQ	Ampicillin (100 µg/mL)	eGFP-pp-CH2IQ (ASPM aa 920-1,321)	N-term FLAG-eGFP	Generated by MH
pFastBac-eGFP-pp-CH1	Ampicillin (100 µg/mL)	eGFP-pp-CH1 domains (ASPM aa 920-1,109)	N-term FLAG-eGFP C-term 6x HIS	Generated by Genscript
pFastBac-eGFP-pp-CH2	Ampicillin (100 µg/mL)	eGFP-pp-CH2 domains (ASPM aa 1,056-1,261)	N-term FLAG-eGFP C-term 6x HIS	Generated by Genscript
pFastBac1-MYL6B	Ampicillin (100 µg/mL)	Myosin light chain 6B	-	Generated by Genscript
pFastBac1-CALM	Ampicillin (100 µg/mL)	Calmodulin	-	Generated by Genscript
pFastBac1-eGFP-21IQ	Ampicillin (100 µg/mL)	eGFP-IQ32-52 (ASPM aa 2,018-2,536)	N-term FLAG-eGFP	Generated by MH
pFastBac1-eGFP-IQ1-52	Ampicillin (100 µg/mL)	eGFP-IQ1-52 (ASPM aa 1,263-2,536)	N-term FLAG-eGFP	Generated by MH

Table 2.5– Continued.

Plasmid Name	Bacterial Resistance Gene	Expression Product	Tag	Source
pFastBac1-eGFP-IQ32-81	Ampicillin (100 μg/mL)	eGFP-IQ32-81 (ASPM aa 2,018-3,234)	N-term FLAG-eGFP	Generated by MH
pFastBac1-eGFP-IQ1-9	Ampicillin (100 μg/mL)	eGFP-IQ1-9 (ASPM aa 1,263-1,493)	N-term FLAG-eGFP	Generated by MH
pFastBac1-eGFP-IQ9-16	Ampicillin (100 μg/mL)	eGFP-IQ9-16 (ASPM aa 1,461-1,661)	N-term FLAG-eGFP	Generated by MH
pFastBac1-eGFP-IQ50-52	Ampicillin (100 μg/mL)	eGFP-IQ50-52 (ASPM aa 2,455-2,536)	N-term FLAG-eGFP	Generated by MH
pFastBac1-eGFP-IQ53-61	Ampicillin (100 μg/mL)	eGFP-IQ53-61 (ASPM aa 2,527-2,744)	N-term FLAG-eGFP	Generated by MH
pFastBac1-eGFP-IQ62-68	Ampicillin (100 μg/mL)	eGFP-IQ62-68 (ASPM aa 2,741-2,915)	N-term FLAG-eGFP	Generated by MH
pFastBac1-eGFP-IQ68-75	Ampicillin (100 μg/mL)	eGFP-IQ68-75 (ASPM aa 2,879-3,085)	N-term FLAG-eGFP	Generated by MH
pFastBac1-eGFP-IQ74-81	Ampicillin (100 μg/mL)	eGFP-IQ74-81 (ASPM aa 3,026-3,234)	N-term FLAG-eGFP	Generated by MH
pFastBac1-eGFP-IQ49-51	Ampicillin (100 μg/mL)	eGFP-IQ49-51 (ASPM aa 2,427-2,509)	N-term FLAG-eGFP	Generated by Genscript
pFastBac1-eGFP-IQ51-53	Ampicillin (100 μg/mL)	eGFP-IQ51-53 (ASPM aa 2,477-2,559)	N-term FLAG-eGFP	Generated by Genscript
pFastBac1-eGFP-C-Term	Ampicillin (100 μg/mL)	eGFP-C-Term (ASPM aa 3,227-3,477)	N-term FLAG-eGFP	Generated by Genscript
pMJ915-Cas9	Ampicillin (100 μg/mL)	Cas9	N-term MBP	Addgene #69090
pMHT-TEVp	Kanamycin (50 μg/mL)	TEV protease	N-term MBP-6x His	DNASU; TvCD00084286
pGEX-6P-1-PP	Ampicillin (100 μg/mL)	PreScission Protease	N-term GST	Gift from Jan Faix, University of Hannover
pSpCas9-2A-Puro (PX459)	Ampicillin (100 μg/mL)	Cas9 – mammalian expression	Puromycin	Addgene #62988
pGEX-6P-1-anti-GFP-nanobody	Ampicillin (100 μg/mL)	Anti-GFP-nanobody	N-term GST	Addgene #61838

2.2 Molecular biology

All DNA stocks were stored at -20°C until required and then thawed at room temperature (~20°C). When in use, DNA was stored on ice.

2.2.1 Quantification of nucleic acids

DNA concentrations were estimated on a NanoPhotometer NP80 spectrophotometer (Implen). Prior to measuring the DNA or RNA concentration, the sensor was washed once with 5 µL 70% ethanol and twice with 5 µL distilled water. A blank measurement was then taken with 2 µL of appropriate buffer (TE buffer or $_{dd}H_2O$) before 2 µL of sample was loaded for measurement. The purity of the sample was determined by the A260 / 280 ratio, where a pure DNA sample has a value of 1.8, and a pure RNA sample has a value of 2.0. The A230 / 280 ratios were also observed where a value of 2.0-2.2 was considered pure, values lower than this suggest the presence of phenols or EDTA contaminants (Sambrook, 2001).

2.2.2 DNA precipitation

DNA was concentrated by isopropanol precipitation when a higher concentration of DNA was required. To a volume of DNA, half the volume of 7.5 M ammonium acetate (NH_4OAc) and 2 volumes of isopropanol were added and incubated at -20°C for 10 mins. The solution was centrifuged at 17,000 x g for 10 mins using a MICRO STAR 17R (VWR) centrifuge. The pellet was washed twice with 70% ethanol and the sample was briefly vortexed to break up the DNA pellet. DNA was pelleted by centrifugation at 17,000 x g for 10 mins. Ethanol was removed with careful pipetting and the pellet allowed to air dry for 10 mins. Pelleted DNA was then resuspended in either TE buffer or $_{dd}H_2O$ depending on downstream uses (Moore & Dowhan, 2002).

2.2.3 Plasmid DNA preparations

2.2.3.1 'Miniprep' DNA preparation

Small scale plasmid DNA was purified from *Escherichia coli* (*E. coli)* using the QIAprep Spin Miniprep Kit (Qiagen) following the manufacturer's instructions. Briefly, 5 mL of an overnight transformed plasmid amplification bacterial culture was centrifuged at 3,000 x g for 15 mins at room temperature in a Thermo Scientific Heraeus Megafuge 16R. The supernatant was discarded, and the pellet thoroughly resuspended in 250 µL buffer P1, containing RNaseA, to remove RNA contamination, and methylene blue which indicates alkaline cell lysis by turning a blue colour. 250 µL of buffer P2 was then added and the solution mixed by inversion 6-8 times. 350 µL buffer N3 was added and mixed by inversion 4-6 times. Lysed cells were centrifuged for 10 mins at 17,000 x g in a MICRO STAR 17R (VWR) centrifuge to pellet the cell debris. The supernatant was applied to a Qiagen spin column and centrifuged at 17,000 x g for 1 min using a MICRO STAR 17R (VWR) centrifuge. The flow through was discarded and the column washed with 500 µL buffer PB. The flow through was again discarded and the column washed with 750 µL of buffer PE. The column was centrifuged at 17,000 x g for 1 min using a MICRO STAR 17R (VWR) centrifuge and the flow-through discarded. Residual wash buffer was removed by centrifugation at 17,000 x g for 1 min using a MICRO STAR 17R (VWR) centrifuge. The column was transferred to a sterile 1.5 mL Eppendorf and the DNA eluted in 30 µL of TE buffer or ${}_{dd}H_2O$ depending on downstream uses.

2.2.3.2 'Maxiprep' DNA preparation

To have sufficient DNA for subsequent cloning steps and for transfection of mammalian cells, larger DNA plasmid preparations were performed using the Qiagen Hi-speed Maxiprep kit, according to the manufacturer's instructions. Briefly, a 250 mL overnight bacterial culture was pelleted by centrifugation at 3,000 x g for 15 mins at 5°C in a Thermo Scientific Heraeus Megafuge 16R. The pellet was then resuspended in 10 mL buffer P1 followed by the addition of 10 mL buffer P2 and the tube was mixed by inversion six times then incubated at room temperature for 5 mins. 10 mL buffer P3 was added and the solution and mixed by inversion 6 times. The lysate was applied to a QIAfilter Maxi Cartridge, with the cap attached to the tip. The solution was then allowed to settle at room temperature for 10 mins. The cleared cell lysate was then applied to a Hi Speed Maxi Tip, equilibrated with 10 mL buffer QBT. The lysate was allowed to enter the resin by gravity flow, enabling the DNA to bind. The QIAGEN Tip was washed with 60 mL buffer QC before the DNA was eluted with 15 mL buffer QF into a 50 mL falcon tube. The DNA was precipitated by the addition of 10.5 mL room temperature isopropanol, gently mixing and incubating at room temperature for 5 mins. The DNA / isopropanol mixture was passed through a QIAprecipitator Maxi module to bind the DNA. The DNA was washed with 2 mL 70% ethanol and the precipitator membrane dried by passing air forcefully over the membrane using a syringe. The DNA was eluted into a 1.5 mL centrifuge tube by passing 1 mL of TE buffer through the precipitator twice to ensure full elution of the DNA.

2.2.4 Restriction digests

DNA constructs were digested with endonucleases to allow for cloning or to indicate the presence of correct DNA inserts into plasmids following manufactures instructions. For cloning purposes, 2 µg of plasmid was incubated with 20 units of the representative restriction enzymes (New England Biolabs (NEB)), in 1x CutSmart buffer for 1 hour at 37°C, with the exception for SmaI which was incubated at 25°C. For diagnostic digests, 100 ng of DNA was incubated with 2 units of enzyme in 1x CutSmart buffer for 1 hour at 37°C, again with the exception for SmaI which was incubated at 25°C.

2.2.5 Separation of DNA fragments with agarose gel electrophoresis

Digested DNA was separated by size using agarose gel electrophoresis. Agarose was melted into TAE buffer (40 mM Tris, 20 mM Acetic acid, 1 mM EDTA, pH 8.3) at concentration between 2 and 0.5% (w/v) depending on the size of the DNA fragments to be separated, and ethidium bromide (EtBr) (Thermo Fisher) was added at approximately 0.5 µg mL^{-1}. The gel was poured into the required size gel casing with appropriately sized comb and allowed to set for 30 mins. The gel was placed in a gel tank with TAE buffer and the DNA was mixed with 6x Gel loading dye Purple (NEB) (15% Ficoll® 400, 60 mM EDTA, 20 mM Tris-HCl, 0.5% SDS, 0.12% Dye 1, 0.006% Dye 2, pH 8.0) to produce a final 1x concentration. The DNA samples, along with 6 µL 1 kb DNA ladder or 1 kb extended DNA ladder (NEB) were loaded into separate lanes of the gel and the gel run at 100 V for ~35 mins until the dye front had reached the end of the gel. The gel was imaged on the Molecular Imager® Gel Doc XR+ System (BioRad) and images processed using the Image LabTM Software (BioRad).

2.2.6 Recovery of DNA from agarose gels

The separation of DNA on agarose gels was used to purify restriction digested fragments. The DNA band of interest was excised from the gel using the QIAquick® gel extraction kit (Qiagen) following the manufacturer's protocol. Briefly, the gel was visualised using a Gel Doc Imager (BioRad, Molecular Imager Gel Doc XR+) and bands were carefully cut out on a transilluminator using a clean scalpel. The band was transferred to a pre-weighed 2 mL Eppendorf tube and the mass of the gel band measured. Three gel volumes of buffer QG was added to the Eppendorf, where 100 mg of gel was equivalent to 100 µL of buffer. The bands were incubated in buffer QG at 50°C for 15 mins until the gel slice had completely dissolved. One gel volume of isopropanol was then added to the Eppendorf tube and mixed to precipitate the DNA. The DNA was applied to a QIAquick spin column and centrifuged at 17,000 x g for 1 min using a MICRO STAR 17R (VWR) centrifuge. 500 µL buffer QG was applied to the column to clean the DNA. This was centrifuged at 17,000 x g for 1 min and the flow through was discarded. 750 µL buffer PE then then added and centrifuged at 17,000 x g for 1 min and the flow through discarded. The column was centrifuged for an additional 1 min to remove any residual PE buffer. The QIAquick column was transferred to a sterile 1.5 mL Eppendorf and the DNA was eluted with 30 µL $_{dd}H_2O$ and centrifugated at 17,000 x g for 1 min after 1 min incubation.

2.2.7 Amplification of nucleic acids by polymerase chain reaction.

The polymerase chain reaction (PCR) was utilised for many manipulations of DNA. Careful design of the primers allowed for the insertion of tags, novel restriction sites or stop codons which were incorporated into the DNA to be amplified. In addition, PCR was also used to verify if a cloning reaction had been successful. All primers were designed to have a GC content of approximately 50% and a melting temperature (T_m) within 5°C between the primer pairs. Primers were synthesised by Integrated DNA Technologies (IDT). Lyophilised DNA primers were prepared as 100 µM stocks in TE buffer and stored at -20°C. PCR reactions were performed using a T100 Thermocycler (BioRad). The PCR protocol was adapted for different PCR primers and products, based on the length of the required product and the primer annealing temperature.

Phusion® High-Fidelity DNA Polymerase (NEB) was used in order to reduce the error rate in PCR products. Phusion PCR reactions were prepared on ice in thin-walled PCR tubes as in Table 2.6. The initial denaturation of DNA was at 95°C for 3 mins, before denaturation at 95°C for 30 secs for subsequent cycles. Following denaturation, the temperature was reduced to the annealing temperature for 30 secs to allow the primers to anneal. The extension of the annealed primers was performed at 72°C for 30 secs per kb. The reaction was repeated for 25 cycles prior to a final 10 min extension at 72°C. Generally, less than 30 cycles were performed as the PCR can introduce random mutations, which increased in likelihood with the number of cycles. PCR products were then resolved by agarose gel electrophoresis (Section 2.2.5).

Table 2.6 – Standard component concentrations used for a PCR reaction.

Component (Stock concentration)	Final concentration	Volume used in 50 µL reaction
H_2O (ultra-pure)	-	32.5 µL
5x Phusion HF Buffer	1x	10 µL
dNTPs (10 mM)	200 µM	1 µL
Forward Primer (10 µM)	0.5 µM	2.5 µL
Reverse Primer (10 µM)	0.5 µM	2.5 µL
Template Plasmid DNA (100 ng µL^{-1})	2 ng µL^{-1}	1 µL
Phusion DNA polymerase (NEB)	0.02 U µL^{-1}	0.5 µL

2.2.8 GeneArt seamless cloning

Cloning was performed using the GeneArt seamless cloning and assembly kit (Thermo Fisher), in which PCR primers are designed specific to the gene of interest but with an additional 5’ 15 bp homologous region to the vector ends (Figure 2.1). The amplified insert could then be cloned into a digested vector by homologous recombination between the vector and overlapping portions added to the insert by high fidelity PCR amplification.

In order to create the cloning reaction, a 2:1 molar ratio of insert to linearised vector was used. The amount of insert required was determined using the following equation:

$$X\ ng\ insert = \frac{2\ \times bp\ insert\ \times 100\ ng\ linearised\ vector}{bp\ linearised\ vector}$$

100 ng of linear vector, along with the appropriate amount of insert, was added to 4 µL of 5x reaction buffer and 2 µL of 10x GeneArt Enzyme Mix, to a final volume of 20 µL with $_{dd}H_2O$. Reactions were incubated at room temperature for 30 mins before 2 µL were immediately transformed into 50 µL One Shot™ Top10 competent *E. coli* cells following the protocol in Section 2.2.14.

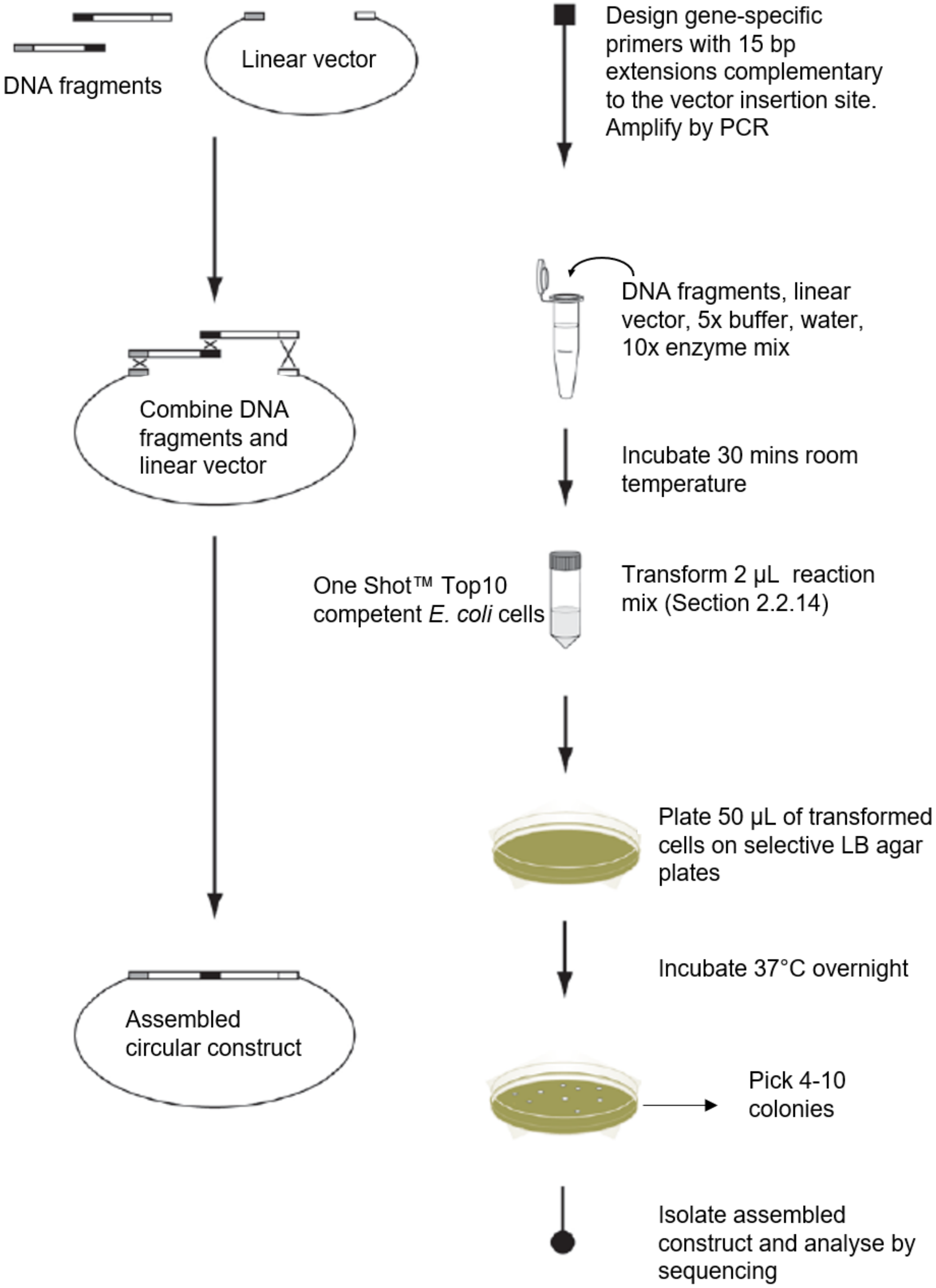

Figure 2.1 – An overview of the GeneArt seamless cloning workflow.

A workflow depicting the steps involved in GeneArt seamless cloning. A linearised plasmid and PCR amplified gene of interest are mixed in the GeneArt cloning reaction for 30 mins at room temperature. Reaction mixture was then transformed into One Shot™ Top10 competent *E. coli* cells and positive clones were selected. Adapted from GeneArt seamless cloning user manual (Thermo Fisher).

2.2.9 NEBuilder HiFi DNA assembly

Alternatively, NEBuilder HiFi DNA assembly cloning kit was used (NEB). This kit allowed for an optional DpnI digestion for insert clean-up. This resulted in the ability to achieve a higher insert concentration and therefore resulted in a more efficient cloning reaction.

The reaction (set up as in Table 2.7) was incubated at 50°C for 15 mins (when 2-3 fragments were being assembles) or 60 mins (when 4-6 fragments were being assembled or when reaction efficiency was low). Following incubation, the assembly reaction was either stored on ice for immediate use or at -20°C for storage until required. Two µL of the assembly was then transformed into NEB 5-alpha competent *E. coli* cells as in Section 2.2.14.

Table 2.7 – NEBuilder assembly reaction.

	2-3 Fragment Assembly	**4-6 Fragment Assembly**
DNA Molar Ratio	Vector:insert 1:2	Vector:insert 1:1
Total Amount of Fragments	0.1 pmols	0.4 pmols
Volume of Vector	x µL	x µL
Volume of Insert	y µL	y µL
NEBuilder HiFi DNA Assembly Master Mix	10 µL	10 µL
$_{dd}H_2O$	10-(x+y) µL	10-(x+y) µL
Total volume	20 µL	20 µL

Both GeneArt seamless cloning and NEBuilder are based on the Gibson assembly method (Gibson et al., 2009). This approach employs an enzyme trio comprising an exonuclease to digest 5’ ends, a polymerase to close annealed fragments and a ligase to seal remaining nicks. However, NEBuilder was preferred over GeneArt seamless cloning as the protocol used had less time constraints and as a result, cloning was more successful.

2.2.10 Removal of restriction sites from pFastBac1

In order to successfully subclone the ASPM gene from pcDNA3-ASPM into pFastBac1, firstly the Kpn1 restriction site, which produces 3' overhangs, was removed from pFastBac1 using T4 DNA Polymerase, which has a strong 3'→5' exonuclease activity thus blunting 3' overhangs. Briefly, 2 µg of pFastBac1 was incubated with 20 units Kpn1-HF (NEB) in 1x CutSmart buffer for 1 hour at

37°C. The linearised plasmid was incubated with 3 units T4 DNA Polymerase (NEB) in 60 µL 1x NEBuffer 2.1 for 12 mins at 12°C, followed by heat inactivation at 75°C for 20 mins. The linearised plasmid was then separated on an Ethidium Bromide pre-stained 0.7% agarose gel (as in Section 2.2.5) and purified using a QIAGEN Gel Purification Kit (as in Section 2.2.6). The purified plasmid was re-circularised by ligation, using 200 units of T4 DNA Ligase in 40 µL 1x Ligase buffer at room temperature overnight to increase possibility of ligation of blunt ends. The enzyme was then heat inactivated at 65°C for 10 mins and 2 µL of the ligation reaction transformed into One Shot™ Top10 cells (as in Section 2.2.14).

2.2.11 DNA sequencing

Purified cloned constructs were sequenced either by Source Bioscience or GATC Biotech Ltd. Available universal sequencing primers were used for common sites, otherwise, custom sequencing primers (Table 2.4) were used. Sequences were aligned and checked using SerialCloner version 2.5.

2.2.12 Bacmid isolation

Prepared pFastBac1 constructs were transposed into bacmid in *E. coli* MAX Efficiency® DH10Bac using the recommended transformation procedure (Section 2.2.14). In addition, the SOC incubation step was increased from 1 to 4 hours. Transformed cells were plated on LB agar plates containing the following antibiotic mix: 50 µg mL^{-1} Kanamycin, 7 µg mL^{-1} Gentamycin, 10 µg mL^{-1} Tetracycline, 100 µg mL^{-1} Bluo-gal and 40 µg mL^{-1} Isopropyl β-D-1-thiogalactopyranoside (IPTG). Plates were incubated at 37°C for 48 hours.

Colonies were selected through blue / white screening. White colonies were re-streaked onto fresh plates to ensure colony purity as mixed blue / white colonies can occur. Single colonies were then used to inoculate 5 mL of LB media containing antibiotics (50 µg mL^{-1} Kanamycin, 7 µg mL^{-1} Gentamycin and 10 µg mL^{-1} Tetracycline) and incubated at 37°C for 24 hours. Cells were pelleted at 3,000 x g for 10 mins and the supernatant was completely removed. The pellet was then resuspended in buffer P1 (15 mM Tris-HCl, 10 mM EDTA, 100 µg mL^{-1} RNase A, pH 8.0), lysed by the addition of buffer P2 (0.2 M NaOH, 1% SDS) and incubated for 5 mins on ice before lysis was stopped by the addition of 3 M potassium acetate (pH 5.5). Cell debris was removed by centrifugation at 17,000 x g for 10 mins and the supernatant transferred into an equal volume of ice-cold isopropanol and incubated on ice for 15 mins. Precipitated DNA was pelleted by centrifugation at 17,000 x g for 15 mins and washed twice with 70% ethanol. The DNA pellet was air dried briefly before dissolving in $_{dd}H_2O$. The presence of the gene of interest in the recombinant bacmid was verified by PCR using M13 Forward and M13 Reverse primers with an annealing temperature of 55°C (as in Table 2.4). The resulting PCR product was visualised on a 1% agarose gel (as in Section 2.2.5).

2.2.13 Growth media

E. coli were cultured using Luria-Bertani (LB) broth (10 g Peptone, 5 g Yeast Extract, 5 g NaCl per Litre (Invitrogen)) or 2xTY broth (16 g Tryptone, 10 g Yeast Extract, 5 g NaCl per Litre). Solid media was prepared using LB Broth with 12 g Agar per litre (Sigma Aldrich). Antibiotics were added to the media according to the concentrations listed in Table 2.8 to select for bacteria containing antibiotic resistant plasmids.

Table 2.8 – Commonly used antibiotics and their working concentrations.

Antibiotic	Working concentration (µg mL^{-1})
Ampicillin	100
Chloramphenicol	25
Gentamicin	7
Kanamycin	50
Tetracycline	10

All media was autoclaved at 121°C for 15 mins before use. LB agar was allowed to cool to ~50°C before the addition of the appropriate antibiotic(s). Cooled agar was then poured into sterile 10 cm petri dishes and allowed to set for 30 mins. All sterile work was performed near a lit Bunsen flame.

2.2.14 Transformation of competent cells

To transform competent *E. coli* cells, 20 ng of purified plasmid was added to 25 µL of freshly thawed competent cells and incubated for 30 mins on ice. The cells were heat shocked at 42°C for 30 secs, using a water bath, and replaced onto ice for 5 mins. 500 µL of sterile SOC media was then added to the cells, and the cells were incubated at 37°C, 120 RPM, for 1 hour. 50 µL of cells were then plated on LB (Luria Broth) agar with appropriate antibiotic for selection and incubated overnight at 37°C.

2.2.15 Bacterial cultures

Single colonies from plates were picked using a sterile metal loop and used to inoculate 5 mL LB cultures containing the appropriate antibiotic. The cultures were incubated overnight at 37°C and 220 RPM. For larger cultures, 800 mL LB broth containing the appropriate antibiotic was inoculated with 5 mL starter culture and incubated overnight under the same conditions.

2.2.16 Glycerol stocks

Glycerol stocks were made for bacterial colonies that carry a validated plasmid of interest. 500 µL of an overnight culture was gently mixed with 500 µL 50% sterile glycerol in a cryovial. Glycerol stocks were stored at -80°C.

2.3 Insect cell culture

All *Spodoptera frugiperda* (Sf9) culture media and reagents were obtained from Lonza. All reagents and materials used were sterile and cell culture was performed in a class II biological safety cabinet. All media was heated to 27°C prior to use.

2.3.1 Growth and passaging Sf9 cells

For baculovirus amplification and expression, Sf9 cells were cultured as a suspension in Insect-XPRESS with L-glutamine medium at 27°C, 100 RPM. For titration of viruses, Sf9-ET derivative cells (Hopkins & Esposito, 2009) were cultured in suspension in Insect-XPRESS with L-glutamine medium supplemented with 150 µg mL^{-1} G418. Virus containing supernatant was stored at 4°C.

Every 2 to 3 days, cells were counted, and cell viability assessed by staining 10 µL cell-culture samples with 10 µL 2x Trypan blue and examining under a light microscope in a haemocytometer (Hawksley BS.748). Once cells had reached a high density (4 – 6x10^{6} cells mL^{-1}), the cells were split into a fresh 125 mL Erlenmeyer flask (Sigma Aldrich) at a lower density of $0.5x10^6$ cells mL^{-1} in a total volume of 50 mL with fresh medium. Cells were passaged to a maximum of 25 times.

2.3.2 Long-term storage of cells

Insect cells were grown in the log phase, to a concentration of $4\text{-}8x10^6$ cells mL^{-1}. Cells where then pelleted by centrifugation at 1,000 x g for 5 mins. Half of the supernatant was removed and mixed with and equal volume of fresh Insect-XPRESS with L-glutamine medium along with Dimethyl sulphoxide (DMSO) to a final concentration of 7.5% (v/v) to make the freezing solution. The freezing solution was then filter sterilised through a 0.22 µm filter (Millipore). The remaining supernatant was discarded and the cell pellet was resuspended with the freezing solution to a final cell concentration of $1x10^7$ cells mL^{-1}. The cell suspension was then aliquoted into 2 mL cryovials (Sarstedt), and frozen using a 1 deg min^{-1} cell cooler (Mr. Frosty, Nalgene) placed in a -80°C freezer. Once frozen, cells were transferred to vapor phase liquid N_2 storage.

2.3.3 Recovery of Sf9 cells from liquid N_2 storage

Frozen stocks were recovered by rapidly thawing the vials at 37°C. The cells were immediately added to 20 mL of Insect-XPRESS with L-glutamine media in a 125 mL Erlenmeyer flask and placed in an incubator at 27°C with 100 RPM shaking.

2.3.4 Transfection

Successfully verified recombinant bacmid DNA was transfected into Sf9 insect cells following the Bac-to-Bac protocol (Thermo Fisher). Briefly, 25 µg isolated bacmid suspended in 300 µL Dulbecco’s phosphate buffered saline (DPBS; Gibco) was incubated with 300 µg polyethylenimine (PEI) for 10 mins at room temperature before being added to 100 mL of $0.6x10^6$ Sf9 cells mL^{-1} and incubated at 27°C, 100 RPM, for 5 days.

2.3.5 Baculovirus harvesting

Baculovirus containing cell suspension was harvested by centrifugation at 3,000 x g for 10 mins in a Thermo Scientific Heraeus Megafuge 16R, recovering the supernatant. Virus containing media was stored in UV-resistant Falcon tubes at 4°C.

2.3.6 Baculovirus titering

Baculovirus titre was determined by an endpoint dilution assay in a 96-well plate. Harvested baculovirus was plated at a starting dilution of 1:1000 (10^{-3}) and serially diluted 5 times in Insect-XPRESS to a final dilution of $10^{-8.6}$. To each well 7.5×10^4 Sf9-ET cells in 100 μL Insect-XPRESS were added. The plate was incubated at 27°C for 5 days without shaking. Sf9-ET cells are derived to contain the eGFP gene under the control of a polyhedrin promoter (Hopkins & Esposito, 2009). During infection, viral DNA is replicated which also expresses early viral gene products such as the late gene polyhedrin promoter. And as such, an Sf9-ET cell infected with a baculovirus results in the expression of early viral proteins and allowing the expression of eGFP (Hopkins & Esposito, 2009). After incubation, the plate was scored by observing wells containing GFP foci. The plaque forming units per mL (PFU mL^{-1}) was calculated by observing the dilution factor at which 50% of the wells are infected (TCID50), normalising for well volume (IC50 mL^{-1}) and then multiplying by 0.69 to predict the number of infectious units (PFU mL^{-1}).

The final step in the calculation is derived from the following equation:

$$P(0) = e(-m)$$

where P(0) is the proportion of negative values, at IC50 this is 0.5, *e* is the irrational constant of the natural log and *m* is mean number of infected units. This equation can then be rearranged to:

$$m = -ln0.5 = 0.69$$

2.3.7 Virus amplification

Baculovirus was amplified by infecting Sf9 cells at a density of 1.0×10^6 cells mL^{-1} with a multiplicity of infection (MOI, the ratio of infectious agents to infected targets) of 0.5. Cells were then incubated at 27°C for 5 days shaking at 100 RPM before the baculovirus was harvested as described (Section 2.3.5).

$$Inoculum\ required\ (m) = \frac{MOI\ \times Total\ number\ of\ cells}{Titre\ (PFU/mL)}$$

2.3.8 Expression and harvest

For expression of the proteins of interest, Sf9 cells were infected at a density of $1.5x10^6$ cells mL^{-1} using an MOI between 2 and 5. Infected cultures were incubated at 27°C, 100 RPM for 48-72 hours before harvesting the cells by centrifugation at 3,000 x g for 10 mins in a Thermo Scientific Heraeus Megafuge 16R. Supernatant was removed and cell pellets were then stored at -80°C.

2.4 Mammalian culture

All cell culture media and reagents were obtained from Gibco (Thermo Fisher Scientific). All reagents and materials used were sterile and cell culture was performed in a class II biological safety cabinet. All media was heated to 37°C prior to use.

2.4.1 Cell culture

Cells were cultured in respective media and temperatures stated in Table 2.3. Cells were typically passaged 2-3 times per week once cells were ~70% confluent and media changed as required. Cells were maintained to passage 35.

2.4.2 Passaging

Once cells had reached a confluence of ~90% they were harvested and seeded at a lower density on a fresh tissue culture flask. Media was removed from the flask and the cells were gently washed with 10 mL Dulbecco phosphate buffered saline (DPBS) before being detached from the flask with 2 mL TrypLE (Thermo Fisher) per 75 cm^3 flask. Cells were incubated with TrypLE for 2-5 mins, the trypsin was then inactivated by the addition of 8 mL growth medium to give a final volume of 10 mL and placed in a 15 mL tube. Cells were centrifuged at 1,000 x g for 5 mins at room temperature in a Harrier 18/80 (MSE) centrifuge to pellet before resuspending in 10 mL fresh growth medium. Cells were counted using a haemocytometer (Hawksley BS.748) and the cells seeded onto flasks at the required density (~$2x10^6$ cells) in growth media. Cells were maintained to passage 35, at which point the cells were discarded.

2.4.3 Storage and recovery

Cells were harvested with TrypLE, pelleted and resuspended at ~1x10^{6} cells mL^{-1} (as in Section 2.4.2) in growth media supplemented with 10% dimethyl sulfoxide (DMSO). The cell suspension was then aliquoted into 2 mL cryovials (Sarstedt), and frozen using a 1 deg min^{-1} cell cooler (Mr. Frosty, Nalgene) placed in a -80°C freezer. Once frozen, cells were transferred to vapor phase liquid N_2 storage.

Frozen stocks were recovered by rapidly thawing at 37°C in a water bath. The thawed cells were immediately transferred into a sterile T-75 tissue culture flask containing 10 mL of pre-warmed media. The flask was incubated in a humidified incubator with 5% CO_2. After 24 hours of recovery, the media was aspirated and replaced with fresh media.

2.4.4 Seeding coverslips / plates

Cells were plated at a density of 1,500 cells mm^{-2} on either acid-etched sterile coverslips or a sterile multi-well plate. Briefly, cells were removed from growth flasks (as in Section 2.4.2), counted using a haemocytometer (Hawksley BS.748), diluted to an appropriate concentration using the appropriate growth medium and then added to the coverslips, or to the plate.

2.4.5 Lipid based transfection of mammalian cells

Cells were seeded onto either a 24-well plate or a 6-well plate and were transfected 16 hours post-seeding at a confluency of 50% with either RNAiMAX (Thermo Fisher), lipofectamine 2000 (Thermo Fisher) or FuGene HD (Promega) following manufactures guidance. Briefly, transfection reagent was warmed to room temperature and mixed with DNA in a 4:1 ratio. 3 µL transfection reagent was mixed with 2 µg DNA in 100 µL Opti-MEM and incubated at room temperature for 10 mins. An appropriate volume was then added to each well (25 µL per well in a 6-well plate or 5 µL per well in a 24-well plate) dropwise and the plate incubated at required growth conditions for 24-48 hours.

2.5 Immunofluorescence

2.5.1 Fixation and permeabilization

Plated cells (Section 2.4.4) were fixed at 50-70% confluency (16-20 hours post plating) with either freshly made 4% paraformaldehyde (in phosphate buffered saline (PBS)) or 100% ice-cold methanol, and permeabilised with PBS, supplemented with 1% bovine serum albumin (BSA) and 0.1% Triton X-100.

2.5.2 Staining

Permeabilised cells were blocked with PBS, 5% BSA. Blocked cells were then incubated with primary antibody for 1 hour (Table 2.9). Cells were washed 5 times in PBS, 1% BSA prior to a 1-hour incubation with appropriate secondary antibody (Table 2.9). Cells were then washed 5 times with PBS, 1% BSA before mounting on slides with ProLong Gold Antifade mounting solution (Thermo Fisher, P10144).

Table 2.9 – List of antibodies used in this study with appropriate dilutions.

Antibody name	Clone type	Epitope	Host	Working dilution	Antibody Type	Source (Cat#)
mEOS2 pAb	Polyclonal	mEos2	Rabbit	WB – 1:1000	Primary	Badrilla (A010-mEOS2)
Anti-eGFP	Polyclonal	GFP	Rabbit	WB – 1:5000	Primary	Invitrogen (A-11122)
Anti-Tubulin (YL1/2)	Monoclonal	Tyrosinated alpha tubulin	Rat	WB – 1:5000 IF – 1:1000	Primary	Abcam (ab6160)
Anti-Gamma Tubulin	Polyclonal	Gamma Tubulin EEFATEGTD RKDVFFY	Rabbit	IF – 1:1000	Primary	Abcam (ab11317)
DAPI	-	DNA	-	IF – 1:500	-	
Anti-FLAG	Monoclonal	FLAG	Mouse	WB – 1:5000	Primary	Sigma (F3165)
Goat Anti-mouse HRP	Polyclonal	Mouse IgG	Goat	WB – 1:3000	Secondary	Sigma (A4416)
Goat anti-mouse Alexa Fluor 546	Polyclonal	Mouse IgG	Goat	IF – 1:400	Secondary	Invitrogen (#A-11003)
Goat anti-rabbit Alexa Fluor 546	Polyclonal	Rabbit IgG	Goat	IF – 1:400	Secondary	Invitrogen (#A-11035)
Goat anti-rat Alexa Fluor 546	Polyclonal	Rat IgG	Goat	IF – 1:400	Secondary	Invitrogen (#A-11081)
Fluorescent Phalloidin (Alexa 488, Alexa 546, Alexa 647)	-	Actin	-	IF – 1:100	-	Thermo Fisher (A12379, A22283, A22287)

IF: Immunofluorescence, WB: Western blot, DAPI: 4',6-diamidino-2-phenylindole, HRP: Horseradish peroxidase.

2.5.3 Visualisation

Immunostained samples were imaged using either a Delta Vision Widefield Deconvolution microscope using the 100x oil objective (NA 1.4) using SoftWoRx software for image acquisition, or the Zeiss LMS880 Inverted Confocal + Airyscan, using the 63x oil objective (NA 1.4).

2.6 Protein purification

2.6.1 PreScission protease (human rhinovirus (HRV) 3C protease) purification

The PreScission protease enzyme was expressed from the plasmid pGEX-6P-1-PP (Table 2.5) using the *E. coli* strain Rosetta II (Merck). Transformed *E. coli.* cells were cultured in 1 L LB containing 100 µg mL^{-1} ampicillin + 25 µg mL^{-1} chloramphenicol at 37°C for 6 hours, shaking 210 RPM. OD600 was measured on a NanoPhotometer NP80 spectrophotometer (Implen) using the OD600 setting. Protein expression was induced by the addition of 0.75 mM IPTG, when the density of the cells had a measured OD600 of 0.6-0.9. The cells were then returned to the 37°C incubator for expression for a further 3 hours, shaking 210 RPM.

Cells were pelleted at 3,500 x g for 25 mins in a Thermo Scientific Heraeus Megafuge 16R and resuspended in 20 mL lysis buffer (50 mM Tris-HCl, 300 mM NaCl, 10% Glycerol, 0.2% NP-40, pH 8.0). The cells were sonicated for 10 secs on / 10 secs off for 18 cycles (3 mins) 50% with a Soniprep 150 MSE (SANYO) and afterwards centrifuged at 30,000 x g for 30 mins in a Beckman Coulter Avanti J25. The clarified supernatant was mixed with 2 mL glutathione-conjugated agarose (Sigma–Aldrich), equilibrated with wash buffer (50 mM Tris-HCl, 300 mM NaCl, 10% glycerol, pH 8.0), in a 5 mL disposable column (Thermo Fisher). The GST-tagged PreScission protease was allowed to bind the resin for 30 mins at room temperature on a roller. Following this, the flow through was collected and the resin subsequently washed with 50 mL wash buffer. PreScission protease was then eluted from the column by the addition of 2 mL elution buffer (50 mM Tris-HCl, 300 mM NaCl, 10% glycerol, 30 mM reduced glutathione, pH 8.0). Several 2 mL elution fractions were then collected and analysed by SDS-PAGE. Fractions containing the largest amounts of protein were pooled. The protein was then dialysed using 10,000 molecular weight cut-off (MWCO) SnakeSkin dialysis tubing overnight into storage buffer (50 mM Tris-HCl, 150 mM NaCl, 10 mM EDTA, 20% glycerol, pH 8.0). The PreScission protease protein concentration was measured using a NanoPhotometer NP80 spectrophotometer (Implen), using the protein UV setting, on the basis of the molar extinction coefficient at 280 nm of 49,195 M^{-1} cm^{-1} and concentrated to 1 mg mL^{-1} using a vivaspin 6 (Satorius).

2.6.2 Anti-GFP-nanobody Purification

The anti-GFP-nanobody was expressed in *E. coli* strain Rosetta II (Merck) using the pGEX-6P-1-anti-GFP-nanobody plasmid (Table 2.5). Transformed cells were cultured in 1 L Auto Induction Media (AIM) (10 g Tryptone, 5 g Yeast extract, 3.3 g $(NH_4)_2SO_4$, 6.8 g KH_2PO_4, 7.1 g Na_2HPO_4, 0.5 g glucose, 2 g α-Lactose, 0.15 g $MgSO_4$) containing 100 µg mL^{-1} ampicillin + 25 µg mL^{-1} chloramphenicol at 37°C for 6 hours, shaking 210 RPM. Protein expression was induced automatically at ~6 hours as the limited level of glucose is depleted, and the lactose is taken up by the bacteria. After the 6-hour incubation, the cells incubated overnight at 23°C, shaking 210 RPM.

Cells were pelleted at 3,500 x g for 25 mins in a Thermo Scientific Heraeus Megafuge 16R and resuspended in 20 mL phosphate-buffered saline (PBS) supplemented with 1 mM DTT, 1 mM EDTA, and cOmplete EDTA-free protease inhibitor cocktail (Roche) (1 tablet / 50 mL), pH 7.3. The cells were sonicated for 10 secs on / 10 secs off for 18 cycles (3 mins) 50% with a Soniprep 150 MSE (SANYO) and afterwards centrifuged at 30,000 x g for 30 mins in a Beckman Coulter Avanti J25. The clarified supernatant was mixed with 2 mL glutathione-conjugated agarose (Sigma–Aldrich), equilibrated with PBS, in a 5 mL disposable column (Thermo Fisher). The GST-tagged nanobody was allowed to bind the resin for 1 hour at 4°C on a roller. Following this, the flow through was collected and the resin subsequently washed with 50 mL PBS. 40 µL of PreScission protease (at 1 mg mL^{-1}) in 2 mL of PreScission protease cleavage buffer (50 mM Tris, 150 mM NaCl, 1 mM EDTA, 1 mM DTT, pH 7.5) was applied to the column and left to incubate overnight at a roller at 4°C.

Cleaved protein was then eluted by the addition of 2 mL PreScission protease cleavage buffer. Elution fractions were then collected and analysed by SDS-PAGE. Fractions containing the largest amounts of protein being pooled. After cleavage, the GST tag was separated from the anti-GFP-nanobodies by cation exchange (SP) using 5 mL Hitrap SP HP column (GE Healthcare) using a salt gradient (from 0.05 M NaCl to 0.5 M NaCl buffered with 20 mM Tris-HCl, pH 7.5). Anti-GFP-nanobody containing fractions were then dialysed using 3,000 MWCO SnakeSkin dialysis tubing against a buffered salt solution containing 0.1 M $NaHCO_3$, 0.5 M NaCl, pH 8.3 and concentrated to 1 mg mL^{-1} using a vivaspin 6 (Satorius). The anti-GFP-nanobody protein concentration was measured using a NanoPhotometer NP80 spectrophotometer (Implen), using the protein UV setting on the basis of the molar extinction coefficient at 280 nm of 26,270 M^{-1} cm^{-1}(calculated using ProtParam, ExPASy). Purified anti-GFP-nanobody was stored at -20°C.

2.6.3 Anti-GFP-nanobody coupling to cyanogen bromide-activated agarose

To couple the anti-GFP-nanobody to cyanogen bromide-activated agarose (CNBr), the following protocol (adapted from (Kavran & Leahy, 2014)) was used. 0.25 g of CNBr Sepharose 4B (Sigma Aldrich) was used for every 10 mg of anti-GFP-nanobody. The CNBr Sepharose was first swelled with 50 mL ice-cold 1 mM HCl for 30 mins on a roller. The resin was then washed briefly with 20 mL $_{dd}H_2O$ before being activated with 20 mL coupling buffer (0.1 M $NaHCO_3$, 0.5 M NaCl, pH 8.3). Following activation, the anti-GFP-nanobody was incubated with the resin for 2 hours at room temperature on a roller in a 5 mL disposable column. The resin was then washed with 3 column volumes of coupling buffer before being incubated with 0.2 M glycine overnight at 4°C on a roller to block unreacted groups. The resin was then washed with 2 column volumes of coupling buffer before alternating washes between high and low pH buffers (0.1 M $NaHCO_3$, 0.5 M NaCl, pH 8.3 & 0.1 M acetate buffer, 0.5 M NaCl pH 4.0, respectively). The prepared resin was then stored in 1 M NaCl, 0.02% (w/v) NaN_3 at 4°C. Resin was equilibrated into appropriate buffer before use.

2.6.4 TEV protease

Tobacco Etch Virus (TEV) protease was required to cleave the affinity tag during Cas9 purification. TEV protease was expressed in the BL21 (DE3) pLysS strain with the pMHT-TEVp plasmid (DNASU; TvCD00084286) grown in 1 L LB medium containing 50 µg mL^{-1} kanamycin to an OD600 between 0.6 and 0.9 and then left to express overnight at 16°C by induction with 1.0 mM IPTG. The protein was purified by affinity chromatography. Briefly, cells were lysed in 25 mM Tris-HCl, 200 mM NaCl, pH 8.0 (supplemented with 10 mM $MgCl_2$, 500 units Benzonase (Sartorius)) using a Dounce homogeniser. The lysate was then clarified by centrifugation at 30,000 x g for 30 mins in a Beckman Coulter Avanti J25 and passed through a 0.22 µm pore size / low-binding filter (Millipore). Protein in the clarified lysate was bound to 4 mL His-tag purification resin (Roche) equilibrated with 25 mM Tris-HCl, 200 mM NaCl, pH 8.0, in a 5 mL column and washed extensively with 50 mL wash buffer (25 mM Tris-HCl, 200 mM NaCl, 50 mM imidazole, pH 8.0), before being eluted with 6 times 2 mL elution buffer (25 mM Tris-HCl, 200 mM NaCl, 200 mM imidazole, pH 8.0). The eluted protein was dialysed overnight against 2 L 25 mM Tris-HCl, 200 mM NaCl, 10 mM imidazole, 5 mM DTT, 50% glycerol, pH 7.6. It was then concentrated to ~1.0 mg mL^{-1} using a 10,000 MWCO VivaSpin 20 protein concentrator. Protein concentration was measured using a NanoPhotometer NP80 spectrophotometer (Implen), using the protein UV setting on the basis of the molar extinction coefficient at 280 nm of 32,220 M^{-1} cm^{-1} (calculated using ProtParam, ExPASy). TEV protease was then aliquoted into 1 mL aliquots and stored at -20°C.

2.6.5 Protein concentration and storage

Protein concentration was estimated by measuring the A280 using a NanoPhotometer NP80 spectrophotometer (Implen) with the appropriate molar extinction coefficient. Prior to measuring the protein concentration, the sensor was washed once with 5 µL 70% ethanol and twice with 5 µL distilled water. A blank measurement was then taken with 2 µL of appropriate buffer before 2 µL of sample was loaded for measurement.

For storing proteins, proteins were frozen dropwise in liquid nitrogen and the drops stored in a cryovial in vapor phase liquid N_2 until required, except for PreScission protease, which was stored at -80°C.

2.6.6 SDS-PAGE

Sodium dodecyl sulphate polyacrylamide gel electrophoresis (SDS-PAGE) was performed in order to separate protein samples according to their size. Glass gel plates (Bio-Rad) with a 1 mm spacer were cleaned with 70 % ethanol and dried. The gel casting assembly was placed in a casting stand and checked for leaks with water. A separating gel was prepared, using the percentage acrylamide best suited to the size of proteins to be resolved, with smaller proteins needing higher percentage acrylamide. Reagents were added in the order listed (Table 2.10), and the gel was poured immediately. A layer of 70% ethanol was added on top allowing the separating gel to have a level top and the gel was polymerised for 20 mins at room temperature. Once the gel had set, a 4% stacking gel was prepared and poured on top of the separating gel (Table 2.11). The 1 mm thick comb (12 or 15 well) was inserted and the gel allowed to set for 20 mins. Alternatively, a pre-cast 4-20% acrylamide gel (Bio-Rad) was used.

Table 2.10 – SDS-PAGE separating gel composition.

	% Acrylamide			
Volume of reagents required for 10 mL (mL)	**15**	**12**	**10**	**7.5**
$_{dd}H_2O$	2.35	3.35	4.02	4.85
1.5 M Tris-HCl pH 8.8	2.50	2.50	2.50	2.50
10% (w/v) SDS	0.10	0.10	0.10	0.10
Acrylamide/Bis (30% stock)	5.00	4.00	3.33	2.50
10% ammonium persulfate (APS)	0.10	0.10	0.10	0.10
N,N,N’,N’-tetramethylethane-1,2-diamine (TEMED)	0.01	0.01	0.01	0.01

Table 2.11 – SDS-PAGE 4% stacking gel composition.

Volume of reagents required for 10 mL (mL)	**4%**
$_{dd}H_2O$	6.10
0.5 M Tris-HCl pH 6.8	2.50
10% (w/v) SDS	0.10
Acrylamide/Bis (30% stock)	1.30
10% APS	0.10
TEMED	0.01

1x running buffer was prepared from 10x stock (30 g L^{-1} Tris base, 144 g L^{-1} glycine, 10% SDS) by diluting 100 mL into 1 L of distilled water. Running buffer was added to the centre of a gel tank and the combs were removed from the set acrylamide gels. Protein samples were denatured in 1x Laemmli buffer, 100°C for 10 mins, before being loaded onto the gel. Additionally, 10 µL of PageRuler plus pre-stained protein ladder (Thermo Scientific) was also loaded onto the gel, and 10 µL of protein sample was loaded into the remaining wells. Remaining running buffer was added to the bottom of the tank, and the gel was run at a constant voltage of 150 V for 50 mins. The gel was removed, placed in a staining box, ~20 mL of Instant Blue Coomassie stain (Expedeon) was added and the gel placed on a rocker for 30 mins to stain. For more dilute protein samples, the staining length was extended to overnight.

2.6.7 Western blotting

For Western blotting, proteins were transferred onto nitrocellulose membrane (0.2 µm pore size) from an SDS-PAGE gel using a Trans-Blot Turbo (Bio-Rad) using the mixed MW setting (5-150 kDa, 7 mins, 1.3 A) in 1x transfer buffer (Bio-Rad). Membranes were blocked in PBS, 0.05% Tween, 5% milk powder, pH 7.4 for 1 hour. The membrane was incubated for 1 hour with appropriate primary antibody (listed in Table 2.9) diluted in PBS, 0.05% Tween, 3% milk. After incubation, the membrane was washed three times for 10 mins with PBS, 0.05% Tween. For detection, the appropriate HRP tagged secondary antibody (see Table 2.9) was diluted in PBS, 0.05% Tween, 3% milk and incubated with the membrane for 1 hour before three 10 min washes with PBS, 0.05% Tween. Membranes were imaged on Li-Cor western blot scanner using Clarity™ Western ECL substrate (Bio-Rad) for 12 mins.

2.6.8 Dot blotting

For dot-blotting, 1 µL of sample was dotted onto marked regions of a nitrocellulose membrane (0.2 µm pore size) and left to air dry before being blocked with 5% milk PBS-T, pH 7.5, for 1 hour. After blocking, primary antibodies were diluted in 3% milk PBS-T, pH 7.5, and incubated at room temperature for 1 hour followed by three 10 min washes with PBS-T, pH 7.5. For detection, HRP tagged secondary antibodies in 3% milk PBS-T, pH 7.5 and incubated for 1 hour followed by three 10 min washes with PBS-T, pH 7.5. Blots were visualised on Li-Cor western blot scanner using Clarity™ Western ECL substrate (Bio-Rad) for 12 mins.

3. The Tandem Calponin Homology Domains of ASPM

3.1 Introduction

Calponin Homology (CH) domains are typically comprised of four α-helices and are about 100 amino acids long. They were first discovered in the N-terminal region of calponin, a protein involved in actin binding (Kolakowski et al., 1995). Based on sequence analysis (Gimona et al., 2002), proteins with a single CH domain, such as EB1 (end-binding 1), are thought to interact with microtubules with the exception of calponin, which interacts with actin. Proteins with two CH domains in tandem, such as α-actinin, generally bind F-actin (Hemmings et al., 1992). Proteins with four CH domains in tandem, such as the fimbrin / plastin family, form two actin binding domains (ABDs) (Korenbaum & Rivero, 2002). When CH domains are in tandem, each domain may have different binding affinities. For example, the first CH domain of α-actinin binds more strongly to actin than the second (Way et al., 1992).

Human ASPM contains two CH domains located between residues 920-1,261. The presence of tandem CH domains suggests that they should bind actin. However, in ASPM homologues, where there is commonly only one CH domain, these CH domains have been shown to bind to microtubules (Ito & Goshima, 2015; Jiang et al., 2017). For example, the homologue of ASPM in *Drosophila* (asp) contains a single CH domain and this binds to microtubules (Ito & Goshima, 2015; Korenbaum & Rivero, 2002). Sequence analysis of the human ASPM CH domains shows that the first CH domain is highly similar (49% homologous at the protein level) to the CH domain of Drosophila asp. This suggests that the first CH domain of ASPM may bind microtubules and not to actin (Figure 3.1). However, the second CH domain of ASPM shown only an 8% similarity to the single asp CH domain, and it is thus unclear what it may bind to. Sequence analysis of ASPM homologues (Figure 3.1) shows that both CH domains are present in mammals, and fish, but not worms and insects, suggesting that tandem CH domains first emerged in vertebrates. Analysis of the two CH domains of *H. sapiens* revealed that there is <1% homology between them, suggesting the second CH domain did not arise by duplication.

```
Sp |Gene   bp    Sequence

Hs |ASPM   920   KASKEILLAFSRDFLSGE-GDLSRHLGLLGLPVNHVQTPFDEFDFAVTNLAVDLQCGVRL
Ce |aspm-1 311   -------SELTKELLTGSSATFKKAFAKVGFIPTYRQSFIENYDYQAKGF-SDFSDGLIL
Dm |asp    836   KETKDILLRFSSELLANI-GDITRELRRLGYVLQHRQTFLDEFDYAFNNLAVDLRDGVRL
Dr |aspm   900   KSSKDLLLAFSRDFLSGE-GILSRHLSHLGLAVSHVQTPLDEFNFAVKKLAVDLKCGIRL
Mm |Aspm   888   KASKELLLAFSRDFLSGE-GDLSRHLSFLGLPVSHVQTPLDEFDFAVTNLAVDLQCGVRL
Pt |ASPM   920   KASKEILLAFSRDFLSGE-GDLSRHLGLLGLPVNHVQTPFDEFDFAVTNLAVDLQCGVRL
                 * .*..*:::: ::*:.  . :.: :  :*    : *: ::::::  . :  *:  *: *

Hs |ASPM   979   VRTMELLT--QNWDLSKKLRIPAISRLQKMHNVDIVLQVLKSRGIELSDEHGNTILSKDI
Ce |aspm-1 363   AKLLETVGEMPHGQILLKLRDPAGDRIRKIGNVKIVLQEMSSLGVPT-----DNVNAESI
Dm |asp    895   TRVMEVIL--LRDDLTRQLRVPAISRLQRIFNVKLALGALGEANFQ----LGGDIAAQDI
Dr |aspm   959   VRVMELFT--LDWTLSRKLRIPAISRLQKVHNVDLALQVLKNKGVDLRDEHGANIDSRDI
Mm |Aspm   947   VRTVELLT--QNWNLSDKLRIPAISRVQKMHNVDLVLQVLKSRGVPLTDEHGSAISSKDV
Pt |ASPM   979   VRTMELLT--QNWDLSKKLRIPAISRLQKMHNVDIVLQVLKSRGIELSDEHGNTILSKDI
                 .: :* .       :  :** ** .*:::: **.:.*  : . ..         : :..:

Hs |ASPM   1037  VDRHREKTLRLLWKIAFAFQVDISLNLDQLKEEIAFLKHTKSIKKTISLLSCHSDDLINK
Ce |aspm-1 418   VGGKKDEILSILWAIIGVRV----------------------------------------
Dm |asp    949   VDGHREKTLSLLWQLIYKFR----------------------------------------
Dr |aspm   1017  VDGHREKTLNLLWKIIFAFQVEVLLDENQLKEEISFLRKTWRTKQKLASIMANNSVTVSR
Mm |Aspm   1005  VDRHREKTLGLLWKIALAFQVDISLNLDQLKEEIDFLKHTHSIKRAMSALTCPSQAITNK
Pt |ASPM   1037  VDRHREKTLRLLWKIAFAFQVDISLNLDQLKEEIAFLKHTKSIKKTISLLSCHSDDLINK
                 *. :::: * :** :     *...*:::****** **:.* ..*   . .        ..

Hs |ASPM   1097  KKGKRDSGSFEQYSENIKLLMDWVNAVCAFYNKKVENFTVSFSDGRVLCYLIHHYHPCYV
Ce |aspm-1       ------------------------------------------------------------
Dm |asp          ------------------------------------------------------------
Dr |aspm   1077  ---MKARRAFEHPSQKVTLLMDWVNAVCEFYSLKAENFTVSFSDGRILCYLIHHYHPGHL
Mm |Aspm   1065  QRDKRISGNFERYGDSVQLLMDWVNAVCAFYNKKVENFTVSFSDGRILCYLIHHYHPCYV
Pt |ASPM   1097  KKGKRDCGSFEQYSENIKLLMDWVNAVCAFYNKKVENFTVSFSDGRVLCYLIHHYHPCYV
                    ...   ** ..  . **********:**..*.***********.*********** .

Hs |ASPM   1157  PFDAICQRTTQTVECTQTGSVVLNSSSESDDSSLDMSLKAFDHENTSELYKELLENEKKN
Ce |aspm-1       ------------------------------------------------------------
Dm |asp          ------------------------------------------------------------
Dr |aspm   1134  HAEEIQQRTTQTIECGHRGRVELNNSSSDSD-CSFENLATMQSESVTVDFRELLENEKSN
Mm |Aspm   1125  PFDAICQRTSQSVACAQTGSVVLNSSSESEGGCLDLSLEALDHESTPEMYKELLENEKKN
Pt |ASPM   1157  PFDAICQRTTQTVECTQTGSVVLNSSSESDDSSLDMSLKAFDHENTSELYKELLENEKKN
                 ....*:***:*:..* ..***:**:**.: . .:. .* . ..* . . ..*******.*

Hs |ASPM   1217  FHLVRSAVRDLGGIPAMINHSDMSNTIPDEKVVITYLSFLCARLL
Ce |aspm-1       ---------------------------------------------
Dm |asp          ---------------------------------------------
Dr |aspm   1193  FQLVNTAVSYLGGVPAMINPEDMSNTIPNEKVVTCYLSFLCARLL
Mm |Aspm   1185  FHLVRSAARDLGGIPAMIHHSDMSNTIPDEKVVITYLSFLCARLL
Pt |ASPM   1217  FHLVRSAVRDLGGIPAMINHSDMSNTIPDEKVVITYLSFLCARLL
                 *:**::*:..***:****...*******.****..**********
```

Figure 3.1 – Protein sequence alignment of the Human ASPM CH domains with its homologues.

Sequence alignment of the *H. sapiens (Hs)* CH domains with the CH domains of *C. elegans (Ce)* aspm-1, *D. melanogaster (Dm)* asp, *D. rerio (Dr)* aspm, *M. musculus (Mm)* Aspm, *P. troglodytes (Pt)* ASPM. CH1 of *Hs* ASPM is displayed in red and CH2 of *Hs* ASPM is displayed in blue. Alignments were performed using CLUSTAL Omega, '*****' indicates fully conserved residues, '**:**' indicates strongly similar propertied between residues (>0.5 in the Gonnet PAM 250 matrix), '**.**' indicates weakly similar properties between residues (<0.5 in the Gonnet PAM 250 matrix). Sp: species, bp: base pair (Sievers et al., 2011).

It is still unclear how human ASPM interacts with microtubules and anchors the spindle pole to the cytoskeleton. Although the microtubule binding domain has been identified within the N-terminal 1,266 residues (Rhoads & Kenguele, 2005), its specific location has not been demonstrated. The CH domains could potentially play a role in this interaction (Kouprina et al., 2005). Therefore, to determine whether the CH domains from human ASPM bind to actin or to microtubules, whether they bind in tandem or if the single CH domains are both competent to bind in isolation, and to understand why there are two CH domains in human ASPM compared to other species, the CH domains (tandem CH domains (CHT; residues 920-1,261) of ASPM and the individual CH domains (CH1: residues 920-1,056, CH2: residues 1,110-1,261)) were cloned, expressed and purified, then investigated for their ability to bind either of these binding partners *in vitro*.

3.2 Methods

3.2.1 Cloning of CH domain constructs

Tandem CH domains (CHT) were expressed with an N-terminal FLAG-eGFP tag. The reason for this is three-fold: firstly, it allows for purification via an anti-GFP-nanobody, a small antibody-like protein with high affinity (Kd ~ 1 nM (Kubala et al., 2010)) to eGFP. Secondly, each ASPM CH domain has a different pI, the first CH domain (CH1; residues 920-1,056 of ASPM) has a predominantly basic pI of 9.06. However, the second CH domain (CH2; residues 1,110-1,261 of ASPM) has a predominantly acidic pI of 5.18. In initial expression attempts, CHT tended to aggregate, possibly due to this difference. The addition of eGFP (pI of 5.58) appears to mitigate this aggregation. Finally, the molecular weight of the untagged CHT protein (39 kDa) is similar to actin (37 kDa) and therefore difficult to distinguish by SDS-PAGE. The eGFP tagged CH domains (68 kDa) are thus more easily distinguishable from actin.

eGFP cDNA was amplified by PCR from peGFP-C1, using the eGFP to FastBac1 forward and reverse primers (Table 3.1). The forward primer includes a FLAG sequence and the reverse primer includes a GGS linker and KpnI restriction site. The PCR product was subcloned into the pFastBac1-KpnI removed (Section 2.2.10) between the BamHI-EcoRI sites to produce pFastBac1-eGFP using the seamless cloning protocol detailed in Section 2.2.8.

The CHT cDNA sequence (2,758-3,783 bp of ASPM) was cloned into the pFastBac1-eGFP vector between the KpnI-SpeI sites together with a PreScission protease site to create pFastBac1-

eGFP-pp-CHT (Figure 3.2), to allow for on column cleavage / removal of the eGFP if required. Cloning was performed using the NEBuilder protocol (Section 2.2.9) and appropriate primers (Table 3.1).

In addition to the CHT, individual CH domains, referred to as CH1 (2,758-3,327 bp of ASPM) and CH2 (3,166-3,783 bp of ASPM) were also cloned into pFastBac1-eGFP together with a PreScission protease site (pFastBac1-eGFP-pp-CH1 and pFastBac1-eGFP-pp-CH2 respectively), and with an additional C-terminal 6xHis tag to add an additional purification option. These two constructs were generated by Genscript.

For mammalian expression, the CHT cDNA sequence (2,758-3,783 bp of ASPM) was cloned into pCMV5 with an eGFP tag and PreScission protease site to create pCMV5-eGFP-pp-CHT (Figure 3.3). Cloning was performed using the NEBuilder protocol (Section 2.2.9) using appropriate primers (Table 3.1).

Table 3.1 – Primers used for cloning within this chapter.

Primer name	Sequence (5' - 3')	Use	Annealing temp (°C)	Restriction site	Additional features
GFP to FastBac1 For	CCATCGGGCGCGGATCCCATGGACTACAAAGACGATGACGACAAGATGGTGAGCAAGGGC	Inserting eGFP into pFastBac1	68	BamHI	FLAG Tag
GFP to FastBac1 Rev	CAGTAGGCCTTTGAATTGGTACCACTACCTCCCTTGTACAGCTCGTCCATG			EcoRI KpnI	GGS linker
PP-CH For	GGGAGGTAGTGGTACCCTGGAAGTTCTGTTCCAGGGGCCCAAGGCTAGTAAAGAAATCCT	Inserting CHT (bp 2,758-3,783) into pFastBac1-eGFP with a PreScission protease site	72	KpnI	PreScission Protease site
GFP-CH Rev	CGAAAGCGGCCGCGATTACAAAAGCCTTGCACAAAGAA			SpeI	STOP
GFP-pp-CH to CMV For	TCAGAATTCAGATCTGGTACATGGACTACAAAGAC	Insert GFP-pp-CHT into pCMV5	72	KpnI	-
GFP-pp-CH to CMV Rev	GTCACAGGGATGCCACCCGGTTACAAAAGCCTTGC			BamHI	-

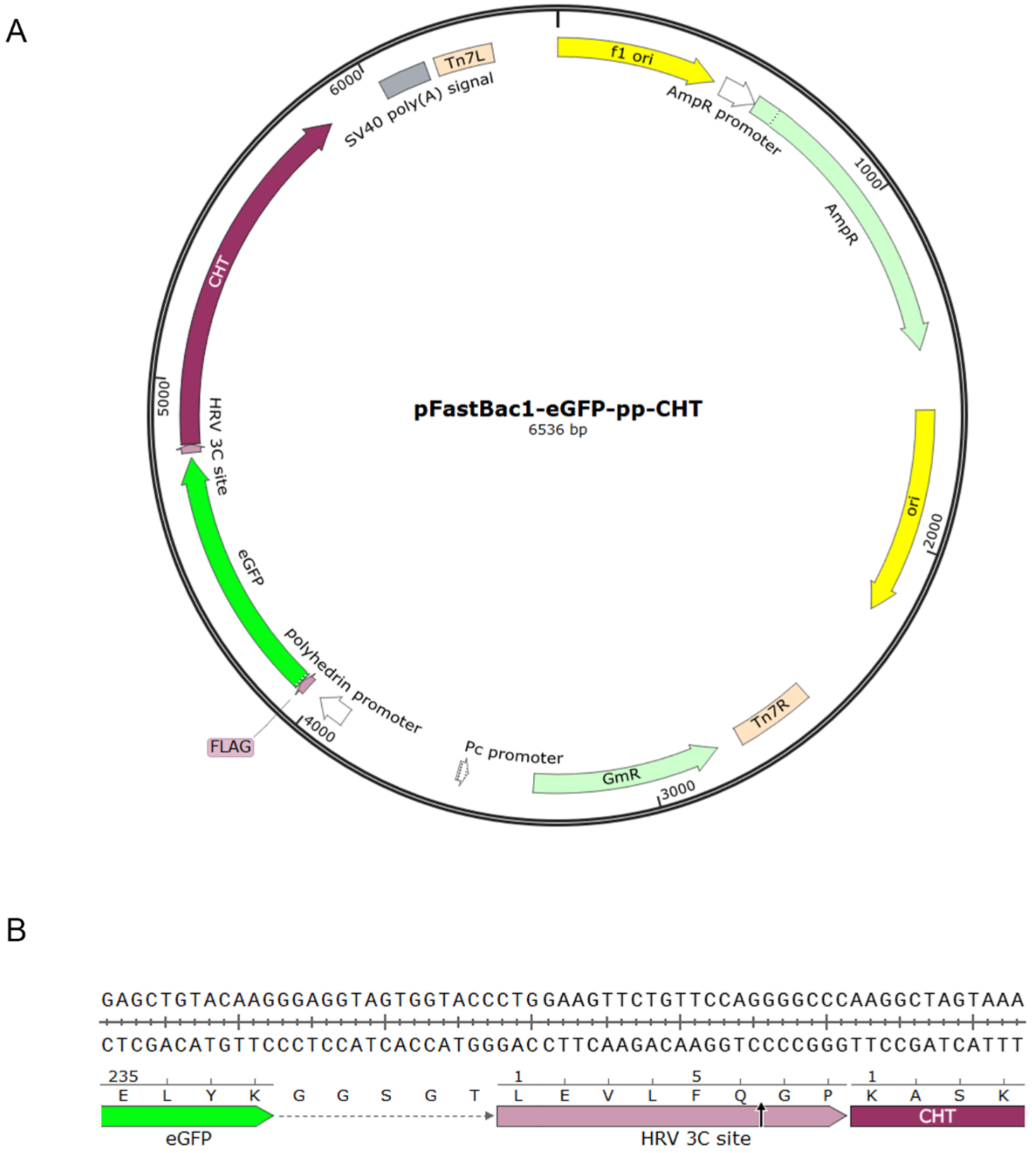

Figure 3.2 – CH vector map.

(A) The vector maps of the pFastBac1-eGFP construct containing CHT with a PreScission protease site. (B) The sequence of the C-term eGFP, the GGS linker, the PreScission protease site and the start of the tandem CH domains. pFastBac1-eGFP-pp-CH1 and pFastBac1-eGFP-pp-CH2 were cloned into the sites as CHT.

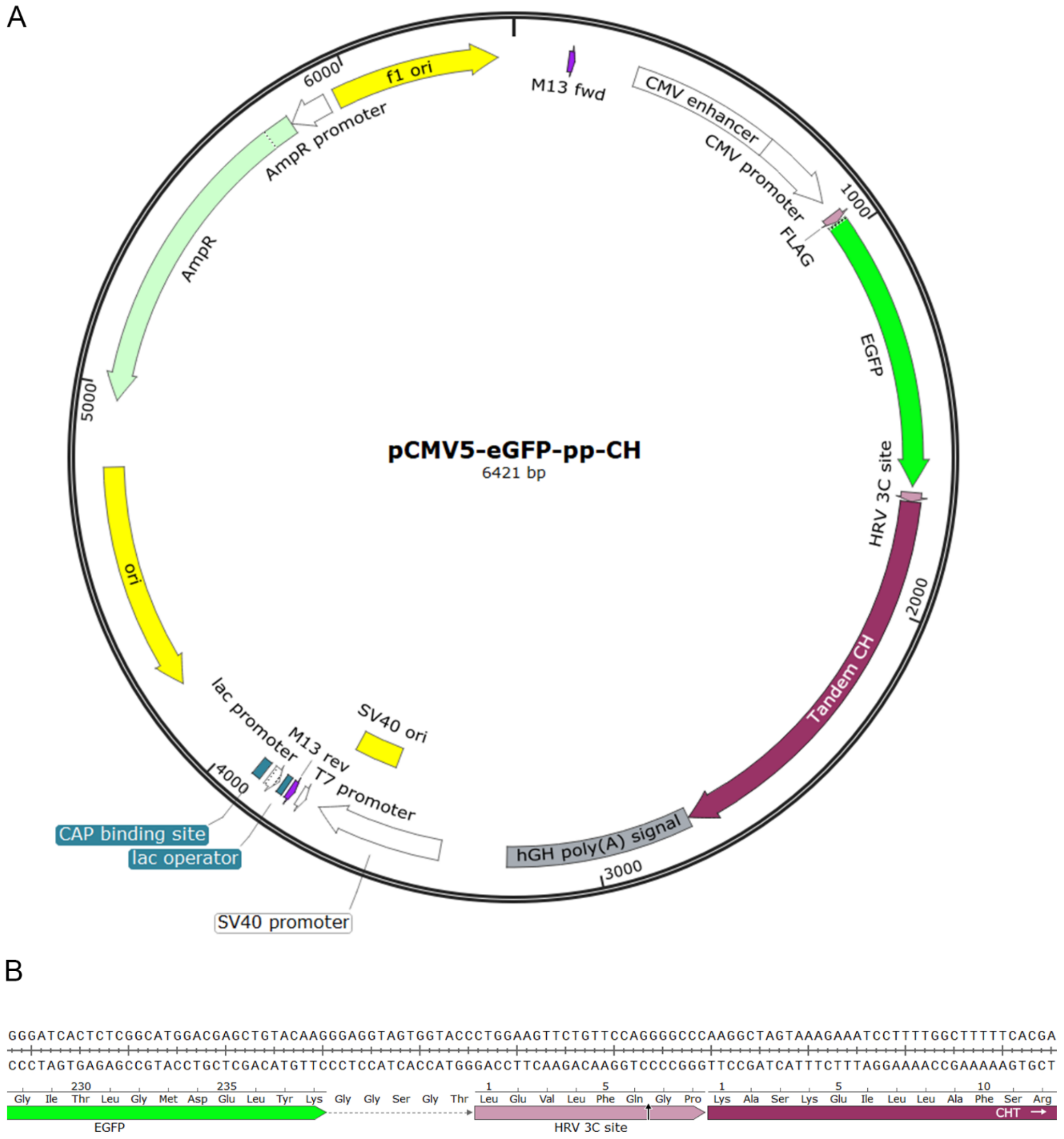

Figure 3.3 – pCMV-eGFP-pp-CHT vector map.

(A) The vector map of the pCMV5 vector containing CHT for mammalian expression. (B) The sequence covering the C-term of eGFP, the GGS linker, the PreScission protease site in frame with the start of the tandem CH domains.

3.2.2 Expression and purification

Virus was prepared (Section 2.3) and protein expressed using a Multiplicity of Infection (MOI) of 2 for all virus constructs (Section 2.3.8). CHT (eGFP-pp-CHT) was purified initially using anti-GFP-nanobody resin (Section 2.6.3). Briefly, Sf9 expression pellets were resuspended in lysis buffer (PBS supplemented with 2 mM DTT, 10 µM Leupeptin, 2 mM PMSF (Phenylmethylsulfonyl fluoride)), homogenised by hand with a Dounce homogeniser and clarified by centrifugation at 30,000 x g for 30 mins at 4°C in a Beckman Coulter Avanti J25. Clarified lysate was incubated with the anti-GFP-nanobody resin in suspension for 1-hour at room temperature and then the column was washed extensively with wash buffer (PBS supplemented with 2 mM DTT). Protein was eluted by the addition of 0.1 M glycine, 0.1 M NaCl, 50 mM arginine, 50 mM glutamate, pH 2.7. Eluted proteins were collected in 1 M Tris-HCl, pH 8.0 (final concentration 50 mM Tris-HCl) to restore the pH to 7.6.

To purify eGFP-pp-CHT by on column cleavage, expression pellets were resuspended in lysis buffer (PBS supplemented with 2 mM DTT, 10 µM Leupeptin, 2 mM PMSF), homogenised by hand with a Dounce homogeniser and clarified by centrifugation at 30,000 x g for 30 mins at 4°C in a Beckman Coulter Avanti J25. Clarified lysate was incubated with the anti-GFP-nanobody resin in suspension for 1-hour at room temperature as before. The resin was then buffer exchanged into PreScission protease buffer (50 mM Tris-HCl, 150 mM NaCl, 10 mM EDTA, pH 8.0) and 80 units of PreScission protease (purified in Section 2.6.1) was added before an overnight incubation at 4°C. Two mL elution fractions (50 mM Tris-HCl, 150 mM NaCl, 10 mM EDTA, pH 8.0) were then collected.

GFP-pp-CHT was also purified using anti-FLAG resin. Sf9 expression pellets were resuspended in lysis buffer (PBS supplemented with 2 mM DTT, 10 µM Leupeptin, 2 mM PMSF) homogenised by hand with a Dounce homogeniser and clarified by centrifugation at 30,000 x g for 30 mins at 4°C in a Beckman Coulter Avanti J25. Clarified lysate was incubated with the anti-FLAG resin in suspension for 1-hour at room temperature and then the column was washed extensively with wash buffer (PBS supplemented with 2 mM DTT). Protein was eluted by the addition of PBS supplemented with 200 ng mL^{-1} 3xFLAG peptide (Sigma Aldrich). GFP-pp-CH1 and GFP-pp-CH2 were purified by anti-FLAG resin following the same protocol as for GFP-pp-CHT.

Following elution, protein concentrations were estimated on a Nanodrop nanophotometer (IMPLEN) and purity was analysed on a 4-20% tris-acetate SDS-PAGE. CHT has an expected mass of 39 kDa, similar to actin, eGFP-pp-CHT has an expected mass of 68 kDa (Table 3.2).

Table 3.2 – expected molecular weight of expressed proteins.

Protein name	Expected protein molecular weight (kDa)
GFP-pp-CHT	68
Cleaved CHT	39
GFP-pp-CH1	52
GFP-pp-CH2	53
Cleaved CH1	23
Cleaved CH2	24

3.2.3 Cycling and dye labelling tubulin with commercial dyes

Tubulin was purified from porcine brain as described previously (Ashford & Hyman, 2006) (purified by Dr Glenn Carrington and Dr Takashi Ochi, University of Leeds). Tubulin was stored at a final concentration of 4.5 mg mL^{-1} in Column buffer (50 mM PIPES (piperazine-N,N′-bis(2-ethanesulfonic acid)), 1 mM EGTA (ethylene glycol-bis(β-aminoethyl ether)-N,N,N′,N′-tetraacetic acid), 0.2 mM $MgCl_2$, pH 6.8) in liquid nitrogen.

Tubulin was initially cycled to remove inactive and denatured tubulin. Briefly, tubulin in Column buffer was half thawed rapidly in a 37°C water bath and the remainder thawed on ice. The buffer the tubulin was stored in was converted into PEM buffer (80 mM PIPES, 1 mM EGTA, 1 mM $MgCl_2$, pH 6.8) by the addition of 1-part Conversion buffer (1.05 M PIPES, 1.6 mM EGTA, 2.8 mM $MgCl_2$, pH 6.8) to 20 parts tubulin in Column buffer. GTP (Guanosine-5'-triphosphate) was then added to 1 mM final and glycerol was added to 15% v/v final. Tubulin was then incubated at 37°C for 40 mins to polymerise before centrifugation in a pre-warmed rotor over a cushion buffer (80 mM PIPES, 1 mM EGTA, 1 mM $MgCl_2$, 60% glycerol, pH 6.8) at 100,000 x g for 40 mins 37°C in a Beckman Coulter Optima MAX-XP benchtop ultracentrifuge, using the TLA-110 rotor. The supernatant was then removed, and the pellet was resuspended in two volumes ice-cold PM buffer (0.1 M PIPES, 1 mM $MgCl_2$, pH 6.9) and incubated on ice for 10 mins. To depolymerise tubulin, polymerised tubulin was sedimented by centrifugation 100,000 x g 15 mins 4°C in a Beckman Coulter Optima MAX-XP benchtop ultracentrifuge, using the TLA-100 rotor. Cycled tubulin in the supernatant was either snap frozen in liquid nitrogen and aliquots stored at -80°C or directly labelled with commercial dyes.

Tubulin was directly labelled with commercial dyes as done previously (Peloquin et al., 2005). Briefly, cycled tubulin (in ice-cold PM buffer) was polymerised by the addition of 1 mM GTP final and 10% DMSO final before incubation at 37°C for 10 mins. Alexa Fluor™ 546 NHS Ester (Succinimidyl Ester) dissolved in DMSO was added to a molar ratio of 1:5 tubulin to dye and incubated 37°C for 40 mins. Labelled microtubules were then centrifuged over a cushion buffer at 100,000 x g 40 mins 37°C in a Beckman Coulter Optima MAX-XP benchtop ultracentrifuge, using the TLA-100 rotor. The pellet was then resuspended in 5 volumes ice-cold PM buffer and incubated on ice for 10 mins. To depolymerise tubulin, polymerised tubulin was sedimented by centrifugation at 100,000 x g 15 mins 4°C in a Beckman Coulter Optima MAX-XP benchtop ultracentrifuge, using the TLA-100 rotor. The concentration of tubulin in the supernatant was estimated as in Section 2.6.5. The dye labelled tubulin was then snap frozen in liquid nitrogen and aliquots stored at -80°C.

3.2.4 Flow cell assays

Flow cells were generated as described previously (Hancock & Howard, 1998; Sellers, 2001). 22 x 30mm No. 1 glass coverslips (Corning; thickness: 0.13 to 0.17mm) were washed in two-parts nitric acid to one-part HCl for 2 hours at room temperature prior to washing extensively with $_dH_2O$. The coverslips were then washed and stored in 100% ethanol. Cleaned coverslips were then quickly dried with compressed air before being coated in 3 µL 0.1% nitrocellulose in pentyl acetate (Sigma-Aldrich) and air-dried for 15 mins. Flow cells were constructed by placing two strips of double-sided tape (permanent double-sided Tape, 12 mm x 6.3 mm x 90 µm, Scotch, 3M) onto a microscope slide and placing the coverslip on the top, nitrocellulose side facing slide, to create a chamber of approximately 40 µL in volume.

Microtubules were polymerised as described previously (Sandoval & Vandekerckhove, 1981; Vallee, 1986). Briefly 2 mg mL^{-1} tubulin, 10% of which was Alexa 546 dye-labelled and 2% was biotinylated (PurSolutions) was polymerised in a buffer containing 80 mM PIPES, 1 mM EGTA, 1 mM $MgCl_2$, 5% glycerol, 1 mM DTT, 1 mM GTP, pH 6.8 for 1 hour at 37°C. Microtubules were then stabilised with equimolar Taxol at 37°C and stored at 37°C until required.

Actin was polymerised at 4°C overnight from acetone powder as described previously (Spudich & Watt, 1971; Walker et al., 2000). Briefly, 100 µM rabbit skeletal muscle actin (10% of which was biotinylated skeletal muscle actin (Cytoskeleton)) was polymerised by the addition of exchange buffer (0.2 mM $MgCl_2$, 1.1 mM EGTA) for 5 mins before addition of polymerisation buffer (30 mM KCl, 12 mM MOPS (3-(N-morpholino)propanesulfonic acid),1.2 mM $MgCl_2$, 0.1 mM EGTA, pH 7.0). F-actin was labelled with 3 µM Rhodamine Phalloidin (Thermo Fisher Scientific) at 4°C for 2 hours.

For filament binding assays, 1 flow cell volume (40 µL) of 1 mg mL^{-1} biotinylated BSA (Pierce) dissolved in $_dH_2O$ was added into the flow cell and allowed to adsorb for 2 mins at room temperature. Next, 1 flow cell volume of 1 mg mL^{-1} NeutrAvidin (Pierce) was added to the flow cell and incubated at room temperature for 2 mins. The flow cell was then washed with 4 flow cell volumes of wash buffer. For microtubule binding assays, the wash buffer was 80 mM PIPES, 1 mM EGTA, 1 mM $MgCl_2$, 1 mM DTT, 20 µM Taxol pH 6.8. For actin binding assays, the wash buffer was 50 mM KCl, 2 mM $MgCl_2$, 0.16 mM EGTA, 20 mM MOPS, pH 7.0. Next, either 50 nM Taxol stabilised microtubules or phalloidin stabilised F-actin (see above) was added to the flow cell and allowed to bind for 2 mins at room temperature. Flow cells were then blocked with 2 cell volumes 5% milk in the appropriate wash buffer and then washed with 4 cell volumes of the appropriate wash buffer.

One flow cell volume of purified GFP tagged CH protein was added to the flow cell and allowed to bind for 2 mins before being washed with 4 cell volumes of appropriate wash buffer. The flow cell was imaged using an Olympus BX 51 microscope, using a 100x objective lens (NA 1.4) and images captured using Watec WAT-902H B&W analogue camera with IC Capture 2.4 software. Several fields of view were sampled per flow cell.

Images were analysed in FIJI using the plot profile tool. Briefly, a 5 nm straight line was measured along a filament and the intensity of the CH domain(s) were recorded using the plot profile function and the area under the graph was recorded in arbitrary units (a.u.).

For the landing assay, 1 flow cell volume of anti-GFP-nanobody (stored in 0.1 M $NaHCO_3$, 0.5 M NaCl, pH 8.3), at concentrations of 19.5 pM, 39.0 pM, 97.5 pM, 195.0 pM, 1.95 µM, 19.5 µM, 39.0 µM, 97.5 µM or 195.0 µM was added into the flow cell and allowed to adsorb for 2 mins. Approximate expected density of molecules was calculated from numbers of molecules added and area of coverslip as 1, 2, 5, 10, 100, 1,000, 2,000, 5,000 and 10,000 molecules μm^{-2} respectively. Flow cells were then blocked by the addition of 2 cell volumes of 5% milk in the appropriate wash buffer and a second incubation at room temperature for 2 mins. One flow cell volume of purified CH protein (CHT: 2.8 μM, CH1: 0.3 μM, CH2: 22.6 μM) was added to the flow cell and allowed to bind for 2 mins. The cell was washed with 4 cell volumes of appropriate buffer before the addition of 1 cell volume of 50 nM Taxol stabilised microtubules or phalloidin stabilised F-actin, which were allowed to bind for 2 mins at room temperature. Flow cells were then washed with 4 cell volumes of the appropriate wash buffer and imaged using an Olympus BX 51 microscope and 100x objective lens as described above. A positive control using either the anti-tubulin or the anti-actin Affimer in place of the anti-GFP-nanobody was also used.

Images were analysed in FIJI. Initially, image type was changed to 8-bit before the threshold was adjusted so that only the filament was selected. Images were then analysed using the Analyse Particles function with the particle size set between 10-infinity and the results were outputted as 'summarise' which displayed the number of particles (filaments) and the total area of the thresholded particles.

3.2.5 Mammalian overexpression and immunofluorescence

HEK293 cells (Deutsche Sammlung von Mikroorganismen und Zellkulturen (DSMZ) ACC 305) at a density of 1,500 cells mm^{-2} plated onto 13 mm diameter glass coverslips were transfected with pCMV5-eGFP-CHT using FuGene HD (Promega) (Section 2.4.5). Cells were fixed 24-hour post transfection with 2% PFA (paraformaldehyde) in PBS for 10 mins at room temperature. Fixed cells were permeabilised with PBS containing 1% BSA and 0.1% Triton X-100 before blocking in PBS containing 5% BSA for 30 mins. Blocked cells were then incubated with rat anti-α-tubulin monoclonal YL1/2 (Abcam; AB6160) at 1:1000 dilution in PBS (containing 1% BSA) for 1 hour, then washed in PBS prior to a 1-hour incubation with goat anti-rat Alexa Fluor 546 secondary antibody (Thermo Fisher Scientific; A-11081) at a dilution of 1:400 in PBS containing 1% BSA. Actin was stained with Alexa Fluor 647 phalloidin (Thermo Fisher Scientific) at a dilution of 1:100 and DNA was stained with DAPI (4′,6-diamidino-2-phenylindole; Thermo Fisher Scientific) at a dilution of 1:500 in PBS containing 1% BSA (as in Section 2.5.2). After the final staining step, coverslips were washed in PBS, and mounted onto glass microscope slides in ProLong Gold Antifade (Thermo Fisher Scientific).

3.2.6 Spin down assay

To measure filament binding of the GFP tagged CH domains, a spin down assay was also used. Briefly, 4 µM purified CH domains (CHT, CH1, CH2) were incubated with 2 µM microtubules or 2 µM F-actin, (Section 3.2.4) for 30 mins at room temperature. Controls were also set up with the CH domains alone, microtubules alone and F-actin alone. For the spin down assay, 100 µL cushion buffer (80 mM PIPES, 1 mM $MgCl_2$, 1 mM EGTA, 60% glycerol, pH 6.9) was added to a 230 µL open top polycarbonate ultracentrifuge tubes (Beckman Coulter, part number 343007). 50 µL of the protein reaction was placed on top of the cushion buffer and then ultracentrifuged at 100,000 x g for 40 mins at 20°C in a Beckman Coulter Optima MAX-XP benchtop ultracentrifuge, using the TLA-100 rotor. After centrifugation, the top 50 µL (supernatant) was removed for analysis and the 100 µL cushion layer was removed and discarded. Finally, the pellet was resuspended in 50 µL 1x SDS sample buffer and analysed by SDS-PAGE (Section 2.6.6).

3.2.7 Protein identification by mass spectrometry

To isolate proteins that bind to the CHT domains, whole cell extract from HEK293 cells was added to the GFP-pp-CHT protein bound to the anti-GFP-nanobody column, and proteins allowed to bind overnight at 4°C. Bound CHT and interacting proteins were eluted by adding 0.1 M glycine, 0.1 M NaCl, pH 2.7. Eluted proteins were collected in 1 M Tris-HCl, pH 8.0 to restore the pH to 7.6 (0.1 M Tris-HCl final). Eluted protein was separated by a 4-20% tris-acetate SDS-PAGE gel, stained with Coomassie blue and bands excised for protein identification by mass spectrometry.

3.3 Results

3.3.1 Expression and purification of CH domains using the baculovirus system

CHT was successfully cloned into pFastBac1 as determined by PCR analysis (Figure 3.4A) and sequencing. Following transposition, PCR using the M13 primers demonstrated the successful transposition to generate the bacmid (Figure 3.4B). PCR of an empty bacmid showed a band of 0.3 kbp as expected (Figure 3.4B). Following transfection into Sf9 cells, two rounds of amplification were used to generate virus for subsequent expression of CHT. Only one round of amplification was required for each of the individual CH domain constructs (eGFP-pp-CH1 and eGFP-pp-CH2) (Table 3.3).

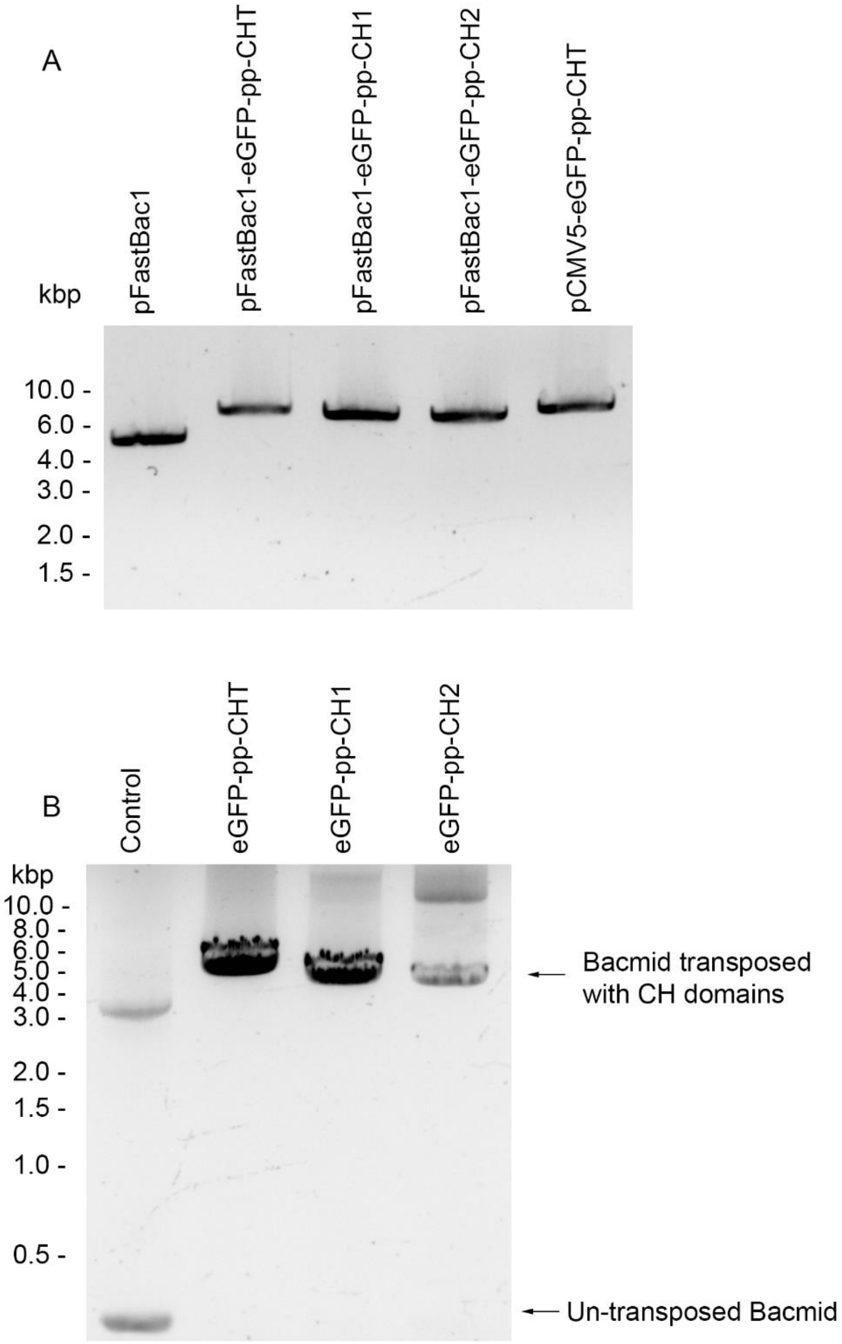

Figure 3.4 – Generation of CH constructs in pFastBac1 and transposition of CH bacmids confirmed by PCR.

(A) A 1.0% agarose gel of the purified pFastBac1-eGFP-pp-CHT (6,536 bp), pFastBac1-eGFP-pp-CH1 (6,096 bp), pFastBac1-eGFP-pp-CH2 (6,141 bp) and pCMV5-eGFP-pp-CHT (6,421 bp) (B) A 1.0% agarose gel of the PCR amplification product of the transposed CH constructs with the M13 primers. A successful transposition of the, eGFP-pp-CHT, eGFP-pp-CH1 and eGFP-pp-CH2 would yield products of 4,109 bp, 3,668 bp and 3,713 bp respectively. Unsuccessful transposition would yield a band of 0.3 kbp.

Table 3.3 – Viral titres for each CH construct, Plaque Forming Units per mL (PFU mL^{-1}). A viral titre ranging from 1x10^{7} to 1x10^{8} PFU mL^{-1} is recommended for expression.

Passage	eGFP-pp-CHT (PFU mL^{-1})	eGFP-pp-CH1 (PFU mL^{-1})	eGFP-pp-CH2 (PFU mL^{-1})
P0	9.03x10^{6}	9.45x10^{8}	8.45x10^{8}
P1	3.46x10^{8}	-	-

Purification of eGFP-CHT (~68 kDa) using the N-terminal FLAG tag resulted in high concentrations of protein (2.8 μM) that was stable in solution and was useable in downstream assays. Some excess free eGFP appeared to be present (Figure 3.5A). This was confirmed by Western blot (data not shown).

Purification of eGFP-pp-CHT using an anti-GFP-nanobody column (Figure 3.5B) resulted in little to no stable soluble protein, neither by acid elution nor by on-column cleavage. CHT tended to dimerise as a result of on-column cleavage of the GFP-pp-CHT construct with PreScission protease. Gel analysis showed a band with a molecular weight of 40 kDa, which is PreScission protease, and a second band with a molecular weight of ~75 kDa, which is likely to be dimerised CHT (Figure 3.5A). Due to several potentially exposed cysteine residues, predicted by *in silico* modelling, it is possible that this dimerisation results from formation of disulphide bonds between free cysteine residues between two molecules. However, any attempts to reduce this dimer, with either DTT or TCEP at a range of concentrations (1-10 mM) proved ineffective. Any attempts to use the protein purified by the anti-GFP column, by acid elution or on-column cleavage resulted in unusable protein. The addition of 50 mM arginine and 50 mM glutamate, which has been shown to increase solubility in other proteins (Golovanov et al., 2004), improved solubility moderately but not completely. Any attempts to further purify remaining soluble protein, such as by size exclusion, resulted in complete loss of all protein. As such, purification by FLAG tag only was used in these experiments.

Purification of eGFP-pp-CH1 using the N-terminal FLAG tag resulted in low concentrations of protein (0.3 μM). However, this was stable in solution and useable for downstream assays. Like eGFP-pp-CHT, excess free eGFP also appeared to be present (Figure 3.5C). Purification of eGFP-pp-CH2 using the N-terminal FLAG tag resulted in higher concentrations of protein (22.6

μM) that was stable in solution. Unlike CHT and CH1, CH2 expressed and purified very well with minimal issues (Figure 3.5D).

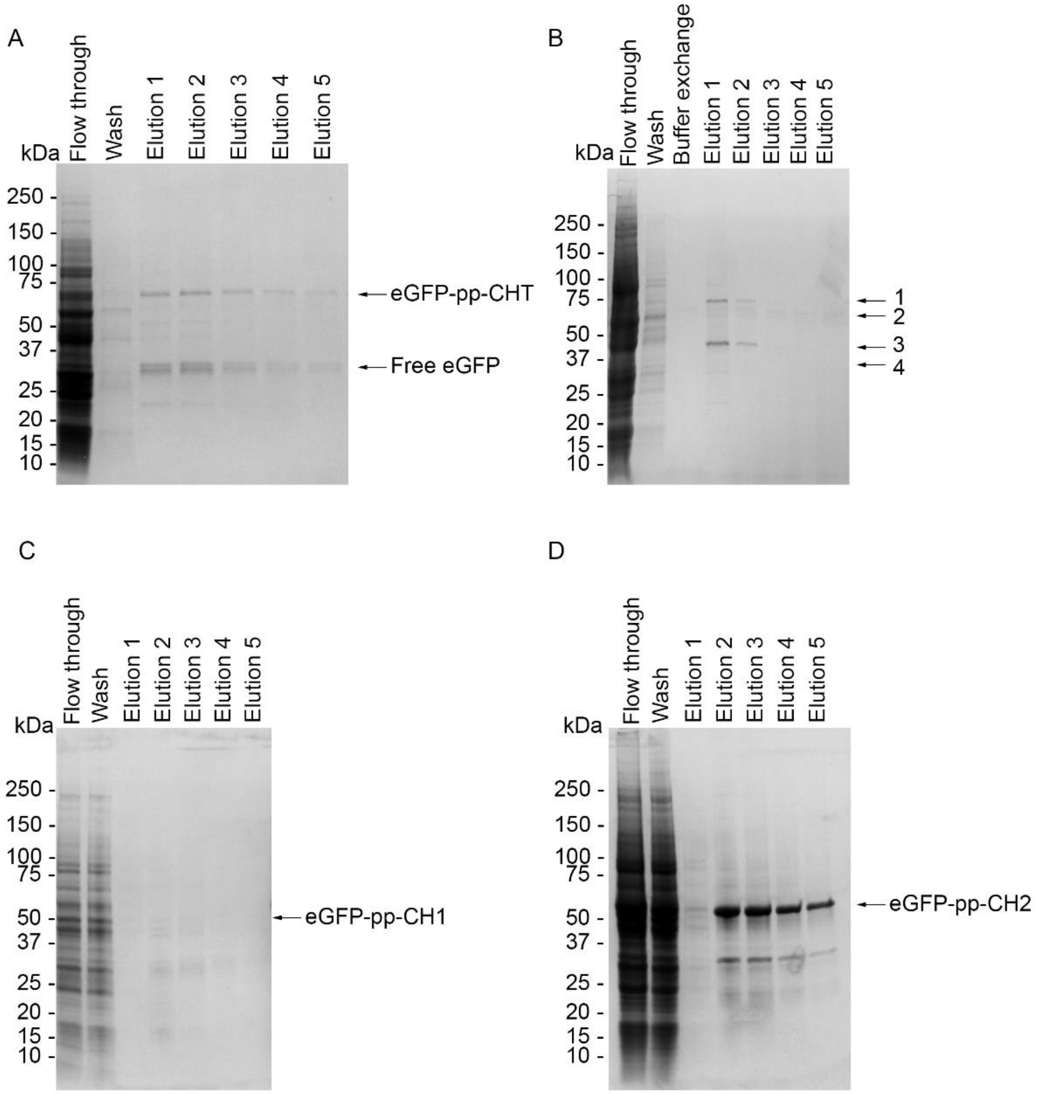

Figure 3.5 – Purification of CH domains.

(A) A 4-20% SDS-PAGE gel of CHT purified by anti-FLAG resin, eluted by competition with 3xFLAG peptide. (B) A 4-20% SDS-PAGE gel of CHT purified using an anti-GFP-nanobody resin and eluted by on-column cleavage with PreScission protease. Arrow 1 indicates the band likely to be dimerised cleaved CHT. Arrow 2 is the expected size of uncleaved eGFP-pp-CHT, as seen in the wash and buffer exchange lanes. PreScission protease has an expected size of 47 kDa (arrow 3). Expected size of cleaved CHT is 37 kDa, indicated by arrow 4. (C) A 4-20% SDS-PAGE gel of CH1 purified by anti-FLAG resin, eluted by competition with 3xFLAG peptide. (D) A 4-20% SDS-PAGE gel of CH2 purified by anti-FLAG resin, eluted by competition with 3xFLAG peptide.

3.3.2 Flow cell assays show that the tandem CH domains (CHT) of ASPM bind microtubules

A flow cell assay was used to test whether CHT binds to F-actin or to microtubules. In these assays, fluorescently labelled F-actin, or microtubules were bound to the coverslip, and purified eGFP-pp-CHT (2.8 μM) was added. Purified eGFP-pp-CHT was found to co-localise with microtubules and not F-actin (Figure 3.6). CHT bound to discrete sites along the whole microtubule and did not tend to bind at either end or to bind evenly along the length of the microtubule. eGFP tagged CHT did not co-localise with F-actin, suggesting it does not bind. Fluorescent puncta of eGFP tagged CHT observed in these images are likely to be molecules that are bound non-specifically to the nitrocellulose coated coverslip.

To determine if there was a concentration dependence for microtubule or F-actin binding to CHT, the concentration of purified eGFP-pp-CHT bound to the coverslip was controlled by varying the concentration of an anti-GFP-nanobody applied to the flow cells. The total area of fluorescence above a set threshold per field of view for microtubules or F-actin filaments that bound to eGFP-pp-CHT was analysed. Increasing concentrations of anti-GFP-nanobody from 10-100 molecules μm^{-2} increased the binding of microtubules (Figure 3.7A). In contrast, F-actin did not bind to CHT across this concentration range (Figure 3.7B).

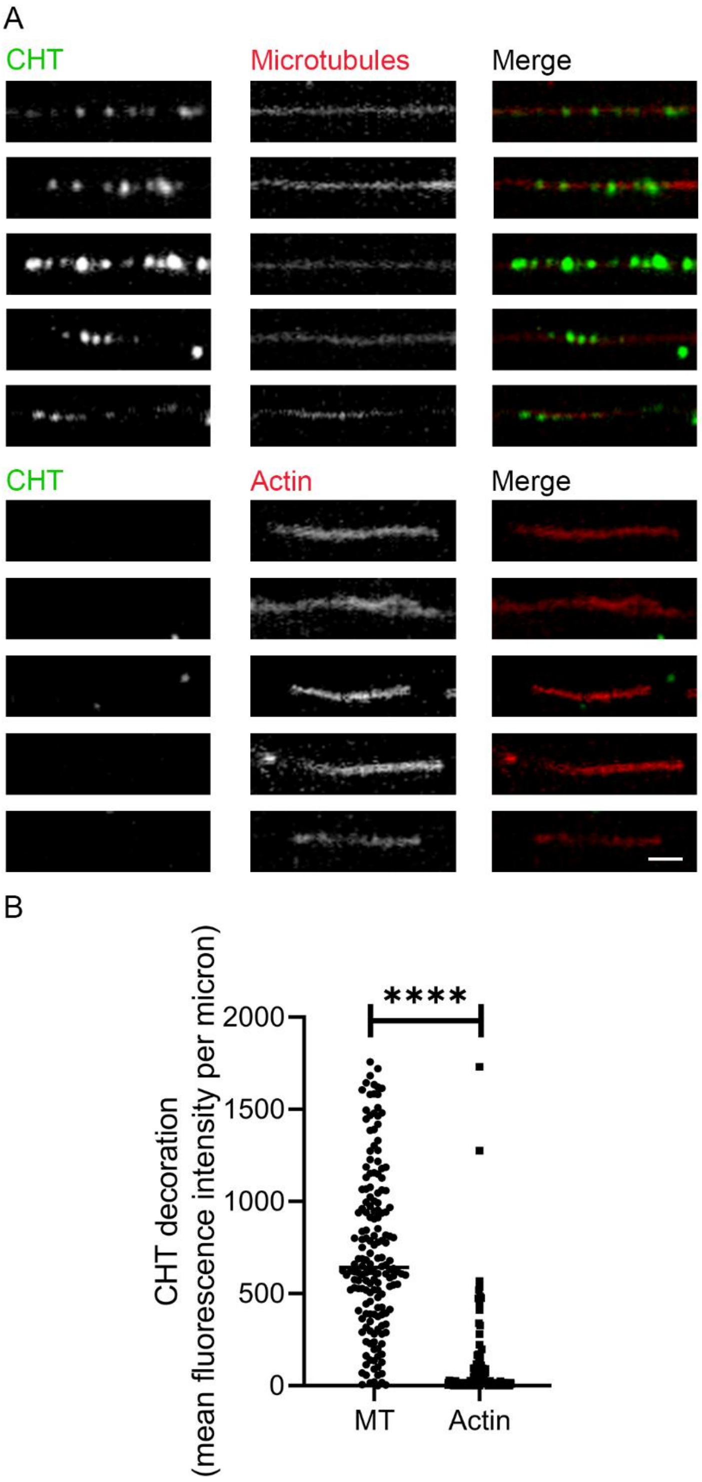

Figure 3.6 – The tandem CH domains of ASPM bind microtubules In vitro.

(A) *In vitro* binding flow cell assays of CHT (green) with microtubules (red) and actin (red). Scale bar = 2 µm. (B) Quantitative analysis of the eGFP tagged CHT along 5 µm of filament using the Plot profile plugin on FIJI and recording the area under the graph. Mann-Whitney test p<0.0001. n=172.

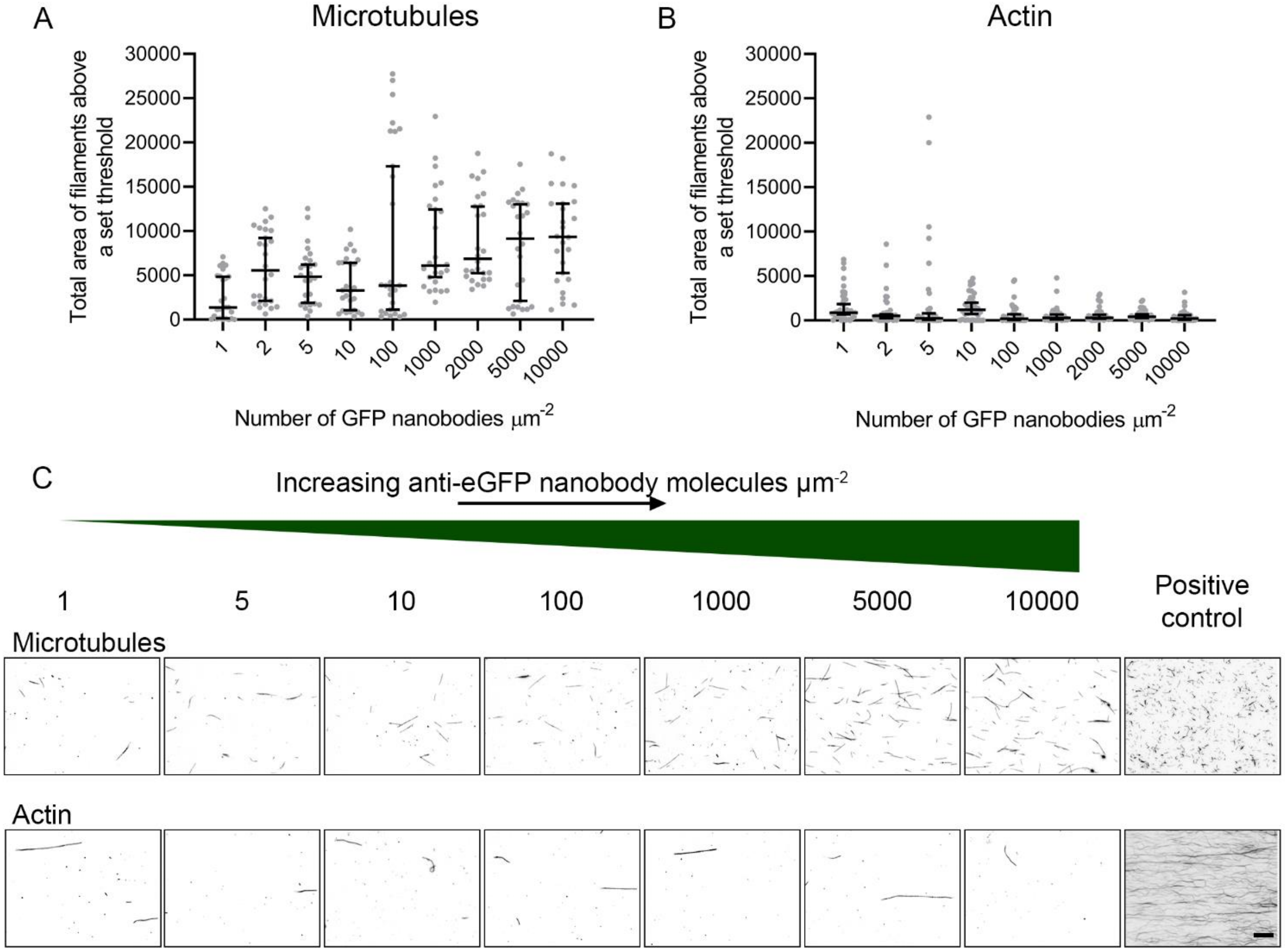

Figure 3.7 – Landing assay of CHT with actin and microtubules.

(A) Graph showing the increasing number of microtubule filaments which corresponds with an increasing number of CHT molecules bound to adsorbed anti-GFP-nanobody molecules μm^{-2} within a flow cell n=26 (B) Graph showing a level number of F-actin filaments corresponds with an increasing number of CHT bound to adsorbed anti-GFP-nanobody molecules μm^{-2} within a flow cell n=36. (C) Representative images of microtubules and F-actin at increasing concentrations of CHT bound to adsorbed anti-GFP-nanobody molecules μm^{-2} relating to graphs A and B. Scale bar = 10 μm.

3.3.3 Flow cell assays show that the individual CH domains of ASPM also bind microtubules

Next, individual CH domains of ASPM were tested to determine if both domains are required for binding to microtubules, and if one domain might bind more strongly than the other, as reported for the two CH domains of α-actinin binding to F-actin (Way et al., 1992). In the filament binding assays, both individual CH domains (GFP-pp-CH1 (0.3 μM) and GFP-pp-CH2 (22.6 μM)) were found to co-localise with microtubules and not F-actin (Figure 3.8 A-B). Like CHT, both individual CH domains bound to discrete sites along the whole microtubule and did not preferentially bind at either end or bind evenly along the length of the microtubule. Profile analysis of CH decoration along filaments shows that the CH domains bind to microtubules and not actin confirming the visual co-localised observations (Figure 3.8C). However, fluorescent puncta for individual CH domains bound to microtubules did not appear as bright as the tandem CH domains (Figure 3.8A-B and Figure 3.6A). Quantification of the fluorescence confirmed this. CHT had a ~4-fold higher mean fluorescence intensity compared to either CH1 or CH2 (Average intensity of fluorescence: CHT: 732 a.u., CH1: 156 a.u., CH2: 139 a.u.) (Figure 3.8C).

The ability of the individual CH domains to bind microtubules or F-actin was also tested using a single concentration of anti-GFP-nanobody bound to the surface (1 molecule per μm^2). In agreement with the filament binding assays, microtubule binding was significantly increased for both of the individual CH domains compared to actin (Figure 3.8D-E). F-actin did not bind to either CH1 or CH2 (Figure 3.8D-E).

3.3.4 Mammalian overexpression of the tandem CH domains shows they co-localise with microtubules

The tandem CH domains also bind microtubules and not F-actin in cells. To test this, eGFP tagged CHT was expressed in HEK293 cells, and the cells were fixed and stained for tubulin and F-actin. eGFP tagged CHT co-localised with microtubules, but not with F-actin in HEK293 cells (Figure 3.9A-B). This colocalisation was more prominent in cells undergoing mitosis (Pearson's R colocalisation value: 0.66 for CH vs MT and 0.20 for CH vs Actin), most notably at the spindle poles during metaphase (Figure 3.9A upper panels) compared to those in interphase (Pearson's R colocalisation value: 0.62 for CH vs MT and 0.10 for CH vs Actin). In cells with high levels of expression of eGFP-pp-CHT, microtubules were highly decorated. Past 24 hours post-transfection, overexpression of the CHT caused apparent aggregation of CHT within the cells (Figure 3.9C), and after 48 hours, all the cells died suggesting that over expression of CHT is toxic to the cells.

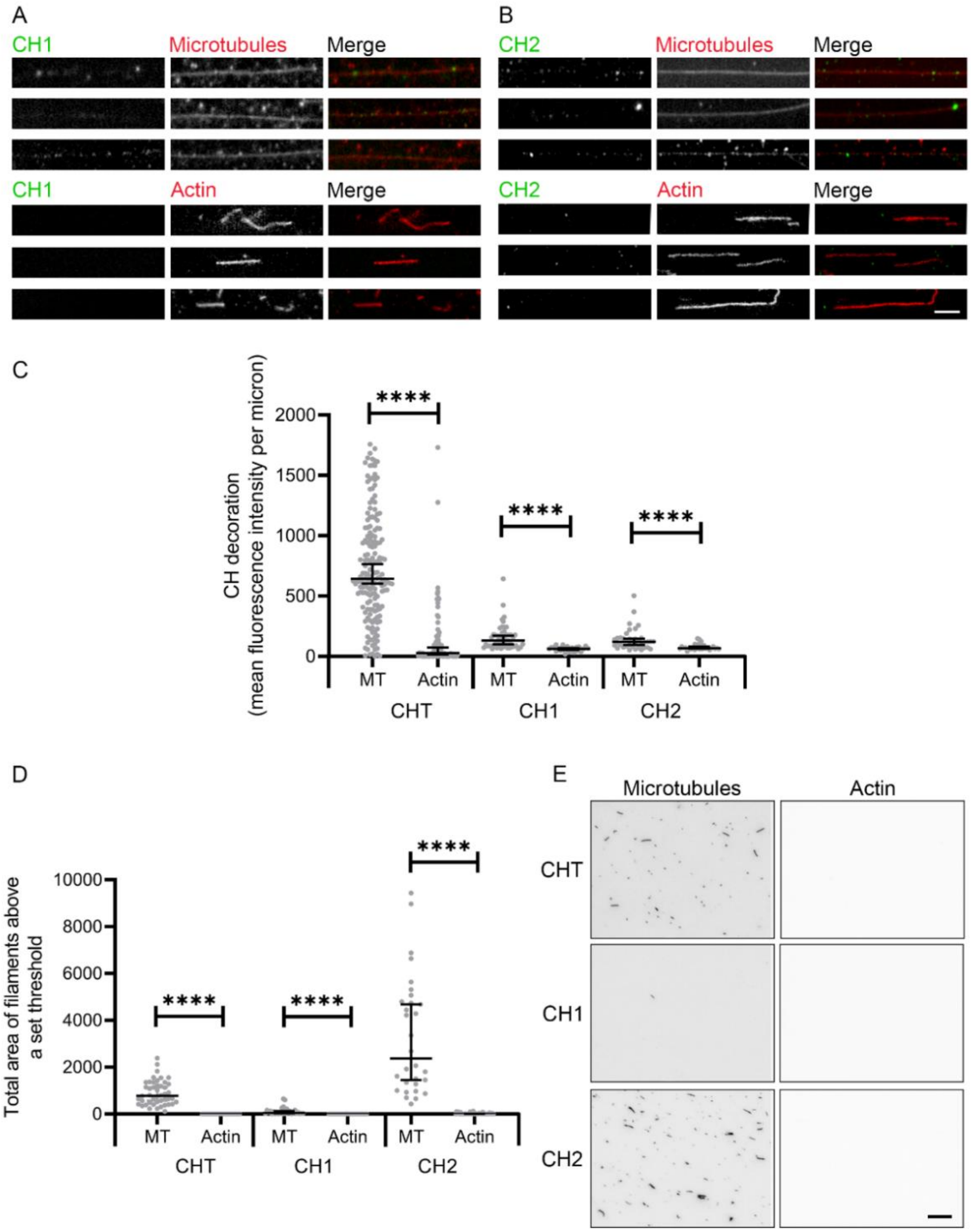

Figure 3.8 – The Individual CH domains bind microtubules in vitro.

A) *In vitro* binding flow cell assays of CH1 (green) with microtubules (red) and actin (red). (B) *In vitro* binding flow cell assays of CH2 (green) with microtubules (red) and actin (red), Scale bar = 2 μm. (C) Quantitative analysis of the eGFP tagged CHT, CH1 and CH2 along 5 μm of filament using the Plot profile plugin on FIJI and recording the area under the graph. Mann-Whitney test $p<0.0001$ for all three constructs. $n=172$. CHT has been included for comparison. (D) Quantitative analysis of microtubules or actin bound to either CHT, CH1 or CH2 bound to 1 anti-GFP-nanobody molecule μm^{-2} within a flow cell. CHT has been included for comparison. Mann-Whitney test $p<0.0001$ for all three constructs. (E) Representative images of microtubules and F-actin bound to CHT, CH1 and CH2 in flow cells with 1 anti-GFP-nanobody molecule μm^{-2} relating to graph D. Scale bar = 10 μm.

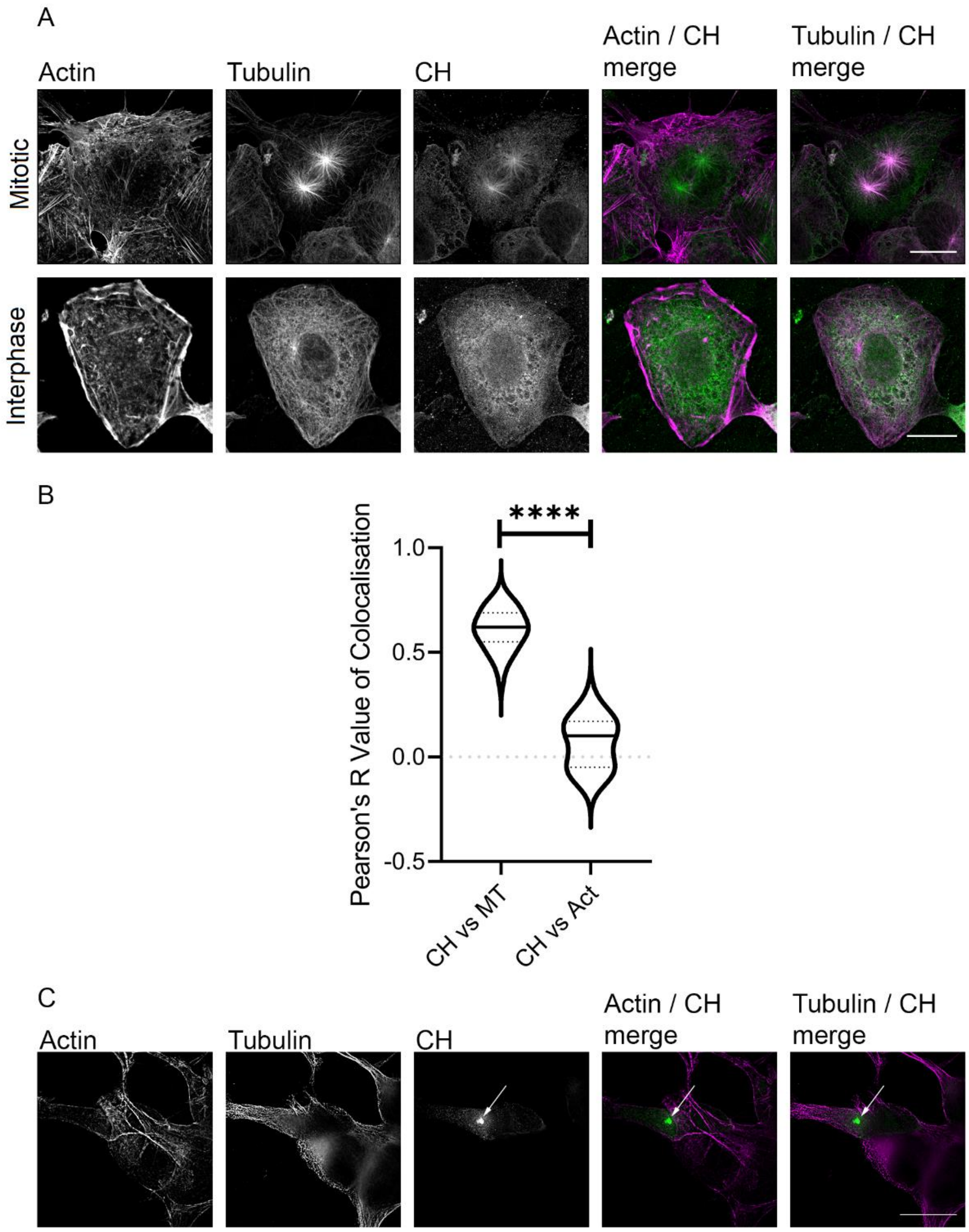

Figure 3.9 – Mammalian over expression of CHT with colocalisation analysis for microtubules and actin.

(A) Confocal images of HEK293 cells transfected with pCMV5-GFP-pp-CHT (green) co-stained for actin with phalloidin (magenta) and α-tubulin with the YL1/2 antibody (magenta) 24 hours post-transfection, showing a mitotic cell (Upper panels) and a cell in interphase (Lower panels), scale bar = 20 µm (B) Colocalisation analysis of CHT against actin and microtubules using the Coloc 2 plugin on FIJI and recording Pearson's R value. On a scale between 1.0 and -1.0 where 1.0 is complete colocalisation and -1.0 is no colocalisation. Wilcoxon's test $p<0.0001$, n=27. (C) Delta Vision images of HEK293 cells transfected with pCMV5-GFP-pp-CHT (green) co-stained for actin with phalloidin (magenta) and α-tubulin with the YL 1/2 antibody (magenta) 48 hours post-transfection, arrow indicates aggregated CHT, scale bar = 20 µm.

3.3.5 Identifying potential CHT binding partners by mass spectrometry

To identify binding partners for CHT in the HEK293 whole cell extract, proteins co-eluting from the anti-GFP-nanobody column were analysed by mass spectrometry. Four bands were present on the SDS-PAGE. Mass spectrometry revealed that the band at ~70 kDa was eGFP-tagged CHT and the band at ~50 kDa was α-tubulin. The remaining two band both contained shorter fragments of the CHT suggesting degradation of the CHT (Figure 3.10, Table 3.4). However, γ-tubulin, which has been reported to bind to ASPM (Jiang et al., 2017) was not found.

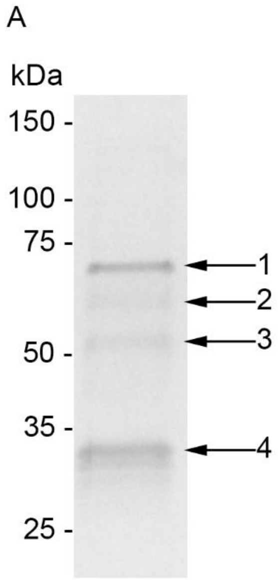

Figure 3.10 – CHT binding partners identified by mass spectrometry.

A) 4-20% tris-acetate SDS-PAGE gel of co-purified proteins from overnight HEK293 whole cell extract incubation with GFP-CHT. Bands labelled with arrows were excised and investigated by mass spectrometry and the proteins identified shown in Table 3.4. Band 1 is expected to be GFP-pp-CHT (68 kDa).

Table 3.4 – Protein identification by mass spectrometry indicating CHT interacting proteins. Band ID relates to Figure 3.10.

Band ID	Proteins identified	Coverage (%)	Number of unique peptides	Expected molecular weight (kDa)
1	Human ASPM (eGFP-pp-CHT)	16	20	68
2	Human ASPM (eGFP-pp-CHT)	10	8	68
3	Human ASPM (eGFP-pp-CHT)	6	5	68
	α-Tubulin	25	8	50
4	Human ASPM (eGFP-pp-CHT)	3	4	68

3.3.6 Microtubule / actin spin down experiments inconclusive due to in CHT aggregation

The spin down assays to observe the binding of CHT to either MT or actin was inconclusive. These spin down experiment resulted in the CHT pelleting in the control sample. Therefore, it cannot be identified if the CHT has pelleted due to binding of the filaments or whether the protein has aggregated during the incubation period causing the CHT to appear in the pellet fraction (Figure 3.11).

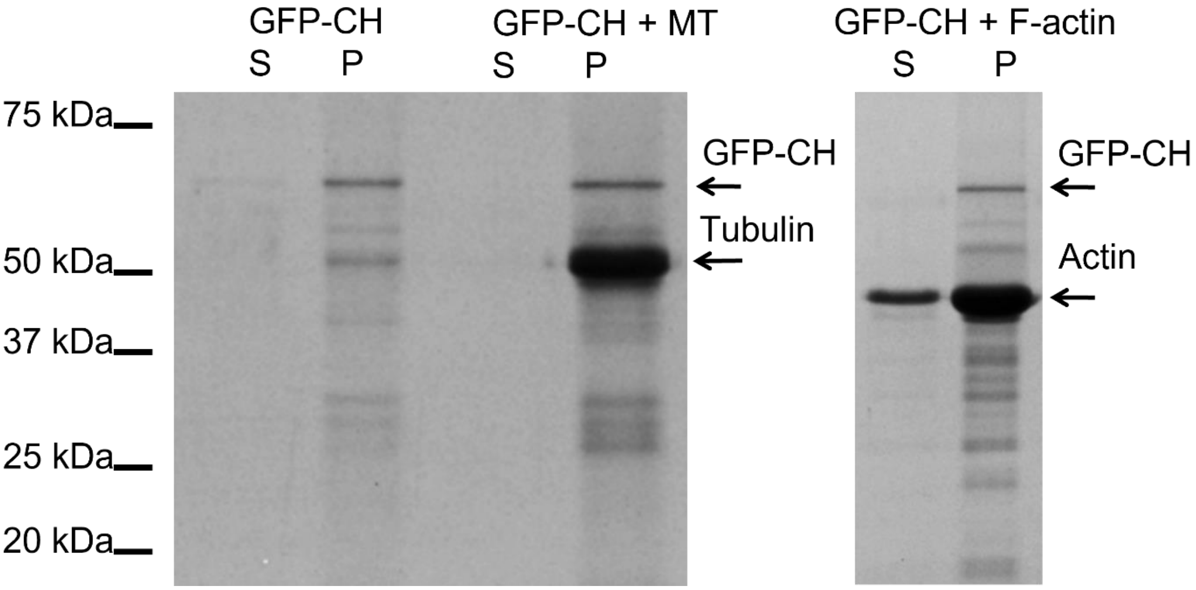

Figure 3.11 – CHT spin down assay against MT and actin.

A 4-20% SDS-PAGE gel of GFP-CHT (68 kDa) incubated either: alone, with microtubules (50 kDa), or with F-actin (40 kDa) showing the supernatant (S) and pellet (P) after a 100,000 x g centrifugation.

3.4 Discussion

This study found that the tandem CH domains (CHT) of ASPM could potentially bind to microtubules rather than to F-actin. Similarly, the individual CH domains, CH1 and CH2, also bound microtubules and not to F-actin. The ability of these CH domains, both individually and in tandem, to bind to microtubules agrees with previous reports that the CH domain of *Drosophila* asp binds to microtubules, even though only CH1 of human ASPM is similar in sequence to the CH domain of asp (Ito & Goshima, 2015; Saunders et al., 1997). However, due to the solubility issues stated, it is not possible to fully suggest that this is the case.

All three constructs, CHT, CH1 and CH2, displayed a punctate binding along the microtubules, rather than full decoration. In contrast, other microtubule binding proteins such as Tau fully decorate the microtubules (Hernández-Vega et al., 2017). It is unclear why these CH domains show this punctate binding pattern. It could be that the relative concentration of the CH domains to microtubules is too low to fully decorate the microtubules. For example, EB1 fully decorates microtubules at high concentrations but binds to the plus end only in lower concentrations (Maurer et al., 2011; Zanic et al., 2009). However, the concentrations of CH domains used in this study were in excess to that of microtubules, making it unlikely that this is the case. Alternatively, the CH domains may preferentially accumulate on specific regions of the microtubule, perhaps through recognition of specific types of post-translationally modified (PTM) tubulin (Janke & Montagnac, 2017). A third possibility is that this is a result of using taxol stabilised microtubules. It was recently shown that binding of taxanes to microtubules generates breaks in the microtubule lattice (Rai et al., 2020). It is thus possible that the purified CH domains prefer to interact with holes in the microtubule lattice (Janke & Montagnac, 2017; Reid et al., 2017) as seen previously with EB1 when examined *in vitro* (Reid et al., 2019). A final explanation may be that this binding pattern is due to the solubility issues stated, and the punctate pattern observed is the binding of aggregated protein.

While this study suggests that the CHT and individual CH domains bind to microtubules, we cannot rule out that upstream sequence in human ASPM also facilitates microtubule binding. Previous studies using constructs from *Drosophila* asp suggest the sequence upstream of the single CH domain is also involved in microtubule binding. In one study using two *Drosophila* asp constructs: an N-terminal construct (residues 94-596), which does not contain the CH domain, and a central construct (residues 596-1,135) which does. Both constructs were shown to bind to microtubules using overlay assays (Saunders et al., 1997). However, the N-terminal construct bound much more strongly suggesting that while the CH domain might bind microtubules, sequence upstream of the single CH domain is also required. A second study that showed that the single CH domain of *Drosophila* asp, homologous to CH1 of ASPM, binds to microtubules. Ito & Goshima, (2015) used a construct consisting of residues 574-972 of asp. This construct contains the CH domain (residues 836-968) in the central region but also includes upstream residues as well as the first two IQ motifs after the CH domain. The upstream region (residues 574-836) could also be involved in binding to microtubules. This region, previously called the MTASP region, was suggested to bind microtubules (Rhoads & Kenguele, 2005) and has been identified as the microtubule binding domain in more recent work (Higgins et al., 2010). Alongside this, addition of the upstream region to the CH constructs may increase the solubility issues seen here.

The data for the landing assays, in which CH domains bound to nanobodies on the surface capture microtubules, suggests that CH2 appears to bind more strongly to microtubules than either CHT or CH1 and that CHT binds more strongly than CH1 (Figure 3.8D). This is unlikely to be due to different concentrations of protein, even though concentrations of purified CH1 (0.3 μM) were low compared to CH2 (22.6 μM) and CHT (2.8 μM) (Figure 3.5), as the concentration of purified protein was in excess of the anti-GFP-nanobody at this density (19.5 pM). Therefore, the anti-GFP-nanobody should be fully occupied by a bound CH domain in each of the experiments. This result is interesting as it is likely that the two CH domains have different binding affinities for microtubules, by analogy with the tandem CH domains of α-actinin and their binding to F-actin (Way et al., 1992). Moreover, the binding of one CH domain could be influenced by the second, suggesting that the conformation of the CH domains might change when they bind to microtubules (e.g. the ‘opening’ up of the tandem CH domains of Utrophin on binding to actin (Lin et al., 2011)).

GFP-CHT domains also labelled microtubules in HEK293 cells. Unlike the punctate binding pattern displayed in flow cells, the expressed CHT domains appear to fully decorate the HEK293 microtubules. Microtubules in HEK293 cells have fewer PTMs (Wloga & Gaertig, 2010) than the microtubules isolated from pig brain used in the *in vitro* assay, which are heavily post translationally modified (Souphron et al., 2019). As PTMs may affect binding, this could lead to limited binding of the CH domains to the MTs. Unlike overexpressed full-length ASPM, it is difficult to distinguish if the CH domains preferentially bound to the spindle minus end of the microtubules. This indicates that another region of ASPM may be required for the minus end localisation, likely the N-terminal microtubule binding region described previously (Saunders et al., 1997). Likewise, this observation could be due to the overexpression of the CH domains leading to full decoration of all available microtubules and a limited expression may have displayed a preference to bind at particular sites on the microtubule.

Mass spectrometry pull-down experiments also confirmed the microtubule binding properties of the tandem CH domains. Interestingly, only α-tubulin was detected, which may be due to a limitation of the mass spectrometry methods when using low levels of sample protein (Fricker, 2015; Mitchell et al., 2015). While ASPM was shown to bind γ-tubulin previously (Jiang et al., 2017), it is likely that this interaction is mediated through another region of ASPM. Binding to γ-tubulin may contribute to the microtubule minus end preference of ASPM and binding of the CH domains could contribute to binding of ASPM on the spindle microtubules.

In summary, the data shown here suggests that the ASPM CH domains may contribute to the binding of ASPM to microtubules, rather than mediate binding to F-actin. In the future, it will be interesting to determine if the individual CH domains and the tandem CH domains do indeed have different binding affinities, and if upstream sequence in human ASPM also helps to mediate microtubule binding and to use electron microscopy to determine precisely how the CH domains bind to microtubules.

4. The IQ motifs of ASPM

4.1 Introduction

The number of IQ motifs present in ASPM homologues varies between species; *C. elegans* aspm-1 has two, the *D. melanogaster* homologue asp contains 24, *M. musculus* Aspm contains 62 and H. sapiens ASPM contains 81, the largest number of IQ repeats reported in any protein (Kouprina et al., 2005). The large number of IQ domains, mostly encoded by exon 18 (the largest exon in ASPM (4,755 bp)) is thought to be the result of a single large duplication of around 900 bp resulting in the exon having 67 IQ repeats (Bond et al., 2002; Kouprina et al., 2005).

IQ motifs are generally 23-27 residues in length, have the consensus sequence of IQXXXRGXXXR (where X is any amino acid) and are predicted to adopt an amphipathic α-helical structure. They were first discovered in unconventional myosins and are repeated in tandem in the heavy chain of all myosin isoforms, where they usually bind myosin-associated light chains or calmodulin (Houdusse & Cohen, 1995). Calmodulin interacts with the IQ motif by forming 4 hydrogen bonds with Q and R (residues 2 and 6 of the IQ motif respectively) (Figure 4.1). Conversely, the essential light chain (ELC; MYL6B) required only the first half of the IQ motif (IQXXXR). The second part of motif (GXXXR) is thought to play a more minor role in light chain binding, is not well conserved and in the case of the ELC, this sequence is replaced by a pattern of 3 hydrophobic residues (Houdusse et al., 1996).

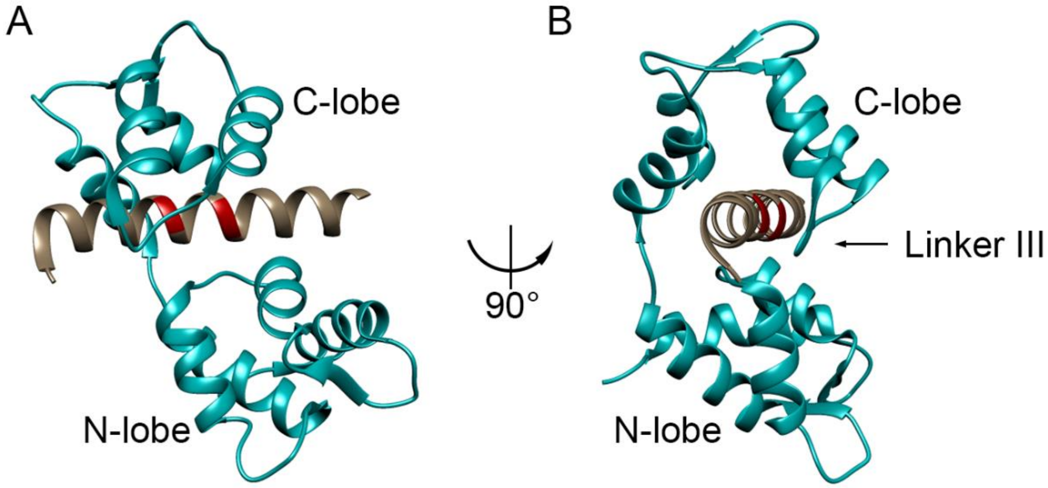

Figure 4.1 – Calmodulin bound to IQ motif.

(A) ribbon depiction of calmodulin (teal) bound to the first IQ motif of myosin-5a (PBD 2IX7). The IQ motif is shown in light brown with the calmodulin interacting residues (residues 2 (Q) and 6 (R)) shown in red. (B) Side view of (A) looking end on down the N-terminus of IQ motif displaying the close interaction of linker III of calmodulin and the indicated residues of the IQ motif.

A bioinformatic analysis of the IQ motifs of ASPM identified a pattern in their length where 55% of the total IQ domains follow the triplet spacing pattern of 23-23-27 residues ((Kouprina et al., 2005), Figure 4.2). The other 45% do not follow this triplet pattern and the length of individual motifs varies, with the smallest IQ motif being 14 amino acids long and the largest, 38 amino acids (Kouprina et al., 2005). The significance of this pattern has yet to be investigated, however, the shorter IQ motifs are less likely to be involved in light chain binding as the minimum length of an IQ motif for calmodulin to bind is thought to be 23 (Jang et al., 2011; Kim et al., 2004).

Calmodulin is a 149 amino acid Ca^{2+} sensing protein, which binds to a wide variety of target proteins modifying their function in turn. Calcium ion binding occurs in the two homologous helix-loop-helix domains known as EF-hands. Calmodulin assumes one of two forms; 'open', in which Ca^{2+} is bound; and 'closed' (or apo) where Ca^{2+} is absent. The 'open' conformation is termed the 'gripping' form and it binds to hydrophobic regions of a target protein. The 'closed' conformation is termed the ‘non-gripping’ form and it is this form that binds to the IQ motifs of the myosin heavy chain (Houdusse et al., 1996). Due to the hydrophobic nature of the IQ domain, calmodulin is thought to bind tightly to the IQ motif in the presence of Ca^{2+} (Houdusse & Cohen, 1995). However, in neuromodulin, neurogranin and in many of the unconventional myosins, it is the Apo form that binds tightly to the IQ motif in a semi-open position. In myosin, this interaction is mostly mediated by the C-lobe of calmodulin (Terrak, 2003; Terrak et al., 2005). The interaction between calmodulin and the IQ motif is thought to stabilise and prevent the collapse of the α-helix. An increase in Ca^{2+} can result in dissociation of calmodulin (Rhoads & Friedberg, 1997; Wang et al., 2000; Wolenski, 1995).

Myosin light chain 6B (MYL6B) is a type of essential (alkali) light chain. Essential light chains are also important in myosin function and typically bind to the first IQ motif following the motor. MYL6B is 208 residues long and contains an N-terminal extension rich in alanine and proline residues (Figure 4.3), similar to the A1 light chain of skeletal muscle myosin (Logvinova & Levitsky, 2018) as well as positively charged lysine residues. This sequence is expected to have a rigid conformation and the corresponding region of the A1 light chain has been shown to interact with actin through the N-terminal APKK sequence and may even facilitate actin polymerisation (reviewed in (Logvinova & Levitsky, 2018)). A potential role of this light chain might be to interact with actin when bound to the IQ motifs of ASPM. Therefore, it is important to determine if this light chain is able to bind to the IQ motifs of ASPM, in addition to calmodulin.

The evidence of an association between ASPM and calmodulin localisation is strong (Schoborg et al., 2015; van der Voet et al., 2009). During mitosis, the distribution of calmodulin and ASPM has been shown to be almost identical possibly indicating an interaction (Schoborg et al., 2015). This binding has been confirmed by co-immunoprecipitation and calmodulin is thought to bind to the IQ motifs (Xu et al., 2012). However, due to the sequence variation of the IQ motifs within ASPM, it is currently unknown as to whether ASPM binds calmodulin at each of its 81 motifs (Bahler & Rhoads, 2002; Kouprina et al., 2005). In addition to binding calmodulin (CALM2), the IQ motifs of ASPM have been shown to interact with both CALM2 and MYL6B by yeast two-hybrid experiments (J Bond – Personal communication).

The aim of the work described in this chapter was to characterise the IQ motifs of ASPM, to determine if they bind CALM2, and / or MYL6B, and to determine the overall structure of IQ constructs by negative stain electron microscopy (nsEM) to gain a better understanding of the IQ domains.

1265	KEIRAARL	IQ	TTW	RK	YKL	K	TDLKRHQ	IQ1	26
1291	EREKAARI	IQ	LAV	IN	FLA	K	QRLR	IQ2	23
1314	KRVNAALV	IQ	KYW	RR	VLA	Q	RKLLMLKKEKLEK	IQ3	32
1346	VQNKAASL	IQ	GYW	RR	YST	R	QRFL	IQ4	23
1369	KLKYYSII	LQ	SRI	RM	IIA	V	TSYK	IQ5	23
1392	RYLWATVT	IQ	RHW	RA	YLR	R	KQDQQRYE	IQ6	27
1419	MLKSSTLI	IQ	SMF	RK	WKQ	R	KMQ	IQ7	22
1441	SQVKATVI	LQ	RAF	RE	WHL	R	KQA	IQ8	22
1463	KEENSAII	IQ	SWY	RM	HKE	L	RKYI	IQ9	23
1486	YIRSCVVI	IQ	KRF	RC	FQA	Q	KLYK	IQ10	23
1509	RRKESILT	IQ	KYY	KA	YLK	G	KIERTNYL	IQ11	27
1536	QKRAAAIQ	LQ	AAF	RR	LKA	H	NLC	IQ12	22
1558	RQIRAACV	IQ	SYW	RM	RQD	R	VRFL	IQ13	23
1581	NLKKTIIK	FQ	AHV	RK	HQQ	R	QKYK	IQ14	23
1604	KMKKAAVI	IQ	THF	RA	YIF	A	MKVLASYQ	IQ15	27
1631	KTRSAVIV	LQ	SAY	RG	MQA	R	KMYI	IQ16	23
1654	HILTSVIK	IQ	SYY	RA	YVS	K	KEFL	IQ17	23
1677	SLKNATIK	LQ	STV	KM	KQT	R	KQYL	IQ18	23
1700	HLRAAALF	IQ	QCY	RS	KKI	A	AQKREEYM	IQ19	27
1727	QMRESCIK	LQ	AFV	RG	YLV	R	KQMR	IQ20	23
1750	LQRKAVIS	LQ	SYF	RM	RKA	R	QYYL	IQ21	23
1773	KMYKAIIV	IQ	NYY	HA	YKA	Q	VNQRKNFL	IQ22	27
1800	QVKKAATC	LQ	AAY	RG	YKV	R	QLIK	IQ23	23
1823	QQSIAALK	IQ	SAF	RG	YNK	R	VKYQ	IQ24	23
1846	SVLQSIIK	IQ	RWY	RA	YKT	L	HDTRTHFL	IQ25	27
1873	KTKAAVIS	LQ	SAY	RG	WKV	R	KQIR	IQ26	23
1896	REHQAALK	IQ	SAF	RM	AKA	Q	KQFR	IQ27	23
1919	LFKTAALV	IQ	QNF	RA	WTA	G	RKQCMEYI	IQ28	27
1946	ELRHAVLV	LQ	SMW	KG	KTL	R	RQLQ	IQ29	23
1969	RQHKCAII	IQ	SYY	RM	HVQ	Q	KKWK	IQ30	23
1992	IMKKAALL	IQ	KYY	RA	YSI	G	REQNHLYL	IQ31	27
2019	KTKAAVVT	LQ	SAY	RG	MKV	R	KRIK	IQ32	23
2042	DCNKAAVT	IQ	SKY	RA	YKT	K	KKYA	IQ33	23
2065	TYRASAII	IQ	RWY	RG	IKI	T	NHQHKEYL	IQ34	27
2092	NLKKTAIK	IQ	SVY	RG	IRV	R	RHIQ	IQ35	23
2115	HMHRAATF	IK	AMF	KM	HQS	R	ISYH	IQ36	23
2138	TMRKAAIV	IQ	VRC	RA	YYQ	G	KMQREKYL	IQ37	27
2165	TILKAVKV	LQ	ASF	RG	VRV	R	RTLR	IQ38	23
2188	KMQTAATL	IQ	SNY	RR	YRQ	Q	TYFN	IQ39	23
2211	KLKKITKT	VQ	QRY	WA	MKE	R	NIQFQRYN	IQ40	27
2238	KLRHSVIY	IQ	AIF	RG	KKA	R	RHLK	IQ41	23
2261	MMHIAATL	IQ	RRF	RT	LMM	R	RRFL	IQ42	23
2284	SLKKTAIL	IQ	RKY	RA	HLC	T	KHHLQFL	IQ43	26
2310	QVQNAVIK	IQ	SSY	RR	WMI	R	KRMR	IQ44	23
2333	EMHRAATF	IQ	STF	RM	HRL	H	MRYQ	IQ45	23
2356	ALKQASVV	IQ	QQY	QA	NRA	A	KLQRQHYL	IQ46	27
2383	RQRHSAVI	LQ	AAF	RG	MKT	R	RHLK	IQ47	23
2406	SMHSSATL	IQ	SRF	RS	LLV	R	RRFI	IQ48	23
2429	SLKKATIF	VQ	RKY	RA	TIC	A	KHKLYQFL	IQ49	27
2456	HLRKAAIT	IQ	SSY	RR	LMV	K	KKLQ	IQ50	23
2479	EMQRAAVL	IQ	ATF	RM	YRT	Y	ITFQ	IQ51	23
2502	TWKHASIL	IQ	QHY	RT	YRA	A	KLQRENYI	IQ52	27
2529	RQWHSAVV	IQ	AAY	KG	MKA	R	QLLR	IQ53	23
2552	EKHKASIV	IQ	STY	RM	YRQ	Y	CFYQ	IQ54	23
2575	KLQWATKI	IQ	EKY	RA	NKK	K	QKVFQH	IQ55	25
2600	NELKKETC	VQ	AGF	QD	MNI	K	KQIQ	IQ56	23
2623	EQHQAAII	IQ	KHC	KA	FKI	R	KHYL	IQ57	23
2646	HLRATVVS	IQ	RRY	RK	LTA			IQ58	18
2664	VRTQAVIC	IQ	SYY	RG	FKV	R	KDIQ	IQ59	23
2687	NMHRAATL	IQ	SFY	RM	HRA	K	VDYE	IQ60	23
2710	TKKTAIVV	IQ	NYY	RL	YVR	V	KTERKNFL	IQ61	27
2737	AVQKSVRT	IQ	AAF	RG	MKV	R	QKLKNVS	IQ62	26
2763	EEKMAAIV	NQ	SAL	CC	YRS	K	TQYE	IQ63	23
2786	AVQSEGVM	IQ	EWY	KA	SGL	A	CSQEAEYH	IQ64	27
2813	SQSRAAVT	IQ	KAF	CR	MVT	R	KLE	IQ65	22
2835	TQKCAALR	IQ	FFL	QM	AVY	R	RRFV	IQ66	23
2858	QQKRAAIT	LQ	HYF	RT	WQT	R	KQFL	IQ67	23
2881	LYRKAAVV	LQ	NHY	RA	FLS	A	KHQRQVYL	IQ68	27
2908	QIRSSVII	IQ	ARS	KG	FIQ	K	RKFQ	IQ69	23
2931	EIKNSTIK	IQ	AMW	RR	YRA	K	KYL	IQ70	22
2953	CKVKAACK	IQ	AWY	RC	WRA	H	KEYL	IQ71	23
2976	AILKAVKI	IQ	GCF	YT	KLE	R	TRFL	IQ72	23
2999	NVRASAII	IQ	RKW	RA	ILP	A	KIAHEHFLMI	IQ73	29
3028	KRHRAACL	IQ	AHY	RG	YKG	R	QVFL	IQ74	23
3051	RQKSAALI	IQ	KYI	RA	REA	G	KHERIKYI	IQ75	27
3078	EFKKSTVI	LQ	ALV	RG	WLV	R	KRFLEQRAKIRLLHFTAAA	IQ76	38
3116	YYHLNAVR	IQ	RAY	KL	YLA	V	KNAN	IQ77	23
3139	KQVNSVIC	IQ	RWF	R				IQ78	14
3153	ARLQEKRF	IQ	KYH	SI	KKI	E	HEGQECLS	IQ79	27
3180	QRNRAASV	IQ	KAV	RH	FLL	R	KKQE	IQ80	23
3203	KFTSGIIK	IQ	ALW	RG	YSW	R	KKNDC	IQ81	24

Figure 4.2 – The 81 IQ motifs of human ASPM.

Identification of all 81 IQ motifs, displaying the starting residue within ASPM, the respective residues correlating to the motif in red, and their respective lengths, adapted from (Kouprina et al., 2005).

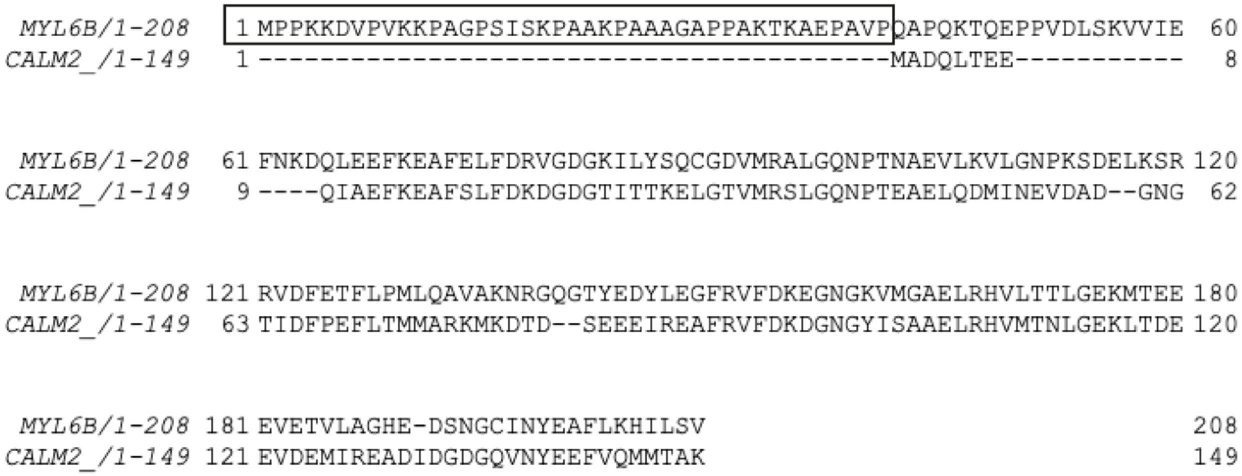

```
MYL6B/1-208    1 MPPKKDVPVKKPAGPSISKPAAKPAAAGAPPAKTKAEPAVPQAPQKTQEPPVDLSKVVIE  60
CALM2_/1-149   1 -----------------------------------------MADQLTEE-----------   8

MYL6B/1-208   61 FNKDQLEEFKEAFELFDRVGDGKILYSQCGDVMRALGQNPTNAEVLKVLGNPKSDELKSR 120
CALM2_/1-149   9 ----QIAEFKEAFSLFDKDGDGTITTKELGTVMRSLGQNPTEAELQDMINEVDAD--GNG  62

MYL6B/1-208  121 RVDFETFLPMLQAVAKNRGQGTYEDYLEGFRVFDKEGNGKVMGAELRHVLTTLGEKMTEE 180
CALM2_/1-149  63 TIDFPEFLTMMARKMKDTD--SEEEIREAFRVFDKDGNGYISAAELRHVMTNLGEKLTDE 120

MYL6B/1-208  181 EVETVLAGHE-DSNGCINYEAFLKHILSV                                208
CALM2_/1-149 121 EVDEMIREADIDGDGQVNYEEFVQMMTAK                                149
```

Figure 4.3 – Sequence comparison between MYL6B and CALM2.

Alignment of the MYL6B and CALM2 sequence showing the N-terminal extension of MYL6B (box).

4.2 Methods

4.2.1 Cloning IQ motif constructs

Several IQ motif constructs (Figure 4.4) were cloned and expressed (Table 4.1). Each of these had an N-terminal FLAG-eGFP tag to help in purification and to assign polarity to the protein when the purified molecules were imaged by negative stain electron microscopy (nsEM).

For each construct, the sequence was amplified by PCR using primers listed (Table 4.2) and subcloned into the KpnI-SpeI sites of pFastBac1-eGFP (generated in Section 3.2.1) using GeneArt seamless cloning (Section 2.2.8) or NEBBuilder (Section 2.2.9). Several smaller IQ constructs were also prepared in the same way and these contained a PreScission protease site for on column cleavage if required. Two further IQ constructs, pFastBac1-eGFP-IQ49-51 and pFastBac1-eGFP-IQ51-53 were generated by Genscript (Table 4.1).

Two human light chain constructs were also generated for co-expression with the IQ constructs. These were calmodulin 2 (CALM2; NCBI GenBank accession: CR541990.1) and myosin light chain 6B (MYL6B; NCBI GenBank accession: NM_001199629.2). These sequences were generated and cloned into the BamHI-HindIII sites of pFastBac1 by Genscript.

Table 4.1 – List of plasmids with their expression products and expectant sizes.

Plasmid name	Plasmid size (bp)	Cloning method	Tag	Expression product	Product mass (kDa)
pFastBac1-eGFP-IQ32-52	7,044	GeneArt seamless cloning (Section 2.2.8)	FLAG-eGFP	eGFP-IQ32-52	91.3
pFastBac1-eGFP-IQ1-52	9,315	GeneArt seamless cloning (Section 2.2.8)	FLAG-eGFP	eGFP-IQ1-52	183.4
pFastBac1-eGFP-IQ32-81	9,138	GeneArt seamless cloning (Section 2.2.8)	FLAG-eGFP	eGFP-IQ32-81	174.9
pFastBac1-eGFP-IQ1-9	6,207	NEBBuilder (Section 2.2.9)	FLAG-eGFP-pp	eGFP-IQ1-9	57.8
pFastBac1-eGFP-IQ9-16	6,117	NEBBuilder (Section 2.2.9)	FLAG-eGFP-pp	eGFP-IQ9-16	53.5
pFastBac1-eGFP-IQ49-51	5,760	Genscript	FLAG-eGFP-pp	eGFP-IQ49-51	39.2
pFastBac1-eGFP-IQ50-52	5,760	NEBBuilder (Section 2.2.9)	FLAG-eGFP-pp	eGFP-IQ50-52	39.2
pFastBac1-eGFP-IQ51-53	5,760	Genscript	FLAG-eGFP-pp	eGFP-IQ51-53	39.2
pFastBac1-eGFP-IQ53-61	6,168	NEBBuilder (Section 2.2.9)	FLAG-eGFP-pp	eGFP-IQ53-61	55.6
pFastBac1-eGFP-IQ62-68	6,039	NEBBuilder (Section 2.2.9)	FLAG-eGFP-pp	eGFP-IQ62-68	49.7
pFastBac1-eGFP-IQ68-75	6,135	NEBBuilder (Section 2.2.9)	FLAG-eGFP-pp	eGFP-IQ68-75	54.0
pFastBac1-eGFP-IQ74-81	6,141	NEBBuilder (Section 2.2.9)	FLAG-eGFP-pp	eGFP-IQ74-81	54.2
pFastBac1-CALM2	5,130	Genscript	-	CALM2	16.8
pFastBac1-MYL6B	5,310	Genscript	-	MYL6B	22.8

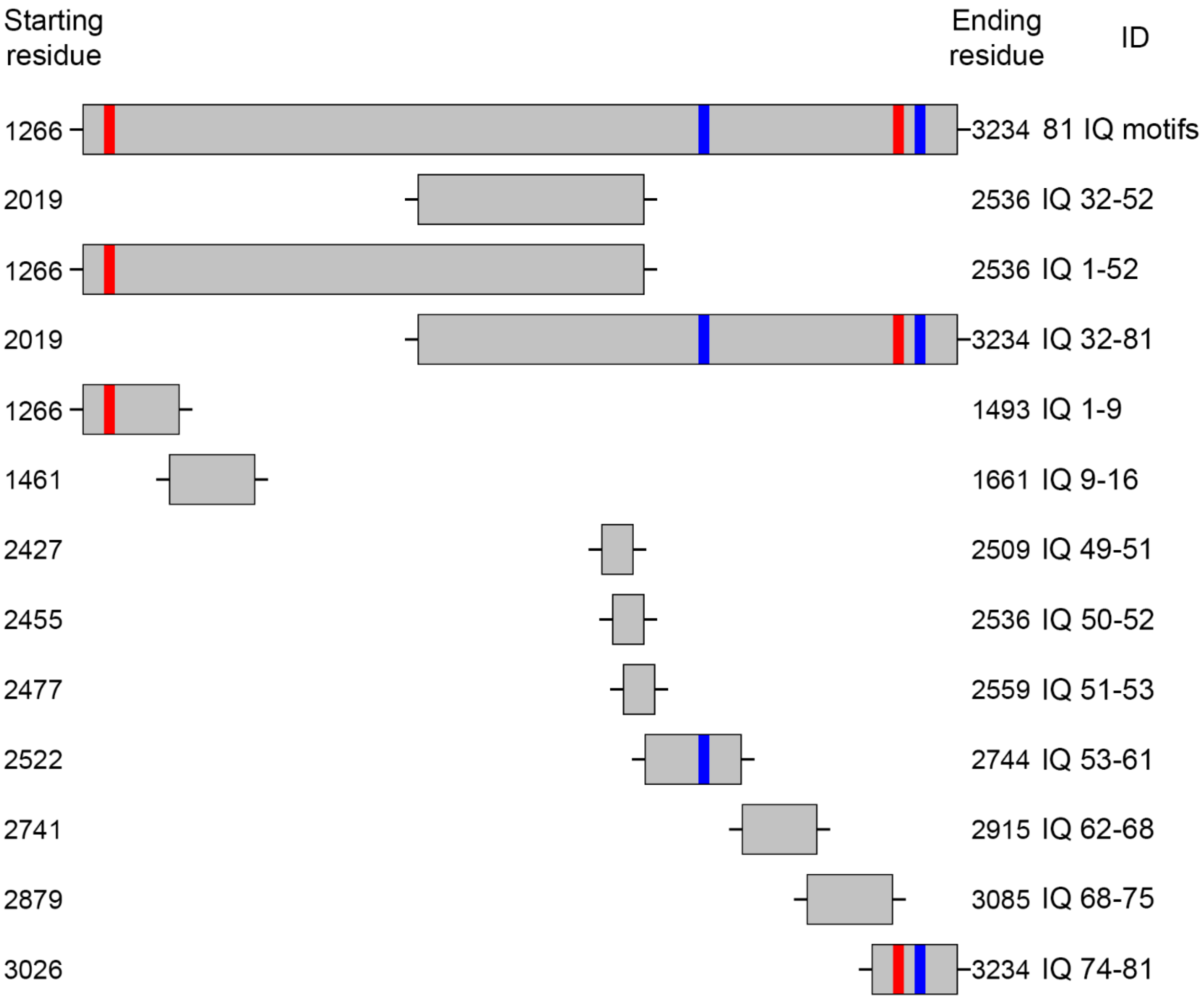

Figure 4.4 – Schematic of the IQ motif constructs used for expression.

Several constructs covering different portions of the 81 IQ motifs were made in order to allow for more manageable expressions and analyses, stating the start and end residues of ASPM that were cloned into pFastBac1-eGFP. The position of short (<20 amino acids; Blue) and long (>30 amino acids; Red) IQ motifs are indicated (see Figure 4.2). ID relates to expression construct names in Table 4.1.

Table 4.2 – The primers used for cloning IQ domains into pFastbac1 eGFP.

Primer name	Sequence (5' - 3')	Use	Annealing temp (°C)	Restriction site	Additional features
IQ For	GGGAGGTAGTGGTACCAAAACAAAAGCAGCTGTAGT	Inserting 21IQ domains (IQ32-IQ52) (bp 6,055-7,608) into pFastBac1-eGFP	60	KpnI	-
IQ Rev	CGAAAGCGGCCGCGATTAAACCACAGCAGAATGCCATT			SpeI	STOP
Half IQ Frag 1 For	GGGAGGTAGTGGTACCGATCTTCGTAAAGAAAT	Insert IQ1-IQ52 (bp 3,787-7,608) into pFastBac1-eGFP	60	KpnI	-
IQ Rev	CGAAAGCGGCCGCGATTAAACCACAGCAGAATGCCATT			SpeI	STOP
IQ For	GGGAGGTAGTGGTACCAAAACAAAAGCAGCTGTAGT	Insert IQ32-IQ81 (bp 6,055-9,702) into pFastBac1-eGFP	60	KpnI	-
Half IQ Frag 2 Rev	AGCGGCCGCGACTAGTTATAGTCGTATAGCTTT			SpeI	STOP
IQ 1-9 For	GGGAGGTAGTGGTACCCTGGAAGTTCTGTTCCAGGGGCCCCTTCGTAAAGAAATA	Insert IQ1-IQ9 (bp 3,787-4,479) into pFastBac1-eGFP	58	KpnI	PreScission Protease site
IQ 1-9 Rev	CGAAAGCGGCCGCGATTAGATAACAACACAAGA			SpeI	STOP
IQ 9-16 For	GGGAGGTAGTGGTACCCTGGAAGTTCTGTTCCAGGGGCCCCAAGCTAAAGAAGAA	Insert IQ9-IQ16 (bp 4,381-4,983) into pFastBac1-eGFP	58	KpnI	PreScission Protease site
IQ 9-16 Rev	CGAAAGCGGCCGCGATTACTTTATAACAGATGT			SpeI	STOP
IQ 50-52 For	GGGAGGTAGTGGTACCCTGGAAGTTCTGTTCCAGGGGCCCTTGCACTTAAGAAAG	Insert IQ50-IQ52 (bp 7,363-7,608) into pFastBac1-eGFP	58	KpnI	PreScission Protease site
IQ Rev	CGAAAGCGGCCGCGATTAAACCACAGCAGAATGCCATT			SpeI	STOP

Table 4.2 – continued.

Primer name	Sequence (5' - 3')	Use	Annealing temp (°C)	Restriction site	Additional features
IQ 53-61 For	GGGAGGTAGTGGTACCCTGGAAGTTCTGTTCCAGGGGCCCTATATCAGACAATGG	Insert IQ53-IQ61 (bp 7,579-8,232) into pFastBac1-eGFP	58	KpnI	PreScission Protease site
IQ 53-61 Rev	CGAAAGCGGCCGCGATTAAGTTCGTACAGATTT			SpeI	STOP
IQ 62-68 For	GGGAGGTAGTGGTACCCTGGAAGTTCTGTTCCAGGGGCCCTCTGTACGAACTATT	Insert IQ62-IQ68 (bp 8,221-8,745) into pFastBac1-eGFP	58	KpnI	PreScission Protease site
IQ 62-68 Rev	CGAAAGCGGCCGCGATTAAATGATAACACTGCT			SpeI	STOP
IQ 68-75 For	GGGAGGTAGTGGTACCCTGGAAGTTCTGTTCCAGGGGCCCTTTTTACTATATAGA	Insert IQ68-IQ75 (bp 8,635-9,255) into pFastBac1-eGFP	45	KpnI	PreScission Protease site
IQ 68-75 Rev	CGAAAGCGGCCGCGATTAGATAACTGTAGATTT			SpeI	STOP
IQ 74-81 For	GGGAGGTAGTGGTACCCTGGAAGTTCTGTTCCAGGGGCCCATGATAAAAAGACAT	Insert IQ74-IQ81 (bp 9,076-9,702) into pFastBac1-eGFP	58	KpnI	PreScission Protease site
IQ 74-81 Rev	CGAAAGCGGCCGCGATTATAGTCGTATAGCTTT			SpeI	STOP

4.2.2 Expression and purification

Virus was prepared as described (Section 2.3). Following transfection into Sf9 cells, several rounds of amplification were used to generate virus for subsequent expression of the longer IQ motifs. However, only one round of amplification was required for each of the shorter IQ constructs (IQ1-9, IQ9-16, IQ50-52, IQ53-61, IQ62-68, IQ68-75, IQ74-81) (Table 4.3) to achieve a high viral titre. Sf9 cells were co-infected with IQ and light chain viruses using an MOI of 2 for all IQ viruses and a MOI of 5 for CALM2 and MYL6B viruses as multiple light chains were needed per heavy chain (optimised by expression tests; data not shown) as described (Section 2.3.8).

For expression, the cells were infected and cultured for 72 hours and then cell pellets frozen prior to purification of the proteins, using the FLAG tag. The cell pellets were thawed on ice, and then resuspended in extraction buffer (10 mM MOPS, 200 mM NaCl, 10 mM $MgCl_2$, 1 mM EGTA, pH 8.0) supplemented with 10 μM Leupeptin, 2 mM PMSF. The cells were lysed by hand with a Dounce homogeniser followed by centrifugation at 30,000 x g for 30 mins at 4°C in a Beckman Coulter Avanti J25 to clarify the lysate. 20 mL of the clarified lysate was then incubated with 2 mL anti-FLAG resin in a 5 mL disposable column (Thermo Fisher), equilibrated with extraction buffer, in suspension for 1-hour at room temperature before the column was washed extensively with 50 mL extraction buffer. Protein was eluted by the addition of extraction buffer supplemented with 200 ng mL^{-1} 3xFLAG peptide (Sigma Aldrich). Following elution, protein was dialysed using 10,000 molecular weight cut-off (MWCO) SnakeSkin dialysis tubing against 2 L extraction buffer, at 4°C overnight, to remove the 3xFLAG peptide. Protein concentrations were estimated using a Nanodrop nanophotometer (IMPLEN) (Section 2.6.5) and purity was analysed on a 4-20% tris-acetate SDS-PAGE (Section 2.6.6).

Table 4.3 – Viral titres for each IQ construct and light chain construct, Plaque Forming Units per mL (PFU mL-1). A viral titre ranging from $1x10^7$ to $1x10^8$ PFU mL^{-1} is recommended for expression (Baculovirus expression system user guide; Invitrogen).

Virus name	Passage 0 (PFU mL^{-1})	Passage 1 PFU mL^{-1})	Passage 2 PFU mL^{-1})	Passage 3 PFU mL^{-1})
eGFP-IQ32-52	$9.03x10^6$	$8.27x10^5$	$1.22x10^8$	$6.13x10^8$
eGFP-IQ1-52	$6.13x10^8$	$7.76x10^8$	-	-
eGFP-IQ32-81	$3.00x10^6$	$7.94x10^6$	$1.37x10^8$	-
eGFP-IQ1-9	$1.52x10^8$	-	-	-
eGFP-IQ9-16	$3.97x10^8$	-	-	-
eGFP-IQ50-52	$1.44x10^8$	-	-	-
eGFP-IQ53-61	$2.35x10^9$	-	-	-
eGFP-IQ62-68	$1.61x10^9$	-	-	-
eGFP-IQ68-75	$4.01x10^8$	-	-	-
eGFP-IQ74-81	$7.98x10^8$	-	-	-
CALM2	$1.28x10^6$	$3.76x10^7$	$6.62x10^7$	$6.13x10^8$
MYL6B	$3.69x10^5$	$4.67x10^7$	$1.98x10^8$	$1.90x10^9$

4.2.3 Negative stain electron microscopy

Purified proteins were imaged by negative stain electron microscopy (nsEM) as follows. Carbon coated 400 mesh copper grids (Agar Scientific), kindly provided by Martin Fuller (EM unit, University of Leeds) were used. Prior to adding the sample, the grids were glow discharged using the PELCO easiGlow™ Glow Discharge Cleaning System (Ted Pella), operating at 10 mA for 1 min. Glow discharge in air increases the hydrophilicity of the carbon surface, allowing the hydrophilic surfaces of proteins to readily adsorb. Hydrophilic surfaces also promote a thin and even layer of stain upon drying (Aebi & Pollard, 1987).

To perform the staining, 5 µL of purified IQ motifs at a concentration of 100 nM, supplemented with 200 nM exogenous calmodulin were applied to the carbon film side of the grid, held with inverted tweezers, and the protein allowed to adsorb onto the grid for 60 secs. All proteins and buffers were kept on ice at 4°C prior to application. After 60 secs the grid was flicked once to remove the excess liquid. A drop (~5-10 µL) of 1% (w/v) aqueous uranyl acetate (at ambient temperature) was applied using a Pasteur pipette. On contact the droplet was quickly flicked off the grid and this was repeated 4 times for a total of 5 drops. Excess liquid was then wicked away from one side of the grid by touching the grid edge with torn filter paper (Whatman, Ashless grade #42 Filtration paper). The grid was then allowed to fully dry under a hot lamp for 5 mins before viewing by electron microscopy.

Grids were examined using a FEI Technai F20 transmission electron microscope equipped with a 200 keV Field Emission Gun (FEG) electron source, operating at 120 kV. Before use, the microscope apertures were aligned, and a grid sample adjusted to the eucentric height using the goniometer. Objective astigmatism was corrected.

To record images, grids were examined at 10,000x magnification to locate areas where negative staining was optimal. Once a suitable area was located images were collected at 50,000x magnification (0.2 nm pixel^{-1}) at a defocus of ~1.5 µm. The collected images were converted into TIF format using the e2proc2d.py command in EMAN2 (Tang et al., 2007).

4.2.4 Image processing

Individual micrographs were opened in RELION software (Fernandez-Leiro & Scheres, 2017). To assign polarity to the particles, the N- and C- termini were first distinguished. To achieve this, particles were manually picked by setting the curser on each end of the particle. Particle ends were then windowed using a circle with a diameter of 300 Å. A total of 6,321 particles were picked and subjected to 25 iterative rounds of reference-free alignment and classification in RELION 3.0.7 using a 275 Å mask and classified into 100 classes. Of the 100 classes, the top 23 classes (organised by number of particles per class; totalling 4,889 particles) were taken forward as they contained particles with a high resolution and alignment, thus removing poorly aligned particles and contaminants (i.e. unrecognisable particles) (Figure 4.5A). Particle classes were then separated into those with or without visible eGFP, subjected to another 25 iterative rounds of reference-free alignment as above, and classified into ~100 particles per class (Figure 4.5B). After discarding classes with poorly aligned particles and contaminants, 4,349 particles remained. These were then converted into HED format using the e2proc2d.py command in EMAN2 and exported into IMAGIC 5 software package (Van Heel et al., 1996) as an image stack.

In IMAGIC 5, `Center-image` was first used to centre all particles around a rotationally symmetrical version of the sum of all particles. The particles were saved as an image stack before a circular mask sufficient to cover the entire particle was generated using `Test-image`. Particles then underwent an initial reference-free 2D alignment using `MSA-run` followed by `MSA-Classify`, to classify the particles into ~150 particles per class, then `MSA-sum`. The particles were then rotationally and translationally aligned so that they were vertical using `Align-rotational`, `Extract-copy` followed by `Prepare-mrarefs` to maintain orientation between iterations. This original reference free alignment was used as a reference for further iterations.

The prepared references were used to perform a fresh alignment of the original particle stack using the `m-r-a` command which performs a set of multi-reference alignments, one after the other, which includes translational and rotational alignment. This was followed by `MSA-run`, `MSA-Classify` and `MSA-sum` as before. Fresh multi-reference alignments were performed after each iteration to avoid the additive interpolation of errors caused by multiple transformations. The resulting aligned image stack was used as input reference to the next round of alignment. The alignment strategy adopted involved multiple rounds of multi-reference alignment and classification. Poorly aligned particles were removed from the image stack using the `MSA-extract` command during subsequent iterations (Figure 4.5C). This procedure generated a final working image stack of 3,794 aligned particles. These aligned particles were then classified into 50 classes and separated into with or without eGFP using `MSA-extract`, producing a stack of 2,275 particles with eGFP and 1,519 particles without eGFP.

The particle stack containing those with eGFP was processed with Backtrace in RELION 3.0.7, a script that takes a particle stack and locates the original location of those particles (script written by Dr. Matthew Iadanza, University of Leeds). Essentially, it indicates the eGFP end of the particle (i.e. the N-terminus). Once particle polarity was assigned, particles were analysed in FIJI in several ways. Initially, the particle contour length and profile plot were measured using the segmented-line tool, and the particle end-to-end length was measure using the straight-line tool. The distance between bends and the bend angle were also measured using the straight-line tool and angle tool respectively.

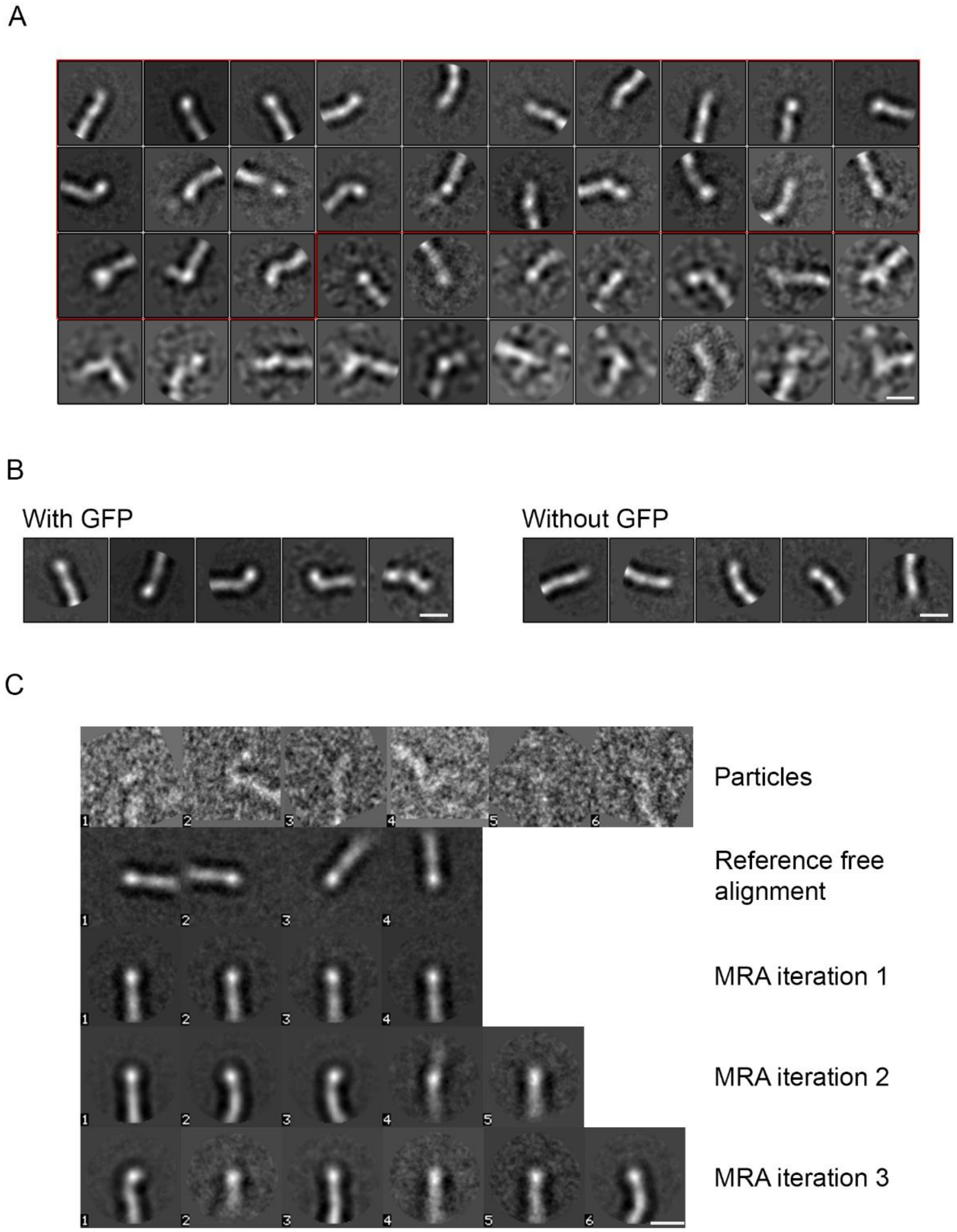

Figure 4.5 – Particle selection and analysis with RELION and IMAGIC.

(A) The selected particle dataset was subjected to iterative rounds of 2D classification and classified into 100 classes using RELION. The top 40 classes are shown with the top 23 classes (highlighted in red) being taken forward for processing. The remaining classes were discarded due to poor alignment. Scale bar = 10 nm. (B) Example classes of the re-classified particles either with or without eGFP as indicated. Scale bar = 10 nm. (C) IMAGIC image alignment and classification. Individual cantered particles (top) were classified by reference-free alignment prior to rotational translation and iterative multi-reference alignment using the previous iteration as a reference. A sample of each step is shown. Scale bar = 10 nm.

The profile plots were aligned to the peak of the eGFP molecule, as manual selection results in a small variance in the starting point. To smooth the data and to allow for analysis, a rolling average of 5 was used. The xy positions of the peaks following the eGFP peak were measured and used to calculate the peak-to-peak distance.

The distance along the particle at which a bend occurs was additionally measured. The frequency of the bends was plotted against the length and the data was described with multiple Gaussian functions by using the following formula:

$$Y = Ae^{-\left(\frac{(x-B)^2}{2C^2}\right)}$$

Where A is the hight of the function, B in the position, C in the full width at half maximum and e is natural log. The Chi squared was calculated by squaring the subtracted sum of the Gaussian functions from the data. To find the A, B and C that best describes the data, the Excel Solver add-in was used with the sum of Chi squared set as the objective to be minimum by changing the variables of all A, B and C values for each Gaussian function.

4.2.5 Model prediction and molecular dynamics of IQ32-52

Model building and molecular dynamics were performed by Dr. Glenn Carrington, University of Leeds. To build the IQ32-52 with calmodulin model, the 2.5 Å resolution structure of apo-calmodulin bound to IQ motifs 1 and 2 of murine myosin-5 (2IX7) was used as a template (Houdusse et al., 2006). The calmodulin bound to IQ2 was removed leaving a CaM+2IQ model. An alpha helix (-57 Φ, -47 Ψ) of the ASPM IQ heavy chain region (residues 2,019-2,536), with 23-23-27 spacing between the IQ motif cores was generated by chimera to yield the ASPM IQ model. Chimera was then used to superimpose the backbone atoms of the core IQ1 motif (IQXXXRGXXR) structure with bound calmodulin from the CaM+2IQ model onto the equivalent core IQ32 motif structure in the ASPM IQ model. This process was repeated for the each of the remaining IQ motifs ASPM IQ model (Figure 4.2). The 2IQ heavy chain from each of the CaM+2IQ models were deleted, leaving 21 calmodulins bound to the ASPM 21 IQ model, yielding the IQ32-52 model, which displays canonical calmodulin binding to the IQ motif at each IQ motif.

Implicit molecular dynamics (MD) simulations, using the General Borne Surface Area (GBSA) model were run with Amber16 molecular dynamics package using the ff14SB force field (Case et al., 2020). Using the IQ32-52 PDB model generated, the xLeaP tool in Amber was used to generate the topology and coordinate files necessary for the MD runs. The system was then minimized using a 5,000 steepest descent minimization steps followed by 2,500 conjugate gradient steps and then thermalized (300 K), whereby the temperature is increased in a stepwise manner with the constraining forces slowly moved over the number of steps. Shake (Ryckaert et al., 1977), found within the AMBER package, which constrains bond length, was used to constrain all bonds involving hydrogen atoms with a time step of 2 fsecs and a 10.0 Å cut-off for non-bonded interactions. Prior to the production run, an additional 100 psecs of equilibration steps at 300 K were performed, whereby the protein backbone atoms were restrained ($2.5\ \mathrm{kcal\ /\ mol{-}Å^2}$) to allow the side chain interactions to form. This was followed by unrestrained MD simulations that were performed at 300 K for 5 nsecs. The simulations were run on ARC4 supercomputer at the Leeds High Performance Computing facility.

4.2.6 Calcium sensitivity assays

To assess if calmodulin binds in a calcium dependent manner to the IQ motifs of ASPM, eGFP-IQ32-52 was co-expressed with CALM2 and MYL6B (Section 4.2.2). Frozen expression pellets were thawed on ice, and then resuspended in extraction buffer (10 mM MOPS, 200 mM NaCl, 10 mM $MgCl_2$, 1 mM EGTA, pH 8.0) supplemented with 10 μM Leupeptin, 2 mM PMSF. The cell suspension was then split into two equal volumes, to one, EGTA was added to a final concentration of 2 mM, to the other, $CaCl_2$ was added to a final concentration of 1 mM. The cells were lysed by hand with a Dounce homogeniser followed by centrifugation at 30,000 x g for 30 mins at 4°C in a Beckman Coulter Avanti J25 to clarify the lysate. The clarified lysate was then incubated with 4 mL anti-FLAG resin in a 5 mL disposable column (Thermo Fisher), equilibrated with extraction buffer, in suspension for 1-hour at room temperature before the column was washed extensively with 50 mL extraction buffer supplemented with either 2 mM final EGTA or 1 mM final $CaCl_2$. Protein was then eluted off the column with the addition of extraction buffer supplemented with 200 ng mL^{-1} 3xFLAG peptide (Sigma Aldrich). This eluted the eGFP-IQ32-52 protein as well as any light chains still bound to the IQ repeats. Samples from each stage were then analysed by SDS-PAGE as described (Section 2.6.6). Gel analysis was performed in FIJI using the ‘Gels’ analysis tools to plot histograms of the lanes which allowed for the area under the curve to be measured which indicated the quantity of sample present.

4.3 Results

4.3.1 Baculovirus expressions of the IQ motifs

All IQ constructs were successfully cloned into pFastBac1-eGFP as determined by PCR analysis (Figure 4.6A) and sequencing. PCR using the M13 primers demonstrated the successful transposition and generation of the bacmids (Figure 4.6B). PCR of an empty bacmid showed a band of 0.3 kbp as expected (Figure 4.6B).

Initial co-expression trials of eGFP-IQ32-52 with either CALM2, MYL6B, both CALM2 and MYL6B or neither CALM2 nor MYL6B indicated that the presence of a light chain is necessary for the stability of the IQ motifs. Cells expressing eGFP-IQ32-52 only either failed to express the construct or expressed a structurally unstable construct as no eGFP fluorescence was observed (data not shown). This fluorescence was recovered by co-expression with at least one light chain however, both light chains provided the greatest protein expression and yield (data not shown).

FLAG purified eGFP-IQ32-52 (Figure 4.7A) co-purified with CALM2 and MYL6B demonstrating that this IQ construct is able to bind to both light chains. The apparent mass of eGFP-IQ32-52 on the SDS-PAGE is ~60 kDa for the heavy chain which is lower than expected for eGFP-IQ32-52 (91 kDa). Bands of the expected size were observed for the two light chains; CALM2 and MYL6B, which co-purify with the IQ motifs. The estimated protein yield from this co-expression in 1 L of Sf9 cells was ~3.6 mg. FLAG-purified eGFP-IQ9-16 heavy chain also co-purified with both CALM2 and MYL6B, and the apparent mass of FLAG-purified eGFP-IQ9-16 heavy chain was also lower (~35 kDa) than expected (53.5 kDa) (Figure 4.7B).

In contrast, a short IQ50-52 construct, only co-purified with calmodulin, although it was co-expressed with both calmodulin and MYL6B (Figure 4.7C). The IQ50-52 band on the SDS-PAGE gel had the expected size of 39.2 kDa (Figure 4.7C).

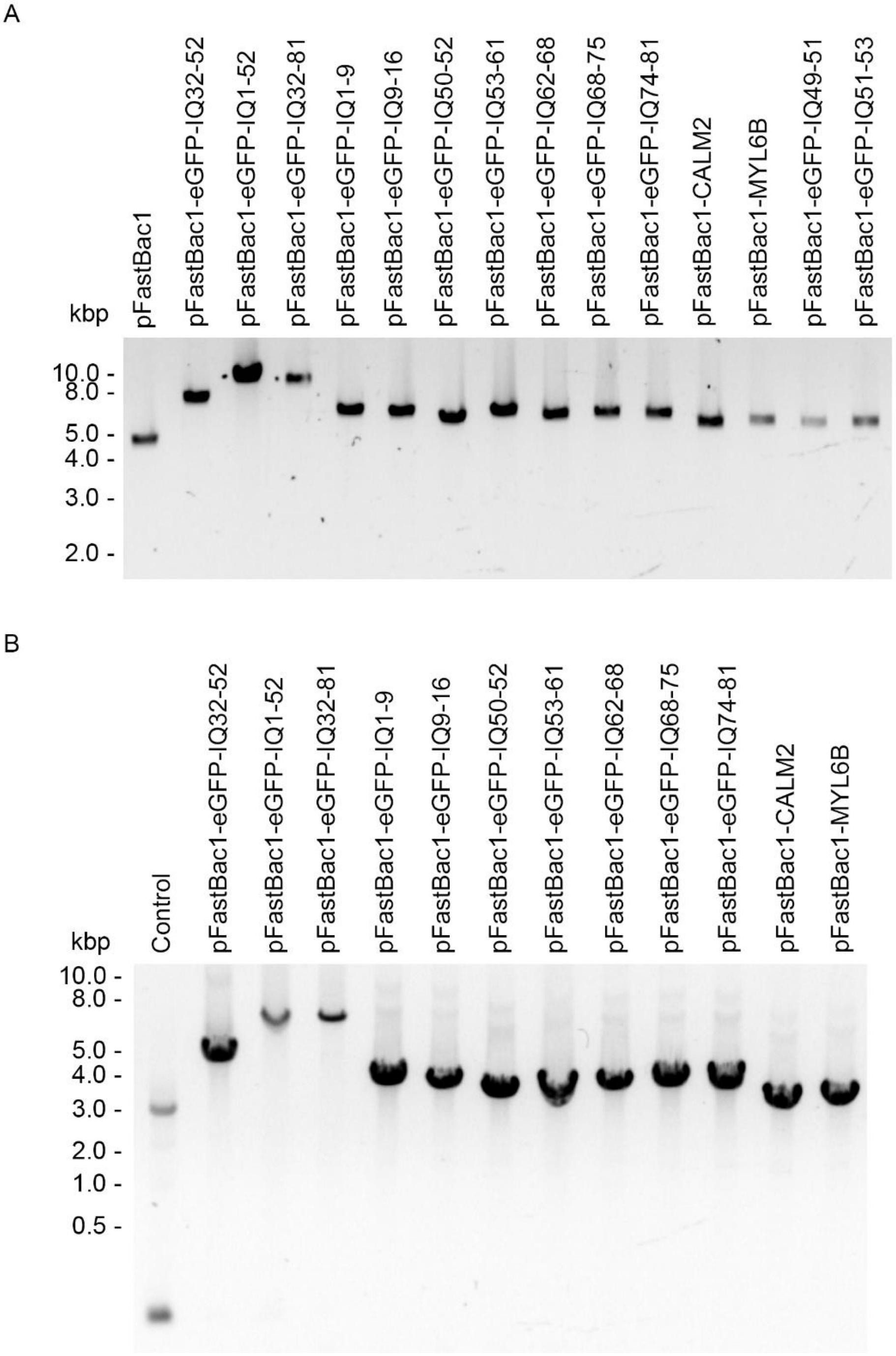

Figure 4.6 – Generation of IQ constructs in pFastBac1 and transposition of IQ bacmids confirmed by PCR.

(A) A 1.0% agarose gel of the purified IQ constructs and light chain constructs, expected plasmid sizes are listed in Table 4.1 (B) A 1.0% agarose gel of the PCR amplification product of the transposed IQ and light chain constructs with the M13 primers. A band size > 3.0 kpb indicates successful transposition, a band size of 0.3 kbp indicates unsuccessful transposition.

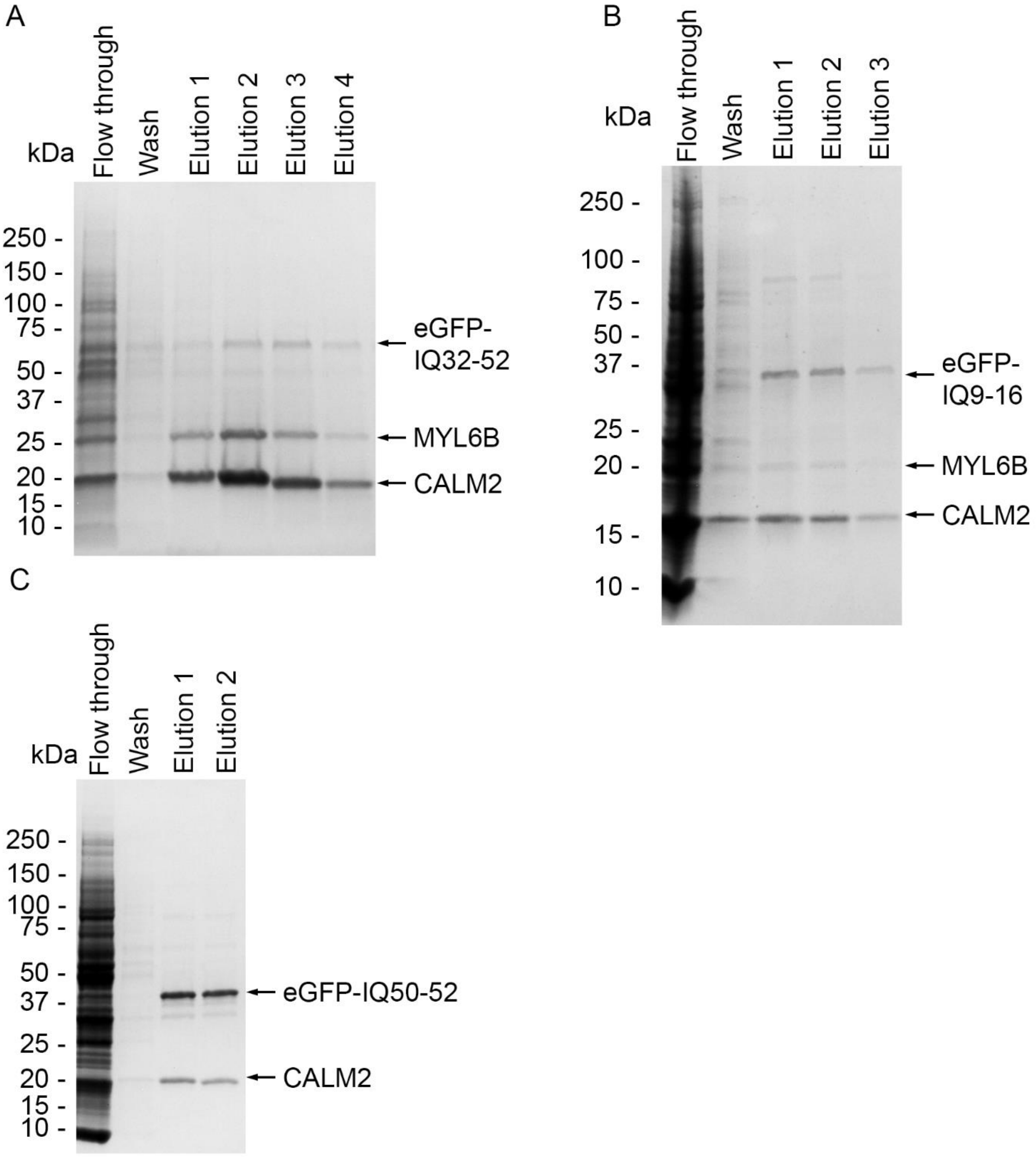

Figure 4.7 – Purification of IQ motifs.

(A) A 4-20% SDS-PAGE gel of eGFP-IQ32-52 co-expressed with CALM2 and MYL6B purified with anti-FLAG resin and eluted by competition with 3xFLAG peptide. Expected size eGFP-IQ32-53 is 91 kDa, band size observed is ~60 kDa. CALM2 has an expected size of 16.8 kDa and MYL6B of 22.8 kDa. (B) A 4-20% SDS-PAGE gel of eGFP-9-16 (expected size 53.5 kDa) co-expressed with CALM2 and MYL6B purified with anti-FLAG resin, eluted by competition with 3xFLAG peptide. (C) A 4-20% SDS-PAGE gel of eGFP-IQ50-52 (expected size 39.2 kDa) co-expressed with CALM2 and MYL6B purified with anti-FLAG resin.

4.3.2 IQ32-52 forms an elongated semi-flexible structure

Negative stain electron microscopy (nsEM) revealed that eGFP-IQ32-52 is an extended semi-flexible structure (Figure 4.8A). With a mean contour length (73.7 ± 5.1 nm, mean ± SD) consistent with the predicted length of an α-helix of this size (76.5 nm) (Figure 4.8B). The mean end-to-end length (direct measurement from one end to the other) was smaller (61.0 ± 8.6 nm, mean ± SD), suggesting the molecule is semi-flexible. The ratio between the total contour length and the end-to-end length is 1.23 ± 0.2 (mean ± SD). The semi-flexible nature of the IQ motifs did not allow for particle alignment via standard EM image processing methods. Interestingly, the appearance of the nsEM particles is similar to the model structures generated using molecular dynamics (Figure 4.8A). In the molecular dynamics simulation, many of the calmodulins (16 / 21) preferentially bound with one lobe only.

The polarity of a subset of particles was assigned successfully, confirmed by the clearly visible GFP molecule at one end of the particle and with a higher plot profile intensity as expected (Figure 4.8C). Plotting the intensity along the molecule and averaging across molecules showed the presence of 20 smaller peaks, which are likely to represent the bound light chains. This suggests that 20 of the 21 IQ motifs are occupied by light chains, and that the IQ motif 47 (IQ47) is likely to be unoccupied. The average peak-to-peak distance is 3.57 nm, which is in agreement with the estimated length of an IQ motif (3.45 nm).

The aligned eGFP-IQ32-52 particles showed that most had one (33%) or two (47%) bends, with a small number (5%) containing up to four (Figure 4.9A). The angles of these bends were mostly in the range of 121-140° (41%). A small number were more acute (as low as 44°) or obtuse (as high as 178°) (Figure 4.9B). A comparison of the angle size against position along the length does not show any trend, suggesting these angles are not fixed and are simply positions of increased flexibility (Figure 4.9C).

An analysis of the frequency of the bends and their position along the molecule (Figure 4.9D) indicated that there are 15 positions along the length of the molecule where the bends are most likely to occur (located in IQs 32, 33, 34, 36, 37, 38, 40, 41, 42, 43, 44, 45, 46, 47 and 49). Further analysis showed that most of the bends (10 / 15 – IQs 32, 33, 37, 38, 40, 41, 42, 43, 46 and 49) occur within the central portion of an IQ motif. These positions were used to estimate which residue within the IQ motif was present at the bend position. Most commonly the residue was either lysine (4), arginine (4) or histidine (1).

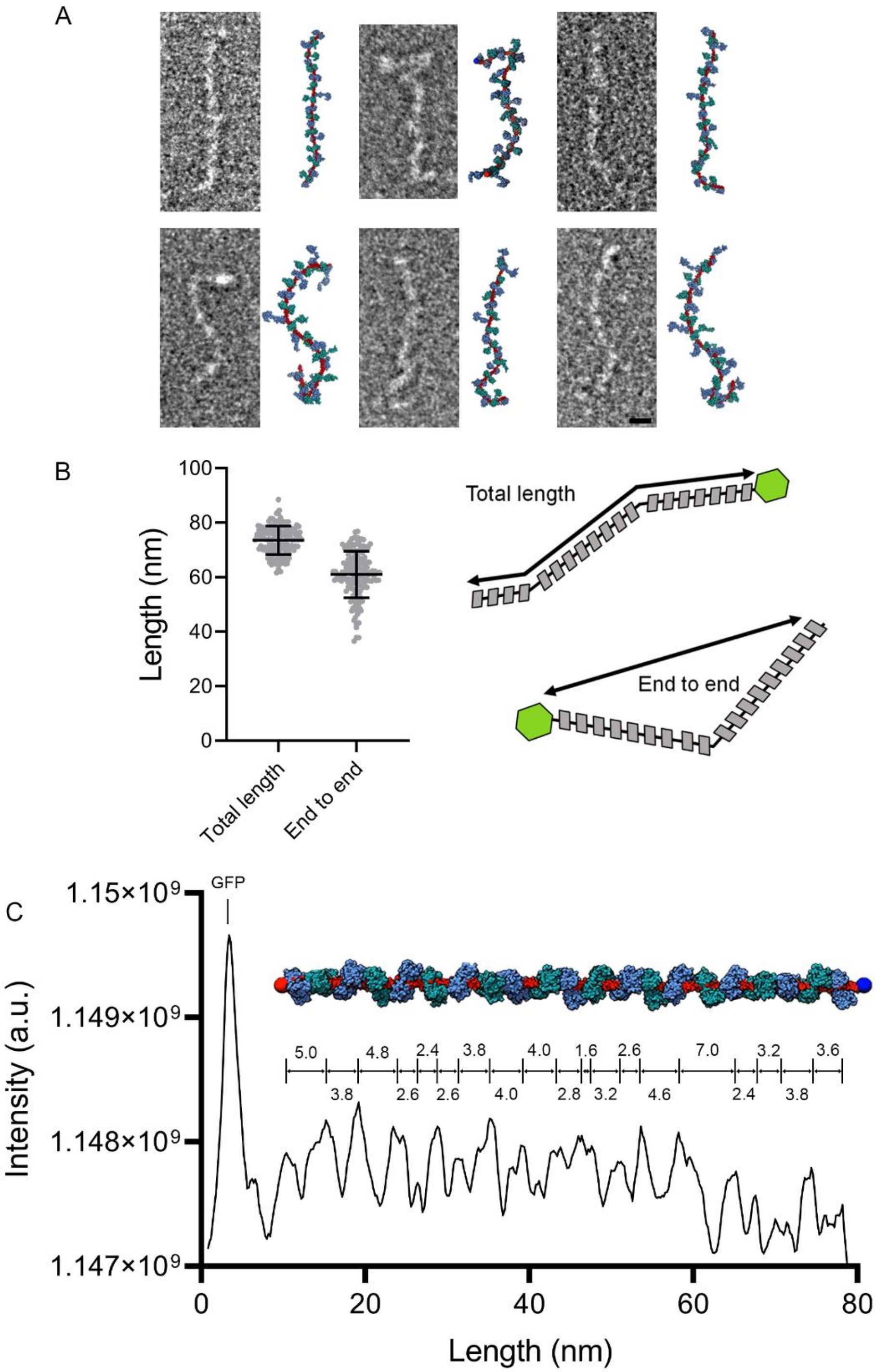

Figure 4.8 – Model comparison, length analysis and light chain prediction of the IQ32-52 construct.

(A) A selection of negative stain EM particles alongside snapshots from molecular dynamics modelling of the same IQ construct. Scale bar = 10 nm. (B) Measurements of total (contour) and end-end length of eGFP-IQ32-52, as diagrammed, n=149. (C) Mean plot profile analysis of the signal intensity along eGFP-IQ32-52 molecules, n=149. The model structure and expected lengths for each individual IQ motif are shown for comparison.

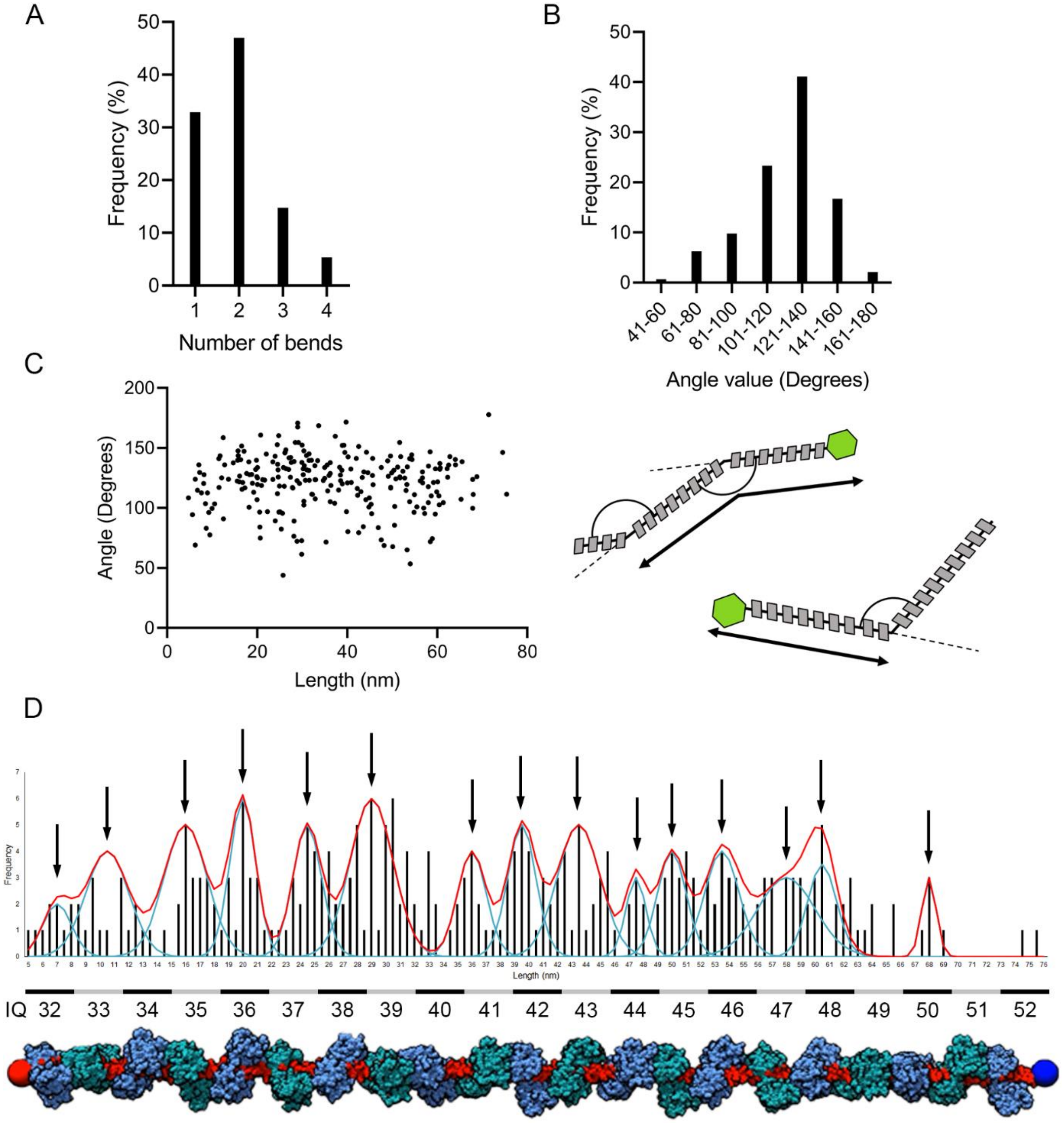

Figure 4.9 – Bend and angle analysis of IQ32-52.

(A) The number of bends per molecule, n=149. (B) The range of angles that occur along eGFP-IQ32-52, n=287. (C) The angular change plotted against length of eGFP-IQ32-52, measurements as diagrammed, n=287. (D) The frequency of the positions of angles along the length of the molecule, described using multiple Gaussians (Gaussian functions in blue and sum of Gaussians in red). Peaks (arrowed) indicate the positions where bends can occur along the length of the molecule. The majority of these bends align with the centre of an IQ motif as shown by the aligned MD model, n=286.

4.3.3 Calmodulin Ca^{2+} sensitivity in IQ motif binding

Experiments in the presence and absence of Ca^{2+} suggest calmodulin binding to the IQ motifs of IQ32-52 is sensitive to Ca^{2+} levels. When the IQ domain construct was eluted in the absence of Ca^{2+} (EGTA), both CALM2 and MYL6B co-eluted with the heavy chain. However, in the presence of Ca^{2+}, MYL6B was absent, and the levels of calmodulin that co-eluted were lower. The concentration of calmodulin decreased by 0.48 fold for elution 1 and by 0.52 fold for elution 2 (Figure 4.10) In contrast to this, the level of free GFP increased in the presence of Ca^{2+} when compared to the absence of Ca^{2+} (EGTA) (3.44 and 1.36 fold change for elution 1 and 2 respectively) (Figure 4.10).

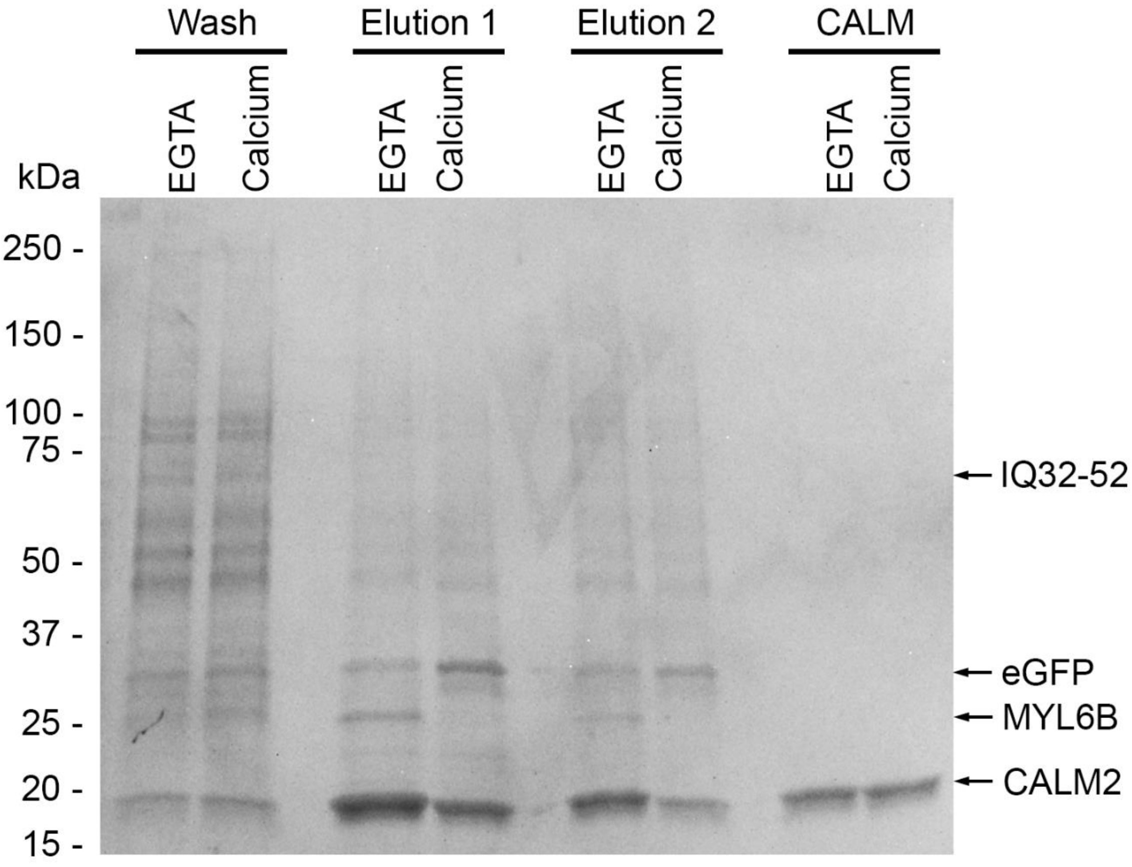

Figure 4.10 – Calcium sensitivity of the light chains of the ASPM IQ motifs.

A 4-20% SDS-PAGE gel of the IQ32-52 motifs co-expressed with CALM2 and MYL6B light chains incubated with calcium or without calcium (EGTA). Showing the wash, the first FLAG elution, the second FLAG elution and a Calmodulin (CALM) only lane. Arrows indicate CALM2, MYL6B, free eGFP and eGFP-IQ32-52.

4.4 Discussion

The results shown here demonstrate that the central 21 IQ motifs of human ASPM forms a semi-flexible, elongated structure. Moreover, full length IQ32-52 co-purified with both calmodulin and MYL6B light chains, suggesting that the IQ motifs can bind to both light chains. The lengths of the IQ constructs analysed from nsEM images (73.7 ± 5.1 nm, mean ± SD) are the expected length for this construct (76.5 nm), and the IQ constructs appear to bind light chains along their length, with the exception of IQ47. The heavy chain runs faster than expected for a globular protein on a gel (~60 kDa verses 90 kDa), possibly due to a larger ratio of bound SDS, an effect also seen in α-helical membrane proteins (Rath et al., 2009).

The finding that the central IQ32-52 domain is an elongated, semi-flexible structure, fully decorated by light chains is interesting. This is the first time such a long IQ motif with bound light chains has been visualised. It is tempting to speculate that the full length 81 IQ domain could also form an elongated structure. If fully elongated, it could be ~295 nm in length, separating the N- and C-terminal regions of ASPM by some distance. It is unknown if it forms this elongated structure in the intact protein when organised into the pericentrosomal matrix of the mitotic spindle or in the midbody. The longest IQ motif studied to date is that of myosin-5, which comprises 6 IQ motifs and forms a stiff lever (Terrak et al., 2005). In myosin-5, the 6 IQ motifs are spaced at intervals of 23-25-23-25-23-25 along the lever helix (Shen et al., 2016). Mutating the lever to a 23-23-23-23-23-23 repeat did not prevent calmodulin binding consistent with the finding here that all the IQ motifs can be occupied in a 23-23-27 repeat (Revill, 2013).

Intriguingly, a shorter construct (IQ50-52, 23-23-27 residue pattern) only bound calmodulin and not MYL6B. It is possible that MYL6B prefers to bind the 27 residue IQ motif, and that it tends to detach if a subsequent 23 IQ motif is absent. Extending the C-terminal sequence of the heavy chain might solve this problem. This will be interesting to test in the future.

The molecular dynamics suggested that calmodulin may only bind to the IQ motif with one lobe (the C-lobe) (Figure 4.8A). In this simulation, this was found for 16 of the 21 calmodulins. Previous simulations of calmodulin interactions with IQ motifs have demonstrated a similar result (Lai et al., 2015) and the interaction of Apo-calmodulin with the IQ motifs of myosin is mostly mediated through the C-lobe of calmodulin. The resolution of nsEM was not sufficient to detect the details of light chain binding to the IQ motifs, or to determine if the interaction of calmodulin is predominantly mediated by the C-lobe, but this would be interesting to follow up in future experiments.

While most IQ32-52 molecules appeared to have two bends, there does not appear to be a specific region along the molecule where the bends occur. Instead, there appeared to be at least 15 positions along the sequence where a bend could occur. Moreover, the angle of these bends is variable. It is likely that the sites of bends are sites of increased flexibility with a range limited by the steric hindrance of the neighbouring light chain as described previously for the calmodulin binding to unconventional myosins (Houdusse et al., 1996). The data shown here (Figure 4.9C) for ASPM suggests that there are no specific sites in which flexibility is restricted and no distinct change in range of angles along the IQ construct.

As there is considerable similarity of the IQ motifs in ASPM with those in myosin, the expectation is that calmodulin binds to these motifs in the absence of Ca^{2+} (Apo-calmodulin) but could detach in the presence of high Ca^{2+} concentrations at specific IQ motifs. In myosins, Ca^{2+} can result in the dissociation of one or more calmodulins (e.g. myosin-5, myo1c) or adoption of a more flexible structure without loss of calmodulin (myo1c) (Lu et al., 2015). The experiments here suggested that Ca^{2+} affected the ability of calmodulin to bind the IQ motifs. The ~0.5-fold change seen suggests that half of the calmodulin detach in the presence of Ca^{2+}, however, MYL6B also appeared to detach. This could be due to the stability of the eGFP-IQ32-52 construct being compromised evidenced by the increase in free eGFP, likely due to breakages in the flexible linker between the eGFP and the IQ motifs. It will be interesting to follow up on whether the calmodulins detach at specific regions and whether this has an effect on structure in future experiments.

The IQ motifs tested here also show the ability to bind to MYL6B which contains an N-terminal extension. This N-terminal extension has been shown to interact with actin in the myosin A1 light chain (MYL1), a homologue of MYL6B, when the myosin head is bound to actin (Logvinova & Levitsky, 2018) and with the motor domain when detached from actin. This raises the intriguing possibility that MYL6B could bind to actin, when ASPM is in actin rich regions, such as the cortex and midbody. This is another finding that will be interesting to follow up on in future experiments.

In summary, this data shows that the central IQ motifs of ASPM form an elongated semi-flexible structure that binds multiple light chains. In the future it will be interesting to investigate the IQ motifs along the whole length of the IQ domain by EM to compare the overall structure, and to determine if Ca^{2+} binding affects calmodulin and light chain binding. Crystal structures of shorter

(3IQ) constructs would reveal how the light chains (calmodulin and MYL6B) bind to the IQ motifs, and if this binding is mediated by an APKK motif.

5. Developing tools to observe the localisation of endogenous ASPM.

5.1 Introduction

Determining the location of ASPM is currently limited to using immunofluorescence staining of fixed cells or live cell imaging of fluorescently labelled fragments of ASPM transfected into cells. It would be advantageous to observe the behaviour of endogenous wild-type and mutant ASPM in live cells to determine its dynamic behaviour during cell division. Recent advancements in CRISPR (clustered, regularly interspaced, short palindromic repeats)-Cas (CRISPR-associated protein) allow for stable genetic manipulation of cells. Fluorescent tags can be introduced into the endogenous gene enabling live cell imaging. The specific nature of CRISPR makes it ideal for direct genome editing. A number of different CRISPR-Cas approaches have been described, of which three different approaches were used here (Kamiyama et al., 2016; Ran et al., 2013; Sakuma et al., 2015).

The first aim of this chapter was to attempt to use CRISPR technology to tag the endogenous ASPM protein with a fluorescent protein. Using single guide RNA (sgRNA) directed Cas9, cDNA encoding the fluorescent tag of choice was inserted into either the N- or C-terminus of the *ASPM* gene using homology driven repair (HDR). Three fluorescent tags were chosen based upon their distinct characteristics. First, eGFP to visualise ASPM and determine binding partners using pull-down assays with the anti-GFP-nanobody. Second, mEos3.2 a photoconvertible fluorescent protein used in PALM (photoactivatable light microscopy). Inducing the switch from green to red fluorescence can be used to determine dynamic behaviour in live cells, and for single molecule fluorescence ‘super-resolution’ imaging in fixed cells. Third, mEos4b, an improved version of mEos3.2, which is suitable for correlative light and electron microscopy imaging (Zitter et al., 2019).

In the first CRISPR method, purified Cas9 and a shorter repair template were used. As CRISPR/Cas9 gene modification can be more successful with shorter repair templates, a split GFP system was also tested. In this approach, the 11th β-strand of GFP is used to tag the endogenous protein, in cells that express a non-fluorescent GFP construct containing β-strands 1-10 (GFP1-10). The 11th strand interacts with the non-fluorescent GFP construct to regenerate the fluorescent protein. This approach has been used successfully to tag tubulin and clathrin

(Kamiyama et al., 2016). Inserting the 11th strand of GFP into the *ASPM* gene, should, in principle, increase the likelihood of correct insertion into the DNA break (Leonetti et al., 2016).

In the second approach, Cas9 was supplied to the target cell as a vector along with a longer repair template of full-length fluorescent protein (eGFP, mEos3.2 or mEos4b) flanked by 1.0 kbp of homology arms to aid in directing homologous repair (Merkle et al., 2015; Ran et al., 2013; Yang et al., 2013).

The third approach involved a collaboration with Tetsushi Sakuma (Hiroshima University, Japan). This approach does not rely upon the cells' natural repair mechanisms and a 1.0 kbp homology arm, instead a 40 bp microhomology sequence and a CtIP repair enhancer promotes microhomology-mediated end-joining (MMEJ) (Sakuma et al., 2016).

In complementary experiments, an Affimer was raised against the CH domains of ASPM to allow visualisation of the endogenous protein. Affimers are small, non-antibody binding proteins that can be used in the same way as antibodies (Carrington et al., 2019). They can also be fused to a fluorescent tag and used to visualise proteins in live cells (Lopata et al., 2018). Raising Affimers to ASPM thus could also be useful in visualising ASPM in fixed and in live cells and was the second aim of this chapter.

5.2 Methods

5.2.1 Ribonuclear particle (RNP) method

Three different CRISPR-Cas9 approaches were used in the attempt to tag the endogenous protein with a fluorophore. The first to these was the ribonuclear particle (RNP) method, in which first cells that express split-GFP (GFP1-10) are generated, the Cas9 protein is then expressed and purified. Purified Cas9 bound to sgRNA and a HDR template (GFP-11 sequence flanked by 70 bp of genomic DNA homology) are then transfected into live cells via electroporation. The Cas9 then cleaves a specific sequence of DNA directed by the sgRNA, and the cell then repairs that DNA break using the HDR template, thus inserting the additional GFP-11 sequence into the gene of interest (Figure 5.1) (Kamiyama et al., 2016; Leonetti et al., 2016).

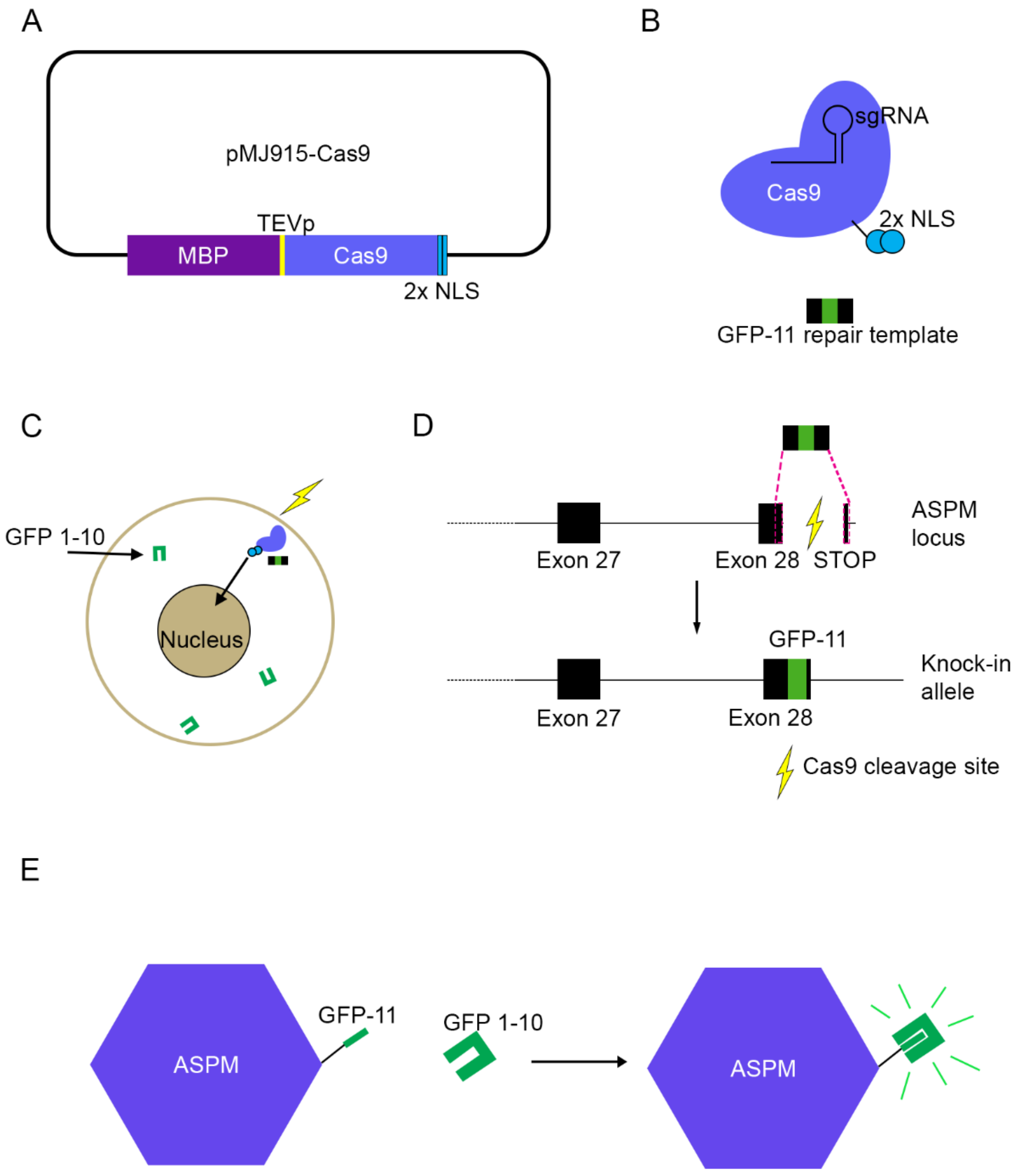

Figure 5.1 – The ribonuclear particle (RNP) method.

(A) A schematic of the pMJ915-Cas9 plasmid. TEVp: Tobacco etch virus protease, NLS: Nuclear localisation signal. (B) Once expressed and purified, Cas9 is incubated with a specific single guide RNA (sgRNA) to create the RNP and a single stranded DNA homology repair template (HRT) designed to introduce the 11th stand of split GFP (GFP-11) into the cleavage site. (C) The RNP and HRT are electroporated into cells stably expressing GFP1-10 where the 2x NLS direct the RNP into the nucleus. (D) Once in the nucleus, Cas9 (directed by the sgRNA to the C-terminus of ASPM) cleaved the genomic DNA and the cell repairs the damage using the HRT as a reference thus inserting GFP-11. (E) GFP-11 tagged ASPM is only fluorescent when GFP1-10 is bound.

5.2.1.1 Expression and purification of Cas9

Cas9 protein containing two C-terminal SV40 nuclear localisation signals (NLS) and tagged with an N-terminal Tobacco Etch Virus protease (TEVp) cleavable 6xHis-Maltose Binding Protein (MBP) tag, was overexpressed in BL21 Rosetta 2 (DE3) strain of *E. coli* from the pMJ915-Cas9 plasmid (a kind gift from Martin Jinek; Addgene plasmid #69090;(Lin et al., 2014)) (Figure 5.1A). The cells were grown in 2x TY (Tryptone Yeast; 16 g Tryptone, 10 g Yeast Extract, 5 g NaCl per Litre) medium at 37°C to an OD600 of between 0.6 and 0.9 before being induction with 0.2 mM IPTG and incubated at 18°C for 16 hours. The protein was purified by affinity chromatography followed by ion exchange. Briefly, 1 L of cells were pelleted then lysed in 20 mL lysis buffer (20 mM Tris, 500 mM NaCl, 1 mM DTT, pH 8.0 (supplemented with protease inhibitor cocktail, 10 mM $MgCl_2$, 500 units Benzonase)) in a Dounce homogeniser, before the lysate was clarified at 20,000 x g for 30 mins in a Beckman Coulter Avanti J25 centrifuge. The clarified lysate was bound to 2 mL Nickel-Nitrilotriacetic acid (Ni-NTA) agarose in a 5 mL disposable column (Thermo Fisher) and washed extensively with 50 mL wash buffer (20 mM Tris, 500 mM NaCl, 10 mM Imidazole, pH 8.0) before being eluted serval times with 2 mL elution buffer (20 mM Tris, 250 mM NaCl, 250 mM Imidazole, pH 8.0).

The 6xHis-MBP affinity tag was removed from Cas9 by cleavage with TEV protease (Section 2.6.4) while the protein was dialysed overnight against 2 L 20 mM HEPES ((4-(2-hydroxyethyl)-1-piperazineethanesulfonic acid)), 150 mM KCl, 1 mM DTT, pH 7.5 at room temperature. The cleaved Cas9 was separated from the fusion tag and protease by ion exchange on a 5 mL SP Sepharose HiTrap column (GE Healthcare) connected to an ÄKTA prime FPLC system (GE Healthcare). Bound Cas9 was eluted with a gradient from 100 mM to 1 M KCl, in 20 mM HEPES, pH 7.5. Fractions containing Cas9, confirmed by SDS-PAGE, were pooled and dialysed against 20 mM HEPES, 150 mM KCl, 1 mM DTT, pH 7.5 at 4°C overnight. Cas9 was concentrated to 8 mg mL^{-1} in a 50,000 MWCO VivaSpin 6 protein concentrator and stored in 20 mM HEPES, 150 mM KCl, 1 mM DTT 10% glycerol, pH 7.5 at -80°C.

5.2.1.2 Synthesising single guide RNA (sgRNA) for Cas9 RNP to the target C-terminus of ASPM

Single guide RNA (sgRNA) was designed by locating suitable protospacer adjacent motifs (PAM; NGG, where N is any base) in the C-terminal region of ASPM. Once selected, 20 nt upstream were used as the target for the sgRNA and assessed for off-target effects *in silico* using the Off-Spotter tool (cm.jefferson.edu/Off-Spotter/) and ensuring there were no less than 4 mismatches (Pliatsika & Rigoutsos, 2015).

To synthesise sgRNA, a DNA template encoding a T7 promoter, the 20 nt target sequence and an sgRNA scaffold was assembled from ssDNA oligonucleotides by overlapping PCR (protocol adapted from (Steven Lin et al., 2014)). The PCR reaction contained 200 nM premix of gRNA Forward Long and gRNA Reverse Long primers (see Table 5.1 for sequences), 2 μM premix of gRNA Forward and gRNA Reverse primers, 400 μM dNTPs and Phusion polymerase (NEB) according to manufacturer's protocol. The thermocycler setting consisted of 31 cycles of 95°C for 15 secs, 57°C for 15 secs and 72°C for 15 secs. The PCR products were purified using a Zymo DNA Clean & Concentrator-5 (Zymo Research) following the manufacturer's instructions, eluting RNA with RNase free $_dH_2O$.

Prior to *in vitro* RNA transcription, all surfaces and equipment were wiped thoroughly with RNase AWAY (Sigma-Aldrich). A 20 μL T7 *in vitro* transcription reaction consisted of 5 nM of each ribonucleotide triphosphate, 1x T7 Reaction Buffer (NEB), 250 ng template DNA and 100 units T7 RNA Polymerase (NEB). The reaction was incubated at 37°C for 4 hours and 5 units of RNase-free DNase I (NEB) was added to digest template DNA at 37°C for 15 mins. The reaction was stopped by the addition of 500 mM sodium acetate (pH 5.0), to a total volume of 150 μL. The RNA was purified by precipitation by the addition of 2 volumes (300 μL) 100% ethanol and incubated at -20°C for 15 mins. The RNA pellet was collected by centrifugation at 17,000 x g for 10 mins using a MICRO STAR 17R (VWR) centrifuge. Supernatant was removed and the pellet washed 3 times with 70% ethanol before air drying for 10 mins. RNA pellet was resuspended in Cas9 buffer (20 mM HEPES, 150 mM KCl, 1 mM DTT 10% glycerol, pH 7.5) and stored at -80°C.

5.2.1.3 Cas9 ribonucleoprotein (RNP) production and sgRNA specificity

To test activity of the purified Cas9, a short (3.5 kbp) DNA bait of the C-terminus of ASPM (8,414-10,424 nt + 1,485 bp of plasmid backbone) was first generated from pcDNA3.1-ASPM vector by PCR (using primers listed in Table 5.1).

The Cas9 RNP was generated by incubating 100 pmol Cas9 with 120 pmol sgRNA in Cas9 buffer supplemented with 1 mM $MgCl_2$ at 25°C for 10 mins. Cas9 activity and sgRNA specificity was determined by incubating the RNP with 200 ng DNA bait and incubating at 37°C for 15 mins. The RNP was digested with 1 Unit proteinase K at 57°C for 10 mins prior to analysis on a 1 % agarose gel (as in Section 2.2.5).

5.2.1.4 GFP1-10 polyclonal antibody production and analysis

HEK293T cells stably expressing GFP1-10 fragment were generated by Alice Lake, University of Leeds. To create the cell line, HEK293T cells were stably transduced with GFP1-10 by lentiviral infection (pHR-SFFV-GFP1-10; Addgene # 80409) based on a previous method (Kamiyama et al., 2016). To confirm that the GFP1-10 fragment has been correctly knocked into HEK293T cells, an antibody specific to the non-fluorescent split-GFP was used to confirm the isolated clones.

To generate the antibody to split-GFP, the hybridoma cell line, GFP-G1 (Yamagata & Sanes, 2012), was purchased from Developmental Studies Hybridoma Bank (DSHB) and cultured in Iscove's Modified Dulbecco's Medium (IMDM) with L-glutamine and HEPES (supplemented with: 20% heat inactivated FBS; 2 mM L-glutamine; 1 mM sodium pyruvate; 0.05 mg mL^{-1} gentamicin; 10 U mL^{-1} penicillin and 0.01 mg mL^{-1} streptomycin) at 37°C, 5.0% CO_2. For expression of antibodies, serum-free medium was used. The antibody was collected by clarifying the medium from the cultured cells by centrifugation at 3,000 x g for 15 mins and stored at -20°C in 50% glycerol.

The presence and specificity of the anti-split-GFP antibody, which also recognises full-length GFP, was assessed by immunostaining GFP expressing Sf9-ET cells. Briefly, Sf9-ET cells were infected with baculovirus (to produce GFP). At 48 hours PI (post infection), cells were fixed with 4% paraformaldehyde and permeabilised with PBS, 1% BSA, 0.1% Triton X-100 before blocking in 5% BSA. Blocked cells were then incubated with undiluted GFP-G1 for 1 hour. Cells were then washed in PBS prior to a 1-hour incubation goat anti-mouse Alexa Fluor 546 (Invitrogen, #A-

11003; 1:400) and DAPI (1:500). After the final staining step, coverslips were washed in PBS, and mounted onto glass microscope slides in ProLong Gold Antifade (Thermo Fisher Scientific). Cells were imaged on a DeltaVision Widefield Deconvolution microscope (Section 2.5.3).

5.2.1.5 Electroporation of HEK293 cells with the Cas9 RNP

The Cas9 RNP was electroporated into HEK293 cells using an Amaxa cell line Nucleofection kit R (Lonza). 2x10^6 cells were resuspended in 900 µL of pre-warmed Opti-MEM and the Cas9 RNP was added along with 400 ng of GFP-11 HDR template: (TGGAAGAAATCACAAATCCCCTGCAAGCTATTCAAATGGTGATGGATACGCTTCGCATTCCTTATGGTGGCTCTGGAGGTCGTGACCACATGGTCCTTCATGAGTATGTAAATGCTGCTGGGATTACATAGTAAATGTAAACATTTTCAGTATGTATAGTGTAAAGAAATATTAAAGCCAATCATGAGTACGTAA). The cell / RNP suspension was transferred to an electroporation cuvette and placed in the Amaxa Nucleofector II (Lonza) and the cells were electroporated using the HEK293 (DSMZ) setting (A-023) (as determined by prior optimisation). After electroporation, 500 µL of DMEM supplemented with 20% FBS was immediately added and the cells seeded in a well of a 6-well plate. The cells were incubated at 37°C, 5.0% CO_2 for 72 hours before assessing for GFP on an EVOS Cell Imaging System (Thermo Fisher).

5.2.2 Dual-plasmid method

The second approach to tagging endogenous ASPM with a fluorescent molecule was the dual plasmid method (Ran et al., 2013). Briefly, sgRNA directed to either the N- or C-terminus of ASPM is cloned into the pSpCas9-2A-Puro plasmid and together with a homology driven repair (HDR) plasmid that contains the cDNA of a fluorescent protein flanked by 1.0 kbp of gene of interest homology are transfected into HEK293 cells (Figure 5.2).

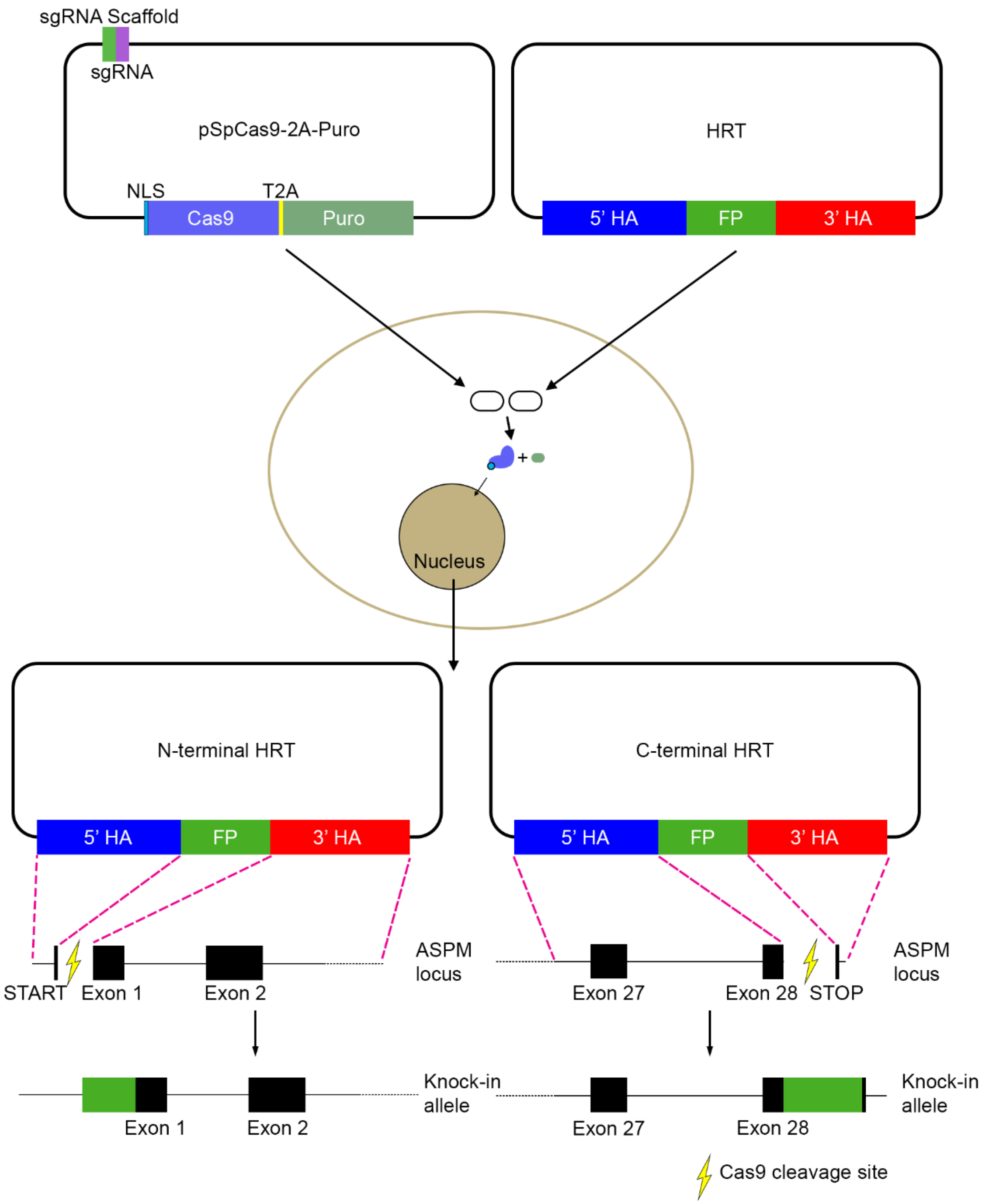

Figure 5.2 – The Dual-plasmid method.

Two plasmids, one containing the Cas9 and sgRNA sequence and one containing the homology driven repair template (HRT), which contains the sequence for a fluorescent protein (FP) and two 1.0 kbp homology arms (HA), are co-transfected into a cell. There, the Cas9, directed by the sgRNA, causes a double strand break at either the N- or C-terminus of the ASPM locus. The cell then repairs the break with the aid of the HRT thus inserting the FP into the genome.

5.2.2.1 Single guide RNA cloning into Cas9 plasmid to target either the N- or C- terminus of ASPM

To insert the sgRNA sequence into the Cas9 plasmid, 1 µg of pSpCas9-2A-Puro plasmid (Addgene #62988) was initially simultaneously digested with 10 Units BbsI and phosphorylated with 5 Units Calf Intestinal Phosphatase (CIP) in 1x CutSmart buffer (NEB) at 37°C for 30 mins. Digested plasmid was then separated on a 0.7% agarose gel (Section 2.2.5) and extracted from the gel (Section 2.2.6). To create the sgRNA sequence, two ssDNA oligos were phosphorylated and annealed (primer listed in Table 5.1). 10 µM of each ssDNA oligo (sgRNA forward and sgRNA reverse for both the N- and C-terminal targets) was incubated with 5 Units T4 Polynucleotide Kinase (NEB) in 1x T4 Ligation Buffer (NEB) in a thermocycler at 37°C for 30 mins, followed by 95°C for 5 mins and then cooled to 25°C at -5°C min^{-1}. A ligation reaction consisting of 50 ng digested plasmid and 5 nM annealed oligoes (ratio Vector:Insert of 1:6.25) in 1x Quickligation Buffer (NEB) was incubated with 400 Units Quick Ligase (NEB) at room temperature for 10 mins before being transformed into NEB 5α *E. coli* cells (Section 2.2.14).

5.2.2.2 Cloning of the Homology Driven Repair (HDR) template for inserting a fluorescent protein into the N- or C-terminus of ASPM

In order to create the HDR template, homology arms (HA) were first amplified by PCR, from genomic DNA (gDNA) (primers listed in Table 5.1). Briefly, gDNA was isolated from HEK293 cells. Trypsinised HEK293 cells were harvested from a 70% confluent T-75 flask (as in Section 2.4.2), pelleted by centrifugation at 1,000 x g for 5 mins in a Harrier 18/80 (MSE) centrifuge, then resuspended in nuclei lysis buffer (10 mM Tris, 0.4 M NaCl, 2 mM EDTA, pH 8.0). Cells were lysed by the addition of 0.6% SDS final and 40 Units proteinase K (NEB) and incubation at 37°C overnight. Proteins were salted out by the addition of 2 M NaCl final and centrifuged at 4,500 x g for 15 mins using a MICRO STAR 17R (VWR) centrifuge. Supernatant was transferred to an equal volume of ice-cold isopropanol to precipitate gDNA and centrifuged at 4,500 x g for 15 mins using a MICRO STAR 17R (VWR) centrifuge. The gDNA pellet was washed twice with 70% ethanol and resuspended in 100 µL TE buffer.

The fluorescent protein inserts (mEos3.2, eGFP or mEos4b) were amplified by PCR. The three DNA fragments (5’HA, 3’HA and fluorescent protein) were inserted into the BamHI-EcoRI sites of pFastBac1 using NEBuilder (Section 2.2.9). Two µL of the cloning reaction was then transfected into NEB10β competent cells (Section 2.2.14). Four HDR templates were created: N-terminal mEos3.2, N-terminal eGFP, N-terminal mEos4b and C-terminal mEos3.2. Cloning was confirmed by sequencing (Source Bioscience) and restriction digest on a 1% agarose gel.

5.2.2.3 Co-transfection of CRISPR plasmid and HDR template into HEK293 cells and isolation of cells

Both the Cas9 plasmid and the HDR template were co-transfected into HEK293 cells with Fugene HD lipofectamine (Section 2.4.5). 24 hours post-transfection, cells containing the Cas9 plasmid were selected for by the addition of 2 µg mL^{-1} puromycin for 72 hours. (The puromyocin concentration used was based on a previous puromycin selectivity screen). Puromycin was then removed, and surviving cells were trypsinised and counted. 100 cells were plated on a 15 cm tissue-culture treated dish (Corning) (following protocols outlined in Section 2.4) to allow growth of individual clones over the next 7 days.

After 7 days, individual clones were then examined for fluorescence using the 10x objective lens (NA 0.25) on a Nikon TMD Diaphot phase contrast inverted microscope fitted with a CoolLED pE-300 illumination system. Individual fluorescent clones were isolated using a cloning ring fashioned from the wide end of a p200 pipette tip, tightly secured to the TC plate with petroleum jelly. Cells inside the cloning ring were dissociated from the plate by adding 20 µL TrypLE to the cloning ring, incubating for 5 mins and then transferring the dissociated cells to a well of a 24-well plate containing 2 mL pre-warmed media.

Cells were then cultured for 48 hours prior to cell sorting with a FACSMelody cell sorter (BD Biosciences). Briefly, individual colonies were removed from the 24-well plate separately with 1 mL TrypLE and pelleted at 1,000 x g for 5 mins in a Harrier 18/80 (MSE) centrifuge. Supernatant was removed and cells were resuspended in FACS media (DPBS supplemented with 25 mM HEPES, 1 mM EDTA, 2% FBS, pH 7.4) to a concentration of 5x10^{6} cells mL^{-1} and stored on ice. Cells were sorted based on fluorescence intensity above a set threshold selected based upon the background fluorescence of un-transfected HEK293 cells. Ten cells per well were sorted into a 96-well plate containing 100 µL pre-warmed medium per well. Cells were then cultured for a further 7 days before being analysed for fluorescence a second time on the Nikon TMD Diaphot microscope.

Living and fixed fluorescent cells were analysed using a Delta Vision Widefield Deconvolution microscope and the 100x oil objective (NA 1.4) using SoftWoRx software for image acquisition, and using the Zeiss LMS880 Inverted Confocal + Airyscan, using the 63x oil objective (NA 1.4).

To confirm correct insertion of fluorescent proteins, gDNA from the knock-in cells were isolated (Section 5.2.2.2), and the corresponding region was amplified by PCR using the appropriate primers (Table 5.1). PCR products were then analysed on a 1% agarose gel (Section 2.2.5).

Table 5.1 – The primers used for generating sgRNA, Cas9 bait and HDR template plasmids.

Primer name	Sequence (5' - 3')	Use	Annealing temp (°C)	Restriction site
gRNA For	TAATACGACTCACTATAGGCAAATG	C-term Guide RNA production for Cas9 Ribonuclear Particles (RNP)	57	-
gRNA Rev	AAAAAAAGCACCGACTCGGTGC			-
gRNA For Long	TAATACGACTCACTATAGCAAATGGTGATGGATACGCTGTTTAAGAGCTATGCTGGAAACAGCATAGCAAGTTTAAATAAGG			-
gRNA Rev Long	AAAAAAAGCACCGACTCGGTGCCACTTTTTCAAGTTGATAACGGACTAGCCTTATTTAAACTTGCTATGCTGTTTCCAGC			-
Cas9 For	GTTCACAGGAAGCAGAGTATCATTC	Produce a 3.5 kb DNA bait fragment of ASPM C-term for purified Cas9 activity confirmation	59	-
Cas9 Rev	TATTAAAGAACGTGGACTCCAACGT			-
C sgRNA For	CACCGCAAATGGTGATGGATACGCT	Guide RNA for annealing and ligating into pSpCas9-2A-puro vector targeting C-term ASPM	-	-
C sgRNA Rev	AAACAGCGTATCCATCACCATTTGC			-
N sgRNA For	CACCGTCGAATCTGCCATGGCGAAC	Guide RNA for annealing and ligating into pSpCas9-2a-puro vector targeting N-term ASPM	-	-
N sgRNA Rev	AAACGTTCGCCATGGCAGATTCGAC			-

Table 5.1 – Continued

Primer name	Sequence (5' - 3')	Use	Annealing temp (°C)	Restriction site
Forward 5'HA	ACCATCGGGCGCGCCCGGGTATGGAGGGGAAGTT	Produce 5' Homology Arm from gDNA for the C-term ASPM mEos3.2 HDR template	59	BamHI SmaI
Reverse 5'HA	CTTAATCGCACTCATACCTCCAGAGCCACCATAAGGAATGCTAAGCGTATC			-
Forward mEos	ATGAGTGCGATTAAG	Produce mEos3.2 fragment for the ASPM mEos3.2 HDR templates	46	-
Reverse mEos	TCGTCTGGCATTGTC			-
Forward 3'HA	GACAATGCCAGACGATAGTAAATGTAAACA	Produce 3' Homology Arm from gDNA for the C-term ASPM mEos3.2 HDR template	59	-
Reverse 3'HA	CGACGTAGGCCTTTGCCCGGGGTTTCTGGAGTT			EcoRI SmaI
pFast mEos C For	CCCGGGCGCGCCCGATGGTG	Amplify the pFastBac1 backbone for C-term ASPM HDR construct	68	-
pFast mEos C Rev	GGGCAAAGGCCTACGTCGAC			-
5HA N Eos For	TCCCACCATCGGGCGCGTGGTACCTACGCCCTAAGAGATACC	Produce 5' Homology Arm from gDNA for the N-term ASPM mEos3.2 HDR template	66	BamHI
5HA N Eos Rev	CTTAATCGCACTCATGGCAGATTCGAGACCCCTCC			-
3HA N Eos For	GACAATGCCAGACGAATGGCGAACCGCCGAGTG	Produce 3' Homology Arm from gDNA for the N-term ASPM mEos3.2 HDR template	62	-
3HA N Eos Rev	CGACGTAGGCCTTTGGGTGAAGGGGATTGGAGCATTACTC			EcoRI

Table 5.1 – Continued

Primer name	Sequence (5' - 3')	Use	Annealing temp (°C)	Restriction site
eGFP For	ATGGTGAGCAAGGGC	Produce eGFP fragment for the ASPM eGFP HDR templates	48	-
eGFP Rev	CTTGTACAGCTCGTC			-
5HA N Eos For	TCCCACCATCGGGCGCGTGGTACCTACGCCCTAAGAGATACC	Produce 5' Homology Arm from gDNA for the N-term ASPM eGFP HDR template	66	BamHI
5HA N GFP Rev	GCCCTTGCTCACCATGGCAGATTCGAGACCCCTCC			-
3HA N GFP For	GACGAGCTGTACAAGATGGCGAACCGCCGAGTG	Produce 3' Homology Arm from gDNA for the N-term ASPM eGFP HDR template	62	-
3HA N Eos Rev	CGACGTAGGCCTTTGGGTGAAGGGGATTGGAGCATTACTC			EcoRI
mEos4b For	ATGGTGAGTGCGATT	Produce mEos4b fragment for the ASPM mEos4b HDR templates	66	-
Reverse mEos	TCGTCTGGCATTGTC			-
5HA N Eos For	TCCCACCATCGGGCGCGTGGTACCTACGCCCTAAGAGATACC	Produce 5' Homology Arm from gDNA for the N-term ASPM mEos4b HDR template	66	BamHI
5HA N Eos4 Rev	AATCGCACTCACCATGGCAGATTCGAGACCCCTCC			-
mEos HRT out For	GGGTATGGAGGGGAA	Produce mEos3.2 C-term HDR template by PCR	55	-
mEos HRT out Rev	GGGGTTTCTGGAGTT			-

Table 5.1 – Continued

Primer name	**Sequence (5' - 3')**	**Use**	**Annealing temp (°C)**	**Restriction site**
mEos HRT out For	GGGTATGGAGGGGAA	Produce mEos3.2 C-term HDR template by PCR	55	-
mEos HRT out Rev	GGGGTTTCTGGAGTT			-
ASPM C-term For	ATGGAGAGAAATAGT	Amplify ASPM C-term for Cas9 digestion assays	62	-
ASPM C-term Rev	TCATCTTATGACATA			-
gDNA ASPM C-Term For	GTTGGGTATGTGTTGAGGCC	Target ASPM C-term to diagnose CRISPR edits	64	-
gDNA ASPM C-Term Rev	GACATCTGTGGCCCTGAAAC			-
ASPM CTerm Ext For	CAACTCAGAAGCAGCTCAGA	Target ASPM C-term to diagnose CRISPR edits, anneal to gDNA but not HDR template	64	-
ASPM CTerm Ext Rev	AGGATGGATTTCTTTAGCTG			-
pFast N HRT For	CGCGCCCGATGGTGGGACGG	Amplify the pFastBac1 backbone for N-term ASPM HDR construct	59	-
pFast N HRT Rev	CAAAGGCCTACGTCGACGAG			-

5.2.3 All-in-one plasmid method

The third method was the All-in-one plasmid method (Sakuma et al., 2015) performed in collaboration with Tetsushi Sakuma (Hiroshima University, Japan). Briefly in this approach, three plasmids are co-transfected into cells. The all-in-one vector which includes the sgRNA sequences and Cas9, a CtIP repair enhancer vector to promote microhomology-mediated end-joining (MMEJ) and a repair donor vector which contains the fluorescent protein and neomycin resistance flanked by genomic homology sequences (Figure 5.3).

5.2.3.1 Generation of the all-in-one CRISPR vector and donor constructs

All constructs were kindly generated and provided by Tetsushi Sakuma (Hiroshima University, Japan). The all-in-one CRISPR vector was generated as previously described (Sakuma et al., 2015), using the following targets against *ASPM* for the sgRNA: N-terminus: CCCCACTCGCCGGTTCGCCATGG, C-terminus: AATGTTTACATTTACTAATAAGG. And the following target: CCAAACGATCGATATCGAAGCAC to cleave the repair template out of the donor vector.

Validation of the sgRNAs ability to correctly target the human ASPM gene was performed by transfecting the all-in-one vector into HEK293T cells (Section 2.4.5). The cells were then collected at 48 hours post transfection, lysed and subjected to the genomic cleavage detection assay (Thermo Fisher, Cat #A24372).

The donor vectors were generated by In-Fusion cloning into the pTA2 vector. These contained a fluorescent protein, either eGFP or mKate2, tagged with T2A self-cleavable NeoR tag for selection flanked on either side by a 40 bp microhomology sequence complementary to the *ASPM* locus (Figure 5.3).

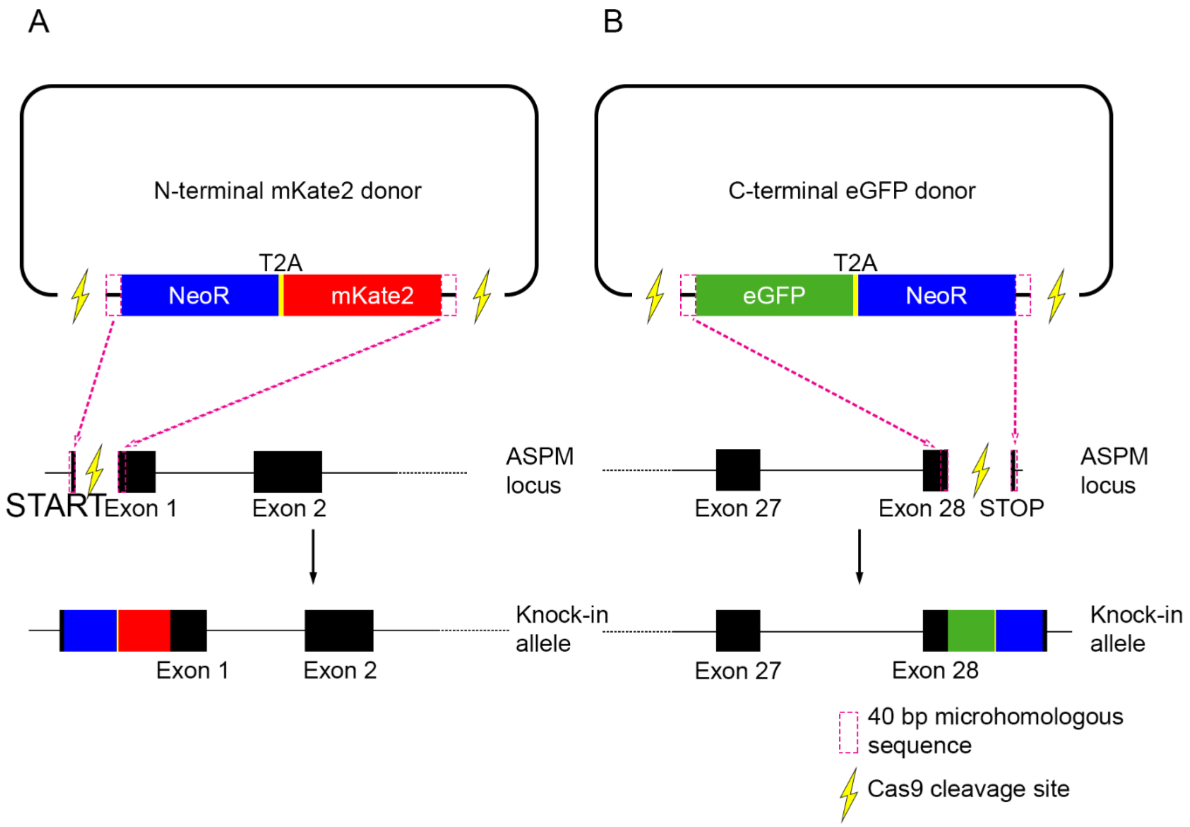

Figure 5.3 – Schematic of the microhomology-mediated end-joining directed repair.

All-in-one Cas9 vector provides cleavage targets against the donor vector and the ASPM locus (either the N- or C-terminus). Donors consist of a fluorescent protein (either eGFP or mKate2) linked to a Neomycin resistance gene with a self-cleavable T2A tag. (A) An example of the N-terminal donor containing the repair template for the mKate2 (eGFP was also used) showing the Cas9 cleavage sites and the upstream and downstream microhomologous sequence. Cas9 also targets exon 1 of the ASPM locus allowing for precise integration into the target chromosome in frame with the start codon. (B) An example of the C-terminal donor containing the repair template for the eGFP (mKate2 was also used) showing the Cas9 cleavage sites and the upstream and downstream microhomologous sequence. Cas9 also targets exon 28 of the ASPM locus allowing for precise integration into the target chromosome upstream of the stop codon. Figure adapted from (Shota Nakade et al., 2018).

5.2.3.2 Co-transfection of the all-in-one CRISPR plasmids

The all-in-one Cas9 vector, along with a donor construct and the MS2-CtIP vector known to enhance the microhomology-mediated end-joining (MMEJ) for gene insertion that this method relies upon (Nakade et al., 2018), were co-transfected into HEK293 cells with Fugene HD lipofectamine (Section 2.4.5). 24 hours post transfection, modified cells were selected for by the addition of 1 mg mL^{-1} G418. Cells were then cultured in 10 cm petri dishes (Section 2.4.1) for 2 weeks to allow cells to recover prior to cell sorting with a FACSMelody cell sorter (BD Biosciences). Briefly, cells were removed from the petri dish with 2 mL TrypLE and pelleted at 1,000 x g for 5 mins in a Harrier 18/80 (MSE) centrifuge. Supernatant was removed and cells were resuspended in FACS media (DPBS supplemented with 25 mM HEPES, 1 mM EDTA, 2% FBS, pH 7.4) to a concentration of 5x10^{6} cells mL^{-1} and stored on ice. Cells were sorted based on fluorescence intensity above a set threshold selected based upon the background fluorescence of un-transfected HEK293 cells. Single cells were sorted into a 96-well plate containing 100 µL pre-warmed medium per well. Cells were then cultured for a further 7 days before being analysed for fluorescence by immunofluorescence (Section 2.5).

5.2.4 Generating and staining with Affimers

As a second approach to visualising ASPM, Affimers were raised against the CH domains of ASPM. Affimers are small non-antibody binding proteins around 11 kDa in size, obtained by phage display to the protein of interest (Carrington et al., 2019; Tiede et al., 2017). They are easily expressed and purified from *E. coli* and then fluorescently labelled using a unique cysteine residue introduced into the C-terminus. They can be used in live cell imaging, as an FP-fusion construct (Lopata et al., 2018). The Affimer contains two variable loops, through which binding occurs, and a scaffold based on the plant protein phytocystatin, a group of inhibitors for cysteine proteinases (Tiede et al., 2014).

5.2.4.1 Generating Affimers that bind the tandem CH domains of ASPM.

GFP tagged tandem CH domains were expressed and purified as in Section 3.2.2. GFP-pp-CHT at 0.5 mg mL^{-1} was used as a protein target for screening of an Affimer library by phage display assay. The phage display assay was performed by Dr. Christian Tiede (BioScreening Technology Group; University of Leeds) as previously described (Tiede et al., 2017; Tiede et al., 2014).

5.2.4.2 Purification of Affimers

Affimers were expressed and purified by Dr. Christian Tiede and Dr. Francine Parker. Affimers were expressed in 400 mL cultures of BL21(DE3) cells by inducing with 0.1 mM IPTG for 6 hours at 25°C shaking 150 RPM. After expression, cells were pelleted by centrifugation at 3,000 x g for 30 mins, and the pellet was resuspended in 10 mL Affimer lysis buffer (50 mM NaH_2PO_4, 300 mM NaCl, 20 mM imidazole, 10% glycerol, pH 7.4) and lysed by sonication for 10 secs on / 10 secs off for 18 cycles (3 mins) 50% with a Soniprep 150 MSE (SANYO). To denature low thermostable *E. coli* host proteins, the lysate was heated at 50°C for 30 mins before being clarified by centrifugation at 30,000 x g for 30 mins in a Beckman Coulter Avanti J25. Affimers were purified by nickel affinity chromatography. Protein in the clarified lysate was bound to 4 mL His-tag purification resin (Roche) equilibrated with 50 mM NaH_2PO_4, 500 mM NaCl, 20 mM imidazole, 10% glycerol, pH 7.4, in a 5 mL column (Qiagen) and washed extensively with 50 mL wash buffer (50 mM NaH_2PO_4, 500 mM NaCl, 20 mM imidazole, 10% glycerol, pH 7.4), before being eluted with 6 times 2 mL elution buffer (50 mM NaH_2PO_4, 500 mM NaCl, 300 mM imidazole, 10% glycerol, pH 7.4). Purified Affimer elutions were pooled and dialysed against PBS supplemented with 1 mM TCEP and stored at -20°C for later use.

5.2.4.3 Labelling Affimers with commercial dyes

Affimers were directly labelled by Dr. Christian Tiede and Dr. Francine Parker for use in fluorescence microscopy. The single C-terminal cysteine residue allowed for direct labelling with a commercial maleimide dye. Purified Affimers at a concentration of 0.5 mg mL^{-1} (~40 μM) was added to an equal volume of TCEP immobilised resin (Thermo Scientific, 77712) and incubated 1 hour room temperature on a roller to ensure the cysteine was reduced prior to addition of the of the dye. The Affimer / resin mixture was centrifuged at 1,500 x g for 2 mins to separate the Affimer from the resin. The Affimer fraction was removed and Alexa fluor 488 maleimide was added to a final concentration of 85 μM before being incubated for 2 hours at room temperature on a roller.

Excess dye was removed with the use of a Zeba desalting column (7 kDa MWCO) following manufacturer's instructions. Dye labelled Affimers were stored in 40% glycerol at -20°C.

5.2.4.4 Staining fixed cells with dye labelled Affimers

Affimers were used to fluorescently label ASPM in fixed HeLa cells (Section 2.5). Briefly, HeLa cells were fixed in 2% PFA at a confluency of 50-70% and permeabilised in PBS containing 1% bovine serum albumin (BSA) and 0.1% Triton X-100. Permeabilised cells were blocked with PBS, 5% BSA. Blocked cells were then incubated with dye labelled Affimer diluted 1:100 in PBS, 1% BSA for 1 hour. Cells were then washed 5 times with PBS, 1% BSA before mounting on slides with ProLong Gold Antifade mounting solution (Thermo Fisher, P10144). Cells co-stained for other targets was performed as described in Section 2.5.2. Images were taken using the Zeiss lattice light sheet, which is a commercialised version of the instrument invented by Betzig (Chen et al., 2014), taken as part of a remote demo using samples of fixed cells, stained with the Affimer, prepared in Leeds.

5.3 Results

5.3.1 Cas9 RNP CRISPR knock-in

Cas9 was successfully expressed and purified (Figure 5.4A). Its concentration of 8 mg mL^{-1} is suitable for use in downstream applications (Jinek et al., 2012). The activity of the pure Cas9, along with the specificity of the *in vitro* transcribed sgRNA was confirmed by the correct digestion of an *ASPM* C-terminal fragment (Figure 5.4B-C). Densiometric analysis of the agarose gel revealed that 100 pmol of Cas9.sgRNA (1:1 ratio) digested 50% of the provided PCR product (~100 pmol DNA) in the 15-minute incubation. As the Cas9 RNP is in equal ratio to the DNA and Cas9 is a single-turnover enzyme (in that after each enzyme cleavage reaction, it stops) (Sternberg et al., 2014), this suggests that half of the purified Cas9 protein is inactive. This is not uncommon however and was not expected to have a great impact upon the downstream experiments (Gong et al., 2018). Expression of the GFP1-10 fragment was tested using an antibody specific to this construct (Figure 5.5A). This antibody recognised full length GFP in Sf9-ET cells (Figure 5.5B).

While transfection with a GFP-11 vector was successful in generating fluorescent cells, using the Cas9 RNP was not. A number of transfection methods were tested (see methods 2.4.5 and 5.2.1.5) but none were able to generate a knock-in cell line successfully.

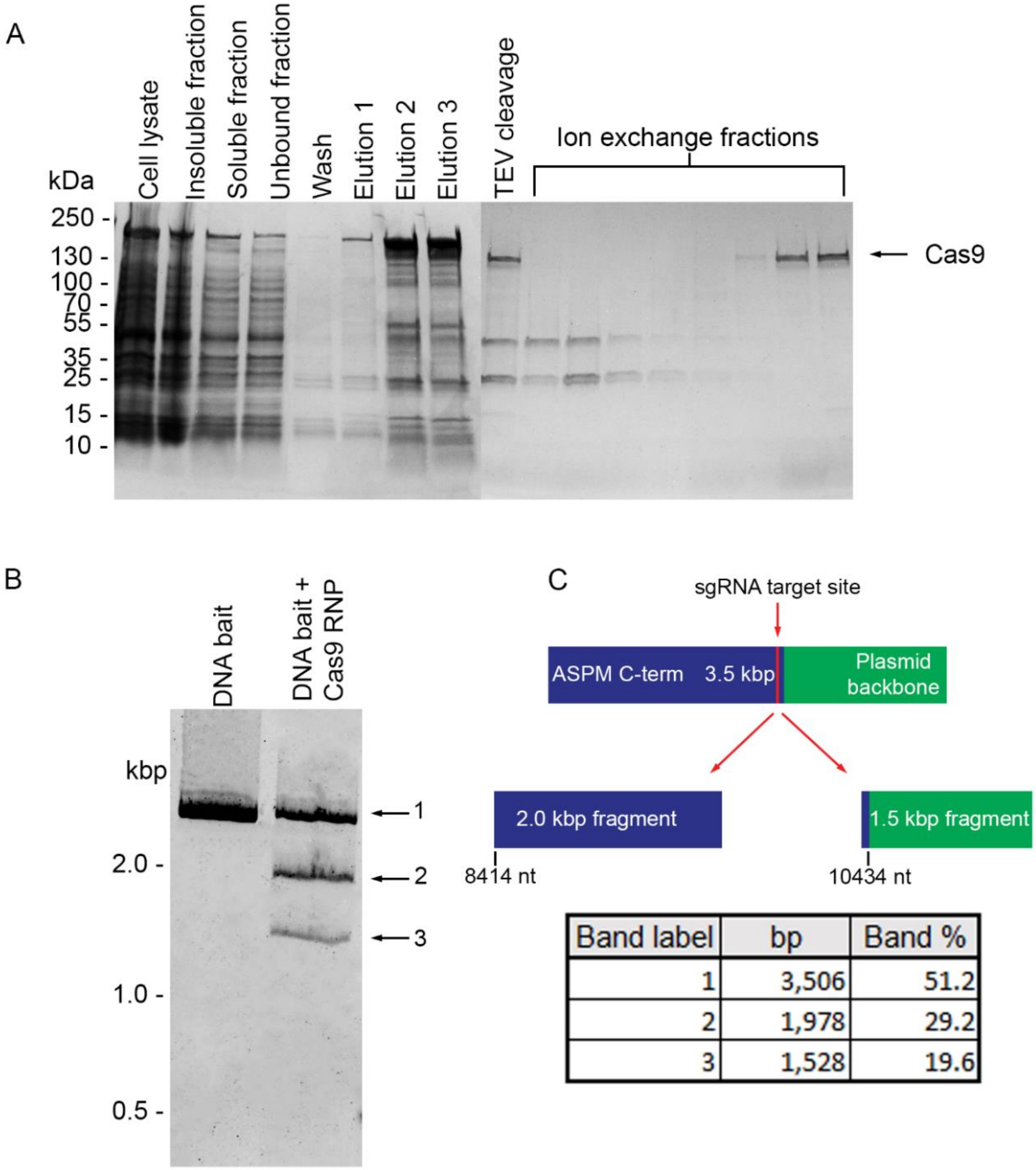

Band label	bp	Band %
1	3,506	51.2
2	1,978	29.2
3	1,528	19.6

Figure 5.4 – Purification and activity of Cas9.

(A) Purification of Cas9 His-tag purification showing samples taken at each stage and the resulting 3 elutions of MBP-Cas9 (205 kDa). This was followed by ion exchange of Cas9 after TEV protease cleavage. Lanes represent samples taken from 5 mL fractions containing protein as indicated by the ÄKTA UV trace. Pure Cas9 (163 kDa), present in the final 2 fractions, eluted between 450-550 mM [KCl]. (B) Analysis of Cas9 activity and sgRNA specificity against an ASPM C-terminal fragment amplified by PCR. Digested products were separated by a 1% agarose gel. (C) A schematic of the digestion showing predicted product lengths and densiometric analysis of DNA bait + Cas9 RNP showing percentage of products relative to the DNA bait. The 3.5 kbp fragment consisted of 2,021 bp (8,414-10,424 nt) of ASPM (blue) and 1,485 bp of plasmid backbone (green).

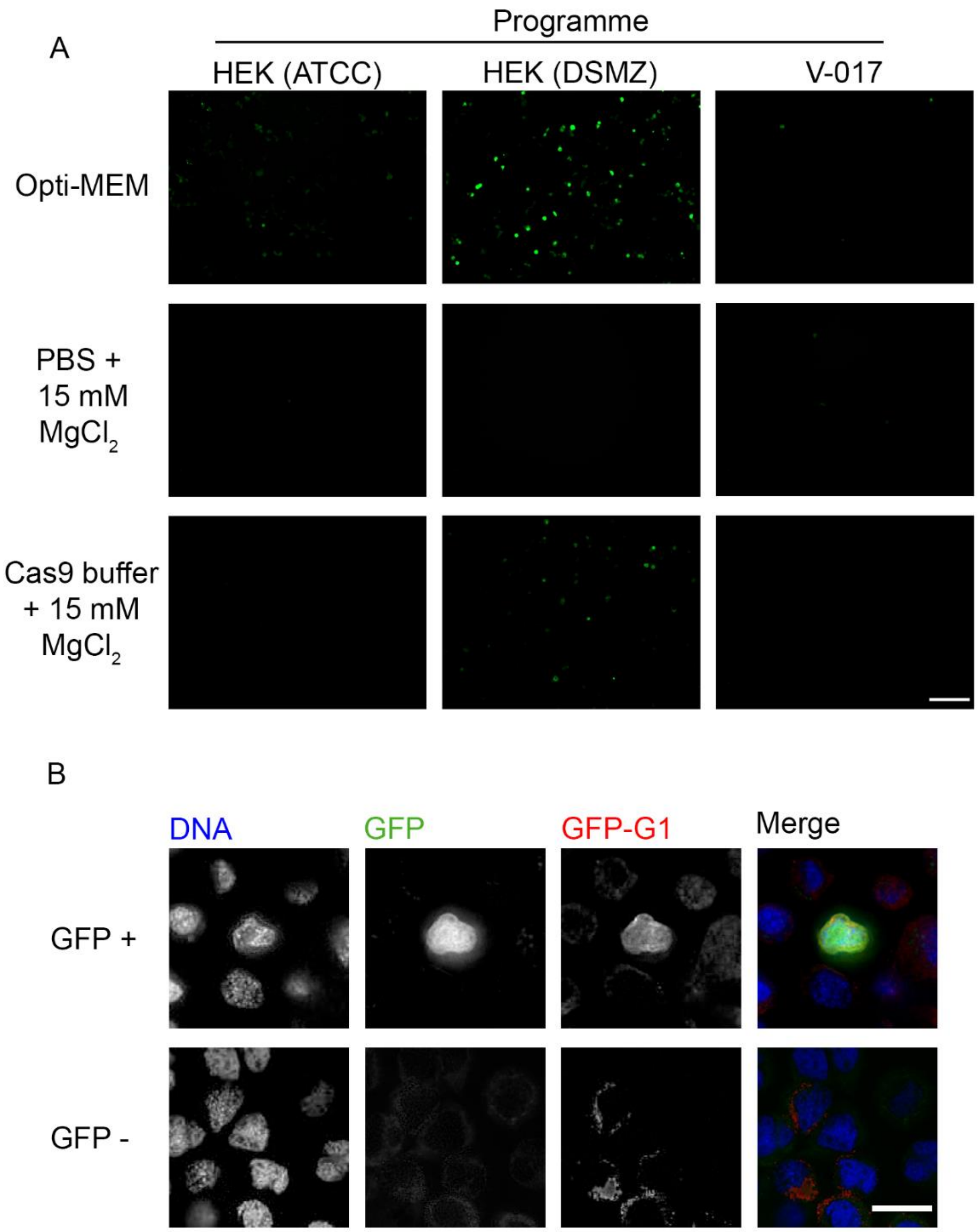

Figure 5.5 – Optimisation of the electroporation method and analysis of the anti-GFP1-10 antibody.

(A) Example images of cells after transfection with a GFP vector, to test the best conditions for transfection. 3 different programmes (HEK (ATCC) = Q-001, HEK (DSMZ) = A-023 and V-017) and 3 different buffers were tested as indicated. Scale bar = 100 µm. (B) Immunofluorescence microscopy of Sf9-ET cells stained with GFP-G1, to test for the presence and specificity of the anti-GFP-G1 antibody in the hybridoma supernatant. Infected Sf9-ET cells, which express GFP due to baculoviral infection, and uninfected Sf9-ET cells were immunostained with the anti-GFP-G1 antibody and visualised using an anti-mouse Alexa 546 (red) secondary antibody. GFP observed in green and DNA stained with DAPI (blue). Scale bar = 15 µm.

5.3.2 Generating CRISPR knock-ins with Cas9 plasmid

As Cas9 RNP CRISPR knock-in was unsuccessful, a different approach was attempted, which used a Cas9 expression vector. Either an N- or a C-terminal sgRNA sequence was cloned into the pSpCas9-2A-Puro vector successfully, confirmed by sequencing. Similarly cloning of the N- and C-terminal mEos3.2 homology driven repair templates (HRT) were successful (Figure 5.6) and confirmed by sequencing. Cells were transfected with the Cas9 vector and respective HRT and transfected clones were selected for using puromycin (see methods and Figure 5.2).

Following puromycin selection, several fluorescent clones were obtained. The correct insertion of mEos3.2 into the C-terminus was confirmed by both PCR amplification of the inserted mEos3.2 (Figure 5.7A) and by Western blot analysis (Figure 5.7B) when compared to untransfected cells. It is unclear whether both alleles have been knocked-in, therefore further testing is required to confirm this. Using whole exome sequencing would reveal if this was the case. However, imaging of live or fixed cells showed that the localisation of fluorescent ASPM was different from that observed for endogenous ASPM (Figure 5.7C-E). In fixed cells, C-terminally tagged mEos3.2-ASPM was found throughout the cytoplasm in interphase cells and not in the nucleus as expected. In mitotic cells, it did not localise to spindle poles in metaphase (Figure 5.7C). In live cells, while fluorescent ASPM appeared to be restricted to the nucleus in interphase cells (Figure 5.7D), it did not localise to the spindle poles in mitosis, or to the cytokinetic furrow in cytokinesis (Figure 5.7E). These results suggest that the addition of a fluorescent tag to the C-terminus of ASPM interferes with the cellular localisation of ASPM.

The N-terminal mEos3.2 ASPM knock-in was also unsuccessful. Individual colonies of fluorescent cells were obtained; however, these were unable to grow to significant numbers (Figure 5.7F).

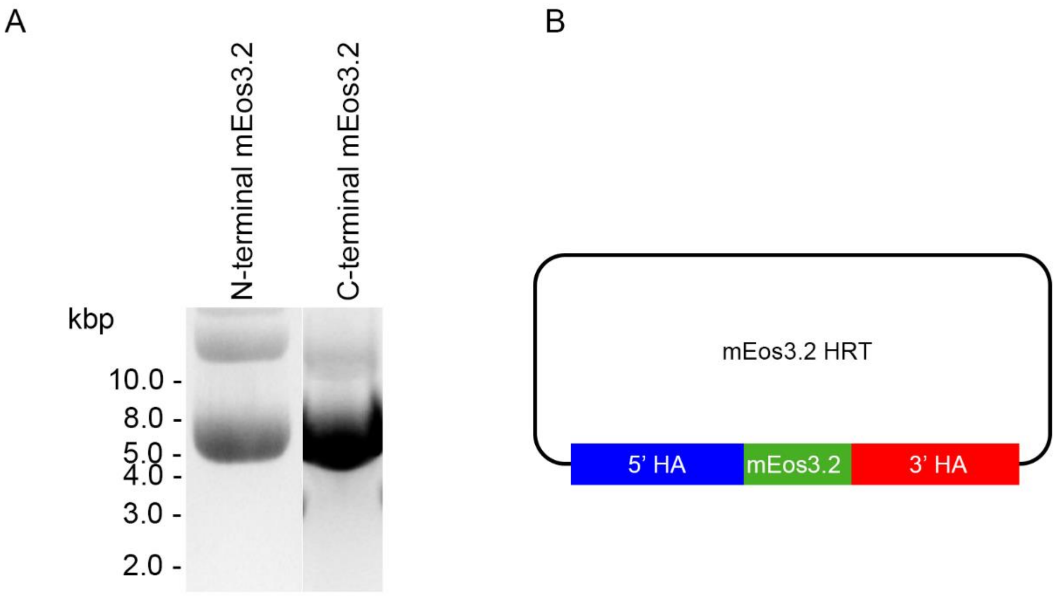

Figure 5.6 – Preparation for mEos3.2 knock-in to the ASPM locus.

(A) A 1% agarose gel of both the N- and C-terminal mEos3.2 homology driven repair templates (HRT). Expected plasmid size: ~7.5 kbp (B) A schematic of the mEos3.2 HRT showing the 1.0 kbp ASPM homology arms (HA) either side of the mEos3.2 sequence.

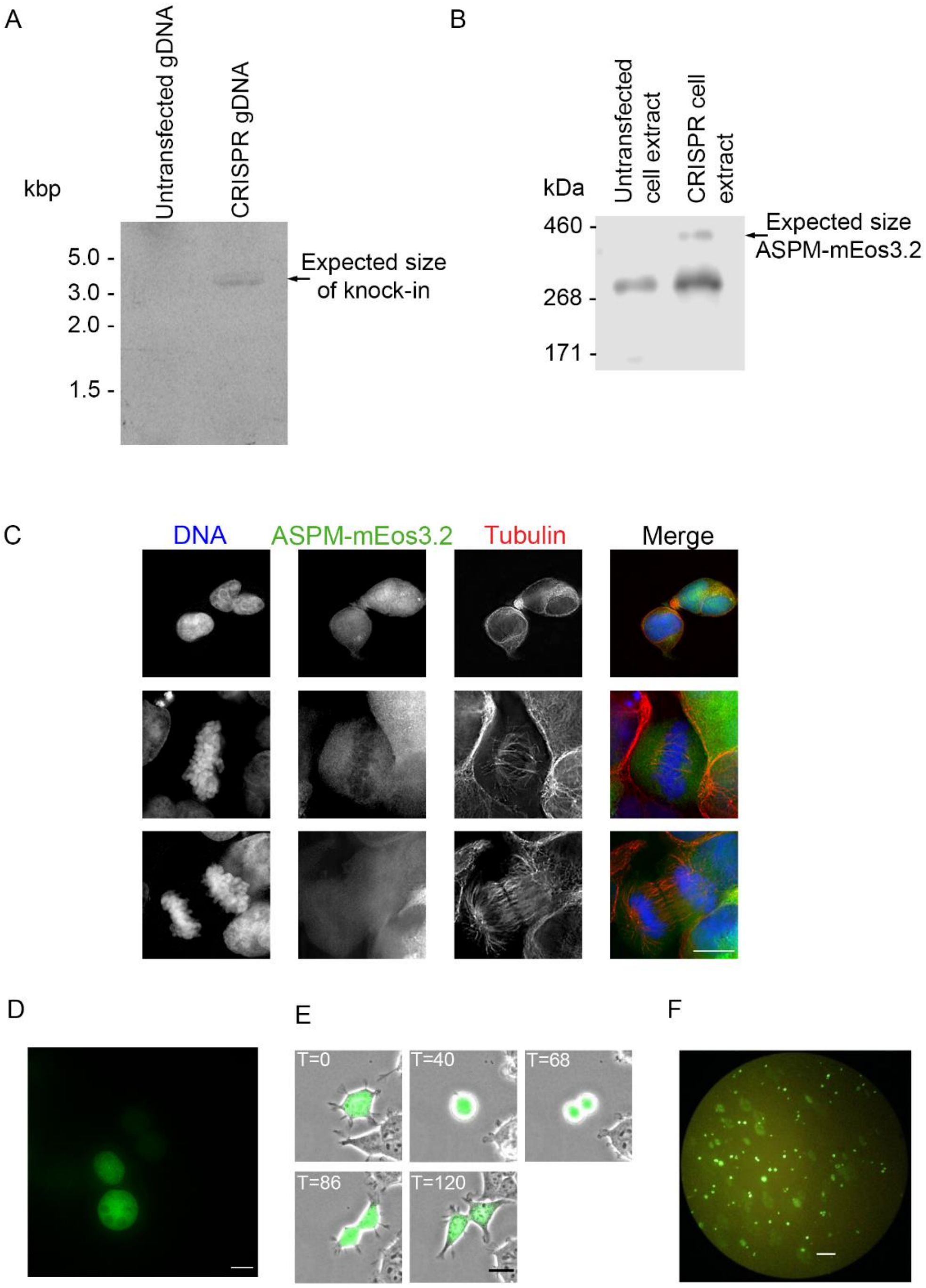

Figure 5.7 – Knock-in of mEos3.2 into the ASPM allele.

(A) A 1% agarose gel of the PCR amplification of the C-terminal knock-in fragment of ASPM with a band at ~3.0 kbp indicating correct knock-in of mEos3.2. (B) Western blot analysis of the mEos3.2 knock-in cell line using mEOS2 pAb antibody, ASPM-mEos3.2 knock-in expected size: 435 kDa. (C) PFA fixed C-terminal knock-in cell stained for tubulin (red) and DNA (blue), Scale bar = 10 µm. (D) Live cell imaging of C-terminal mEos3.2 showing ASPM localising to the nucleus during interphase. Scale bar = 10 µm (E) Live cell imaging of mEos3.2 knock-in cell undergoing mitosis. T= time in mins, scale bar =10 µm. (F) N-terminal mEos3.2 knock-in cells round up and detached shortly after sorting. Scale bar = 100 µm.

5.3.3 Generation of a knock-in cell line using the all-in-one CRISPR vector and MMEJ donor constructs

As neither of the previous CRISPR approaches were successful, a different approach was attempted. The sgRNAs were successfully cloned into the all-in-one CRISPR vector and validated for their specificity by Tetsushi Sakuma (affiliation) (Figure 5.8A). The donor vectors were also successfully cloned and validated by Tetsushi Sakuma (Figure 5.8B).

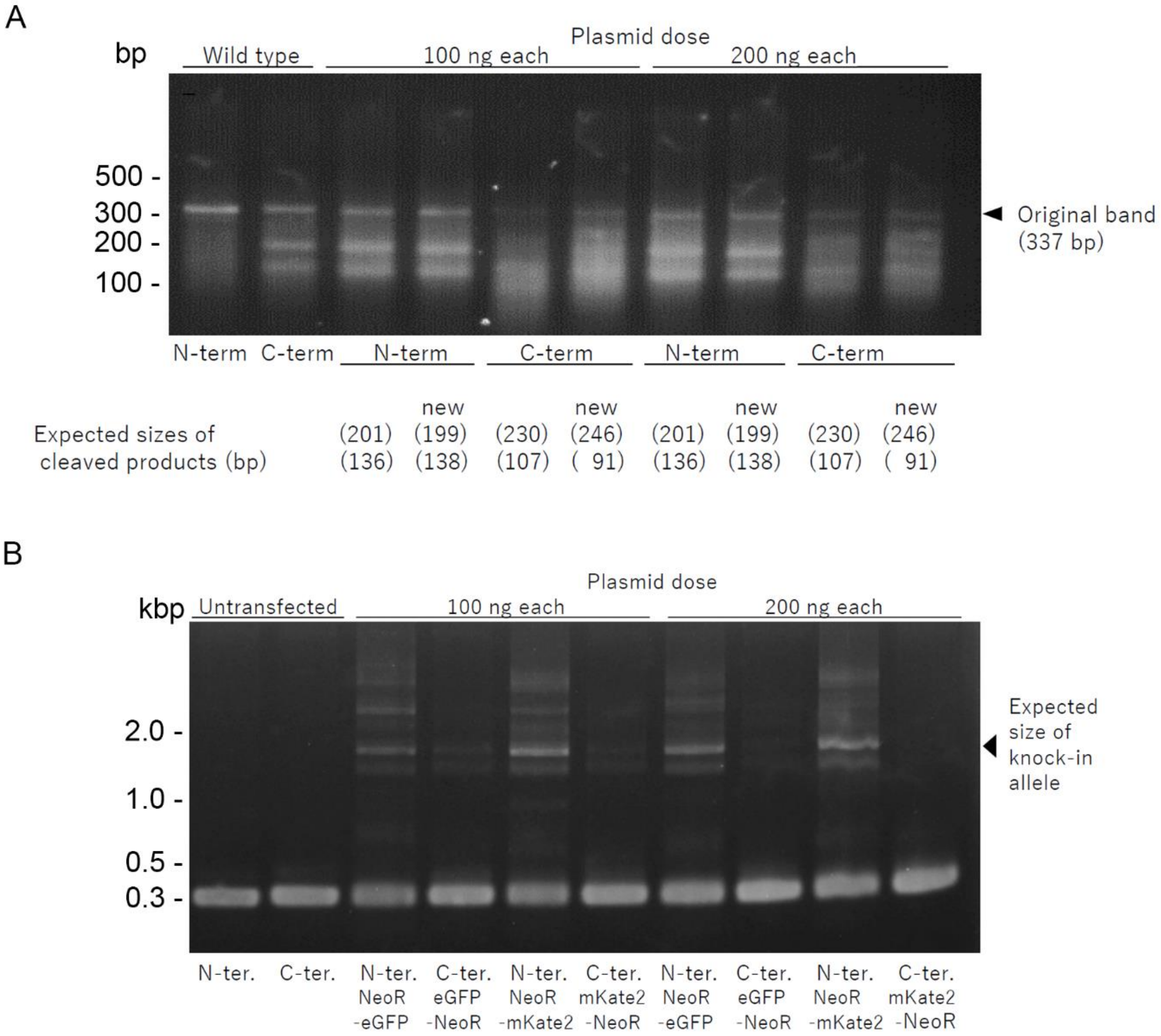

Figure 5.8 – Validation of the all-in-one CRISPR vector and MMEJ donor constructs.

(A) Validation of the sgRNAs targeting the human ASPM gene. Genomic cleavage analysis of the all-in-one CRISPR-cas9 vectors containing the sgRNAs against either the N- or C-terminus of ASPM comparing the old (Section 5.3.2) and the new as indicated. Cleavage of the original band (337 bp) into the expected cleavage products indicates correct targeting. (B) Validation of knock-in donor constructs of the human ASPM gene. PCR analysis of the co-transfected all-in-one CRISPR-Cas9 and donor vectors, band present at ~1.9 kbp indicated successful knock-in. Data and figures curtesy of Tetsushi Sakuma.

From the validation, the N-terminal knock-in was the most successful and therefore was taken forward. Cells were successfully transfected, and a large portion of cells survived the neomycin selection suggesting successful incorporation of eGFP. FACS was used to isolate single cell colonies of cells positive for the N-terminal eGFP knock-in. Using 200 ng of each vector resulted in a higher percentage of cells reading above the fluorescence threshold than cells transfected with 2 μg total DNA (~666 ng each plasmid) (Figure 5.9). However, in both cases, there was a higher percentage of cells reading above the fluorescence threshold than in the negative control indicating a presence of knock-in cells in the transfected cells. The eGFP knock-in was confirmed by PCR of isolated genomic DNA and anti-GFP Western blot (Figure 5.10A-B). However, no specific eGFP-ASPM fluorescence was seen when examined by microscopy (Figure 5.10C).

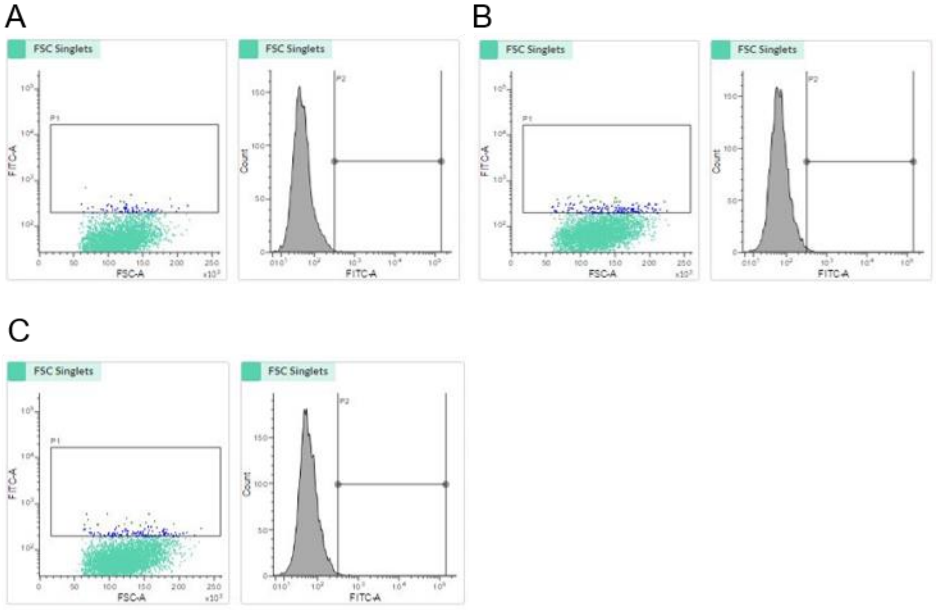

Figure 5.9 – FACS single cell analysis of N-terminal GFP-ASPM knock-in HEK293 cells.

(A) 10,000 cell events recorded on the FACSMelody cell sorter during a cell sort of non-transfected HEK293 cells to set a lenient negative control window with 1.61% cells above a fluorescent threshold. (B) 10,000 cell events recorded on the FACSMelody cell sorter during a cell sort of HEK293 cells transfected with 200 ng each of the all-in-one Cas9 vector, the donor construct and the MS2-CtIP vector. Using the window outlines in the negative control, 3.41% cells scored above the threshold. (C) 10,000 cell events recorded on the FACSMelody cell sorter during a cell sort of HEK293 cells transfected with 2 μg total DNA. Using the window outlines in the negative control, 2.48% cells scored above the threshold.

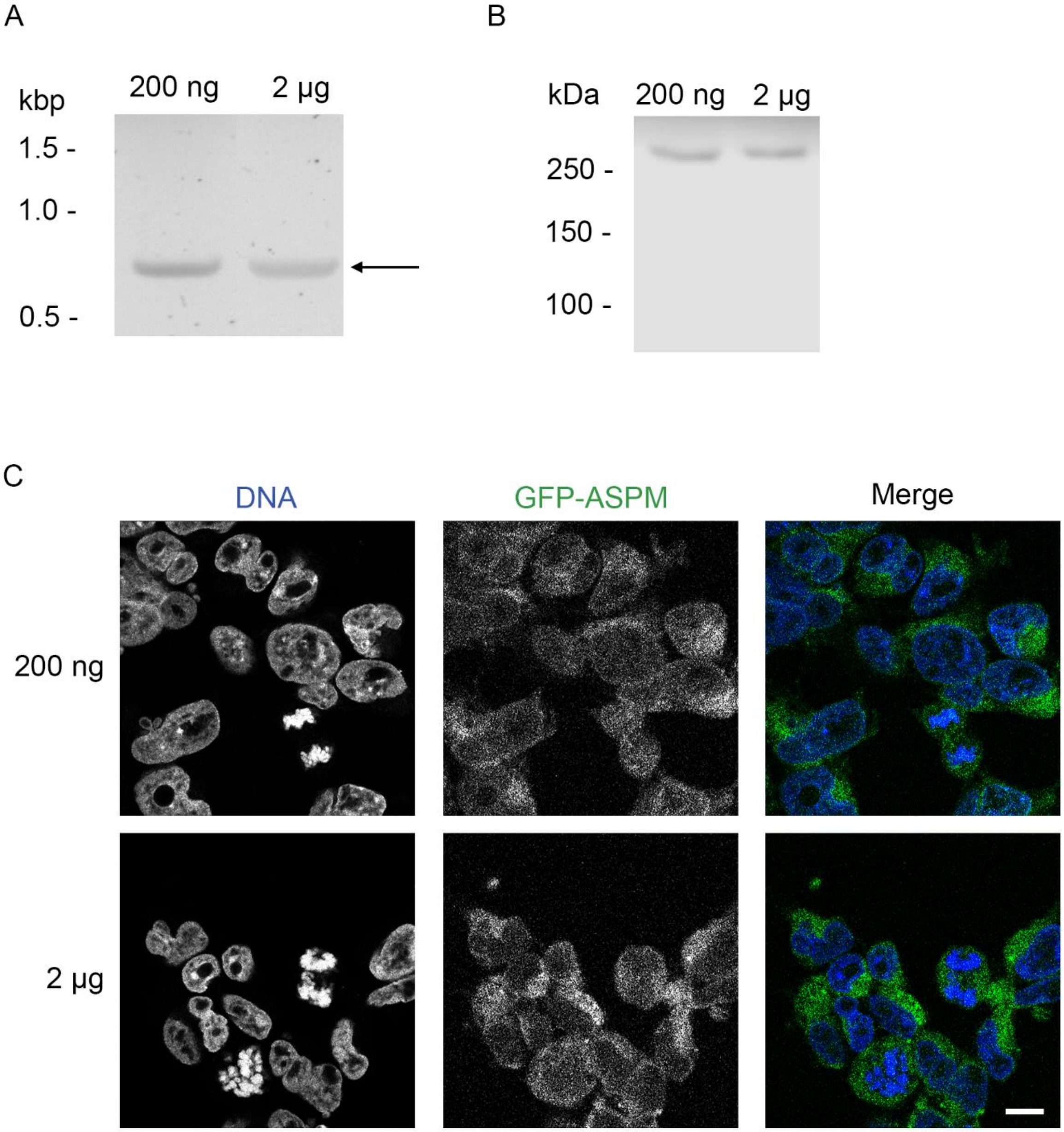

Figure 5.10 – Confirmation of GFP knock-in and imaging of Knock-in cells.

(A) A 1% agarose gel of the PCR amplification of the N-terminal knock-in fragment of ASPM in HEK293 cells transfected with either 200 ng each of the all-in-one Cas9 vector, the donor construct and the MS2-CtIP vector or 2 µg total DNA, a band at ~0.7 kbp indicating knock-in of eGFP. (B) Western blot analysis of the eGFP knock-in HEK293 cell line transfected with either 200 ng each of the all-in-one Cas9 vector, the donor construct and the MS2-CtIP vector or 2 µg total DNA, using anti-eGFP antibody, eGFP-ASPM knock-in expected size: 435 kDa. (C) PFA fixed N-terminal eGFP (green) knock-in cell stained for DNA (blue), Scale bar = 10 µm.

5.3.4 Using Affimers to stain ASPM

The second aim of this chapter was to raise Affimers against sections of ASPM. Due to time constraints, Affimers were raised against the tandem CH domains only. The Affimer screen identified 48 potential Affirmers against the GFP-CHT construct. From the ELISA assay, 10 potential strong binders were selected, of these, Affimer number 11 was taken forward for staining (Figure 5.11A). CH Affimer 11 recognised endogenous ASPM and stains the spindle poles of mitotic cells (Figure 5.11B) as well as showing localisation to the midbody during cytokinesis (arrowed, Figure 5.11C). The Affimer also stains endogenous ASPM located in the nucleus of interphase cells.

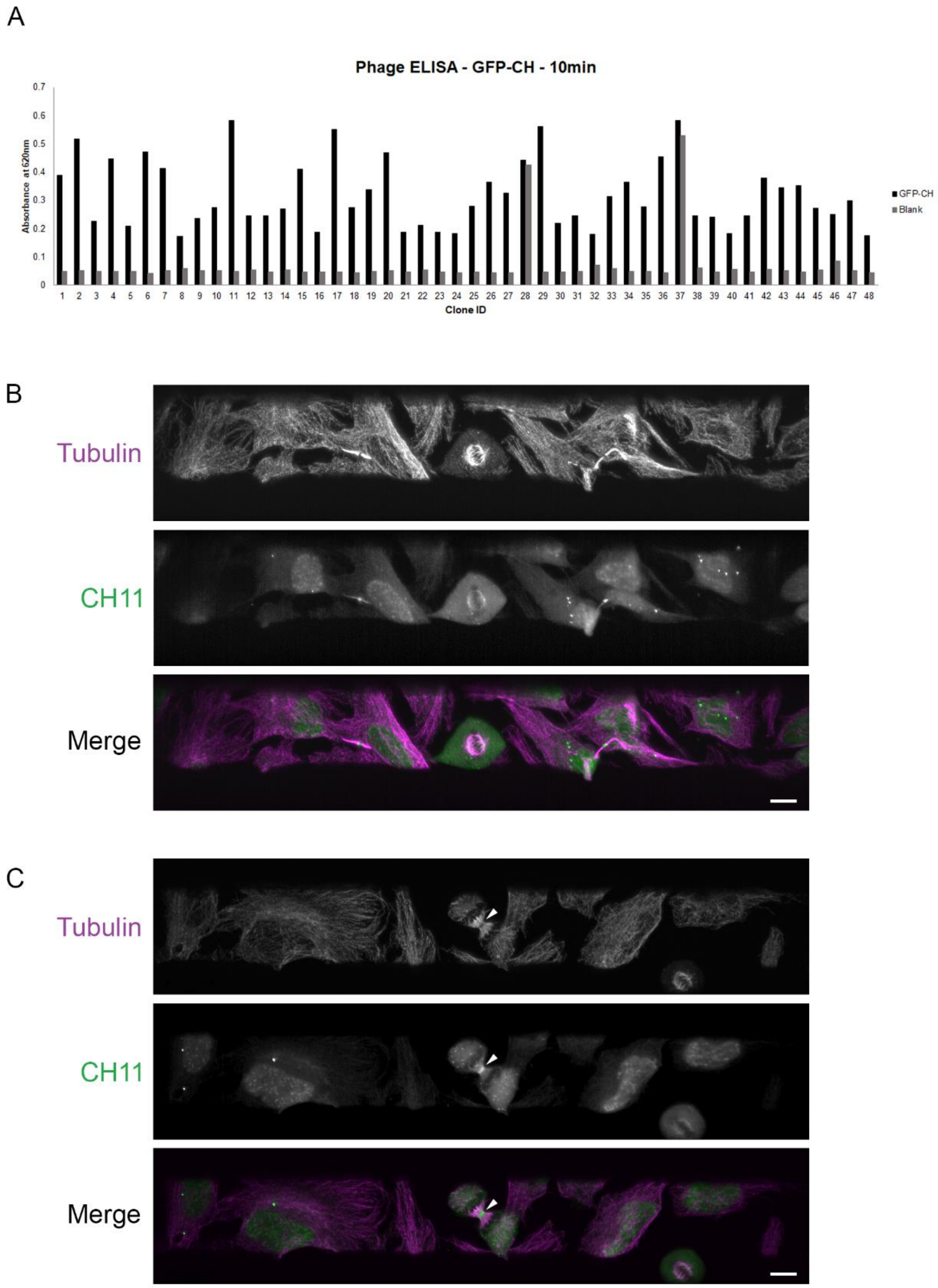

Figure 5.11 – Using Affimers to label endogenous ASPM.

(A) Phage ELISA assay results showing the specificity of the GFP-CH Affimers compared to a blank. (B) and (C) Lattice light sheet images of cells stained with the CH11 Affimer (green) and tubulin (magenta). Showing a mitotic cell (B) and a cell undergoing cytokinesis (C) Arrow indicating large amount of staining at the midbody. Scale bar = 10 µm.

5.4 Discussion

In this chapter, several attempts were made to tag endogenous ASPM using CRISPR/Cas9 using three different approaches and tagging both the N- and C-terminals. As this was not successful, a second approach using affirmers that were raised against the tandem CH domains of ASPM was investigated. This provided a reliable and simple method to stain endogenous ASPM in live and fixed cells without the use of antibodies.

CRISPR methods outlined here have previously shown to be successful in tagging endogenous proteins with fluorescent protein tags. Kamiyama et al., (2016) used a split-GFP method to tag endogenous lamin A / C, histone H2B (H2B), cAMP-dependent protein kinase catalytic subunit a (PKA) and heterochromatin protein 1 homologue (HP1) with GFP-11. Compared to ASPM (~410 kDa), these protein targets are relatively small (69 / 62 kDa, 14 kDa, 44 kDa and 22 kDa respectively). This may suggest that this method is more successful with smaller targets. Unlike ASPM, these targets are not involved in mitosis, a well-regulated process (Mcintosh et al., 2012). Alongside this, small mutations in *ASPM* result in a significant disease phenotype, which may provide an explanation to the difficulty of modifying such a protein at the genetic level. However, CRISPR has been previously successful in tagging other, albeit smaller, endogenous mitotic spindle proteins (Mann & Wadsworth, 2018), suggesting that protein size may be a limiting factor.

To further diagnose the issues, a T7 endonuclease I assay could be used to confirm whether the RNP is correctly localising to the nucleus and cleaving the genomic DNA. This will also show whether the issue lies with the RNP localisation or the repair mechanism efficiency.

Using a Cas9 plasmid and a homology driven repair template (HRT) plasmid appeared to be slightly more successful as fluorescent cells were generated. This may be due to enrichment of the tagged cell population at an early stage in the experiment. However, this method did not produce a correctly localised ASPM throughout the cell cycle when tagging the C-terminus. This may suggest that the C-terminal region of ASPM is involved in the localisation and therefore not ideal for tagging. Tagging the N-terminus was therefore the better option, unfortunately, tagging the N-terminus using the dual plasmid method had a potential toxic effect which reduced the survivability of the cells. Another reason for the visual mis-localisation is the potential issue of off-target effects of the CRISPR technique. Although the gRNA target was selected to have minimal off-target effects and the repair template was specific to ASPM, the resulting chance of this occurring is minimal.

The all-in-one plasmid provided a promising start to tagging the N-terminal of endogenous ASPM. Although the knock-in was confirmed by both Western blot and PCR, no fluorescence was seen in live or fixed cells. This is likely due to endogenous ASPM being expressed at very low levels and therefore potentially difficult to detect ((Uhlén et al., 2015); data available from v20.1.proteinatlas.org). In contrast, the dual-plasmid method resulted in very bright diffuse fluorescence. The main difference between these two methods was the fluorescent protein used (mEos3.2 verses eGFP). However, this is unlikely to cause the severe difference observed. Due to the erroneous localisation observed, it is difficult to identify the cause.

Western blot analysis also displayed a potentially shorter isoform of ASPM (~250 kDa), as seen in previous knock-in attempts (Jiang et al., 2017). This shorter isoform, likely due to a lack of exon 18, has previously been linked to pancreatic cancer and is associated with nuclear ASPM (Hsu et al., 2019). As both this study and Jiang et al., (2017) used the HEK293 cell line, which is of a cancerous origin, it may suggest that these cells mainly express the shorter ASPM isoform. This indicates that this cell line may not be ideal for tagging of endogenous long isoform ASPM, as tagging of the shorter isoform would likely also occur and little is known about its localisation or function. Therefore, future investigation of a non-cancerous cell line would be beneficial.

A second approach to visualise ASPM involving Affimers showed an expected pattern of ASPM localisation, similar to previous antibody staining (Higgins et al., 2010). However, centrosomal localisation was not seen during interphase as previously reported (Zhong et al., 2005). This is the first instance a non-antibody agent has been raised against ASPM. Although this could not be examined further due to time constraints, this promising approach is likely a useful tool for the future. However, further validation through ASPM knockdown experiments is first required.

In summary, exhaustive attempts were made to tag endogenous ASPM using CRISPR technology. This indicates the difficulty in tagging such a large mitotic protein, rendering this an unlikely target for future CRISPR experiments. In contrast to this, raising Affirmers against the tandem CH domains of ASPM proved to be an easy and reliable method for tagging endogenous ASPM in fixed cells and live cells. It is likely that raising Affimers against other regions of ASPM would prove useful in deciphering the cellular locations of the different regions of ASPM (i.e. the N-terminal region (CH Affimer) and the C-terminal region) at specific points in the cell cycle.

6. Final summary and concluding remarks

6.1 Summary

This thesis has provided novel information on the structure and protein binding capabilities of human ASPM. Alongside this, a useful tool to visualise ASPM in live and fixed cells was also developed. In the first part of this thesis, the binding partner of the CH domains of ASPM were investigated and revealed that they may interact with microtubules rather than the predicted F-actin. In the second part of this thesis the light chain binding capabilities and structure of the central portion of IQ motifs of human ASPM were investigated. This revealed that the IQ motifs interact with both calmodulin and MYL6B, confirming the previous yeast two-hybrid experiments (J Bond – Personal communication). The central 21 IQ motifs were found to have a flexible elongated structure as shown by negative stain electron microscopy (nsEM). The third chapter of this thesis aimed to develop tools to visualise the cellular location of ASPM in more detail. Exhaustive CRISPR attempts to fluorescently label the endogenous ASPM proved to be difficult. However, an Affimer raised against the tandem CH domains labelled ASPM in fixed cells successfully and is likely to be an invaluable tool for future experiments.

6.2 Summary of specific findings

6.2.1 The CH domains of ASPM bind microtubules both in tandem and singularly

The experiments here have revealed that the CH domains of ASPM may bind to microtubules and not to F-actin. Flow cell experiments showed a clear co-localisation between microtubules and purified CH domains, for tandem CH domains (CH1, CH2) and for individual CH domains (CH1 or CH2). Experiments in cultured cells, in which tandem GFP-tagged CH domains localised to microtubules, support this finding. This is an interesting finding as tandem CH domains typically bind to F-actin (Gimona et al., 2002; Korenbaum & Rivero, 2002).

Interestingly, it was not found that the CH domains bound preferentially to the ends of microtubules. This gives rise to the question of how ASPM tracks to the microtubule minus-ends as observed *in vivo*? It is possible that another domain of the N-terminal ‘microtubule binding’ region is important for this. It is therefore important to determine the identity of this region within the ASPM sequence and to determine if further constructs do show preferential binding to the ends of microtubules. Alongside this, γ-tubulin was not detected in pull-down experiments which has previously been observed to interact with ASPM (Paramasivam et al., 2007; Singhmar & Kumar, 2011). Potentially, this interaction is also mediated by the N-terminal 'microtubule binding' region. As ASPM also binds katanin within this region, this would bring katanin in proximity with the minus end of microtubules resulting in severing of the microtubule. This highlights the need to investigate this region thoroughly to fully understand the role that the N-terminus of ASPM plays in microtubule interaction.

Finally, the binding affinity of each individual CH domain was not measured for microtubules in these experiments. It would be of interest to determine if the CH domains bind to microtubules with different affinities, as seen with the CH domains of α-actinin (Way et al., 1992).

6.2.2 The ASPM IQ motifs: structure and effect of Ca^{2+}

Using nsEM, these experiments have revealed that the central 21 IQ motifs of ASPM (IQ32-52) form a semi-flexible extended structure rather than a rigid rod, and that the flexibility of this region varied across the length of the molecules. This region of the heavy chain of ASPM was fully decorated with light chains. Most IQ32-52 particles displayed one or two bends. It is possible that the positions of these bends might be related to the lengths of IQ motifs, and their interaction with light chains in some way. The sequences of the IQ motifs in this region are the most canonical out of the 81 IQ motifs found in ASPM. It will be interesting to investigate the other regions of ASPM in which the IQ motifs are less canonical and do not follow the 23-23-27 pattern, to determine how this affects flexibility in these other regions.

If the full-length, 81 IQ motif domain of ASPM is elongated and semi-flexible, then the N- and C-terminal domains could be separated by ~295 nm. However, if some IQ motif regions are more flexible than the one studied here, then the full-length IQ region could have a smaller end-end distance *in vivo*. Moreover, while the 21IQ motifs appear to be fully occupied by light chains in the absence of Ca^{2+}, this occupancy could change in areas of the cell where Ca^{2+} is increased. Ca^{2+} is known to be important in mitosis (Lagos-Cabré et al., 2020). A local increase in Ca^{2+} causing the loss of calmodulin light chains binding ASPM IQ motifs which could lead to a local collapse of the heavy chain and increased flexibility of the IQ motif region (Figure 6.1), with the potential of bringing the N- and C-terminal regions closer together. In addition, knockdown of calmodulin reduces ASPM localisation to the spindle pole (van der Voet et al., 2009). A partial explanation for this might be that ASPM mislocalises if the IQ motif region collapses as a result of a lack of calmodulin. Calmodulin bound to ASPM has also been suggested to act as a Ca^{2+} 'sponge' to remove Ca^{2+} from polymerising microtubules in the spindle pole, as microtubules are sensitive to free Ca^{2+} thus stabilising the spindle microtubules (Hepler, 1994). However, if Ca^{2+} causes calmodulin to dissociate from ASPM, compromising its structural integrity, it is unclear how this would be an effective mechanism for removing Ca^{2+}. It will be fascinating to determine the overall behaviour of the 81 IQ motif region, its response to Ca^{2+} and how this contributes to the function of ASPM in vivo.

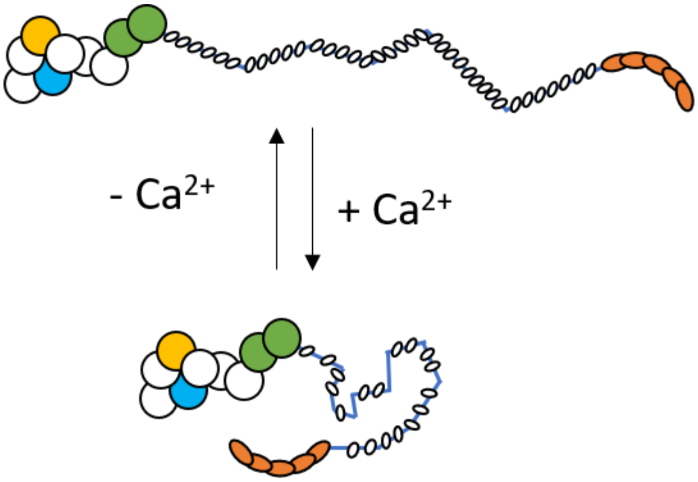

Figure 6.1 – The structural effect of calcium on the IQ motifs of ASPM.

The N-terminal region (LHS) consisting of the ASH domain (light blue), the ASNP (yellow), tandem CH domains (green), IQ motifs (blue) with light chains (white ovals) and the C-terminal region (RHS) consisting of the 5 potential ARM repeats (orange).

6.2.3 Both calmodulin and MYL6B bind the IQ motifs of ASPM

The IQ motifs are able to bind both calmodulin and MYL6B (Chapter 4) in both the IQ32-52 and IQ9-16 constructs. However, the shorter IQ50-52 only co-purified with calmodulin indicating that MYL6B may require additional downstream residues to form a stable interaction with the IQ motif.

It is important to determine if the different light chains prefer to bind to specific IQ motifs or can bind to any, in a random manner. Native mass spectrometry would be an ideal tool to investigate this question. This will shed light on the binding site recognition of the light chains and how the light chains affect the conformational change seen in the work reported in this thesis.

Previous pull-down experiments have not shown ASPM to bind to actin (Jiang et al., 2017). However, an interaction of ASPM with actin could play a role in the midbody during cytokinesis, an area rich in F-actin (Cheffings et al., 2016), which suggests this is a reasonable projection. MYL6B contains an N-terminal extension found in other myosin light chains, which has been suggested to bind to actin (Logvinova & Levitsky, 2018). Although this interaction is weak at physiological ionic strength, if multiple MYL6Bs at suitable spacings along the ASPM IQ region were present, they could sum to a stronger binding to an actin filament. A canonical IQ triplet (23-23-27) is 73 residues in length and at 100° per residue in an α-helix, this corresponds to 20.3 turns. This means that it would only take a small unwinding of the helix to align the azimuth of MYL6B on every 27-residue motif. Also, this spacing of the MYL6B along the ASPM IQ helix calculates to around 10.95 nm, which is similar to a 2 x 5.5 nm subunit repeat along the actin pitch (i.e. a MYL6B may bind to every other actin subunit). This may suggest that the IQ motifs of ASPM mimic tropomyosin in terms of actin binding. It would be interesting to determine if the presence of MYL6B is able to allow the binding of ASPM to actin. This may be how both katanin and citron kinase are held within the midbody during cytokinesis as seen previously (Matsuo et al., 2013; Mckenzie et al., 2016) (Figure 6.2).

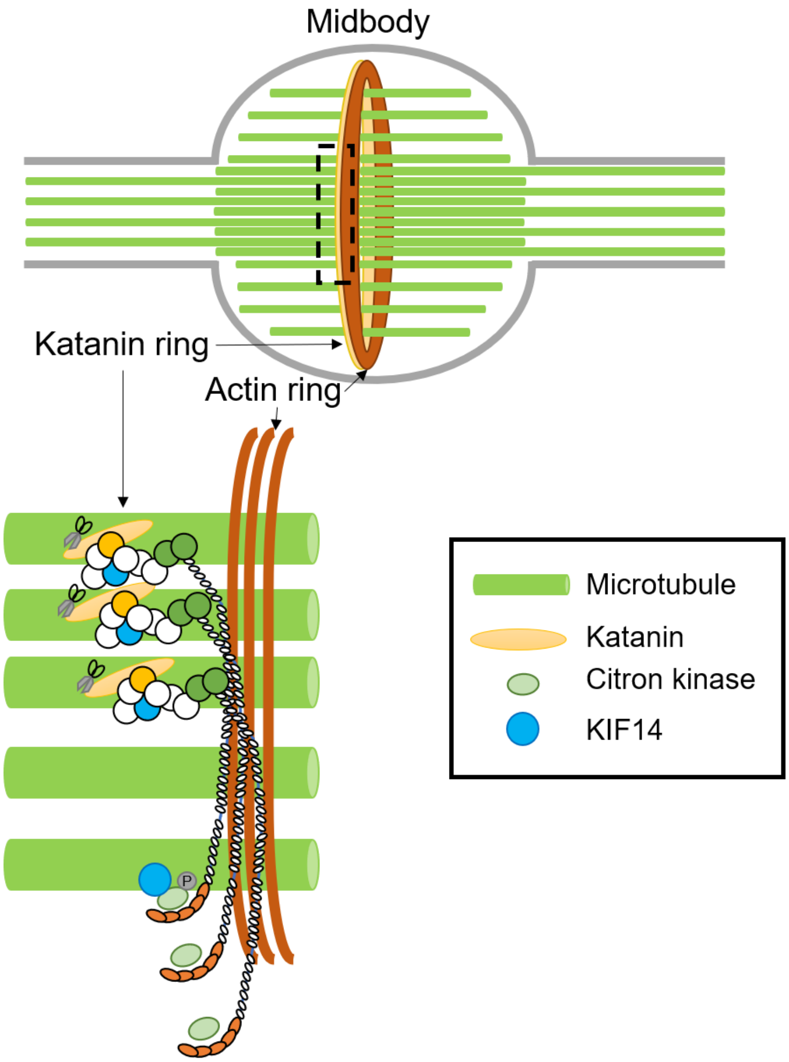

Figure 6.2 – ASPM localises to the midbody during cytokinesis.

A schematic of ASPM (consisting of the ASH domain (light blue), the ASNP (yellow), tandem CH domains (green), IQ motifs (blue) with light chains (white ovals) and ARM repeats (orange)) at the midbody interacting with the actin ring (orange band) through MYL6B bound to its IQ motifs. ASPM interacting with katanin (light yellow) through the ASNP repeats forming the katanin ring which severs microtubules (green rod). The ARM repeats interact with citron kinase (light green), which stabilises microtubules through phosphorylation (grey) and interacts with KIF14 (light blue).

6.2.4 CRIPSR/Cas9 methods are not suited to large mitotic proteins

Multiple unsuccessful attempts were made to introduce a fluorescent tag into the endogenous protein using three different CRISPR/Cas9 methods and introducing the sequence into the C- or N-termini of endogenous ASPM. Tagging either the N-terminus or the C-terminus with mEos3.2

resulted in large amounts of mislocalised ASPM. This indicates that tagging ASPM with this fluorescent protein may interfere with the localisation and degradation pathway. Tagging the N-terminus with eGFP resulted in a shorter isoform of ASPM (~250 kDa) rather than full-length ASPM (~410 kDa), as reported earlier, in experiments in which the N-terminus of endogenous ASPM was tagged with Strep-eGFP (Jiang et al., 2017). However, this isoform was not seen with the C-terminal tag. This may indicate that modifying the N-terminal results in a splicing error, as seen in cancers (Hsu et al., 2019).

6.2.5 Affimers provide a reliable tool for future investigations of endogenous ASPM

An Affimer raised against the tandem CH domains was successful (Chapter 5) and is likely to be a reliable tool to investigate the cellular localisation of ASPM in fixed cells. Once fully validated, it would be interesting to investigate this tool further and determine if it could be used to label ASPM in live cells, as done previously with Affimers to F-actin (Lopata et al., 2018). It would be interesting to determine if the Affimer interferes with the CH-MT interaction, if so then the Affimer may be used as a tool to disrupt this interaction *in vivo* and observe the effect this has on ASPMs ability to function.

6.3 The role of ASPM

The findings reported here have built upon the work of previous studies to gain a better understanding of the function of ASPM in mitosis. From this study, it has been shown that the tandem CH domains bind microtubules, and from previous work, that the upstream ASNP repeats bind katanin, a microtubule severing protein (Jiang et al., 2017). Katanin regulates microtubule dynamics by destabilising microtubules at spindle poles (Shin et al., 2019), which may aid in driving a poleward flux observed during anaphase (Figure 6.3). Citron kinase interacts with the astral microtubules and the C-terminal region of ASPM (Gai et al., 2017). Therefore, if the 81 IQ motifs act as a 295 nm spacer, this would allow the N-terminal region of ASPM to interact with kinetochore microtubules while the C-terminal region interacts with astral microtubules (Figure 6.3).

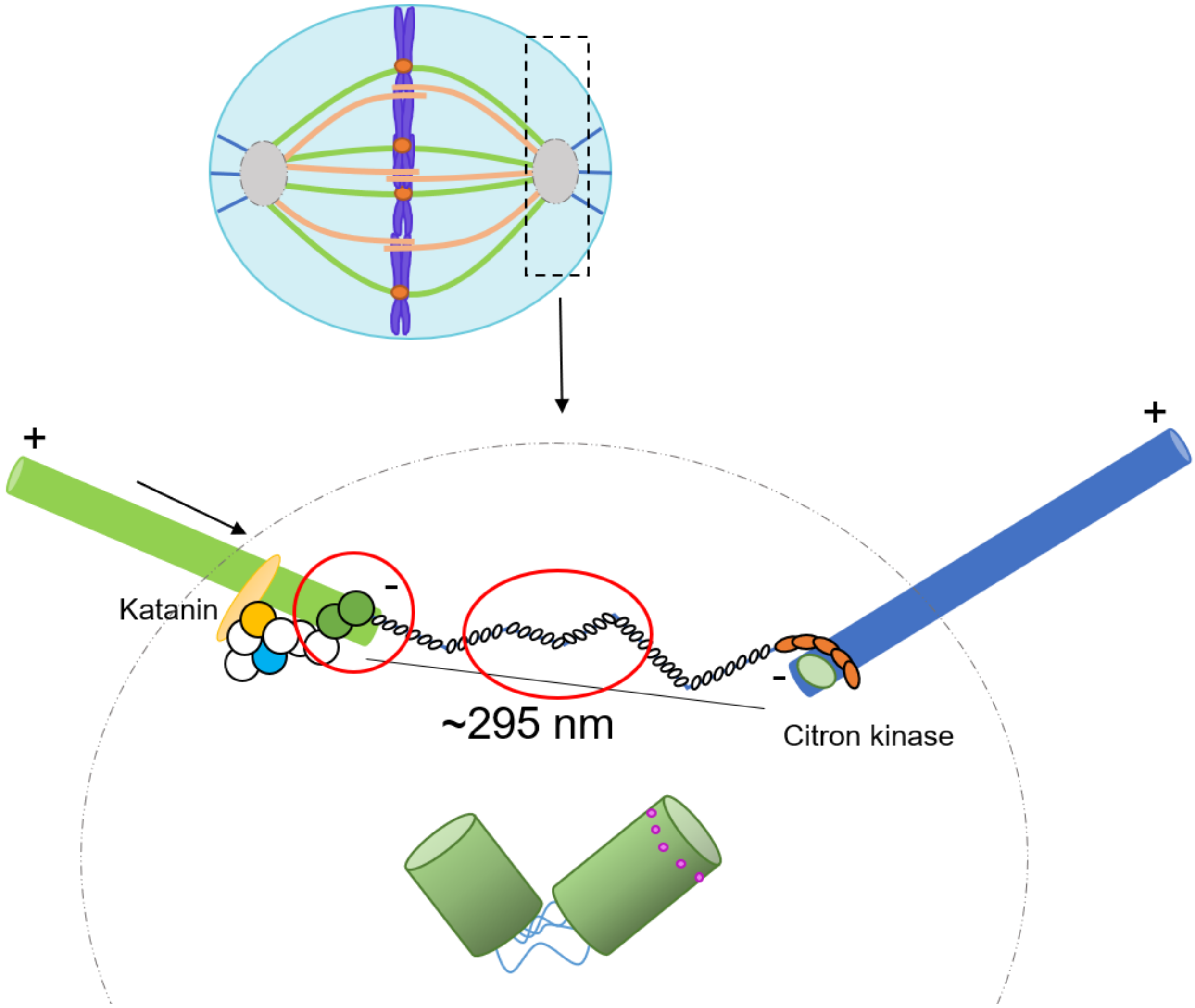

Figure 6.3 – ASPM interacts with kinetochore and astral microtubules through its many domains.

A schematic of ASPM in the pericentriolar matrix in a metaphase cell interacting with the kinetochore microtubules (light green tube) through the CH domains (green) and katanin through the ASNP repeats (yellow). The C-terminal region of ASPM, containing the ARM domain (orange) interacting with citron kinase (light green) which targets the minus end of astral microtubules. The two centrioles (green tubes) are surrounded by a pericentriolar matrix (dotted grey), the mother centriole contains appendages (pink). The areas contributed by this thesis are circled in Red.

During cytokinesis, ASPM localises to the midbody (Higgins et al., 2010). The role ASPM plays here is still unknown. Alongside this, citron kinase, known to interact with the C-terminal region of ASPM plays an important role in abscission control (Bassi et al., 2011), therefore, it is possible that ASPM plays in important part in translocating citron kinase to the midbody. As such, mutations in *ASPM* and ASPM knockdown cause an elongated central spindle and increased time in mitosis, this also interferes with correct abscission causing cytokinesis to occur through mechanical breakage rather than microtubule severing (Aljuhni, 2019).

6.4 Final remarks

This study into ASPM, a very large protein with very little known about the structure, has given some insights into its possible function, but many questions remain. With the novel results outlined here, future research into the other ASPM domains can answer some of these questions. This will allow further understanding of the relationship between structure and function in this important mitotic protein. Thus, aiding in understanding the reason why mutations that lead to the loss of this vital protein causes the dramatic MCPH phenotype, and why its overexpression is associated with cancer.

7. Bibliography

Abdel-Hamid, M. S., Ismail, M. F., Darwish, H. A., Effat, L. K., Zaki, M. S., & Abdel-Salam, G. M. (2016). Molecular and phenotypic spectrum of ASPM-related primary microcephaly: Identification of eight novel mutations. *American journal of medical genetics.Part A*, *170*(8), 2133-2140. https://doi.org/10.1002/ajmg.a.37724 [doi]

Abe, K., Rossman, K. L., Liu, B., Ritola, K. D., Chiang, D., Campbell, S. L., . . . Der, C. J. (2000). Vav2 Is an Activator of Cdc42, Rac1, and RhoA. *Journal of Biological Chemistry*, *275*(14), 10141-10149. https://doi.org/10.1074/jbc.275.14.10141

Abouelhoda, M., Sobahy, T., El-Kalioby, M., Patel, N., Shamseldin, H., Monies, D., . . . Alkuraya, F. S. (2016). Clinical genomics can facilitate countrywide estimation of autosomal recessive disease burden. *Genetics in Medicine*, *18*(12), 1244-1249. https://doi.org/10.1038/gim.2016.37

Acquaviva, C. (2006). The anaphase-promoting complex/cyclosome: APC/C. *Journal of Cell Science*, *119*(12), 2401-2404. https://doi.org/10.1242/jcs.02937

Aebi, U., & Pollard, T. D. (1987). A glow discharge unit to render electron microscope grids and other surfaces hydrophilic. *Journal of Electron Microscopy Technique*, *7*(1), 29. https://doi.org/10.1002/jemt.1060070104

Ahmad, F. J., Yu, W., Mcnally, F. J., & Baas, P. W. (1999). An Essential Role for Katanin in Severing Microtubules in the Neuron. *Journal of Cell Biology*, *145*(2), 305-315. https://doi.org/10.1083/jcb.145.2.305

Ahmad, I., Baig, S. M., Abdulkareem, A. R., Hussain, M. S., Sur, I., Toliat, M. R., . . . Nürnberg, P. (2017). Genetic heterogeneity in Pakistani microcephaly families revisited. *Clinical Genetics*, *92*(1), 62-68. https://doi.org/10.1111/cge.12955

Ahmed, J., Windpassinger, C., Salim, M., Wiener, M., Petek, E., Schaflinger, E., . . . Khan, M. (2019). Genetic Study of Khyber-Pukhtunkhwa Resident Pakistani Families Presenting Primary Microcephaly With Intellectual Disability. *Journal of the Pakistan Medical Association*(0), 1. https://doi.org/10.5455/jpma.300681

Akbariazar, E., Ebrahimpour, M., Akbari, S., Arzhanghi, S., Abedini, S. S., Najmabadi, H., & Kahrizi, K. (2013). A Novel Deletion Mutation in ASPM Gene in an Iranian Family with Autosomal Recessive Primary Microcephaly. (1735-4668 (Print)).

Al-Gazali, L., & Ali, B. R. (2010). Mutations of a country: a mutation review of single gene disorders in the United Arab Emirates (UAE). *Human Mutation*, *31*(5), 505-520. https://doi.org/10.1002/humu.21232

Alabdullatif, M. A., Al Dhaibani, M. A., Khassawneh, M. Y., & El-Hattab, A. W. (2017). Chromosomal microarray in a highly consanguineous population: diagnostic yield, utility of regions of homozygosity, and novel mutations. *Clinical Genetics*, *91*(4), 616-622. https://doi.org/10.1111/cge.12872

Alby, C., Malan, V., Boutaud, L., Marangoni, M. A., Bessières, B., Bonniere, M., . . . Attié-Bitach, T. (2016). Clinical, genetic and neuropathological findings in a series of 138 fetuses with a corpus callosum malformation. *Birth Defects Research Part A: Clinical and Molecular Teratology*, *106*(1), 36-46. https://doi.org/10.1002/bdra.23472

Alfares, A., Alfadhel, M., Wani, T., Alsahli, S., Alluhaydan, I., Al Mutairi, F., . . . Zada, A. A. P. (2017). A multicenter clinical exome study in unselected cohorts from a consanguineous population of Saudi Arabia demonstrated a high diagnostic yield. *Molecular Genetics and Metabolism*, *121*(2), 91-95. https://doi.org/10.1016/j.ymgme.2017.04.002

Alfieri, C., Zhang, S., & Barford, D. (2017). Visualizing the complex functions and mechanisms of the anaphase promoting complex/cyclosome (APC/C). *Open Biology*, *7*(11), 170204. https://doi.org/10.1098/rsob.170204

Alieva, I. B., & Uzbekov, R. E. (2008). The centrosome is a polyfunctional multiprotein cell complex. *Biochemistry.Biokhimiia*, *73*(6), 626-643. https://doi.org/BCM73060782 [pii]

Aljuhni, M. M. A. (2019). *Determining the role of ASPM in human brain size regulation.* PhD Thesis, University of Leeds.

Ariani, F., Mari, F., Amitrano, S., Di Marco, C., Artuso, R., Scala, E., . . . Renieri, A. (2013). Exome sequencing overrides formal genetics: ASPM mutations in a case study of apparent X-linked microcephalic intellectual deficit. *Clinical Genetics*, *83*(3), 288-290. https://doi.org/10.1111/j.1399-0004.2012.01901.x

Asencio, C., Davidson, I. F., Santarella-Mellwig, R., Ly-Hartig, T. B., Mall, M., Wallenfang, M. R., . . . Gorjanacz, M. (2012). Coordination of kinase and phosphatase activities by Lem4 enables nuclear envelope reassembly during mitosis. *Cell*, *150*(1), 122-135. https://doi.org/10.1016/j.cell.2012.04.043 [doi]

Ashford, A. J., & Hyman, A. A. (2006). Chapter 22 - Preparation of Tubulin from Porcine Brain. In J. E. Celis (Ed.), *Cell Biology (Third Edition)* (pp. 155-160). Academic Press. https://doi.org/https://doi.org/10.1016/B978-012164730-8/50094-0

Avery, A. W., Fealey, M. E., Wang, F., Orlova, A., Thompson, A. R., Thomas, D. D., . . . Egelman, E. H. (2017). Structural basis for high-affinity actin binding revealed by a β-III-spectrin SCA5 missense mutation. *Nature Communications*, *8*(1). https://doi.org/10.1038/s41467-017-01367-w

Awad, S., Al-Dosari, M. S., Al-Yacoub, N., Colak, D., Salih, M. A., Alkuraya, F. S., & Poizat, C. (2013). Mutation in PHC1 implicates chromatin remodeling in primary microcephaly pathogenesis. *Human molecular genetics*, *22*(11), 2200-2213. https://doi.org/10.1093/hmg/ddt072 [doi]

Bahler, M., & Rhoads, A. (2002). Calmodulin signaling via the IQ motif. *FEBS letters*, *513*(1), 107-113. https://doi.org/S0014579301032392 [pii]

Barbelanne, M., & Tsang, W. Y. (2014). Molecular and cellular basis of autosomal recessive primary microcephaly. *BioMed research international*, *2014*, 547986. https://doi.org/10.1155/2014/547986 [doi]

Basit, S., Al-Harbi, K. M., Alhijji, S. A., Albalawi, A. M., Alharby, E., Eldardear, A., & Samman, M. I. (2016). CIT, a gene involved in neurogenic cytokinesis, is mutated in human primary microcephaly. *Human genetics*, *135*(10), 1199-1207. https://doi.org/10.1007/s00439-016-1724-0 [doi]

Bassi, Z. I., Verbrugghe, K. J., Capalbo, L., Gregory, S., Montembault, E., Glover, D. M., & D’Avino, P. P. (2011). Sticky/Citron kinase maintains proper RhoA localization at the cleavage site during cytokinesis. *Journal of Cell Biology*, *195*(4), 595-603. https://doi.org/10.1083/jcb.201105136

Bañuelos, S., Saraste, M., & Carugo, K. D. (1998). Structural comparisons of calponin homology domains: implications for actin binding. *Structure*, *6*(11), 1419-1431. https://doi.org/10.1016/s0969-2126(98)00141-5

Bhargav, D. S., Sreedevi, N., Swapna, N., Vivek, S., & Kovvali, S. (2017). Whole exome sequencing identifies a novel homozygous frameshift mutation in the ASPM gene, which causes microcephaly 5, primary, autosomal recessive. *F1000Research*, *6*, 2163. https://doi.org/10.12688/f1000research.12102.1

Bikeye, S.-N., Colin, C., Marie, Y., Vampouille, R., Ravassard, P., Rousseau, A., . . . Sanson, M. (2010). ASPM-associated stem cell proliferation is involved in malignant progression of gliomas and constitutes an attractive therapeutic target. *Cancer Cell International*, *10*(1), 1. https://doi.org/10.1186/1475-2867-10-1

Bond, J., Roberts, E., Mochida, G. H., Hampshire, D. J., Scott, S., Askham, J. M., . . . Woods, C. G. (2002). ASPM is a major determinant of cerebral cortical size. *Nature genetics*, *32*(2), 316-320. https://doi.org/10.1038/ng995 [doi]

Bond, J., Roberts, E., Springell, K., Lizarraga, S. B., Scott, S., Higgins, J., . . . Woods, C. G. (2005). A centrosomal mechanism involving CDK5RAP2 and CENPJ controls brain size. *Nature genetics*, *37*(4), 353-355. https://doi.org/ng1539 [pii]

Bond, J., Scott, S., Hampshire, D. J., Springell, K., Corry, P., Abramowicz, M. J., . . . Woods, C. G. (2003). Protein-truncating mutations in ASPM cause variable reduction in brain size. *American Journal of Human Genetics*, *73*(5), 1170-1177. https://doi.org/S0002-9297(07)61979-X [pii]

Bornens, M. (2012). The centrosome in cells and organisms. *Science (New York, N.Y.)*, *335*(6067), 422-426. https://doi.org/10.1126/science.1209037 [doi]

Borrell, V., & Götz, M. (2014). Role of radial glial cells in cerebral cortex folding. *Current Opinion in Neurobiology*, *27*, 39-46. https://doi.org/10.1016/j.conb.2014.02.007

Bowling, K. M., Thompson, M. L., Amaral, M. D., Finnila, C. R., Hiatt, S. M., Engel, K. L., . . . Cooper, G. M. (2017). Genomic diagnosis for children with intellectual disability and/or developmental delay. *Genome Medicine*, *9*(1). https://doi.org/10.1186/s13073-017-0433-1

Bramham, J., Hodgkinson, J. L., Smith, B. O., UhríN, D., Barlow, P. N., & Winder, S. J. (2002). Solution Structure of the Calponin CH Domain and Fitting to the 3D-Helical Reconstruction of F-Actin:Calponin. *Structure*, *10*(2), 249-258. https://doi.org/10.1016/s0969-2126(02)00703-7

Braun, D. A., Lovric, S., Schapiro, D., Schneider, R., Marquez, J., Asif, M., . . . Hildebrandt, F. (2018). Mutations in multiple components of the nuclear pore complex cause nephrotic syndrome. *Journal of Clinical Investigation*, *128*(10), 4313-4328. https://doi.org/10.1172/jci98688

Bruning-Richardson, A., Bond, J., Alsiary, R., Richardson, J., Cairns, D. A., McCormack, L., . . . Bell, S. M. (2011). ASPM and microcephalin expression in epithelial ovarian cancer correlates with tumour grade and survival. *Br J Cancer*, *104*(10), 1602-1610. https://doi.org/10.1038/bjc.2011.117

Brust-Mascher, I., & Scholey, M., Jonathan. (2011). Mitotic motors and chromosome segregation: the mechanism of anaphase B. *Biochemical Society Transactions*, *39*(5), 1149-1153. https://doi.org/10.1042/bst0391149

Buchman, J. J., Durak, O., & Tsai, L. H. (2011). ASPM regulates Wnt signaling pathway activity in the developing brain. *Genes & development*, *25*(18), 1909-1914. https://doi.org/10.1101/gad.16830211 [doi]

Campanale, J. P., Sun, T. Y., & Montell, D. J. (2017). Development and dynamics of cell polarity at a glance. *Journal of Cell Science*, *130*(7), 1201-1207. https://doi.org/10.1242/jcs.188599

Capecchi, M. R., & Pozner, A. (2015). ASPM regulates symmetric stem cell division by tuning Cyclin E ubiquitination. *Nature communications*, *6*, 8763. https://doi.org/10.1038/ncomms9763 [doi]

Carrington, G., Tomlinson, D., & Peckham, M. (2019). Exploiting nanobodies and Affimers for superresolution imaging in light microscopy. *Molecular Biology of the Cell*, *30*(22), 2737-2740. https://doi.org/10.1091/mbc.e18-11-0694

Case, D. A., Belfon, K., Ben-Shalom, I. Y., Brozell, S. R., Cerutti, D. S., Cheatham, I., T.E., . . . Kollman, P. A. (2020). AMBER 20. In. University of California, San Francisco.

Ceyhan-Birsoy, O., Murry, J. B., Machini, K., Lebo, M. S., Yu, T. W., Fayer, S., . . . Yu, T. W. (2019). Interpretation of Genomic Sequencing Results in Healthy and Ill Newborns: Results from the BabySeq Project. *The American Journal of Human Genetics*, *104*(1), 76-93. https://doi.org/10.1016/j.ajhg.2018.11.016

Chavali, P. L., Putz, M., & Gergely, F. (2014). Small organelle, big responsibility: the role of centrosomes in development and disease. *Philosophical transactions of the Royal*

Society of London.Series B, Biological sciences, *369*(1650), 10.1098/rstb.2013.0468. https://doi.org/10.1098/rstb.2013.0468 [doi]

Cheeseman, I. M. (2014). The Kinetochore. *Cold Spring Harbor Perspectives in Biology*, *6*(7), a015826-a015826. https://doi.org/10.1101/cshperspect.a015826

Cheffings, H., Thomas, Burroughs, J., Nigel, & Balasubramanian, K., Mohan. (2016). Actomyosin Ring Formation and Tension Generation in Eukaryotic Cytokinesis. *Current Biology*, *26*(15), R719-R737. https://doi.org/10.1016/j.cub.2016.06.071

Chen, B.-C., Legant, W. R., Wang, K., Shao, L., Milkie, D. E., Davidson, M. W., . . . Betzig, E. (2014). Lattice light-sheet microscopy: Imaging molecules to embryos at high spatiotemporal resolution. *Science*, *346*(6208), 1257998. https://doi.org/10.1126/science.1257998

Cho, J.-H., Chang, C.-J., Chen, C.-Y., & Tang, T. K. (2006). Depletion of CPAP by RNAi disrupts centrosome integrity and induces multipolar spindles. *Biochemical and Biophysical Research Communications*, *339*(3), 742-747. https://doi.org/10.1016/j.bbrc.2005.11.074

Chou, Y.-H., Bischoff, J. R., Beach, D., & Goldman, R. D. (1990). Intermediate filament reorganization during mitosis is mediated by p34cdc2 phosphorylation of vimentin. *Cell*, *62*(6), 1063-1071. https://doi.org/10.1016/0092-8674(90)90384-q

Coates, J. (2003). Armadillo repeat proteins: beyond the animal kingdom. *Trends in Cell Biology*, *13*(9), 463-471. https://doi.org/10.1016/s0962-8924(03)00167-3

Cox, J., Jackson, A. P., Bond, J., & Woods, C. G. (2006). What primary microcephaly can tell us about brain growth. *Trends in molecular medicine*, *12*(8), 358-366. https://doi.org/S1471-4914(06)00136-5 [pii]

Darvish, H., Esmaeeli-Nieh, S., Monajemi, G. B., Mohseni, M., Ghasemi-Firouzabadi, S., Abedini, S. S., . . . Najmabadi, H. (2010). A clinical and molecular genetic study of 112 Iranian families with primary microcephaly. *Journal of Medical Genetics*, *47*(12), 823-828. https://doi.org/10.1136/jmg.2009.076398

Desir, J., Abramowicz, M., & Tunca, Y. (2006). Novel mutations in prenatal diagnosis of primary microcephaly. *Prenatal Diagnosis*, *26*(10), 989-989. https://doi.org/10.1002/pd.1536

Desir, J., Cassart, M., David, P., Van Bogaert, P., & Abramowicz, M. (2008). Primary microcephaly with ASPM mutation shows simplified cortical gyration with antero-posterior gradient pre- and post-natally. *American Journal of Medical Genetics Part A*, *146A*(11), 1439-1443. https://doi.org/10.1002/ajmg.a.32312

Distasio, A., Driver, A., Sund, K., Donlin, M., Muraleedharan, R. M., Pooya, S., . . . Stottmann, R. W. (2017). Copb2 is essential for embryogenesis and hypomorphic mutations cause human microcephaly. *Human Molecular Genetics*, *26*(24), 4836-4848. https://doi.org/10.1093/hmg/ddx362

do Carmo Avides, M., & Glover, D. M. (1999). Abnormal spindle protein, Asp, and the integrity of mitotic centrosomal microtubule organizing centers. *Science (New York, N.Y.)*, *283*(5408), 1733-1735.

do Carmo Avides, M., Tavares, A., & Glover, D. M. (2001). Polo kinase and Asp are needed to promote the mitotic organizing activity of centrosomes. *Nature cell biology*, *3*(4), 421-424. https://doi.org/10.1038/35070110 [doi]

Duerinckx, S., & Abramowicz, M. (2018). The genetics of congenitally small brains. *Seminars in Cell & Developmental Biology*, *76*, 76-85. https://doi.org/10.1016/j.semcdb.2017.09.015

Elting, M. W., Hueschen, C. L., Udy, D. B., & Dumont, S. (2014). Force on spindle microtubule minus ends moves chromosomes. *Journal of Cell Biology*, *206*(2), 245-256. https://doi.org/10.1083/jcb.201401091

Faheem, M., Naseer, M. I., Rasool, M., Chaudhary, A. G., Kumosani, T. A., Ilyas, A. M., . . . Saleh Jamal, H. (2015). Molecular genetics of human primary microcephaly: an overview. *BMC medical genomics*, *8 Suppl 1*, S4-8794-8798-S8791-S8794. Epub 2015 Jan 8715. https://doi.org/10.1186/1755-8794-8-S1-S4 [doi]

Fernandez-Leiro, R., & Scheres, S. H. W. (2017). A pipeline approach to single-particle processing inRELION. *Acta Crystallographica Section D Structural Biology*, *73*(6), 496-502. https://doi.org/10.1107/s2059798316019276

Fish, J. L., Kosodo, Y., Enard, W., Paabo, S., & Huttner, W. B. (2006). Aspm specifically maintains symmetric proliferative divisions of neuroepithelial cells. *Proceedings of the National Academy of Sciences of the United States of America*, *103*(27), 10438-10443. https://doi.org/0604066103 [pii]

Fricker, L. D. (2015). Limitations of Mass Spectrometry-Based Peptidomic Approaches. *Journal of The American Society for Mass Spectrometry*, *26*(12), 1981-1991. https://doi.org/10.1007/s13361-015-1231-x

Frémont, S., Hammich, H., Bai, J., Wioland, H., Klinkert, K., Rocancourt, M., . . . Echard, A. (2017). Oxidation of F-actin controls the terminal steps of cytokinesis. *Nature Communications*, *8*(1), 14528. https://doi.org/10.1038/ncomms14528

Gai, M., Bianchi, F. T., Vagnoni, C., Verni, F., Bonaccorsi, S., Pasquero, S., . . . Di Cunto, F. (2017). ASPM and CITK regulate spindle orientation by affecting the dynamics of astral microtubules (vol 17, pg 1396, 2016). *Embo Reports*, *18*(10), 1870-1870.

Genin, A., Desir, J., Lambert, N., Biervliet, M., Van Der Aa, N., Pierquin, G., . . . Abramowicz, M. (2012). Kinetochore KMN network gene CASC5 mutated in primary microcephaly. *Human molecular genetics*, *21*(24), 5306-5317. https://doi.org/10.1093/hmg/dds386 [doi]

Gibson, D. G., Young, L., Chuang, R.-Y., Venter, J. C., Hutchison, C. A., & Smith, H. O. (2009). Enzymatic assembly of DNA molecules up to several hundred kilobases. *Nature Methods*, *6*(5), 343-345. https://doi.org/10.1038/nmeth.1318

Gil-Sanz, C., Franco, J., Santos, Martinez-Garay, I., Espinosa, A., Harkins-Perry, S., & Müller, U. (2013). Cajal-Retzius Cells Instruct Neuronal Migration by Coincidence Signaling between Secreted and Contact-Dependent Guidance Cues. *Neuron*, *79*(3), 461-477. https://doi.org/10.1016/j.neuron.2013.06.040

Gimona, M., Djinovic-Carugo, K., Kranewitter, W. J., & Winder, S. J. (2002). Functional plasticity of CH domains. *FEBS letters*, *513*(1), 98-106. https://doi.org/S0014579301032409 [pii]

Golovanov, A. P., Hautbergue Gm Fau - Wilson, S. A., Wilson Sa Fau - Lian, L.-Y., & Lian, L. Y. (2004). A simple method for improving protein solubility and long-term stability. (0002-7863 (Print)).

Gong, S., Yu, H. H., Johnson, K. A., & Taylor, D. W. (2018). DNA Unwinding Is the Primary Determinant of CRISPR-Cas9 Activity. *Cell Reports*, *22*(2), 359-371. https://doi.org/10.1016/j.celrep.2017.12.041

Guemez-Gamboa, A., Nguyen, L. N., Yang, H., Zaki, M. S., Kara, M., Ben-Omran, T., . . . Gleeson, J. G. (2015). Inactivating mutations in MFSD2A, required for omega-3 fatty acid transport in brain, cause a lethal microcephaly syndrome. *Nature genetics*, *47*(7), 809-813. https://doi.org/10.1038/ng.3311 [doi]

Guernsey, D. L., Jiang, H., Hussin, J., Arnold, M., Bouyakdan, K., Perry, S., . . . Samuels, M. E. (2010). Mutations in centrosomal protein CEP152 in primary microcephaly families linked to MCPH4. *American Journal of Human Genetics*, *87*(1), 40-51. https://doi.org/10.1016/j.ajhg.2010.06.003 [doi]

Gul, A., Hassan, M. J., Mahmood, S., Chen, W., Rahmani, S., Naseer, M. I., . . . Ahmad, W. (2006). Genetic studies of autosomal recessive primary microcephaly in 33 Pakistani families: novel sequence variants in ASPM gene. *Neurogenetics*, *7*(2), 105-110. https://doi.org/10.1007/s10048-006-0042-4

Gul, A., Tariq, M., Khan, M. N., Hassan, M. J., Ali, G., & Ahmad, W. (2007). NOVEL PROTEIN-TRUNCATING MUTATIONS IN THEASPMGENE IN FAMILIES WITH AUTOSOMAL

RECESSIVE PRIMARY MICROCEPHALY. *Journal of Neurogenetics*, *21*(3), 153-163. https://doi.org/10.1080/01677060701508594

Götz, M., & Huttner, W. B. (2005). The cell biology of neurogenesis. *Nature Reviews Molecular Cell Biology*, *6*(10), 777-788. https://doi.org/10.1038/nrm1739

Güttinger, S., Laurell, E., & Kutay, U. (2009). Orchestrating nuclear envelope disassembly and reassembly during mitosis. *Nature Reviews Molecular Cell Biology*, *10*(3), 178-191. https://doi.org/10.1038/nrm2641

Hagemann, C. (2008). Expression analysis of the autosomal recessive primary microcephaly genes MCPH1 (microcephalin) and MCPH5 (ASPM, abnormal spindle-like, microcephaly associated) in human malignant gliomas. *Oncology Reports*. https://doi.org/10.3892/or_00000007

Halsall, S., Nicholas, A. K., Thornton, G., Martin, H., & Geoffrey Woods, C. (2010). Critical consequences of finding three pathogenic mutations in an individual with recessive disease. *Journal of Medical Genetics*, *47*(11), 769-770. https://doi.org/10.1136/jmg.2010.079277

Hancock, W. O., & Howard, J. (1998). Processivity of the Motor Protein Kinesin Requires Two Heads. *The Journal of Cell Biology*, *140*(6), 1395-1405. https://doi.org/10.1083/jcb.140.6.1395

Hansen, D. V., Lui, J. H., Parker, P. R. L., & Kriegstein, A. R. (2010). Neurogenic radial glia in the outer subventricular zone of human neocortex. *Nature*, *464*(7288), 554-561. https://doi.org/10.1038/nature08845

Hashmi, J. A., Al-Harbi, K. M., Ramzan, K., Albalawi, A. M., Mehmood, A., Samman, M. I., & Basit, S. (2016). A novel splice-site mutation in the ASPM gene underlies autosomal recessive primary microcephaly. *Annals of Saudi Medicine*, *36*(6), 391-396. https://doi.org/10.5144/0256-4947.2016.391

Hayashi, I., & Ikura, M. (2003). Crystal Structure of the Amino-terminal Microtubule-binding Domain of End-binding Protein 1 (EB1). *Journal of Biological Chemistry*, *278*(38), 36430-36434. https://doi.org/10.1074/jbc.m305773200

Heissler, S. M., & Sellers, J. R. (2014). Myosin light chains: Teaching old dogs new tricks. *BioArchitecture*, *4*(6), 169-188. https://doi.org/10.1080/19490992.2015.1054092

Hemmings, L., Kuhlman, P. A., & Critchley, D. R. (1992). Analysis of the actin-binding domain of alpha-actinin by mutagenesis and demonstration that dystrophin contains a functionally homologous domain. *The Journal of Cell Biology*, *116*(6), 1369-1380. https://doi.org/10.1083/jcb.116.6.1369

Hepler, P. K. (1994). The role of calcium in cell division. *Cell Calcium*, *16*(4), 322-330. https://doi.org/10.1016/0143-4160(94)90096-5

Hernández-Vega, A., Braun, M., Scharrel, L., Jahnel, M., Wegmann, S., Hyman, B. T., . . . Hyman, A. A. (2017). *Local nucleation of microtubule bundles through tubulin concentration into a condensed tau phase*. Cold Spring Harbor Laboratory.

Higgins, J., Midgley, C., Bergh, A. M., Bell, S. M., Askham, J. M., Roberts, E., . . . Bond, J. (2010). Human ASPM participates in spindle organisation, spindle orientation and cytokinesis. *BMC cell biology*, *11*, 85-2121-2111-2185. https://doi.org/10.1186/1471-2121-11-85 [doi]

Hopkins, R., & Esposito, D. (2009). A rapid method for titrating baculovirus stocks using the Sf-9 Easy Titer cell line. *BioTechniques*, *47*(3), 785-788. https://doi.org/10.2144/000113238 [doi]

Houdusse, A., & Cohen, C. (1995). Target sequence recognition by the calmodulin superfamily: implications from light chain binding to the regulatory domain of scallop myosin. *Proceedings of the National Academy of Sciences of the United States of America*, *92*(23), 10644-10647.

Houdusse, A., Silver, M., & Cohen, C. (1996). A model of Ca(2+)-free calmodulin binding to unconventional myosins reveals how calmodulin acts as a regulatory switch. *Structure (London, England : 1993)*, *4*(12), 1475-1490.

Hoyt, M. A. (2001). A new view of the spindle checkpoint. *Journal of Cell Biology*, *154*(5), 909-912. https://doi.org/10.1083/jcb.200108010

Hsu, C. C., Liao, W. Y., Chan, T. S., Chen, W. Y., Lee, C. T., Shan, Y. S., . . . Tsai, K. K. (2019). The differential distributions of ASPM isoforms and their roles in Wnt signaling, cell cycle progression, and pancreatic cancer prognosis. *The Journal of Pathology*, *249*(4), 498-508. https://doi.org/10.1002/path.5341

Hu, H., Kahrizi, K., Musante, L., Fattahi, Z., Herwig, R., Hosseini, M., . . . Najmabadi, H. (2019). Genetics of intellectual disability in consanguineous families. *Molecular Psychiatry*, *24*(7), 1027-1039. https://doi.org/10.1038/s41380-017-0012-2

Hu, H., Suckow, V., Musante, L., Roggenkamp, V., Kraemer, N., Ropers, H.-H., . . . Kaindl, A. M. (2014). Previously reported new type of autosomal recessive primary microcephaly is caused by compound heterozygousASPMgene mutations. *Cell Cycle*, *13*(10), 1650-1651. https://doi.org/10.4161/cc.28706

Huber, A. H., Nelson, W. J., & Weis, W. I. (1997). Three-dimensional structure of the armadillo repeat region of beta-catenin. *Cell*, *90*(5), 871-882. https://doi.org/S0092-8674(00)80352-9 [pii]

Hussain, M. S., Baig, S. M., Neumann, S., Nurnberg, G., Farooq, M., Ahmad, I., . . . Nurnberg, P. (2012). A truncating mutation of CEP135 causes primary microcephaly and disturbed centrosomal function. *American Journal of Human Genetics*, *90*(5), 871-878. https://doi.org/10.1016/j.ajhg.2012.03.016 [doi]

Hussain, M. S., Baig, S. M., Neumann, S., Peche, V. S., Szczepanski, S., Nurnberg, G., . . . Noegel, A. A. (2013). CDK6 associates with the centrosome during mitosis and is mutated in a large Pakistani family with primary microcephaly. *Human molecular genetics*, *22*(25), 5199-5214. https://doi.org/10.1093/hmg/ddt374 [doi]

Iossifov, I., O'Roak, B. J., Sanders, S. J., Ronemus, M., Krumm, N., Levy, D., . . . Wigler, M. (2014). The contribution of de novo coding mutations to autism spectrum disorder. *Nature*, *515*(7526), 216-221. https://doi.org/10.1038/nature13908

Ishida, H., Borman, M. A., Ostrander, J., Vogel, H. J., & Macdonald, J. A. (2008). Solution Structure of the Calponin Homology (CH) Domain from the Smoothelin-like 1 Protein. *Journal of Biological Chemistry*, *283*(29), 20569-20578. https://doi.org/10.1074/jbc.m800627200

Issa, L., Kraemer, N., Rickert, C. H., Sifringer, M., Ninnemann, O., Stoltenburg-Didinger, G., & Kaindl, A. M. (2013). CDK5RAP2 expression during murine and human brain development correlates with pathology in primary autosomal recessive microcephaly. *Cerebral cortex (New York, N.Y.: 1991)*, *23*(9), 2245-2260. https://doi.org/10.1093/cercor/bhs212 [doi]

Ito, A., & Goshima, G. (2015). Microcephaly protein Asp focuses the minus ends of spindle microtubules at the pole and within the spindle. *The Journal of cell biology*, *211*(5), 999-1009. https://doi.org/10.1083/jcb.201507001 [doi]

Jang, D.-J., Ban, B., & Lee, J.-A. (2011). Characterization of novel calmodulin binding domains within IQ motifs of IQGAP1. *Molecules and Cells*, *32*(6), 511-518. https://doi.org/10.1007/s10059-011-0109-4

Janke, C., & Montagnac, G. (2017). Causes and Consequences of Microtubule Acetylation. *Current Biology*, *27*(23), R1287-R1292. https://doi.org/10.1016/j.cub.2017.10.044

Jayaraman, D., Kodani, A., Gonzalez, D. M., Mancias, J. D., Mochida, G. H., Vagnoni, C., . . . Walsh, C. A. (2016). Microcephaly Proteins Wdr62 and Aspm Define a Mother Centriole Complex Regulating Centriole Biogenesis, Apical Complex, and Cell Fate. *Neuron*, *92*(4), 813-828. https://doi.org/10.1016/j.neuron.2016.09.056

Jiang, K., Rezabkova, L., Hua, S., Liu, Q., Capitani, G., Altelaar, A. F., . . . Akhmanova, A. (2017). Microtubule minus-end regulation at spindle poles by an ASPM-katanin complex. *Nature cell biology*, *19*(5), 480-492. https://doi.org/10.1038/ncb3511 [doi]

Jinek, M., Chylinski, K., Fonfara, I., Hauer, M., Doudna, J. A., & Charpentier, E. (2012). A programmable dual-RNA-guided DNA endonuclease in adaptive bacterial immunity. *Science (New York, N.Y.)*, *337*(6096), 816-821. https://doi.org/10.1126/science.1225829 [doi]

Kadir, R., Harel, T., Markus, B., Perez, Y., Bakhrat, A., Cohen, I., . . . Birk, O. S. (2016). ALFY-Controlled DVL3 Autophagy Regulates Wnt Signaling, Determining Human Brain Size. *PLOS Genetics*, *12*(3), e1005919. https://doi.org/10.1371/journal.pgen.1005919

Kahrizi, K., Hu, H., Hosseini, M., Kalscheuer, V. M., Fattahi, Z., Beheshtian, M., . . . Ropers, H. H. (2019). Effect of inbreeding on intellectual disability revisited by trio sequencing. *Clinical Genetics*, *95*(1), 151-159. https://doi.org/10.1111/cge.13463

Kaindl, A. M., Passemard, S., Kumar, P., Kraemer, N., Issa, L., Zwirner, A., . . . Gressens, P. (2010). Many roads lead to primary autosomal recessive microcephaly. *Progress in neurobiology*, *90*(3), 363-383. https://doi.org/10.1016/j.pneurobio.2009.11.002 [doi]

Kajava, A. V., Gorbea, C., Ortega, J. N., Rechsteiner, M., & Steven, A. C. (2004). New HEAT-like repeat motifs in proteins regulating proteasome structure and function. *Journal of Structural Biology*, *146*(3), 425-430. https://doi.org/10.1016/j.jsb.2004.01.013

Kamiyama, D., Sekine, S., Barsi-Rhyne, B., Hu, J., Chen, B., Gilbert, L. A., . . . Huang, B. (2016). Versatile protein tagging in cells with split fluorescent protein. *Nature communications*, *7*, 11046. https://doi.org/10.1038/ncomms11046 [doi]

Karaca, E., Harel, T., Pehlivan, D., Jhangiani, N., Shalini, Gambin, T., Akdemir, C., Zeynep, . . . Lupski, R., James. (2015). Genes that Affect Brain Structure and Function Identified by Rare Variant Analyses of Mendelian Neurologic Disease. *Neuron*, *88*(3), 499-513. https://doi.org/10.1016/j.neuron.2015.09.048

Kato, T. A., Okayasu, R., Jeggo, P. A., & Fujimori, A. (2011). ASPM influences DNA double-strand break repair and represents a potential target for radiotherapy. *International Journal of Radiation Biology*, *87*(12), 1189-1195. https://doi.org/10.3109/09553002.2011.624152

Kavran, J. M., & Leahy, D. J. (2014). Coupling Antibody to Cyanogen Bromide-Activated Sepharose. In (pp. 27-34). Elsevier. https://doi.org/10.1016/b978-0-12-420119-4.00003-3

Kemp, C. A., Kopish, K. R., Zipperlen, P., Ahringer, J., & O'Connell, K. F. (2004). Centrosome Maturation and Duplication in C. elegans Require the Coiled-Coil Protein SPD-2. *Developmental Cell*, *6*(4), 511-523. https://doi.org/10.1016/s1534-5807(04)00066-8

Khan, A., Wang, R., Han, S., Ahmad, W., & Zhang, X. (2018). Identification of a Novel Nonsense ASPM Mutation in a Large Consanguineous Pakistani Family Using Targeted Next-Generation Sequencing. (1945-0257 (Electronic)).

Khan, M. A., Rupp, V. M., Orpinell, M., Hussain, M. S., Altmuller, J., Steinmetz, M. O., . . . Windpassinger, C. (2014). A missense mutation in the PISA domain of HsSAS-6 causes autosomal recessive primary microcephaly in a large consanguineous Pakistani family. *Human molecular genetics*, *23*(22), 5940-5949. https://doi.org/10.1093/hmg/ddu318 [doi]

Khan, M. A., Windpassinger, C., Ali, M. Z., Zubair, M., Gul, H., Abbas, S., . . . Nawaz, Z. (2017). Molecular genetic analysis of consanguineous families with primary microcephaly identified pathogenic variants in the ASPM gene. *Journal of Genetics*, *96*(2), 383-387. https://doi.org/10.1007/s12041-017-0759-x

Kim, J., Ghosh, S., Liu, H., Tateyama, M., Kass, R. S., & Pitt, G. S. (2004). Calmodulin Mediates Ca2+ Sensitivity of Sodium Channels. *Journal of Biological Chemistry*, *279*(43), 45004-45012. https://doi.org/10.1074/jbc.m407286200

Kippert, F., & Gerloff, D. L. (2004). Timeless and Armadillo: A link too far (Comment on Vodovar et al. Curr. Biol. (2002) 12, R610–R611). *Current Biology*, *14*(16), R650-R651. https://doi.org/10.1016/j.cub.2004.08.008

Kippert, F., & Gerloff, D. L. (2009). Highly Sensitive Detection of Individual HEAT and ARM Repeats with HHpred and COACH. *PLoS ONE*, *4*(9), e7148. https://doi.org/10.1371/journal.pone.0007148

Kirschner, M. (1986). Beyond self-assembly: From microtubules to morphogenesis. *Cell*, *45*(3), 329-342. https://doi.org/10.1016/0092-8674(86)90318-1

Kolakowski, J., Makuch, R., Stepkowski, D., & Dabrowska, R. (1995). Interaction of calponin with actin and its functional implications. *The Biochemical journal*, *306 (Pt 1)*(Pt 1), 199-204.

Korenbaum, E., & Rivero, F. (2002). Calponin homology domains at a glance. *Journal of cell science*, *115*(Pt 18), 3543-3545.

Kouprina, N., Pavlicek, A., Collins, N. K., Nakano, M., Noskov, V. N., Ohzeki, J., . . . Larionov, V. (2005). The microcephaly ASPM gene is expressed in proliferating tissues and encodes for a mitotic spindle protein. *Human molecular genetics*, *14*(15), 2155-2165. https://doi.org/ddi220 [pii]

Kousar, R., Nawaz, H., Khurshid, M., Ali, G., Khan, S. U., Mir, H., . . . Ansar, M. (2009). Mutation Analysis of the ASPM Gene in 18 Pakistani Families With Autosomal Recessive Primary Microcephaly. *Journal of Child Neurology*, *25*(6), 715-720. https://doi.org/10.1177/0883073809346850

Kraemer, N., Picker-Minh, S., Abbasi, A. A., Fröhler, S., Ninnemann, O., Khan, M. N., . . . Kaindl, A. M. (2016). Genetic causes of MCPH in consanguineous Pakistani families. *Clinical Genetics*, *89*(6), 744-745. https://doi.org/10.1111/cge.12685

Kubala, M. H., Kovtun, O., Alexandrov, K., & Collins, B. M. (2010). Structural and thermodynamic analysis of the GFP:GFP-nanobody complex. *Protein Science*, *19*(12), 2389-2401. https://doi.org/10.1002/pro.519

Kumar, A., Blanton, S., Babu, M., Markandaya, M., & Girimaji, S. (2004). Genetic analysis of primary microcephaly in Indian families: novel ASPM mutations. *Clinical Genetics*, *66*(4), 341-348. https://doi.org/10.1111/j.1399-0004.2004.00304.x

Kumar, A., Girimaji, S. C., Duvvari, M. R., & Blanton, S. H. (2009). Mutations in STIL, encoding a pericentriolar and centrosomal protein, cause primary microcephaly. *American Journal of Human Genetics*, *84*(2), 286-290. https://doi.org/10.1016/j.ajhg.2009.01.017 [doi]

Lagos-Cabré, R., Ivanova, A., & Taylor, C. W. (2020). Ca2+ Release by IP3 Receptors Is Required to Orient the Mitotic Spindle. *Cell Reports*, *33*(11), 108483. https://doi.org/10.1016/j.celrep.2020.108483

Lai, M., Brun, D., Edelstein, S. J., & Le Novère, N. (2015). Modulation of Calmodulin Lobes by Different Targets: An Allosteric Model with Hemiconcerted Conformational Transitions. *PLOS Computational Biology*, *11*(1), e1004063. https://doi.org/10.1371/journal.pcbi.1004063

Leinweber, B. D., Leavis, P. C., Grabarek, Z., Wang, C. L., & Morgan, K. G. (1999). Extracellular regulated kinase (ERK) interaction with actin and the calponin homology (CH) domain of actin-binding proteins. *The Biochemical journal*, *344 Pt 1*(Pt 1), 117-123.

Leonetti, M. D., Sekine, S., Kamiyama, D., Weissman, J. S., & Huang, B. (2016). A scalable strategy for high-throughput GFP tagging of endogenous human proteins. *Proceedings of the National Academy of Sciences of the United States of America*, *113*(25), E3501-3508. https://doi.org/10.1073/pnas.1606731113 [doi]

Lin, A. Y., Prochniewicz, E., James, Z. M., Svensson, B., & Thomas, D. D. (2011). Large-scale opening of utrophin's tandem calponin homology (CH) domains upon actin binding by an induced-fit mechanism. *Proceedings of the National Academy of Sciences*, *108*(31), 12729-12733. https://doi.org/10.1073/pnas.1106453108

Lin, S., Staahl, B. T., Alla, R. K., & Doudna, J. A. (2014). Enhanced homology-directed human genome engineering by controlled timing of CRISPR/Cas9 delivery. *3*. https://doi.org/10.7554/elife.04766

Liu, R., & Jin, J.-P. (2016). Calponin isoforms CNN 1, CNN 2 and CNN 3: Regulators for actin cytoskeleton functions in smooth muscle and non-muscle cells. *Gene*, *585*(1), 143-153. https://doi.org/10.1016/j.gene.2016.02.040

Liu, Y., & Robinson, D. (2018). Recent advances in cytokinesis: understanding the molecular underpinnings. *F1000Research*, *7*, 1849. https://doi.org/10.12688/f1000research.16502.1

Logvinova, D. S., & Levitsky, D. I. (2018). Essential Light Chains of Myosin and Their Role in Functioning of the Myosin Motor. *Biochemistry (Moscow)*, *83*(8), 944-960. https://doi.org/10.1134/s0006297918080060

Lopata, A., Hughes, R., Tiede, C., Heissler, S. M., Sellers, J. R., Knight, P. J., . . . Peckham, M. (2018). Affimer proteins for F-actin: novel affinity reagents that label F-actin in live and fixed cells. *Scientific Reports*, *8*(1). https://doi.org/10.1038/s41598-018-24953-4

Lu, Q., Li, J., Ye, F., & Zhang, M. (2015). Structure of myosin-1c tail bound to calmodulin provides insights into calcium-mediated conformational coupling. *Nature Structural & Molecular Biology*, *22*(1), 81-88. https://doi.org/10.1038/nsmb.2923

Lumb, J. H., Connell, J. W., Allison, R., & Reid, E. (2012). The AAA ATPase spastin links microtubule severing to membrane modelling. *Biochimica et Biophysica Acta (BBA) - Molecular Cell Research*, *1823*(1), 192-197. https://doi.org/10.1016/j.bbamcr.2011.08.010

Létard, P., Drunat, S., Vial, Y., Duerinckx, S., Ernault, A., Amram, D., . . . Passemard, S. (2018). Autosomal recessive primary microcephaly due to ASPM mutations: An update. *Human Mutation*, *39*(3), 319-332. https://doi.org/10.1002/humu.23381

Ma, Hoi T., & Poon, Randy Y. C. (2011). How protein kinases co-ordinate mitosis in animal cells. *Biochemical Journal*, *435*(1), 17-31. https://doi.org/10.1042/bj20100284

Maddox, P., Desai, A., Oegema, K., Mitchison, T. J., & Salmon, E. D. (2002). Poleward Microtubule Flux Is a Major Component of Spindle Dynamics and Anaphase A in Mitotic Drosophila Embryos. *Current Biology*, *12*(19), 1670-1674. https://doi.org/10.1016/s0960-9822(02)01183-1

Maller, J. L. (1986). Mitogenic signalling and protein phosphorylation in Xenopus oocytes. *Journal of cyclic nucleotide and protein phosphorylation research*, *11*(7), 543-555.

Mann, B. J., & Wadsworth, P. (2018). Distribution of Eg5 and TPX2 in mitosis: Insight from CRISPR tagged cells. *Cytoskeleton*, *75*(12), 508-521. https://doi.org/10.1002/cm.21486

Marakhonov, A. V., Konovalov, F. A., Makaov, A. K., Vasilyeva, T. A., Kadyshev, V. V., Galkina, V. A., . . . Zinchenko, R. A. (2018). Primary microcephaly case from the Karachay-Cherkess Republic poses an additional support for microcephaly and Seckel syndrome spectrum disorders. *BMC Medical Genomics*, *11*(S1). https://doi.org/10.1186/s12920-018-0326-1

Martin, C.-A., Murray, J. E., Carroll, P., Leitch, A., Mackenzie, K. J., Halachev, M., . . . Jackson, A. P. (2016). Mutations in genes encoding condensin complex proteins cause microcephaly through decatenation failure at mitosis. *Genes & Development*, *30*(19), 2158-2172. https://doi.org/10.1101/gad.286351.116

Martínez-Balbás, M. A., Dey, A., Rabindran, S. K., Ozato, K., & Wu, C. (1995). Displacement of sequence-specific transcription factors from mitotic chromatin. *Cell*, *83*(1), 29-38. https://doi.org/10.1016/0092-8674(95)90231-7

Matsuo, M., Shimodaira, T., Kasama, T., Hata, Y., Echigo, A., Okabe, M., . . . Kishimoto, T. (2013). Katanin p60 Contributes to Microtubule Instability around the Midbody and Facilitates Cytokinesis in Rat Cells. *PLoS ONE*, *8*(11), e80392. https://doi.org/10.1371/journal.pone.0080392

Maurer, S. P., Bieling, P., Cope, J., Hoenger, A., & Surrey, T. (2011). GTP S microtubules mimic the growing microtubule end structure recognized by end-binding proteins (EBs). *Proceedings of the National Academy of Sciences*, *108*(10), 3988-3993. https://doi.org/10.1073/pnas.1014758108

Mayor, R., & Theveneau, E. (2014). The role of the non-canonical Wnt-planar cell polarity pathway in neural crest migration. *The Biochemical journal*, *457*(1), 19-26. https://doi.org/10.1042/BJ20131182 [doi]

Mcintosh, J. R. (2016). Mitosis. *Cold Spring Harbor Perspectives in Biology*, *8*(9), a023218. https://doi.org/10.1101/cshperspect.a023218

Mcintosh, J. R., Molodtsov, M. I., & Ataullakhanov, F. I. (2012). Biophysics of mitosis. *Quarterly Reviews of Biophysics*, *45*(2), 147-207. https://doi.org/10.1017/s0033583512000017

Mckenzie, C., Bassi, Z. I., Debski, J., Gottardo, M., Callaini, G., Dadlez, M., & D'Avino, P. P. (2016). Cross-regulation between Aurora B and Citron kinase controls midbody architecture in cytokinesis. *Open Biology*, *6*(3), 160019. https://doi.org/10.1098/rsob.160019

Mcneely, K. C., & Dwyer, N. D. (2020). Cytokinesis and postabscission midbody remnants are regulated during mammalian brain development. *Proceedings of the National Academy of Sciences*, *117*(17), 9584-9593. https://doi.org/10.1073/pnas.1919658117

Mcsherry, M., Masih, K. E., Elcioglu, N. H., Celik, P., Balci, O., Cengiz, F. B., . . . Tekin, M. (2018). Identification of candidate gene FAM183A and novel pathogenic variants in known genes: High genetic heterogeneity for autosomal recessive intellectual disability. *PLOS ONE*, *13*(11), e0208324. https://doi.org/10.1371/journal.pone.0208324

Meng, L., Pammi, M., Saronwala, A., Magoulas, P., Ghazi, A. R., Vetrini, F., . . . Lalani, S. R. (2017). Use of Exome Sequencing for Infants in Intensive Care Units. *JAMA Pediatrics*, *171*(12), e173438. https://doi.org/10.1001/jamapediatrics.2017.3438

Merkle, F. T., Neuhausser, W. M., Santos, D., Valen, E., Gagnon, J. A., Maas, K., . . . Eggan, K. (2015). Efficient CRISPR-Cas9-mediated generation of knockin human pluripotent stem cells lacking undesired mutations at the targeted locus. *Cell reports*, *11*(6), 875-883. https://doi.org/10.1016/j.celrep.2015.04.007

Mirzaa, G. M., Vitre, B., Carpenter, G., Abramowicz, I., Gleeson, J. G., Paciorkowski, A. R., . . . O'Driscoll, M. (2014). Mutations in CENPE define a novel kinetochore-centromeric mechanism for microcephalic primordial dwarfism. *Human genetics*, *133*(8), 1023-1039. https://doi.org/10.1007/s00439-014-1443-3 [doi]

Mitchell, M., Mali, S., King, C. C., & Bark, S. J. (2015). Enhancing MALDI Time-Of-Flight Mass Spectrometer Performance through Spectrum Averaging. *PLOS ONE*, *10*(3), e0120932. https://doi.org/10.1371/journal.pone.0120932

Mitchison, T., Evans, L. F., Schulze, E. F., & Kirschner, M. (1986). Sites of microtubule assembly and disassembly in the mitotic spindle. (0092-8674 (Print)).

Mitchison, T. J. (1989). Polewards microtubule flux in the mitotic spindle: evidence from photoactivation of fluorescence. *Journal of Cell Biology*, *109*(2), 637-652. https://doi.org/10.1083/jcb.109.2.637

Mitsushima, M., Aoki, K., Ebisuya, M., Matsumura, S., Yamamoto, T., Matsuda, M., . . . Nishida, E. (2010). Revolving movement of a dynamic cluster of actin filaments during mitosis. *Journal of Cell Biology*, *191*(3), 453-462. https://doi.org/10.1083/jcb.201007136

Miya, F., Kato, M., Shiohama, T., Okamoto, N., Saitoh, S., Yamasaki, M., . . . Tsunoda, T. (2015). A combination of targeted enrichment methodologies for whole-exome sequencing reveals novel pathogenic mutations. *Scientific Reports*, *5*(1), 9331. https://doi.org/10.1038/srep09331

Moawia, A., Shaheen, R., Rasool, S., Waseem, S. S., Ewida, N., Budde, B., . . . Hussain, M. S. (2017). Mutations of KIF14 cause primary microcephaly by impairing cytokinesis. *Annals of Neurology*, *82*(4), 562-577. https://doi.org/10.1002/ana.25044

Moore, D., & Dowhan, D. (2002). Purification and Concentration of DNA from Aqueous Solutions. *Current Protocols in Molecular Biology*, *59*(1). https://doi.org/10.1002/0471142727.mb0201as59

Moriwaki, T., Yamazaki, N., So, T., Kosuga, M., Miyazaki, O., Narumi-Kishimoto, Y., . . . Fukuhara, Y. (2019). Normal early development in siblings with novel compound heterozygous variants in ASPM. *Human Genome Variation*, *6*(1). https://doi.org/10.1038/s41439-019-0088-0

Morris-Rosendahl, D. J., & Kaindl, A. M. (2015). What next-generation sequencing (NGS) technology has enabled us to learn about primary autosomal recessive microcephaly (MCPH). *Molecular and cellular probes*, *29*(5), 271-281. https://doi.org/10.1016/j.mcp.2015.05.015 [doi]

Muhammad, F., Mahmood Baig, S., Hansen, L., Sajid Hussain, M., Anjum Inayat, I., Aslam, M., . . . Kjaer, K. W. (2009). Compound heterozygous ASPM mutations in Pakistani MCPH families. *American Journal of Medical Genetics Part A*, *149A*(5), 926-930. https://doi.org/10.1002/ajmg.a.32749

Mullins, J. M., & Mcintosh, J. R. (1982). Isolation and initial characterization of the mammalian midbody. *Journal of Cell Biology*, *94*(3), 654-661. https://doi.org/10.1083/jcb.94.3.654

Nakade, S., Mochida, K., Kunii, A., Nakamae, K., Aida, T., Tanaka, K., . . . Yamamoto, T. (2018). Biased genome editing using the local accumulation of DSB repair molecules system. *Nature Communications*, *9*(1). https://doi.org/10.1038/s41467-018-05773-6

Nakamura, K., Inui, T., Miya, F., Kanemura, Y., Okamoto, N., Saitoh, S., . . . Kato, M. (2015). Primary Microcephaly With Anterior Predominant Pachygyria Caused by Novel Compound Heterozygous Mutations in ASPM. *Pediatric Neurology*, *52*(5), e7-e8. https://doi.org/10.1016/j.pediatrneurol.2015.01.019

Nicholas, A. K., Swanson, E. A., Cox, J. J., Karbani, G., Malik, S., Springell, K., . . . Woods, C. G. (2009). The molecular landscape of ASPM mutations in primary microcephaly. *Journal of Medical Genetics*, *46*(4), 249-253. https://doi.org/10.1136/jmg.2008.062380

O'Neil, K. T., & Degrado, W. F. (1990). How calmodulin binds its targets: sequence independent recognition of amphiphilic α-helices. *Trends in Biochemical Sciences*, *15*(2), 59-64. https://doi.org/10.1016/0968-0004(90)90177-d

Ohta, T., Essner, R., Ryu, J. H., Palazzo, R. E., Uetake, Y., & Kuriyama, R. (2002). Characterization of Cep135, a novel coiled-coil centrosomal protein involved in microtubule organization in mammalian cells. *The Journal of cell biology*, *156*(1), 87-99. https://doi.org/10.1083/jcb.200108088 [doi]

Okamoto, N., Kohmoto, T., Naruto, T., Masuda, K., & Imoto, I. (2018). Primary microcephaly caused by novel compound heterozygous mutations in ASPM. *Human Genome Variation*, *5*(1), 18015. https://doi.org/10.1038/hgv.2018.15

Pai, V. C., Hsu, C.-C., Chan, T.-S., Liao, W.-Y., Chuu, C.-P., Chen, W.-Y., . . . Tsai, K. K. (2019). ASPM promotes prostate cancer stemness and progression by augmenting Wnt−Dvl-3−β-catenin signaling. *Oncogene*, *38*(8), 1340-1353. https://doi.org/10.1038/s41388-018-0497-4

Papari, E., Bastami, M., Farhadi, A., Abedini, S., Hosseini, M., Bahman, I., . . . Najmabadi, H. (2013). Investigation of primary microcephaly in Bushehr province of Iran: novelSTILand ASPMmutations. *Clinical Genetics*, *83*(5), 488-490. https://doi.org/10.1111/j.1399-0004.2012.01949.x

Paramasivam, M., Chang, Y. J., & LoTurco, J. J. (2007). ASPM and citron kinase co-localize to the midbody ring during cytokinesis. *Cell cycle (Georgetown, Tex.)*, *6*(13), 1605-1612. https://doi.org/4356 [pii]

Passemard, S., Kaindl, A. M., & Verloes, A. (2013). Microcephaly. *Handbook of clinical neurology*, *111*, 129-141. https://doi.org/10.1016/B978-0-444-52891-9.00013-0 [doi]

Passemard, S., Titomanlio, L., Elmaleh, M., Afenjar, A., Alessandri, J. L., Andria, G., . . . Verloes, A. (2009). Expanding the clinical and neuroradiologic phenotype of primary microcephaly due to ASPM mutations. *Neurology*, *73*(12), 962. https://doi.org/10.1212/WNL.0b013e3181b8799a

Peloquin, J., Komarova, Y., & Borisy, G. (2005). Conjugation of fluorophores to tubulin. *Nature Methods*, *2*(4), 299-303. https://doi.org/10.1038/nmeth0405-299

Penisson, M., Ladewig, J., Belvindrah, R., & Francis, F. (2019). Genes and Mechanisms Involved in the Generation and Amplification of Basal Radial Glial Cells. *Frontiers in Cellular Neuroscience*, *13*. https://doi.org/10.3389/fncel.2019.00381

Perez, Y., Bar-Yaacov, R., Kadir, R., Wormser, O., Shelef, I., Birk, O. S., . . . Birnbaum, R. Y. (2019). Mutations in the microtubule-associated protein MAP11 (C7orf43) cause microcephaly in humans and zebrafish. *Brain*, *142*(3), 574-585. https://doi.org/10.1093/brain/awz004

Peterman, E., Gibieža, P., Schafer, J., Skeberdis, V. A., Kaupinis, A., Valius, M., . . . Prekeris, R. (2019). The post-abscission midbody is an intracellular signaling organelle that regulates cell proliferation. *Nature Communications*, *10*(1). https://doi.org/10.1038/s41467-019-10871-0

Pichon, B., Vankerckhove, S., Bourrouillou, G., Duprez, L., & Abramowicz, M. J. (2004). A translocation breakpoint disrupts the ASPM gene in a patient with primary microcephaly. *European Journal of Human Genetics*, *12*(5), 419-421. https://doi.org/10.1038/sj.ejhg.5201169

Pliatsika, V., & Rigoutsos, I. (2015). “Off-Spotter”: very fast and exhaustive enumeration of genomic lookalikes for designing CRISPR/Cas guide RNAs. *Biology Direct*, *10*(1), 4. https://doi.org/10.1186/s13062-015-0035-z

Ponting, C. P. (2006). A novel domain suggests a ciliary function for ASPM, a brain size determining gene. *Bioinformatics*, *22*(9), 1031-1035. https://doi.org/10.1093/bioinformatics/btl022

Rai, A., Liu, T., Glauser, S., Katrukha, E. A., Estévez-Gallego, J., Rodríguez-García, R., . . . Akhmanova, A. (2020). Taxanes convert regions of perturbed microtubule growth into rescue sites. *Nature Materials*, *19*(3), 355-365. https://doi.org/10.1038/s41563-019-0546-6

Ran, A. F., Hsu, P. D., Wright, J., Agarwala, V., Scott, D. A., & Zhang, F. (2013). Genome engineering using the CRISPR-Cas9 system. *Nature Protocols*, *8*(11), 2281-2308. https://doi.org/10.1038/nprot.2013.143

Rath, A., Glibowicka, M., Nadeau, V. G., Chen, G., & Deber, C. M. (2009). Detergent binding explains anomalous SDS-PAGE migration of membrane proteins. *Proceedings of the National Academy of Sciences*, *106*(6), 1760-1765. https://doi.org/10.1073/pnas.0813167106

Reichen, C., Madhurantakam, C., Plückthun, A., & Mittl, P. R. E. (2014). Crystal structures of designed armadillo repeat proteins: Implications of construct design and crystallization conditions on overall structure. *Protein Science*, *23*(11), 1572-1583. https://doi.org/10.1002/pro.2535

Reid, T. A., Coombes, C., & Gardner, M. K. (2017). Manipulation and quantification of microtubule lattice integrity. *Biology Open*, *6*(8), 1245-1256. https://doi.org/10.1242/bio.025320

Reid, T. A., Coombes, C., Mukherjee, S., Goldblum, R. R., White, K., Parmar, S., . . . Gardner, M. K. (2019). Structural state recognition facilitates tip tracking of EB1 at growing microtubule ends. *eLife*, *8*. https://doi.org/10.7554/elife.48117

Retterer, K., Juusola, J., Cho, M. T., Vitazka, P., Millan, F., Gibellini, F., . . . Bale, S. (2016). Clinical application of whole-exome sequencing across clinical indications. *Genetics in Medicine*, *18*(7), 696-704. https://doi.org/10.1038/gim.2015.148

Revill, D. J. (2013). *Flexibility in the heads of myosin 5.* PhD Thesis, University of Leeds.

Rhoads, A., & Kenguele, H. (2005). Expression of IQ-motif genes in human cells and ASPM domain structure. (1049-510X (Print)).

Rhoads, A. R., & Friedberg, F. (1997). Sequence motifs for calmodulin recognition. *The FASEB Journal*, *11*(5), 331-340. https://doi.org/10.1096/fasebj.11.5.9141499

Roberts, B. T., Farr, K. A., & Hoyt, M. A. (1994). The Saccharomyces cerevisiae checkpoint gene BUB1 encodes a novel protein kinase. *Molecular and cellular biology*, *14*(12), 8282-8291. https://doi.org/10.1128/mcb.14.12.8282

Roberts, E., Hampshire, D. J., Pattison, L., Springell, K., Jafri, H., Corry, P., . . . Woods, C. G. (2002). Autosomal recessive primary microcephaly: an analysis of locus heterogeneity and phenotypic variation. *Journal of medical genetics*, *39*(10), 718-721.

Rump, P., Jazayeri, O., van Dijk-Bos, K. K., Johansson, L. F., van Essen, A. J., Verheij, J. B., . . . Sikkema-Raddatz, B. (2016). Whole-exome sequencing is a powerful approach for establishing the etiological diagnosis in patients with intellectual disability and microcephaly. *BMC medical genomics*, *9*, 7-016-0167-0168. https://doi.org/10.1186/s12920-016-0167-8 [doi]

Ryckaert, J.-P., Ciccotti, G., & Berendsen, H. J. C. (1977). Numerical integration of the cartesian equations of motion of a system with constraints: molecular dynamics of n-alkanes. *Journal of Computational Physics*, *23*(3), 327-341. https://doi.org/10.1016/0021-9991(77)90098-5

Sajid Hussain, M., Marriam Bakhtiar, S., Farooq, M., Anjum, I., Janzen, E., Reza Toliat, M., . . . Hansen, L. (2013). Genetic heterogeneity in Pakistani microcephaly families. *Clinical Genetics*, *83*(5), 446-451. https://doi.org/10.1111/j.1399-0004.2012.01932.x

Sakuma, T., Nakade, S., Sakane, Y., Suzuki, K. T., & Yamamoto, T. (2016). MMEJ-assisted gene knock-in using TALENs and CRISPR-Cas9 with the PITCh systems. *Nature Protocols*, *11*(1), 118-133. https://doi.org/10.1038/nprot.2015.140

Sakuma, T., Nishikawa, A., Kume, S., Chayama, K., & Yamamoto, T. (2015). Multiplex genome engineering in human cells using all-in-one CRISPR/Cas9 vector system. *Scientific Reports*, *4*(1). https://doi.org/10.1038/srep05400

Sambrook, J. (2001). *Molecular cloning : a laboratory manual*. Third edition. Cold Spring Harbor, N.Y. : Cold Spring Harbor Laboratory Press, [2001] ©2001.

Sandoval, I. V., & Vandekerckhove, J. S. (1981). A comparative study of the in vitro polymerization of tubulin in the presence of the microtubule-associated proteins MAP2 and tau. *J Biol Chem*, *256*(16), 8795-8800.

Saunders, R. D., Avides, M. C., Howard, T., Gonzalez, C., & Glover, D. M. (1997). The Drosophila gene abnormal spindle encodes a novel microtubule-associated protein that associates with the polar regions of the mitotic spindle. *J Cell Biol*, *137*(4), 881-890. https://doi.org/10.1083/jcb.137.4.881

Schoborg, T., Zajac, A. L., Fagerstrom, C. J., Guillen, R. X., & Rusan, N. M. (2015). An Asp-CaM complex is required for centrosome-pole cohesion and centrosome inheritance in neural stem cells. *The Journal of cell biology*, *211*(5), 987-998. https://doi.org/10.1083/jcb.201509054 [doi]

Sellers, J. R. (2001). In vitro motility assay to study translocation of actin by myosin. *Curr Protoc Cell Biol*, *Chapter 13*, Unit 13.12. https://doi.org/10.1002/0471143030.cb1302s00

Shams, H., Golji, J., Garakani, K., & Mofrad, R. K., Mohammad. (2016). Dynamic Regulation of α-Actinin's Calponin Homology Domains on F-Actin. *Biophysical Journal*, *110*(6), 1444-1455. https://doi.org/10.1016/j.bpj.2016.02.024

Sharp, D. J., Rogers, G. C., & Scholey, J. M. (2000). Cytoplasmic dynein is required for poleward chromosome movement during mitosis in Drosophila embryos. *Nature Cell Biology*, *2*(12), 922-930. https://doi.org/10.1038/35046574

Shen, J. (2005). ASPM mutations identified in patients with primary microcephaly and seizures. *Journal of Medical Genetics*, *42*(9), 725-729. https://doi.org/10.1136/jmg.2004.027706

Shen, M., Zhang, N., Zheng, S., Zhang, W.-B., Zhang, H.-M., Lu, Z., . . . Li, X.-D. (2016). Calmodulin in complex with the first IQ motif of myosin-5a functions as an intact calcium sensor. *Proceedings of the National Academy of Sciences*, *113*(40), E5812-E5820. https://doi.org/10.1073/pnas.1607702113

Shin, S. C., Im, S.-K., Jang, E.-H., Jin, K. S., Hur, E.-M., & Kim, E. E. (2019). Structural and Molecular Basis for Katanin-Mediated Severing of Glutamylated Microtubules. *Cell Reports*, *26*(5), 1357-1367.e1355. https://doi.org/10.1016/j.celrep.2019.01.020

Shota Nakade, Keiji Mochida, Atsushi Kunii, Kazuki Nakamae, Tomomi Aida, Kohichi Tanaka, . . . Takashi Yamamoto. (2018). Biased genome editing using the local accumulation of DSB repair molecules system. *Nature Communications*, *9*(1). https://doi.org/10.1038/s41467-018-05773-6

Shtutman, M., Zhurinsky, J., Simcha, I., Albanese, C., D'Amico, M., Pestell, R., & Ben-Ze'ev, A. (1999). The cyclin D1 gene is a target of the beta-catenin/LEF-1 pathway. *Proceedings of the National Academy of Sciences of the United States of America*, *96*(10), 5522-5527.

Sievers, F., Wilm, A., Dineen, D., Gibson, T. J., Karplus, K., Li, W., . . . Higgins, D. G. (2011). Fast, scalable generation of high-quality protein multiple sequence alignments using Clustal Omega. *Molecular Systems Biology*, *7*(1), 539. https://doi.org/10.1038/msb.2011.75

Silkworth, W. T., Nardi, I. K., Paul, R., Mogilner, A., & Cimini, D. (2012). Timing of centrosome separation is important for accurate chromosome segregation. *Molecular Biology of the Cell*, *23*(3), 401-411. https://doi.org/10.1091/mbc.e11-02-0095

Singhmar, P., & Kumar, A. (2011). Angelman Syndrome Protein UBE3A Interacts with Primary Microcephaly Protein ASPM, Localizes to Centrosomes and Regulates Chromosome Segregation. *PLoS ONE*, *6*(5), e20397. https://doi.org/10.1371/journal.pone.0020397

Skop, A. R. (2004). Dissection of the Mammalian Midbody Proteome Reveals Conserved Cytokinesis Mechanisms. *Science*, *305*(5680), 61-66. https://doi.org/10.1126/science.1097931

Souphron, J., Bodakuntla, S., Jijumon, A. S., Lakisic, G., Gautreau, A. M., Janke, C., & Magiera, M. M. (2019). Purification of tubulin with controlled post-translational modifications by polymerization–depolymerization cycles. *Nature Protocols*, *14*(5), 1634-1660. https://doi.org/10.1038/s41596-019-0153-7

Spudich, J., & Watt, S. (1971). The regulation of rabbit skeletal muscle contraction. I. Biochemical studies of the interaction of the tropomyosin-troponin complex with actin and the proteolytic fragments of myosin. *The Journal of biological chemistry*, *246*, 4866-4871.

Sternberg, S. H., Redding, S., Jinek, M., Greene, E. C., & Doudna, J. A. (2014). DNA interrogation by the CRISPR RNA-guided endonuclease Cas9. *Nature*, *507*(7490), 62-67. https://doi.org/10.1038/nature13011

Steven Lin, T Staahl, B., K Alla, R., & A Doudna, J. (2014). Enhanced homology-directed human genome engineering by controlled timing of CRISPR/Cas9 delivery. *3*. https://doi.org/10.7554/elife.04766

Szczepanski, S., Hussain, M. S., Sur, I., Altmuller, J., Thiele, H., Abdullah, U., . . . Nurnberg, P. (2016). A novel homozygous splicing mutation of CASC5 causes primary microcephaly in a large Pakistani family. *Human genetics*, *135*(2), 157-170. https://doi.org/10.1007/s00439-015-1619-5 [doi]

Takahashi, K., Hiwada, K., & Kokubu, T. (1986). Isolation and characterization of a 34000-dalton calmodulin- and F-actin-binding protein from chicken gizzard smooth muscle.

Biochemical and Biophysical Research Communications, *141*(1), 20-26. https://doi.org/10.1016/s0006-291x(86)80328-x

Tan, C., Del Gaudio, D., Dempsey, M. A., Arndt, K., Botes, S., Reeder, A., & Das, S. (2014). Analysis ofASPMin an ethnically diverse cohort of 400 patient samples: perspectives of the molecular diagnostic laboratory. *Clinical Genetics*, *85*(4), 353-358. https://doi.org/10.1111/cge.12172

Tanaka, K., Kitamura, E., Kitamura, Y., & Tanaka, T. U. (2007). Molecular mechanisms of microtubule-dependent kinetochore transport toward spindle poles. *Journal of Cell Biology*, *178*(2), 269-281. https://doi.org/10.1083/jcb.200702141

Tang, G., Peng, L., Baldwin, P. R., Mann, D. S., Jiang, W., Rees, I., & Ludtke, S. J. (2007). EMAN2: An extensible image processing suite for electron microscopy. *Journal of Structural Biology*, *157*(1), 38-46. https://doi.org/10.1016/j.jsb.2006.05.009

Taverna, E., Gotz, M., & Huttner, W. B. (2014). The cell biology of neurogenesis: toward an understanding of the development and evolution of the neocortex. *Annual Review of Cell and Developmental Biology*, *30*, 465-502. https://doi.org/10.1146/annurev-cellbio-101011-155801 [doi]

Terrak, M. (2003). Two distinct myosin light chain structures are induced by specific variations within the bound IQ motifs--functional implications. *The EMBO Journal*, *22*(3), 362-371. https://doi.org/10.1093/emboj/cdg058

Terrak, M., Rebowski, G., Lu, R. C., Grabarek, Z., & Dominguez, R. (2005). Structure of the light chain-binding domain of myosin V. *Proceedings of the National Academy of Sciences*, *102*(36), 12718-12723. https://doi.org/10.1073/pnas.0503899102

Tiede, C., Bedford, R., Heseltine, S. J., Smith, G., Wijetunga, I., Ross, R., . . . Tomlinson, D. C. (2017). Affimer proteins are versatile and renewable affinity reagents. *eLife*, *6*. https://doi.org/10.7554/elife.24903

Tiede, C., Tang, A. A. S., Deacon, S. E., Mandal, U., Nettleship, J. E., Owen, R. L., . . . Mcpherson, M. J. (2014). Adhiron: a stable and versatile peptide display scaffold for molecular recognition applications. *Protein Engineering, Design and Selection*, *27*(5), 145-155. https://doi.org/10.1093/protein/gzu007

Trimborn, M., Bell, S. M., Felix, C., Rashid, Y., Jafri, H., Griffiths, P. D., . . . Jackson, A. P. (2004). Mutations in Microcephalin Cause Aberrant Regulation of Chromosome Condensation. *The American Journal of Human Genetics*, *75*(2), 261-266. https://doi.org/10.1086/422855

Trujillano, D., Bertoli-Avella, A. M., Kumar Kandaswamy, K., Weiss, M. E., Köster, J., Marais, A., . . . Abou Jamra, R. (2017). Clinical exome sequencing: results from 2819 samples reflecting 1000 families. *European Journal of Human Genetics*, *25*(2), 176-182. https://doi.org/10.1038/ejhg.2016.146

Tungadi, E. A., Ito, A., Kiyomitsu, T., & Goshima, G. (2017). Human microcephaly ASPM protein is a spindle pole-focusing factor that functions redundantly with CDK5RAP2. *J Cell Sci*, *130*(21), 3676-3684. https://doi.org/10.1242/jcs.203703

Uhlmann, F. (2001). Chromosome cohesion and segregation in mitosis and meiosis. *Current Opinion in Cell Biology*, *13*(6), 754-761. https://doi.org/10.1016/s0955-0674(00)00279-9

Uhlén, M., Fagerberg, L., Hallström, B. M., Lindskog, C., Oksvold, P., Mardinoglu, A., . . . Pontén, F. (2015). Tissue-based map of the human proteome. *Science*, *347*(6220), 1260419. https://doi.org/10.1126/science.1260419

Vallee, R. B. (1986). Reversible assembly purification of microtubules without assembly-promoting agents and further purification of tubulin, microtubule-associated proteins, and MAP fragments. *Methods Enzymol*, *134*, 89-104. https://doi.org/10.1016/0076-6879(86)34078-3

van der Voet, M., Berends, C. W., Perreault, A., Nguyen-Ngoc, T., Gonczy, P., Vidal, M., . . . van den Heuvel, S. (2009). NuMA-related LIN-5, ASPM-1, calmodulin and dynein promote meiotic spindle rotation independently of cortical LIN-5/GPR/Galpha. *Nature cell biology*, *11*(3), 269-277. https://doi.org/10.1038/ncb1834 [doi]

Van Heel, M., Harauz, G., Orlova, E. V., Schmidt, R., & Schatz, M. (1996). A New Generation of the IMAGIC Image Processing System. *Journal of Structural Biology*, *116*(1), 17-24. https://doi.org/10.1006/jsbi.1996.0004

Venkei, Z. G., & Yamashita, Y. M. (2018). Emerging mechanisms of asymmetric stem cell division. *Journal of Cell Biology*, *217*(11), 3785-3795. https://doi.org/10.1083/jcb.201807037

Verhey, K. J., & Hammond, J. W. (2009). Traffic control: regulation of kinesin motors. *Nature Reviews Molecular Cell Biology*, *10*(11), 765-777. https://doi.org/10.1038/nrm2782

Wagers, A. J., Christensen, J. L., & Weissman, I. L. (2002). Cell fate determination from stem cells. *Gene Therapy*, *9*(10), 606-612. https://doi.org/10.1038/sj.gt.3301717

Wakefield, J. G., Bonaccorsi, S., & Gatti, M. (2001). The Drosophila Protein Asp Is Involved in Microtubule Organization during Spindle Formation and Cytokinesis. *Journal of Cell Biology*, *153*(4), 637-648. https://doi.org/10.1083/jcb.153.4.637

Walker, M. L., Burgess, S. A., Sellers, J. R., Wang, F., Hammer, J. A., Trinick, J., & Knight, P. J. (2000). Two-headed binding of a processive myosin to F-actin. *Nature*, *405*(6788), 804-807. https://doi.org/10.1038/35015592

Wang, F., Chen, L., Arcucci, O., Harvey, E. V., Bowers, B., Xu, Y., . . . Sellers, J. R. (2000). Effect of ADP and Ionic Strength on the Kinetic and Motile Properties of Recombinant Mouse Myosin V. *Journal of Biological Chemistry*, *275*(6), 4329-4335. https://doi.org/10.1074/jbc.275.6.4329

Wang, R., Khan, A., Han, S., & Zhang, X. (2017). Molecular analysis of 23 Pakistani families with autosomal recessive primary microcephaly using targeted next-generation sequencing. *Journal of human genetics*, *62*(2), 299-304. https://doi.org/10.1038/jhg.2016.128 [doi]

Waterman-Storer, C. M., & Salmon, E. D. (1997). Microtubule dynamics: Treadmilling comes around again. *Current Biology*, *7*(6), R369-R372. https://doi.org/10.1016/s0960-9822(06)00177-1

Way, M., Pope, B., & Weeds, A. G. (1992). Evidence for functional homology in the F-actin binding domains of gelsolin and alpha-actinin: implications for the requirements of severing and capping. *The Journal of cell biology*, *119*(4), 835-842. https://doi.org/10.1083/jcb.119.4.835

Weitensteiner, V., Zhang, R., Bungenberg, J., Marks, M., Gehlen, J., Ralser, D. J., . . . Reutter, H. (2018). Exome sequencing in syndromic brain malformations identifies novel mutations inACTB, andSLC9A6, and suggestsBAZ1Aas a new candidate gene. *Birth Defects Research*, *110*(7), 587-597. https://doi.org/10.1002/bdr2.1200

Wiszniewski, W., Gawlinski, P., Gambin, T., Bekiesinska-Figatowska, M., Obersztyn, E., Antczak-Marach, D., . . . Lupski, J. R. (2018). Comprehensive genomic analysis of patients with disorders of cerebral cortical development. *European Journal of Human Genetics*, *26*(8), 1121-1131. https://doi.org/10.1038/s41431-018-0137-z

Wloga, D., & Gaertig, J. (2010). Post-translational modifications of microtubules. *123*(20), 3447-3455. https://doi.org/10.1242/jcs.063727

Wolenski, J. S. (1995). Regulation of calmodulin-binding myosins. *Trends in Cell Biology*, *5*(8), 310-316. https://doi.org/10.1016/s0962-8924(00)89053-4

Wood, K. W., Chua, P., Sutton, D., & Jackson, J. R. (2008). Centromere-Associated Protein E: A Motor That Puts the Brakes on the Mitotic Checkpoint: Fig. 1. *Clinical Cancer Research*, *14*(23), 7588-7592. https://doi.org/10.1158/1078-0432.ccr-07-4443

Woods, C. G. (2004). Human microcephaly. *Current opinion in neurobiology*, *14*(1), 112-117. https://doi.org/10.1016/j.conb.2004.01.003 [doi]

Woods, C. G., Bond, J., & Enard, W. (2005). Autosomal recessive primary microcephaly (MCPH): a review of clinical, molecular, and evolutionary findings. *American Journal of Human Genetics*, *76*(5), 717-728. https://doi.org/S0002-9297(07)60720-4 [pii]

Woolner, S., O'Brien, L. L., Wiese, C., & Bement, W. M. (2008). Myosin-10 and actin filaments are essential for mitotic spindle function. *The Journal of cell biology*, *182*(1), 77-88. https://doi.org/10.1083/jcb.200804062 [doi]

Wu, J., Yu, P., Jin, X., Xu, X., Li, J., Li, Z., . . . Sun, Z. S. (2018). Genomic landscapes of Chinese sporadic autism spectrum disorders revealed by whole-genome sequencing. *Journal of Genetics and Genomics*, *45*(10), 527-538. https://doi.org/10.1016/j.jgg.2018.09.002

Xu, X. L., Ma, W., Zhu, Y. B., Wang, C., Wang, B. Y., An, N., . . . Tian, J. H. (2012). The microtubule-associated protein ASPM regulates spindle assembly and meiotic progression in mouse oocytes. *PLoS One*, *7*(11), e49303. https://doi.org/10.1371/journal.pone.0049303

Xu, Z., Zhang, Q., Luh, F., Jin, B., & Liu, X. (2018). Overexpression of the ASPM gene is associated with aggressiveness and poor outcome in bladder cancer. *Oncology Letters*. https://doi.org/10.3892/ol.2018.9762

Yamagata, M., & Sanes, J. R. (2012). Transgenic strategy for identifying synaptic connections in mice by fluorescence complementation (GRASP). *5*. https://doi.org/10.3389/fnmol.2012.00018

Yang, H., Wang, H., Shivalila, S., Chikdu, Cheng, W., Albert, Shi, L., & Jaenisch, R. (2013). One-Step Generation of Mice Carrying Reporter and Conditional Alleles by CRISPR/Cas-Mediated Genome Engineering. *Cell*, *154*(6), 1370-1379. https://doi.org/10.1016/j.cell.2013.08.022

Yang, Y. J., Baltus, A. E., Mathew, R. S., Murphy, E. A., Evrony, G. D., Gonzalez, D. M., . . . Walsh, C. A. (2012). Microcephaly gene links trithorax and REST/NRSF to control neural stem cell proliferation and differentiation. *Cell*, *151*(5), 1097-1112. https://doi.org/10.1016/j.cell.2012.10.043 [doi]

Yin, L.-M., Schnoor, M., & Jun, C.-D. (2020). Structural Characteristics, Binding Partners and Related Diseases of the Calponin Homology (CH) Domain. *Frontiers in Cell and Developmental Biology*, *8*. https://doi.org/10.3389/fcell.2020.00342

Yu, T. W., Mochida, G. H., Tischfield, D. J., Sgaier, S. K., Flores-Sarnat, L., Sergi, C. M., . . . Walsh, C. A. (2010). Mutations in WDR62, encoding a centrosome-associated protein, cause microcephaly with simplified gyri and abnormal cortical architecture. *Nature genetics*, *42*(11), 1015-1020. https://doi.org/10.1038/ng.683 [doi]

Yuan, Y.-J., Sun, Y., Gao, R., Yin, Z.-Z., Yuan, Z.-Y., & Xu, L.-M. (2020). Abnormal spindle-like microcephaly-associated protein (ASPM) contributes to the progression of Lung Squamous Cell Carcinoma (LSCC) by regulating CDK4. *Journal of Cancer*, *11*(18), 5413-5423. https://doi.org/10.7150/jca.39760

Zanic, M., Stear, J. H., Hyman, A. A., & Howard, J. (2009). EB1 Recognizes the Nucleotide State of Tubulin in the Microtubule Lattice. *PLoS ONE*, *4*(10), e7585. https://doi.org/10.1371/journal.pone.0007585

Zecevic, N. (2004). Specific characteristic of radial glia in the human fetal telencephalon. *Glia*, *48*(1), 27-35. https://doi.org/10.1002/glia.20044

Zhong, X., Liu, L., Zhao, A., Pfeifer, G. P., & Xu, X. (2005). The abnormal spindle-like, microcephaly-associated (ASPM) gene encodes a centrosomal protein. *Cell cycle (Georgetown, Tex.)*, *4*(9), 1227-1229. https://doi.org/2029 [pii]

Zitter, E. D., Thédié, D., Mönkemöller, V., Hugelier, S., Beaudouin, J., Adam, V., . . . Bourgeois, D. (2019). Mechanistic investigation of mEos4b reveals a strategy to reduce track interruptions in sptPALM. *Nature Methods*, *16*(8), 707-710. https://doi.org/10.1038/s41592-019-0462-3

Zwaveling-Soonawala, N., Alders, M., Jongejan, A., Kovačič, L., Duijkers, F. A., Maas, S. M., . . . Hennekam, R. C. (2018). Clues for Polygenic Inheritance of Pituitary Stalk Interruption Syndrome From Exome Sequencing in 20 Patients. *The Journal of Clinical Endocrinology & Metabolism*, *103*(2), 415-428. https://doi.org/10.1210/jc.2017-01660

8. Appendix

Table 8.1 – Missense / nonsense mutations found in ASPM.

Codon change	Nucleotide	Protein	Reported phenotype	Reference
CGA-TGA	349C>T	R117*	Primary Microcephaly	(Bond et al., 2003)
CAA-TAA	577C>T	Q193*	Primary Microcephaly	(Nicholas et al., 2009)
CAG-TAG	1138C>T	Q380*	Primary Microcephaly	(Tan et al., 2014)
GAA-TAA	1366G>T	E456*	Primary Microcephaly	(Nicholas et al., 2009)
CGA-TGA	1789C>T	R597*	Primary Microcephaly	(Abdel-Hamid et al., 2016)
CAG-TAG	1990C>T	Q664*	Primary Microcephaly	(Bond et al., 2003)
CAG-TAG	2101C>T	Q701*	Primary Microcephaly	(Kousar et al., 2009)
CGA-TGA	2389C>T	R797*	Primary Microcephaly	(Passemard et al., 2009)
TGG-TGA	2571G>A	W857*	Primary Microcephaly	(Tan et al., 2014)
GAA-TAA	2638G>T	E880*	Primary Microcephaly	(Létard et al., 2018)
CGA-TGA	2791C>T	R931*	Primary Microcephaly	(Tan et al., 2014)
CGA-TGA	2938C>T	R980*	Primary Microcephaly	(Muhammad et al., 2009)
CAG-TAG	2959C>T	Q987*	Primary Microcephaly	(Meng et al., 2017)
TGG-TGA	2967G>A	W989*	Primary Microcephaly	(Nicholas et al., 2009)
CGA-TGA	3055C>T	R1019*	Primary Microcephaly	(Nicholas et al., 2009)
TTA-TGA	3188T>G	L1063*	Primary Microcephaly	(Nicholas et al., 2009)
TAT-TAG	3327T>G	Y1109*	Primary Microcephaly	(Tan et al., 2014)
TCA-TGA	3527C>G	S1176*	Primary Microcephaly	(Bond et al., 2003)
TCA-TGA	3710C>G	S1237*	Primary Microcephaly	(Nicholas et al., 2009)
GAA-TAA	3796G>T	E1266*	Primary Microcephaly	(Nicholas et al., 2009)
CGA-TGA	3811C>T	R1271*	Primary Microcephaly	(Bond et al., 2003)
TGG-TAG	3977G>A	W1326*	Primary Microcephaly	(Halsall et al., 2010)
TGG-TGA	3978G>A	W1326*	Primary Microcephaly	(Kumar et al., 2004)
CGA-TGA	3979C>T	R1327*	Primary Microcephaly	(Sajid Hussain et al., 2013)
TGG-TGA	4074G>A	W1358*	Primary Microcephaly	(Passemard et al., 2009)
TGG-TAG	4184G>A	W1395*	Primary Microcephaly	(Halsall et al., 2010)
TGG-TGA	4185G>A	W1395*	Primary Microcephaly	(Wang et al., 2017)
TGG-TGA	4212G>A	W1404*	Primary Microcephaly	(Ahmad et al., 2017)
CGT-AGT	4309C>A	R1437S	Autism spectrum disorder	(Wu et al., 2018)

GAA-TAA	4363G>T	E1455*	Primary Microcephaly	(Alfares et al., 2017)
CGA-TGA	4612C>T	R1538*	Primary Microcephaly	(Abdel-Hamid et al., 2016)
TGT-CGT	4669T>C	C1557R	Autism spectrum disorder	(Iossifov et al., 2014)
CAA-TAA	4720C>T	Q1574*	Primary Microcephaly	(Ceyhan-Birsoy et al., 2019)
CGA-TGA	4732C>T	R1578*	Primary Microcephaly	(Létard et al., 2018)
CGA-TGA	4795C>T	R1599*	Primary Microcephaly	(Bond et al., 2003)
TAT-TAG	4806T>G	Y1602*	Primary Microcephaly	(Létard et al., 2018)
CGA-TGA	4849C>T	R1617*	Primary Microcephaly	(Papari et al., 2013)
CGT-CAT	5000G>A	R1667H	Autism spectrum disorder	(Wu et al., 2018)
TAC-TAA	5136C>A	Y1712*	Primary Microcephaly	(Gul et al., 2007)
GAA-TAA	5188G>T	E1730*	Primary Microcephaly	(Darvish et al., 2010)
TGT-TGA	5196T>A	C1732*	Primary Microcephaly	(Tan et al., 2014)
AAG-CAG	5584A>C	K1862Q	Primary Microcephaly	(Darvish et al., 2010)
AAG-GAG	5584A>G	K1862E	Primary Microcephaly	(Sajid Hussain et al., 2013)
TAT-TGT	5654A>G	Y1885C	Autism spectrum disorder	(Wu et al., 2018)
ATG-TTG	5947A>T	M1983L	Moderate intellectual disability with facial dysmorphism and seizures	(Bowling et al., 2017)
CAA-TAA	5959C>T	Q1987*	Primary Microcephaly	(Ahmad et al., 2017)
CAG-TAG	6151C>T	Q2051*	Primary Microcephaly	(Sajid Hussain et al., 2013)
TAT-TAG	6189T>G	Y2063*	Primary Microcephaly	(Shen, 2005)
CGA-TGA	6232C>T	R2078*	Primary Microcephaly	(Passemard et al., 2009)
CAG-TAG	6568C>T	Q2190*	Primary Microcephaly	(Létard et al., 2018)
CAG-TAG	6658C>T	Q2220*	Primary Microcephaly	(Létard et al., 2018)
CAG-TAG	6919C>T	Q2307*	Primary Microcephaly	(Létard et al., 2018)
CAG-TAG	6928C>T	Q2310*	Malformation of cortical development	(Wiszniewski et al., 2018)
CGA-TGA	6994C>T	R2332*	Primary Microcephaly	(Halsall et al., 2010)
CAG-TAG	7129C>T	Q2377*	Primary Microcephaly	(Ahmad et al., 2017)
TAT-TAA	7323T>A	Y2441*	Primary Microcephaly	(Trujillano et al., 2017)
CGA-TGA	7324C>T	R2442*	Primary Microcephaly	(Weitensteiner et al., 2018)
TAT-TAG	7491T>G	Y2497*	Primary Microcephaly	(Abdel-Hamid et al., 2016)
CGA-TGA	7543C>T	R2515*	Primary Microcephaly	(Khan et al., 2018)
CAG-TAG	7612C>T	Q2538*	Primary Microcephaly	(Tan et al., 2014)
CAA-TAA	7642C>T	Q2548*	Primary Microcephaly	(Alby et al., 2016)
GAA-TAA	7753G>T	E2585*	Primary Microcephaly	(Létard et al., 2018)
TAT-TAG	7761T>G	Y2587*	Primary Microcephaly	(Bond et al., 2002)

CAG-TAG	7825C>T	Q2609*	Primary Microcephaly	(Tan et al., 2014)
CAG-TAG	7894C>T	Q2632*	Primary Microcephaly	(Muhammad et al., 2009)
CAG-TAG	8017C>T	Q2673*	Primary Microcephaly	(Tan et al., 2014)
CGA-GGA	8098C>G	R2700G	Autism spectrum disorder	(Wu et al., 2018)
CGA-TGA	8098C>T	R2700*	Primary Microcephaly	(Miya et al., 2015)
CGA-TGA	8227C>T	R2743*	Primary Microcephaly	(Hu et al., 2014)
TTG-TAG	8273T>A	L2758*	Primary Microcephaly	(Passemard et al., 2009)
CGG-CAG	8558G>A	R2853Q	Moderate intellectual disability with facial dysmorphism and seizures	(Bowling et al., 2017)
CAA-TAA	8668C>T	Q2890*	Primary Microcephaly	(Muhammad et al., 2009)
TGG-TAG	8903G>A	W2968*	Primary Microcephaly	(Tan et al., 2014)
CGA-TGA	9091C>T	R3031*	Primary Microcephaly	(Darvish et al., 2010)
TTG-TAG	9104T>A	L3035*	Primary Microcephaly	(Tan et al., 2014)
CAA-TAA	9178C>T	Q3060*	Primary Microcephaly	(Kumar et al., 2004)
CGA-TGA	9190C>T	R3064*	Primary Microcephaly	(Bond et al., 2003)
AAA-TAA	9238A>T	K3080*	Primary Microcephaly	(Gul et al., 2006)
CGA-TGA	9286C>T	R3096*	Primary Microcephaly	(Darvish et al., 2010)
CGA-TGA	9319C>T	R3107*	Primary Microcephaly	(Muhammad et al., 2009)
CGA-TGA	9454C>T	R3152*	Primary Microcephaly	(Tan et al., 2014)
TAT-TAG	9492T>G	Y3164*	Primary Microcephaly	(Muhammad et al., 2009)
CAG-CCG	9539A>C	Q3180P	Primary Microcephaly	(Gul et al., 2006)
CGA-TGA	9541C>T	R3181*	Primary Microcephaly	(Abdel-Hamid et al., 2016)
TCA-TGA	9557C>G	S3186*	Primary Microcephaly	(Bond et al., 2003)
AAA-TAA	9595A>T	K3199*	Primary Microcephaly	(Muhammad et al., 2009)
CGA-TGA	9697C>T	R3233*	Primary Microcephaly	(Muhammad et al., 2009)
CGA-TGA	9730C>T	R3244*	Primary Microcephaly	(Gul et al., 2007)
TAT-TAA	9789T>A	Y3263*	Primary Microcephaly	(Nicholas et al., 2009)
AGA-TGA	9841A>T	R3281*	Primary Microcephaly	(Desir et al., 2006)
CGA-TGA	9910C>T	R3304*	Primary Microcephaly	(Tan et al., 2014)
TAC-TAA	10059C>A	Y3353*	Primary Microcephaly	(Gul et al., 2007)
CGA-TGA	10060C>T	R3354*	Primary Microcephaly	(Halsall et al., 2010)
GCC-ACC	10156G>A	A3386T	Autism spectrum disorder	(Wu et al., 2018)
CGA-TGA	10168C>T	R3390*	Primary Microcephaly	(Miya et al., 2015)

Table 8.2 – Splicing mutations found in ASPM.

Splicing mutation	Nucleotide	Reported phenotype	Reference
IVS1 ds G-C +1	297+1G>C	Primary Microcephaly	(Darvish et al., 2010)
IVS6 ds T-C +2	2419+2T>C	Primary Microcephaly	(Tan et al., 2014)
IVS9 as A-G -25	2761-25A>G	Primary Microcephaly	(Nicholas et al., 2009)
IVS10 as A-G -2	2937-2A>G	Primary Microcephaly	(Kraemer et al., 2016)
IVS10 ds G-A +1	2936+1G>A	Primary Microcephaly	(Abdel-Hamid et al., 2016)
IVS10 ds T-C +2	2936+2T>C	Primary Microcephaly	(Létard et al., 2018)
IVS10 ds G-A +5	2936+5G>A	Primary Microcephaly	(Ahmed et al., 2019)
IVS10 ds G-T +5	2936+5G>T	Primary Microcephaly	(Bond et al., 2003)
IVS11 ds T-G -16	3067T>G	Primary Microcephaly	(Al-Gazali & Ali, 2010)
IVS11 ds G-A -1	3082G>A	Primary Microcephaly	(Bond et al., 2003)
IVS12 ds G-C +1	3168+1G>C	Primary Microcephaly	(Rump et al., 2016)
IVS15 as G-C -1	3742-1G>C	Primary Microcephaly	(Hashmi et al., 2016)
IVS15 ds G-A +1	3741+1G>A	Primary Microcephaly	(Nicholas et al., 2009)
IVS15 ds A-G +3	3741+3A>G	Primary Microcephaly	(Létard et al., 2018)
IVS19 ds G-A +1	8987+1G>A	Abnormality of the nervous System	(Retterer et al., 2016)
IVS20 ds G-A +5	9084+5G>A	Primary Microcephaly	(Karaca et al., 2015)
IVS20 ds G-T +5	9084+5G>T	Primary Microcephaly	(Alabdullatif et al., 2017)
IVS25 ds G-T +1	9984+1G>T	Primary Microcephaly	(Bond et al., 2003)
IVS26 ds G-C +5	10161+5G>C	Pituitary stalk interruption syndrome	(Zwaveling-Soonawala et al., 2018)

Table 8.3 – Small deletions found in ASPM.

Small deletion	Nucleotide	Protein	Reported phenotype	Reference
GGGGCTG^^{25}CGGgGCCCCGCGGC	77delG	Gly26Alafs*42	Primary Microcephaly	(Nicholas et al., 2009)
CGCCG^^{38}GTCCTgtCTCTCAGCCA	117_118delGT	Leu41Glnfs*30	Primary Microcephaly	(Tan et al., 2014)
AGAAA^^{145}AAGAAaAAG_E2I2_GTAATGT	440delA	Lys147Argfs*54	Primary Microcephaly	(Nicholas et al., 2009)
CAATTCT^^{212}TTAaTACTTGAAGA	637delA	Ile213Tyrfs*47	Primary Microcephaly	(Tan et al., 2014)
TGCTTTC^^{229}AATgAATGCCATGG	688delG	Glu230Asnfs*30	Primary Microcephaly	(Abdel-Hamid et al., 2016)
GCTTG^^{238}CCACTctCTGTACGTCG	719_720delCT	Ser240Cysfs*16	Primary Microcephaly	(Bond et al., 2002)
AACGTT^^{267}TCAAaaGTTTCTTTTA	803_804delAA	Lys268Serfs*4	Primary Microcephaly	(Tan et al., 2014)
TTGTA^^{323}AATAAtaGTCATGGAGC	972_973delTA	Asn324Lysfs*5	Primary Microcephaly	(Wiszniewski et al., 2018)
AACTA^^{333}GAATTaGTAACATGTC	1002delA	Val335*	Primary Microcephaly	(Muhammad et al., 2009)
CTAGAA^^{384}TCAGagTCAGTTAATC	1154_1155delAG	Glu385Valfs*3	Primary Microcephaly	(Nicholas et al., 2009)
TTTTA^^{392}TCCCCtAATCAATTTT	1179delT	Asn394Ilefs*4	Primary Microcephaly	(Nicholas et al., 2009)
CAAACA^^{411}TGTAaagtaCCATTATCAA	1235_1239delAAGTA	Lys412Thrfs*5	Primary Microcephaly	(Ahmad et al., 2017)
AAATGAA^^{419}AATtctcaagTCCCACAGTC	1260_1266delTCAAGTC	Gln421Hisfs*32	Primary Microcephaly	(Bond et al., 2002)
CAAAT^^{461}TACTAcAGTTTTATAA	1386delC	Tyr462*	Microcephaly with Seckel syndrome features	(Marakhonov et al., 2018)
TATAAAA^^{467}CAAaataaTCCTAAATTT	Not yet available	Not yet available	Primary Microcephaly	(Moriwaki et al., 2019)
AAACAA^^{468}AATAatcctaaaTTTTCTGCAG	1406_1413delATCCTAAA	Asn469Ilefs*9	Primary Microcephaly	(Nicholas et al., 2009)
TGAACAT^^{529}GAAaAAGTAATAAA	1590delA	Val531*	Primary Microcephaly	(Nicholas et al., 2009)
TTTCAT^^{543}TCTTatcttCCAATTATAG	1631_1635delATCTT	Tyr544Serfs*9	Primary Microcephaly	(Passemard et al., 2009)
TCGGAAA^^{575}AGAaagaGCGATGGAAG	1726_1729delAAGA	Lys576Alafs*10	Primary Microcephaly	(Tan et al., 2014)
GAAAAGA^^{576}AAGagCGATGGAAGC	1729_1730delAG	Ser577Argfs*33	Primary Microcephaly	(Bond et al., 2003)

GTTAAG^^{616}AAAAcaaaAAATGTGACA	1850_1853delCAAA	Thr617Lysfs*3	Primary Microcephaly	(Létard et al., 2018)
GCAAC^^{631}AGAGAgaAATTAAACCT	1896_1897delGA	Lys633Ilefs*8	Intellectual disability	(Kahrizi et al., 2019)
ATTTA^^{643}TCAATaTTCAGAACTC	1932delA	Phe645Serfs*23	Primary Microcephaly	(Létard et al., 2018)
CTAAA^^{652}ACAAAcaaaAGGACAAAAC	1959_1962delCAAA	Asn653Lysfs*14	Primary Microcephaly	(Bond et al., 2003)
TGCATTTCAG_IE_gA^^{808}GAACGTCAG	2420delG	Gly807Glufs*7	Primary Microcephaly	(Ahmad et al., 2017)
ATAGA^^{876}GATG_E8I8_GtAAGTATCTCT	2629+2delT	Not yet available	Primary Microcephaly	(Akbariazar et al., 2013)
ACAGAAC^^{989}TGGgACCTCTCAAA	2968delG	Asp990Thrfs*11	Primary Microcephaly	(Tan et al., 2014)
CTAAG^^{1035}GATATtgtggatAGGCACAGAG	3108_3114delTGTGGAT	Val1037Glyfs*13	Primary Microcephaly	(Abdel-Hamid et al., 2016)
ATTTCC^^{1061}CTTAacttaGATCAATTAA	3185_3189delACTTA	Asn1062Argfs*28	Primary Microcephaly	(Létard et al., 2018)
AAAACAC^^{1076}ACAaaGAGTATAAAG	3229_3230delAA	Lys1077Glufs*14	Primary Microcephaly	(Darvish et al., 2010)
TGAAAAC^^{1113}ATAaAGTTATTGAT	3341delA	Lys1114Serfs*3	Primary Microcephaly	(Abdel-Hamid et al., 2016)
ATAAA^^{1130}AAG_E13I13_GTaagtTTCTTTGTTT	3390+3_3390+6delAAGT	Not yet available	Primary Microcephaly	(Tan et al., 2014)
TGCCA^^{1158}TTTGAcgctaTATGTCAGCG	3477_3481delCGCTA	Ala1160Metfs*23	Primary Microcephaly	(Muhammad et al., 2009)
ATATGT^^{1163}CAGCgtacTACTCAAACT	3491_3494delGTAC	Arg1164Leufs*15	Primary Microcephaly	(Ahmad et al., 2017)
TACTCAA^^{1168}ACTgtGGAATGTACG	3506_3507delTG	Val1169Glyfs*15	Primary Microcephaly	(Darvish et al., 2010)
ACTTG^^{1220}GTTAGgTCTGCAGTTA	3663delG	Arg1221Serfs*13	Primary Microcephaly	(Bond et al., 2003)
ACTAAAA^^{1284}ACAgaTCTCAAACGC	3853_3854delGA	Asp1285Serfs*32	Primary Microcephaly	(Tan et al., 2014)
TGAGA^^{1314}AAAAGagTTAATGCAGC	3945_3946delAG	Arg1315Serfs*2	Primary Microcephaly	(Passemard et al., 2009)
CAACAA^^{1416}AGATatGAAATGCTAA	4250_4251delAT	Tyr1417*	Primary Microcephaly	(Létard et al., 2018)
TCTGAAA^^{1527}GGAaAGATTGAGCG	4583delA	Lys1528Argfs*24	Primary Microcephaly	(Bond et al., 2003)
GACAA^^{1575}GACAGagTTCGATTTTT	4728_4729delAG	Arg1576Serfs*7	Primary Microcephaly	(Tan et al., 2014)
TCCGA^^{1618}GCTTAtaTTTTTGCCAT	4858_4859delAT	Ile1620Phefs*24	Primary Microcephaly	(Nicholas et al., 2009)
TGCAG^^{1687}TCAACtGTTAAGATGA	5064delT	Val1689Leufs*3	Intellectual Disability	(Abouelhoda et al., 2016)

CCGTTCC^^{1715}AAAaAAATAGCTGC	5149delA	Ile1717*	Primary Microcephaly	(Gul et al., 2007)
GCATTT^^{1739}GTTAgaggataCCTTGTCCGA	5219_5225delGAGGATA	Arg1740Thrfs*7	Intellectual disability, non-syndromic	(Mcsherry et al., 2018)
GTACAAG^^{1863}ACTctTCATGATACA	5590_5591delCT	Leu1864Serfs*2	Primary Microcephaly	(Létard et al., 2018)
AGGGA^^{1961}AAAACacTGAGAAGACA	5886_5887delAC	Leu1963Glufs*9	Primary Microcephaly	(Létard et al., 2018)
TACAG^^{1979}TCATAcTATAGAATGC	5940delC	Tyr1981Ilefs*13	Primary Microcephaly	(Létard et al., 2018)
TAGAAGA^^{2112}CATatTCAACACATG	6337_6338delAT	Ile2113Serfs*11	Primary Microcephaly	(Nicholas et al., 2009)
AAATA^^{2216}ACAAAaacaGTACAGCAAA	6651_6654delAACA	Thr2218Tyrfs*8	Primary Microcephaly	(Passemard et al., 2009)
ATGAAA^^{2228}GAAAgaaaCATACAATTT	6686_6689delGAAA	Arg2229Thrfs*10	Primary Microcephaly	(Passemard et al., 2009)
AAGGTAT^^{2237}AACaaacTGAGGCATTC	6712_6715delAAAC	Lys2238*	Abnormality of the nervous system	(Retterer et al., 2016)
ATTCT^^{2243}GTAATaTACATTCAGG	6732delA	Tyr2245Thrfs*15	Primary Microcephaly	(Muhammad et al., 2009)
AGGCT^^{2249}ATTTTtAGGGGAAAGA	6750delT	Phe2250Leufs*10	Primary microcephaly with anterior predominant pachygyria	(Nakamura et al., 2015)
AGATTC^^{2283}CTCTctctCAAGAAAACT	6852_6855delTCTC	Leu2285Argfs*6	Primary Microcephaly	(Ahmad et al., 2017)
CATCAC^^{2306}TTACagTTCCTTCAGG	6920_6921delAG	Gln2307Leufs*10	Primary Microcephaly	(Létard et al., 2018)
CATTAT^^{2382}CTCAgacaAAGACACTCT	7148_7151delGACA	Arg2383Lysfs*6	Abnormality of the nervous system	(Retterer et al., 2016)
GTACAGA^^{2496}ACAtatatTACATTTCAG	7491_7495delTATTA	Thr2499Serfs*18	Primary Microcephaly	(Nicholas et al., 2009)
CAAAA^^{2522}TTACAaaGAGAAAATTA	7569_7570delAA	Glu2525Lysfs*17	Primary Microcephaly	(Halsall et al., 2010)
AAAAA^^{2554}CACAAaGCTTCTATCG	7665delA	Ala2556Leufs*4	Primary Microcephaly	(Tan et al., 2014)
GGCTACA^^{2581}AAAaTCATACAAGA	7744delA	Ile2582Serfs*34	Primary Microcephaly	(Létard et al., 2018)
AGAGCA^^{2590}AATAaaaaGAAACAGAAA	7772_7775delAAAA	Lys2591Argfs*24	Primary Microcephaly	(Hu et al., 2014)
AAAAAG^^{2593}AAACagaaAGTATTTCAA	7783_7786delAAAG	Lys2595Tyrfs*20	Primary Microcephaly	(Rump et al., 2016)

AAAAG^^{2593}AAACAgaAAGTATTTCA	7782_7783delGA	Lys2595Serfs*6	Primary Microcephaly	(Nicholas et al., 2009)
TTAAG^^{2604}AAAGAgaCTTGTGTTCA	7815_7816delGA	Glu2605Aspfs*31	Primary Microcephaly	(Ariani et al., 2013)
ATAAAA^^{2619}AAACagATTCAGGAAC	7860_7861delGA	Gln2620Hisfs*16	Primary Microcephaly	(Nicholas et al., 2009)
ATTATT^^{2631}ATTCagAAGCATTGTA	7896_7897delGA	Lys2633Alafs*3	Primary Microcephaly	(Bond et al., 2003)
ATGAA^^{2710}ACAAAgaaaACTGCAATTG	8133_8136delGAAA	Lys2712Leufs*16	Primary Microcephaly	(Tan et al., 2014)
TTATGAA^^{2710}ACAaaGAAAACTGCA	8131_8132delAA	Lys2711Glufs*12	Primary Microcephaly	(Nicholas et al., 2009)
GAGTA^^{2729}AAAACagAAAGAAAAAA	8191_8192delGA	Glu2731Lysfs*19	Primary Microcephaly	(Passemard et al., 2009)
AGTAAAA^^{2730}ACAgaaaGAAAAAACTT	8195_8198delGAAA	Arg2732Lysfs*4	Primary Microcephaly	(Passemard et al., 2009)
AGAAAGA^^{2733}AAAaaCTTTTTAGCA	8200_8201delAA	Asn2734Leufs*16	Primary Microcephaly	(Sajid Hussain et al., 2013)
GAAGGT^^{2792}GTTAtGATTCAAGAG	8378delT	Met2793Argfs*27	Primary Microcephaly	(Nicholas et al., 2009)
TGGAA^^{2835}ACACAgaAATGTGCTGC	8508_8509delGA	Lys2837Metfs*34	Primary Microcephaly	(Bond et al., 2003)
AACCAGA^^{2877}AAAcaGTTTTTACTA	8632_8633delCA	Gln2878Valfs*5	Abnormality of the nervous system	(Retterer et al., 2016)
TCTGCA^^{2900}AAACaTCAAAGACAA	8702delA	His2901Leufs*37	Primary Microcephaly	(Létard et al., 2018)
CATCAA^^{2903}AGACaaGTCTATTTAC	8711_8712delAA	Gln2904Argfs*15	Primary Microcephaly	(Tan et al., 2014)
GATAT^^{2947}AGAGCcAAGAAATATT	8844delC	Lys2949Argfs*7	Primary Microcephaly	(Nicholas et al., 2009)
CTCAT^^{3022}GAACActtcttaATGATAAAA_EI_G	9069_9075delCTTCTTA	His3023Glnfs*2	Primary Microcephaly	(Létard et al., 2018)
CTTCGG^^{3052}CAGAaATCTGCTGCT	9159delA	Lys3053Asnfs*5	Primary Microcephaly	(Bond et al., 2002)
TAGAA^^{3102}CAGAGagCCAAAATTCG	9309_9310delAG	Arg3103Serfs*20	Primary Microcephaly	(Tan et al., 2014)
TTTAAACAG_IE_Aga^^{3150}TGGTTTCGAG	9446_9447delGA	Arg3149Metfs*17	Primary Microcephaly	(Létard et al., 2018)
GCATC^^{3168}AAAAAgATTGAGCATG	9507delG	Ile3170Leufs*9	Primary Microcephaly	(Passemard et al., 2009)
GATTGT^^{3227}ACAAaAATTAAAGCT	9685delA	Ile3229Leufs*6	Primary Microcephaly	(Nicholas et al., 2009)
TGTACA^^{3228}AAAAttaaaGCTATACGAC	9686_9690delTTAAA	Ile3229Serfs*10	Primary Microcephaly	(Passemard et al., 2009)
AGAAGAA^^{3247}AACaaacTCTACAAAAG	9742_9745delAAAC	Lys3248Serfs*13	Primary Microcephaly	(Okamoto et al., 2018)

AAAAC^$^{\mathbf{3248}}$AAACTctACAAAAGAAC	9747_9748delCT	Tyr3250Glnfs*14	Primary Microcephaly	(Nicholas et al., 2009)
AACTC^$^{\mathbf{3250}}$TACAAaAGAACTGCAC	9754delA	Arg3252Glufs*10	Primary Microcephaly	(Bond et al., 2003)
GCAGTT^$^{\mathbf{3337}}$TATGaTGTAGAAAAT	10013delA	Asp3338Valfs*2	Primary Microcephaly	(Khan et al., 2017)
AGATAAC^$^{\mathbf{3456}}$ATGgAAGAAATCAC	10369delG	Glu3457Lysfs*13	Primary Microcephaly	(Létard et al., 2018)

Table 8.4 – Small insertions found in ASPM.

Small insertion	Nucleotide	Protein	Reported phenotype	Reference
TCAGA^^{647}ACTCCcAATTTCTAAA	1943dupC	Ile649Asnfs*3	Primary Microcephaly	(Létard et al., 2018)
CTGCA^^{687}AAAAAaCATGTTTTAT	2063dupA	Asn688Lysfs*5	Primary Microcephaly	(Létard et al., 2018)
TGCGC^^{978}CTTGTt_E10I10_GTACGTATAA	2936dupT	Not yet available	Primary Microcephaly	(Tan et al., 2014)
CATGC^^{1089}CATTCcTGATGATCTT	3269dupC	Asp1091*	Primary Microcephaly	(Létard et al., 2018)
CTTCTAT^^{1128}AATtAAAAAG_EI_GTAA	3384dupT	Lys1129*	Primary Microcephaly	(Bhargav et al., 2017)
TGCAGCA^^{1320}CTCaGTCATTCAGA	3960_3961insA	Val1321Serfs*29	Primary Microcephaly	(Tan et al., 2014)
GCTACA^^{1398}GTTAaCAATTCAGAG	4195dupA	Thr1399Asnfs*20	Primary Microcephaly	(Desir et al., 2008)
CAATCA^^{1665}TATTatattATCGTGCTTA	4994_4998dupATTAT	Arg1667Ilefs*12	Primary Microcephaly	(Létard et al., 2018)
ATACA^^{1868}AGAACcACATTTTTTG	5606dupC	His1870Thrfs*26	Primary Microcephaly	(Kraemer et al., 2016)
AGCTGTT^^{2171}AAAaGTCCTTCAGG	6513dupA	Val2172Serfs*7	Primary Microcephaly	(Létard et al., 2018)
TACTATT^^{2436}TTTtGTTCAGAGGA	7308dupT	Val2437Cysfs*14	Primary Microcephaly	(Tan et al., 2014)
CATAAAA^^{2619}AAAaCAGATTCAGG	7857dupA	Gln2620Thrfs*17	Primary Microcephaly	(Tan et al., 2014)
GAAAG^^{2684}GATATatTCAAAATATG	8053_8054dupAT	Gln2686Phefs*10	Intellectual disability	(Hu et al., 2019)
CAAGCA^^{3039}CATTcattATAGAGGATA	9115_9118dupCATT	Tyr3040Serfs*3	Primary Microcephaly	(Gul et al., 2006)
AAAAT^^{3225}GATTGgTACAAAAATT	9677dupG	Cys3226Trpfs*5	Primary Microcephaly	(Muhammad et al., 2009)
TTTTG^^{3351}CAGATggATACCGAGAA	10055_10056insGG	Ile3352Metfs*30	Primary Microcephaly	(Alby et al., 2016)

Table 8.5 – Small indels found in ASPM.

Small indel	Nucleotide	Protein	Reported phenotype	Reference
TATCACT^^{2866}TTAcAGCATTATTT **Ins:** at	8599delCinsAT	Gln2867Ilefs*5	Primary Microcephaly	(Létard et al., 2018)
TGTCT^^{2899}GCAAAacaTCAAAGACAA **Ins:** cc	8700_8702delACAinsCC	Lys2900Asnfs*38	Primary Microcephaly	(Létard et al., 2018)

Table 8.6 – Gross deletions found in ASPM.

Gross deletion	Nucleotide	Protein	Reported phenotype	Reference
21844 bp incl. ex. 2-13	c.298-581_3391-242del21845	Pro100_Lys1130del	Primary Microcephaly	(Nicholas et al., 2009)
entire gene	Not yet available	Not yet available	Primary Microcephaly	(Passemard et al., 2009)

Table 8.7 – Complex rearrangement found in ASPM.

Complex rearrangement	Reported phenotype	Reference
Translocation t(1;4)(q31;p15.3)	Primary Microcephaly	(Pichon et al., 2004)